Low Temperature Heat Capacities of SrF_2 and Other Fluoride Compounds

Lawrence T. Ho

Institute of Physics, Academia Sinica

Taipei, Taiwan

D. P. Dandekar

Army Materials and Mechanics Research

Center, Watertown, MA 02172

and

James C. Ho

Physics Department, Wichita State University,

Wichita, KS 67208

Heat capacity measurements between 2 and 22K have been made on SrF_2, yielding a limiting value of Debye temperature $\Theta_D(0)$=385K. A brief review is then given, for various fluoride compounds XF_2 (X= Ba, Ca, Cd, Mn, Pb and Sr), on the general agreement between their $\Theta_D(0)$ values as determined from calorimetric measurements and those from elastic constant measurements, as well as on the general trend of deviations of their lattice heat capacity from a simple Debye behavior.

This article describes low temperature heat capacity of SrF_2, similar to those previously reported on several other fluoride compounds: CaF_2, [1] MnF_2, [2] CdF_2, [3] BaF_2, [4] and PbF_2 [5]. Discussions center around their deviations from a simple Debye behavior, as well as the general agreement between the limiting values of Debye temperature $\Theta_D(0)$ as obtained from calorimetric and elastic constant measurements.

The 72-g, single crystal SrF_2 sample was obtained from the Harshaw Chemical Company. Heat capacity measurements by standard adiabatic calormimetry were made between 2 and 22K. Sample temperature determinations were based on the electrical resistance of

a precalibrated germanium thermometer. Pulsed Joule heating was obtained by passing a current through a manganin wire which, along with the thermometer, was thermally anchored to the sample. The heat capacity of the thermometer-heater assembly was separately measured for addenda corrections, ranging from 10 to 30% of the total measured heat capacity at 22 to 2K.

Figure 1 shows experimental data in the format of C/T^3 versus T^2. They can be well fitted as

$$C = .1023T^3 + .9599\times10^{-4}T^5 + .3577\times10^{-7}T^7 - .2946\times10^{-9}T^9 + .2325\times10^{-12}T^{11} \quad (1)$$

Such a least-square fit is typical for the lattice heat capacity of solids at low temperatures.[6] The coefficient of the dominating T^3 -term is proportional to $\Theta_D(0)^{-3}$; in this case $\Theta_D(0)$ is thus obtained as 385 K. Another conventional way of representing the same set of heat capacity data is shown in Figure 2 in terms of temperature-dependent Θ_D values based on the Debye function: [7]

$$\Theta_D = 384.8 - .1229T^2 + .6856\times10^{-4}T^4 + .1503\times10^{-6}T^6 - .1618\times10^{-9}T^8 \ . \quad (2)$$

Since the Debye model only predicts relatively small deviations from a constant C/T^3 or Θ_D value at reasonably low temperatures (e.g., $T<\Theta_D(0)/10$), for most solids higher order terms in both equations have no easily identifiable physical significance. They are basically associated with dispersion in the phonon spectrum. However, recent experiments on a number of materials indicated that their more substantial deviations from the Debye behavior can be explained with additional Einstein type contributions.[8] The latter has an exponential temperature dependence, yielding a maximum in C/T^3 at about $\Theta_E/3$, where Θ_E is the characteristic Einstein temperature (a fitting parameter). Since most of these materials are para-, ferro- or antiferroelectrics, Lawless[8] suggested that the somewhat unexpected Einstein contributions were associated with the presence of soft phonon modes. Among the six fluoride compounds being considered here, only BaF_2[4] and α- and β-PbF_2[5,8] have been reported to exhibit C/T^3 peaks. These peaks were suggested to be associated with zone boundary transverse acoustic modes in BaF_2[4] and β-PbF_2, and a Raman-active mode (A_{1g} + B_{2g}) involving lead atoms in α-PbF_2.[9] However, these suggestions await (low-temperature) experimental confirmations. Also the alternative interpretation of Burns[10] for the C/T^3

peaks should not be ignored.

While the lack of direct observations of low lying modes at low temperatures in these materials makes the interpretation uncertain, it is of further interest to realize that both BaF_2 and PbF_2 involve heavier elements. Pederson and Brewer[11] recently pointed out a linear relationship between $\Theta_D(0)$ and the reduced mass $\mu = M_X M_F/(M_X + 2M_F)$ for cubic fluoride compounds. Consequently, one would expect a more meaningful comparison by scaling the temperature with individual $\Theta_D(0)$ values. Such a comparison is shown in Figure 3, along with a curve representing the Debye function. There are clearly different degrees of deviations from the Debye behavior, but one feature is apparent: For compounds without known C/T^3 peaks, the heat capacity data cover relatively small reduced temperature $T/\Theta_D(0)$ ranges. In this respect, one can not rule out the possibility of having a C/T^3 peak for SrF_2 at higher temperatures not covered by the experiment.

Finally, Table 1 shows comparisons between $\Theta_D(0)$ values as calculated from calorimetric and elastic constant data. Excellent agreement prevails in all six fluoride compounds, including the non-cubic MnF_2 and PbF_2. In this respect, Figure 3 also supports the generally applied approximation in assuming the lattice heat capacity to have a simple T^3 dependence at temperatures below about $\Theta_D(0)/50$. Even for SrF_2, such an assumption would introduce an error in $\Theta_D(0)$ of less than 2%. However, precautions should still be taken when dealing with much more complicated situations for very anisotropic solids.[18]

Acknowledgment: The authors would like to thank Dr. John J. Fontanella of US Naval Academy for providing the SrF_2 sample and for helpful discussions.

REFERENCES

(1) D. R. HUFFMAN and M. H. NORWOOD, Phys. Rev. 117, 709 (1960).

(2) A. J. HENDERSON, Jr., H. MEYER and H. J. GUGGENHEIM, J. Phys. Chem. Solids 32, 1047 (1971).

(3) D. O. PEDERSON ,J. A. BREWER AND J. C. HO ,Phys. Rev. B 17, 866 (1978).

(4) D. P. DANDEKAR, J. FONTANELLA, C. L. HUOH and J. C. HO, Phys. Rev. 26, 2264 (1982).

(5) D. P. DANDEKAR, J. J. TSOU and J. C. HO, Phys. Rev. B 20, 3523 (1979).

(6) See, e.g. T. H. K. BARRON and J. A. MORRISON, Can. J. Phys. 35, 799 (1957).

(7) See, e.g. E. S. R. GOPAL, Specific Heat at Low Temperatures (Plenum, New York, 1966).

(8) W. N. LAWLESS, Phys. Rev. B 14, 134 (1976); Phys. Rev. B 17, 1458 (1978).

(9) G. A. OZIN, Can. J. Chem. 48, 2931 (1970).

(10) G. BURNS, Solid State Commun. 35, 811 (1980).

(11) D. O. PEDERSON and J. A. BREWER, Phys. Rev. B 16, 4546 (1977).

(12) R. L. MELCHER, Phys. Rev. B 2, 733 (1970). See corrected $\Theta_D(0)$ value in Rev. 2.

(13) D. GERLICH, Phys. Rev. 136, A1366 (1964).

(14) D. GERLICH, Phys. Rev. 135, A1331 (1964).

(15) J. H. WASILIK and M. L. WHEAT, J. Appl. Phys. 36, 791. (1965).

(16) S. HART, J. Phys. D: Appl. Phys. 3, 430 (1970).

(17) D. P. DANDEKAR (unpublished)-- based on room-temperature sound velocity measurements on seven orthorhombic samples with specific density between 6.92 and 7.38.

(18) See, e.g. C. W. GARLAND and J. SILVERMAN, Phys. Rev. 34, 781 (1961).

Table 1. Limiting Values of Debye Temperature for Various Fluoride Compounds

Compound	Reduced mass*	Structure	$\Theta_D(0)$ in K (From Heat capacity data)	$\Theta_D(0)$ in K (From elastic constant data)
CaF_2	9.75	Cubic (fluorite)	508 ± 5 (Huffman and Norwood - Ref. 1)	513.6 ± 2.5 (Huffman and Norwood - Ref. 1)
MnF_2	11.23	Tetragonal (rutile)	463 ± 5 (Henderson et. al. - Ref. 2)	475 ± 10 (Melcher - Ref. 12)
SrF_2	13.25	Cubic (fluorite)	385 (This work)	380 (Gerlich Ref. 13)
CdF_2	14.20	Cubic (fluorite)	332.0 ± 1.0 (Pederson et al. - Ref. 3)	331.6 ± 0.7 (Pederson and Brewer - Ref. 11)
BaF_2	14.88	Cubic (fluorite)	286 (Dandekar et al. - Ref. 4)	282 (Gerlich - Ref. 14)
PbF_2	16.06	Cubic (fluorite)	225 (Lawless - Ref. 8) 237 (Dandekar et al. - Ref. 5)	221 ± 3 (Wasilik and Wheat - Ref. 15; Hart - Ref. 16)
PbF_2	16.06	Orthorhombic ($PbCl_2$)	188 (Dandekar et al. - Ref. 5)	185 ± 5 (Dandekar - Ref. 17)

*$\mu = M_X M_F/(M_X+2M_F)$ - Ref. 11

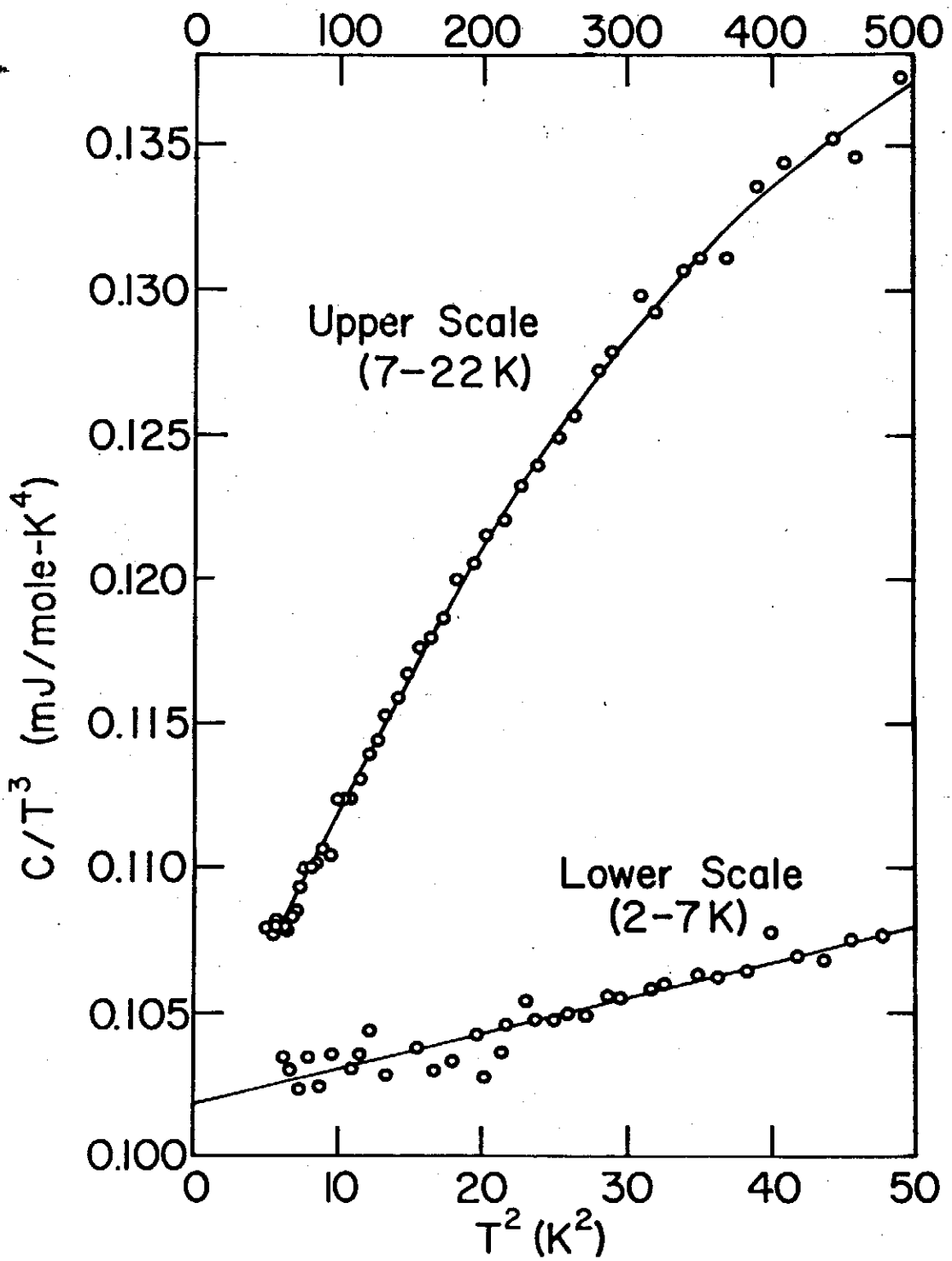

Figure 1. C/T^3 versus T^2 for SrF_2. The solid line represents least square fit of the data to Equation (1).

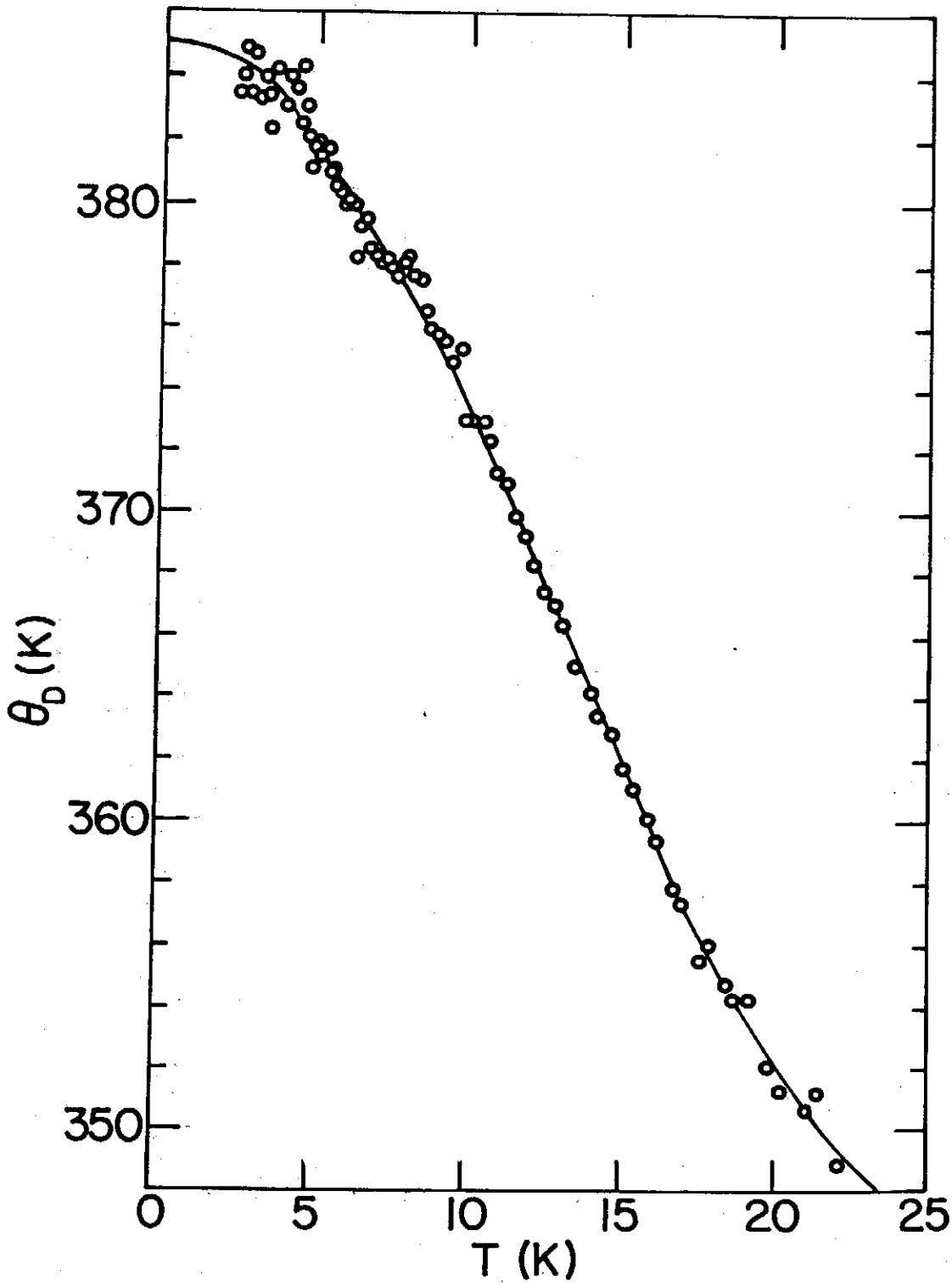

Figure 2. Temperature dependence of Θ_D for SrF_2 based on the same set of heat capacity data in Figure 1 and the Debye function.

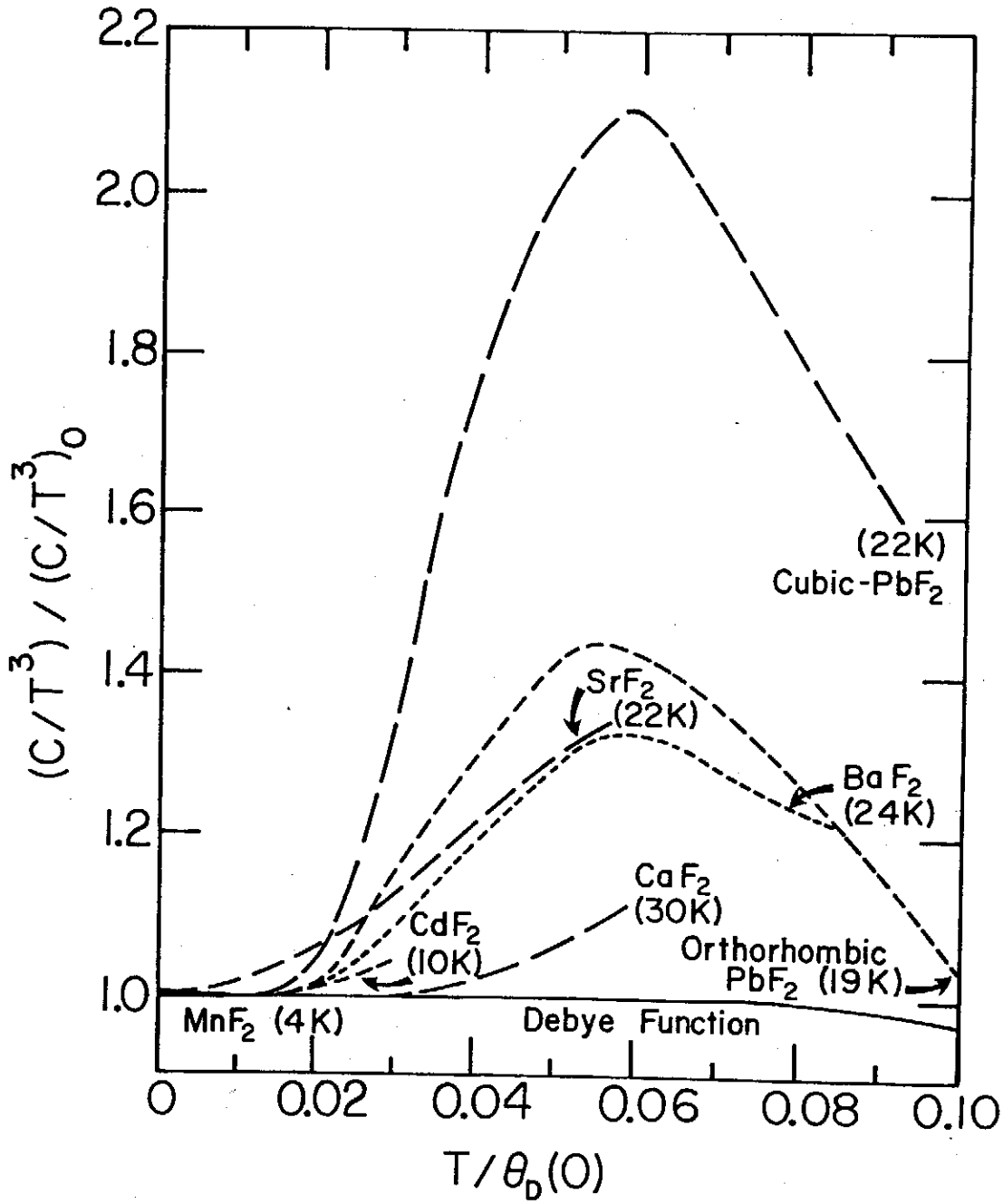

Figure 3. Lattice heat capacities of various fluoride compounds -- deviations from a constant T^3 -dependence as a function of reduced temperature. Maximum temperature of data represented for each compound is given in parentheses.

ANNUAL REPORT

of

THE INSTITUTE OF PHYSICS

ACADEMIA SINICA

VOLUME 12 DECEMBER 1982

THE INSTITUTE OF PHYSICS, ACADEMIA SINICA

TAIPEI, TAIWAN, REPUBLIC OF CHINA

中央研究院物理研究所集刊

發 行 人 (Publisher)
林 爾 康 (E. K. Lin)

執行編輯 (Executive Editor)
謝 雲 生 (W. S. Tse)

The Annual Report is published annually by the Institute of Physics, Academia Sinica, Taipei, Taiwan 115, Republic of China.

本集刊每年出版一次

非　賣　品

中央研究院

物理研究所集刊

第十二卷

發行人：林　爾　康

編輯者：中央研究院物理研究所集刊編輯委員會

出版者：中央研究院物理研究所　臺北市南港區

印刷者：萬達打字印刷有限公司

電話：三九四〇七一八

中華民國七十一年十二月出版

中央研究院物理研究所集刊

第十二卷

中央研究院物理研究所印行

CONTENTS 目 錄

ARTICLES

Nonlinearly Coupled Oscillators..... Ta-You Wu.... 1
Low Temperature Heat Capacities of SrF_2 and Other Fluoride Compounds..L. T. Ho, D. P. Dandekar and J. C. Ho.... 10
Ferromagnetic Multifilamentary Composites Produced by Cold Powder Metallurgy Processing....Y. D. Yao and S. Foner.... 18
On the Stability, Switching Voltage and Transient on-Characteristics of Amorphous Thin Films..... C. Chiang.... 29
Multidyon Solutions in SU(2) Gauge Group.....
.....J. C. Shaw and J. C. Chen.... 37
Force Constant Model of Crystalline HI in its Low Temperature Phase .....C. N. Chang and W. S. Tse.... 54
Lattice Vibrations of Solid Hydrofluoride Acid.....
..... W. S. Tse and C. N. Chang.... 59
Lattice Dynamics of the Hydrogen Halide Crystals.....
..... C. N. Chang, W. S. Tse and L. Chang.... 67
Impulsively Started Viscous Flow Over A Rotating Circular Cylinder.....L. C. Chien and C. S. Chen.... 77
Modified Differential Quarature Method for Numerical Solution of Primitive Equations ..... L. C. Chien..... 87
小型質子加速器之研製 …… 程斌、陳志遠、陳明壽、江紀成、王建萬 …· 103

密度層變流通過障礙體受阻的數值研究 ……黃榮鑑、蔣修德… 119
垂直浮昇射流在靜止密度層變水域中之浮昇與混合研究
……蔡西銘、黃榮鑑、王德忠… 140
氣象衛星遙測資料之應用——海面溫度之求取 ……曾忠一、曹幼民… 166
空氣品質監測系統之設置原理與應用……梁文傑、林釗信… 173

ABSTRACT

High Excited α Cluster State Calculation of Nuclei . . .
. . . . . S. Y. Lee, E. K. Lin and C. W. Wang... 238
The α—^{7}LI and α—^{12}C Elastic Scattering At E = 5, and
6, MEV. . . . . C. W. Wang, G. C. Kiang,
L. L. Kiang, G. C. Jon and E. K. Lin... 239
Excitation Spectrum of Neutral and Singly Ionized
Beryllium Acceptors in Germanium. . . . . .
. . . . . L. T. Ho, J. W. Cross, A. K. Ramdas and R. Sauer... 240
Excitation Spectrum of Magnesium Acceptors in Germanium
. . . . . L. T. Ho, J. W. Cross and A. K. Ramdas... 241
The Influence of Cr and W Contents on The Isomer Shift,
Hyperfine Field Distribution, and Magnetic Anisotropy
of Fe-Based Amorphous Alloys. . . . . S. T. Lin, L. Y. Jang,
W. T, Ku, L. S. Chou and Y. D. Yao... 242
Electrical Resistivity and Magnetoresistivity of Amorphous
$Fe_{80}B_{20}$, $Fe_{80}B_{18}Si_2$, $Fe_{80}B_{13}Si_4C_3$ and $Cu_{60}Zr_{40}$
Alloys. . . . . Y. D. Yao, S. Arajs and S. T. Lin... 243
Electrical Magnetoresistivity of Amorphous $(Fe\text{-}Ni)_{80}B_{20}$,
$(Fe\text{-}Ni)_{80}P_{14}B_6$, $(Fe\text{-}W)_{80}B_{14}Si_6$, and $(Fe\text{-}Cr)_{80}B_{14}Si_6$
Alloys. . . . . Y. D. Yao, S. Arajs and S. T. Lin... 244
Surface Effects on Raman Scattering From Semi-Metal Sb
Deposited on Island Ag Films . . . . . N. T. Liang, T. T. Chen,
. . . . . Hua Chang, Y. C. Chou and Shou-Yih Wang... 245
Observations of Crystalline and Amorphous Sb Films by
Raman Scattering. . . . . N. T. Liang, Y. C. Chou,

.....Shou-Yih Wang,and Hua Chang... 246
Inhibition of Dopamine Biosynthesis by Gonadotropin-
Releasing Hormone in Rat.....
.....W. K. Wang, L. S. Jeng, Y. Chiang and N. K. Chien... 247
Heat Transfer From an Impulsively Started Circular
Cylinder.....Lai-Chen Chien and In-Shieh Kung... 248
Laboratory Study on the Two-Dimensional Flows of
Stratified Fluids over Barriers.....
.....Robert R. Hwang and Shain-Way Jang... 249
Mixing and Diffusion of Heated Water Discharge for
Power Plants.. Robert R. Hwang, S. W. Jeng and B. S. Shiau... 250
Numerical Study on Flow Developments for the Rise of
Buoyant Plumes in a Stratified Environment.....
..... Robert R. Hwang and Chyi-Jang Shiau... 251
Viscous Flows of Stably Stratified Fluids over Semi-
Circular Obstacles .....Robert R. Hwang and Shain-Way Lang... 252
用有限元素法進行正壓原始方程式預報…曾忠一、潘陵華、李永安... 253

RESEARCH PROPOSAL

Boson Mapping in The Deformed Nilsson Scheme.....
..... H. T. Chen, S. Y. Lee, L. Lin and S. F. Tsai... 254
Systematic Analysis of Medium Heavy Spectroscopy in
The Interacting-Boson Model .....
..... H. C. Chiang, S. T. Hsieh, M. M. King, S. Y. Lee... 255

NONLINEARLY COUPLED OSCILGATORS: DYNAMICS AND STATISTICAL MECHANICS

Ta-You Wu

Institute of Physics, Academia Sinica

Nankang, Taipei

In connection with the principle of equipartition of energy, the distinction between strict dynamics and statistical theory is illustrated by an example of two oscillators coupled by anharmonic potentials. Instead of solving an initial value problem in dynamics (such as in the work of Fermi-Pasta-Ulam), an element of randomness is introduced by the use of two independent time scales, a fast time for the oscillations and a slow time for the energy transfer due to the non-linear coupling. The non-linear equations of motions have been solved by numerical integration. The result is that an initial state of excitatin does not recur as in Fermi-Pasta-Ulam's work, but approaches asymptotically (logarithmically) a redistributed state.

I. SYSTEMS GOVERNED BY DYNAMICS

In the classic study of Fermi, Pasta and Ulam[1], it is found from a computer calculation that the motion from an initial state of excitation of a linear chain of 64 particles coupled by anharmonic forces does not tend to an equipartition of energy among the various modes of motion, but exhibits a recurrence (i.e., periodic) behavior. This result was unexpected and therefore exciting since it has been generally thought that even in dynamics, any nonlinear coupling will cause any initial mode of excitation to redistribute its energy into other modes of oscillation. In a more learned parlance, the implication of the Fermi-Pasta-Ulam result is as follows. In classical dynamics, a system of harmonic oscillators is a "completely integrable system" and the motion is (multiply) periodic. It was believed that when the oscillators are nonlinearly (i.e., anharmonically) coupled, the motion will in general have no more first integrals other than the energy integral and the system will become

godic. It is the recurrence (soliton) behavior of Fermi-Pasta-Ulam's solution that was ought to be "unexpected". This result has since excited extensive studies from the point view of solitons by many authors.

Since the late 1950's and the early 1960's, there have been great advances in the udies of classical dynamical systems. It was shown by Kolmogorov[2], Arnold[3] and Moser[4] at under certain conditions of "small" perturbations (nonlinearity), the multiply periodic tion of the original completely integrable system remains "stable", i.e., will not become godic. On the basis of this so-called KAM Theorem, the recurrence behavior shown in Fermi-sta-Ulam's work is then understandable.

It remains then to bridge an apparent "gap" between this nonergodic behavior of system of nonlinearly coupled oscillators and the principle of equipartition of energy in atistical mechanics.

II. Introduction of Statistical Elements

Let us recall that in statistical mechanics, one arrives at the principle of ipartition of energy not from dynamics, but through statistical methods, such as that of ensemble[5]. Had the ergodic hypothesis of Maxwell and Boltzmann been valid, then, only then, could the equipartition of energy be considered a consequence of classical amics (through the theorem that shows the equality of the "long time average" of the tem and the "ensemble average"). But when a system is not ergodic (on the Kolmogorov-old-Moser theorem), one cannot hope to arrive at the equipartition principle on dynamics ne. The derivation of the equipartition principle by the use of the ensemble comes ut only because of the statistical element of the ensemble concept.

From this point of view, we propose, in the present work, to introduce an element randomness in a dynamical system through an artifice other than that of the ensemble hod, namely, the method of independent multiple time scales.

The method of independent time scales originates with Krylov and Bogoliubov[6] treating the nonlinear problems of systems having complicated time behavior. It was adopted Frieman and by Sandri in the kinetic theory of gases (and Plasmas)[7]. The characteristic e scales are short "time of a collision" between two molecules, the long "time between two cessive collisions" and the still longer time of relaxation of the gas to equilibrium. On

assuming these time scales to be independent, the description of the complicated motion of a gas is successively reduced from the Liouville equation, to the Boltzmann equation and finally to the hydrodynamical equations.

III. Nonlinearly Coupled Oscillators: Independent Time Scales

To test the effect of independent time scales as an element of randomness into a dynamical system on the long-time behavior of the system, we shall start with the simplest of systems, namely, two nonlinearly coupled oscillators. Let two harmonic oscillators of frequencies ω_1 and ω_2 be coupled by weak anharmonic potentials. This weak coupling causes a transfer of excitation between the two oscillators, in a time scale τ_1 which is very long compared with the time scale τ_0 defined by the frequencies ω_1 and ω_2. Now an element of randomness is introduced by assuming the two time scales τ_0 and τ_1 to be independent, thereby changing the nature of the system from strict dynamical to probabilistic. Of course, for a system consisting of only two oscillators, a probabilistic theory does not have meaning. We are to understand the assumption of two independent time scales in the following sense: we are viewing the average behaving of a large collection (ensemble) of systems each consisting of two oscillators.

Let a system of two harmonic oscillators be linearly coupled,

$$\begin{aligned} 2T &= \dot{y}_1^2 + \dot{y}_2^2 \\ 2V_o &= \lambda_1 y_1^2 + \lambda_2 y_2^2 + 2B y_1 y_2 \end{aligned} \tag{1}$$

The normal vibrations are given by a transformation to the normal corrdinates X_1, X_2

$$(y_1, y_2) = (X_1, X_2) \begin{pmatrix} \cos\theta & -\sin\theta \\ \sin\theta & \cos\theta \end{pmatrix} \tag{2}$$

where

$$\left.\begin{matrix} \cos\theta \\ \sin\theta \end{matrix}\right\} = \frac{1}{\sqrt{2}} \left[1 \pm \frac{\lambda_2 - \lambda_1}{(\lambda_2-\lambda_1)^2 + 4B^2}\right]^{\frac{1}{2}}$$

into

$$2T = \dot{X}_1^2 + \dot{X}_2^2 \ , \tag{3}$$

$$2V_o = \omega_1^2 X_1^2 + \omega_2^2 X_2^2 \ ,$$

with

$$\left.\begin{matrix}\omega_2^2 \\ \omega_1^2\end{matrix}\right\} = \frac{\lambda_1 + \lambda_2 \pm \sqrt{(\lambda_2-\lambda_1)^2 + 4B^2}}{2}$$

$$X_1 = A_1 \begin{cases} \cos\omega_1 t \\ \sin\omega_1 t \end{cases} , \qquad X_2 = A_2 \begin{cases} \cos\omega_2 t \\ \sin\omega_2 t \end{cases} \tag{4}$$

On introducing the anharmonic potential V_2 to (3),

$$V_1 = C(X_1^2 X_2 + X_1 X_2^2) + F(X_1^3 X_2 + \tfrac{3}{2} X_1^2 X_2^2 + X_1 X_2^3) \ , \tag{5}$$

the equations of motion are the nonlinear equations

$$\begin{aligned} \ddot{X}_1 &= -\omega_1^2 X_1 - C(2X_1X_2 + X_2^2) - F(3X_1^2X_2 + 3X_1X_2^2 + X_2^3) \ , \\ \ddot{X}_2 &= -\omega_2^2 X_2 - C(X_1^2 + 2X_1X_2) - F(X_1^3 + 3X_1^2X_2 + 3X_1X_2^2) \ , \end{aligned} \tag{6}$$

whose solutions are of course not given by (4) or any linear combinations of X_1 and X_2 in (4). But we may make the Ansatz that the solutions of (6) is of the form

$$\begin{aligned} \xi_1 &= \cos\theta \ X_1 + \sin\theta \ X_2 \\ \xi_2 &= -\sin\theta \ X_1 + \cos\theta \ X_2 \end{aligned} \tag{7}$$

where $\theta = \theta(t)$ is a function of time and

$$\cos^2\theta + \sin^2\theta = 1 \ .$$

Then substitution of ξ_1, ξ_2 for X_1, X_2 in (6) will lead to two nonlinear equations for $c \equiv \cos\theta$, $s \equiv \sin\theta$ in a strictly dynamical treatment of the coupled oscillators.

We shall assume that the X_1, X_2 in (2) are functions in the fast time scale τ_0 of $\frac{1}{\omega_1}$, $\frac{1}{\omega_2}$, while $\cos\theta$, $\sin\theta$ are functions in a slow time scale τ_1 determined by the nonlinear coupling C, F in (5), i.e.,

$$\xi_1(\tau_0, \tau_1) = c(\tau_1)X_1(\tau_0) + s(\tau_1)X_2(\tau_0) \ , \tag{7a}$$

$$\xi_2(\tau_0, \tau_1) = -s(\tau_1)X_1(\tau_0) + c(\tau_1)X_2(\tau_0) ,$$

where

$$c(\tau_1) = \cos\theta(\tau_1) , \qquad s(\tau_1) = \sin\theta(\tau_1) .$$

The assumption of two time scales τ_0, τ_1 is expressed by

$$\frac{d}{dt} = \frac{d}{d\tau_0} + (\varepsilon)\frac{d}{d\tau_1} . \tag{8}$$

where ε is of the order of the ratio $(V_1/V_0) << 1$. We shall point out that this weakness of anharmonic coupling is assumed to assure a vast difference in the time scales τ_0, τ_1 so that the assumption of their being independent may be more reasonable. In the following, no perturbation based on the smallness of ε is made.

Substitution of (7) and (8) into the equations of motion (6) leads to the following pair

$$\begin{aligned}\frac{d^2c}{d\tau_1^2}X_1 + \frac{d^2s}{d\tau_1^2}X_2 + 2\left(\frac{dc}{d\tau_1}\frac{dX_1}{d\tau_0} + \frac{ds}{d\tau_1}\frac{dX_2}{d\tau_0}\right) - s(\omega_2^2 - \omega_1^2)X_2 \\ = -C\left[(-2cs + s^2)X_1^2 + 2(c^2 - s^2 - cs)X_1X_2 + (2cs + c^2)X_2^2\right] \\ -F\left[(-3c^2s + 3cs^2 - s^3)X_1^3 + 3(c^3 - 2c^2s - cs^2 + s^3)X_1^2X_2\right. \\ \left. + 3(c^3 + c^2s - 2cs^2 - s^3)X_1X_2^2 + (c^3 + 3c^2s + 3cs^2)X_2^3\right]\end{aligned} \tag{9a}$$

$$\begin{aligned}\frac{d^2c}{d\tau_1^2}X_2 - \frac{d^2s}{d\tau_1^2}X_1 + 2\left(-\frac{ds}{d\tau_1}\frac{dX_1}{d\tau_0} + \frac{dc}{d\tau_1}\frac{dX_2}{d\tau_0}\right) - s(\omega_2^2 - \omega_1^2)X_1 \\ = -C\left[(-2cs + c^2)X_1^2 + 2(c^2 - s^2 + cs)X_1X_2 + (2cs + s^2)X_2^2\right] \\ -F\left[(c^3 - 3c^2s + 3cs^2)X_1^3 + 3(c^3 - c^2s - 2cs^2 + s^3)X_1^2X_2\right. \\ \left. + 3(c^3 + 2c^2s - cs^2 - s^3)X_1X_2^2 + (3c^2s + 3cs^2 + s^3)X_2^3\right]\end{aligned} \tag{9b}$$

The terms involving $\frac{d^2X_1}{d\tau_0^2}$, $\frac{d^2X_2}{d\tau_0^2}$ drop out by virtue of equations (3).

We shall now introduce a random element into the system by assuming the two time scales to be independent, in the sense that the fast time scale for the oscillations has arbitrary origin independent of that of slow time scale for the transfer of excitation. In studying the transfer of excitation between the two oscillators, we may average

over the fast oscillations $T_1 = \frac{2\pi}{\omega_1}$, $T_2 = \frac{2\pi}{\omega_2}$. Thus we shall average equations (9a), (9b) respectively over the periods T_2 and T_1. This averaging at the same time removes the second derivatives $\frac{d^2s}{d\tau_1^2}$ in both equations, as well as the linear term X_2 in (9a) and X_1 in (9b). From the two equations, we can eliminate $\frac{d^2c}{d\tau_1^2}$, and obtain a first order differential equation in c.

For generality, X_1, X_2 in (7a) may be taken to be

$$X_1 = A_1 \cos(\omega_1\tau_0 + \delta_1) , \qquad X_2 = A_2 \cos(\omega_2\tau_0 + \delta_2)$$

where δ_1, δ_2 are functions of the slow time τ_1. But on averaging over the fast time τ_0, only the relative phase $\delta_1-\delta_2$ is relevant, and during the short time T_1 or T_2, the relative phase is "constant". Hence

$$X_1 = A_1 \cos\omega_1\tau_0 , \qquad X_2 = A_2 \cos(\omega_2\tau_0 - \delta) \tag{10}$$

where δ is constant but arbitrary. It must be noted that an averaging over the arbitrary δ is not to be carried out, for then almost everything will vanish from equations (9). We have carried out the calculations for two special values of δ, namely $\delta = 0$ and $\delta = \frac{\pi}{2}$.

For the amplitudes A_1 and A_2, which are of dimension mass$^{\frac{1}{2}}$ x length, we take

$$(\omega_1 A_1)^2 = (\omega_2 A_2)^2 \tag{10a}$$

to insure energy constancy, and for the frequencies ω_1, ω_2 , to avoid resonance, we take

$$\omega_2^2 = 2\,\omega_1^2$$

For the anharmonic potentials, let

$$\frac{FA_1}{C} = -k, \qquad k > 0 , \qquad c < 0 \tag{10b}$$

and

$$-\frac{CA_1}{\omega_1^2} = \varepsilon .$$

We shall omit all the lengthy details which are elementary and give the resulting equation for $\theta(\tau_1)$ from (9a) and (9b):

For $\delta = \frac{\pi}{2}$,

$$\alpha \frac{dc}{d\tau_1} = \varepsilon[9.971\ c^2 - 3.976\ cs - 2.160\ s^2$$

$$- k(5.140\ c^2 s + 1.669\ cs^2 - 1.806\ c^3 + 0.150\ s^3)]$$

$$\alpha = -\frac{1.653}{\omega_1} . \tag{11}$$

For $\delta = 0$,

$$\alpha \frac{dc}{d\tau_1} = \varepsilon[4.6234\ c^2 - 3.6175\ cs + 0.4775\ s^2$$

$$- k(0.5044\ c^2 s + 0.5171\ cs^2 - 0.2767\ c^3 + 0.8396\ s^3)]$$

$$\alpha = -\frac{3.183}{\omega_1} . \tag{12}$$

A numerical integration shows that for both (11) and (12), the angle $\theta(\tau_1)$ approaches (logarithmically) asymptotically a constant θ_s as $\tau_1 \to \infty$, namely

$$\theta_s = 45°25' \qquad \text{in the case} \qquad \delta = \frac{\pi}{2} ,$$

$$\theta = 47°0' \qquad \text{in the case} \qquad \delta = 0 . \tag{13}$$

The solution of (11) is shown in curve (a) in the accompanying figure. In this case, the system asymptotically approaches, as $\tau_1 \to \infty$, the state

$$\xi_1 = 0.702\ A_1 \cos\omega_1\tau_0 + 0.712\ A_2 \sin\omega_2\tau_0$$

$$\xi_2 = -0.712\ A_1 \cos\omega_1\tau_0 + 0.702\ A_2 \sin\omega_2\tau_0$$

That in both cases the asymptotic state almost corresponds to a state of equipartition of energy is rather accidental, as the above result obviously depends on the model (such as the numerical values in (10a) and (10b)). The noteworthy feature of the result of the present work is that the introduction of a non-dynamical element (independent time scales in (7a)) has removed the recurring feature of a strictly dynamical treatment (Fermi-Pasta-Ulam) and led to an asymptotic approach to mixed state.

The nature of the asymptotic (instead of the recurring) behavior may be made clear by the following analytical treatment of the above problem simplified by taking only the cubic anharmonicities in (5) i.e., $k = 0$ in (11). In that case, the equation (11) can be integrated analytically, by noting

$$\frac{s}{f} = \frac{s}{9.9713\ c^2 - 3.9758\ cs - 2.1598\ s^2} \tag{14}$$

$$= \frac{0.14035}{a_1 c + b_1 s} - \frac{0.69687}{a_2 c + b_2 s}$$

where

$$a_1 = 1.4171, \qquad b_1 = -1\ ,$$

$$a_2 = 7.03645\ , \qquad b_2 = 2.1598\ ,$$

and

$$\int \frac{sd\theta}{f} = 0.14035\ \ell n\ \{\frac{\tan(\frac{\theta}{2} + 62°38')}{1.9320}\} \tag{15}$$

$$+ 0.69687\ \ell n\ \{\frac{\tan 126°28'}{\tan(\frac{\theta}{2} + 126°28')}\}$$

The first integral diverges logarithmically as

$$\theta \to 54°44'$$

while the second diverges logarithmically as

$$\theta \to 107°4'$$

Of course the first limit $\theta_s = 54°44'$ prevents the system from ever reaching the second θ_s, unless the initial conditions are changed. The result (15) is shown in curve (b), in the figure.

From (14) and (15), it is seen that each limiting θ_s corresponds to a zero of the expression $f = 0$ in (14). This applies also to (11)-(12).

To compare the above result, namely, of an asymptotic state with that of a strict dynamical treatment of the motion, we start with equs. (6) and again the Ansatz (7), but with only <u>one</u> time variable i.e., X_1, X_2, θ are all functions of the same time t. From equation (9a) and (9b), with $\tau_0 = \tau_1$, and

$$c^2 + s^2 = 1\ ,$$

we obtain a first-order equation in $\frac{d\theta}{dt}$. To simplify notation, let t be the dimensionless time $t = \omega_1 \tau_0$, so that, corresponding to the model (10a) and (11),

$$x \equiv x_1 = \cos t \ , \qquad y \equiv x_2 = \frac{1}{\sqrt{2}} \sin \sqrt{2}\ t$$

$$c \equiv \cos\theta \ , \qquad s \equiv \sin\theta \ ,$$

with k = 1,

$$\begin{aligned}(x^2 + y^2)(\frac{d\theta}{dt})^2 - 2(x \frac{dy}{dt} - y \frac{dx}{dt}) \frac{d\theta}{dt} \\ = - \{2xyc + (y^2 - x^2)s\}\, s \\ + \varepsilon\{3xy(x + y)c^3 - 3(x^3 + 2x^2y - 2xy - y^3)\, c^2 s \\ + 3(x^3 - 2x^2y - 2xy^2 + y^3)cs^2 + 3xy(x - y)s^3 \\ - 2(2x^2 + 3xy + 2y^2)xyc^4 + 4(x^4 + 3x^3y - 3xy^3 - y^4)c^3 s \\ - 6(x^4 - 4x^2y^2 + y^4)c^2 s^2 + 4(x^4 - 3x^2y + 3xy^2 - y^4)cs^3 \\ + 2(2x^2 - 3xy + 2y^2)xy\, s^4\}\end{aligned} \tag{16}$$

The initial condition is

$$c = 1 \ , \quad s = 0 \ , \quad (\frac{d\theta}{dt} = 0) \text{ at } t = 0 \ .$$

Integration of equ. (16) with the aid of a computer shows that, for $\varepsilon = 10^{-2}$, 10^{-3} up to $t = 10^4$, 10^5, θ oscillates and does not show the asymptotic behavior of the figure.

The author wishes to thank Professor C. S. Hsue of the Physics Department, National Tsinghua University, for performing the computer calcuations of equation (16); and Professor Y. C. Lee, of the Physics Department, State University of New York at Buffalo, for his interest and discussions.

REFERENCE

(1) E. FERMI, J. R. PASTA and S. M. ULAM, Los Alamos Sci. Lab. Rep. LA-1940, (1955); in Collected Works of Enrico Fermi, 2, 978, Univ. of Chicago Press.

(2) For literature up to 1973, cf. article by A. C. SCOTT, F. Y. F. CHU and D. W. MCLAUGHLIN, Proc. IEEE, 60, 1443 (1973).

(3) N. M. KRYLOV and N. N. BOGOLIUBOV, Introduction to Nonlinear Mechanics, (1937), translated by S. LEFSHETZ, Princeton Univ. Press (1947).

(4) N. N. BOGOLIUBOV, Monograph in Studies in Statistical Mechanics, ed. J. de BOER and C. E. UHLENBECK, N-Y., Interscience Publ. 1962; E. A. FRIEMAN, J. Math. Phys. 4, 410 (1963); G. SANDRI, Ann. Phys. 24, 322 (1963); cf T. Y. WU, Kinetic Equations of Gases and Plasmas, chap. 3, sects. 1, 6, Addison-Wesley, 1966.

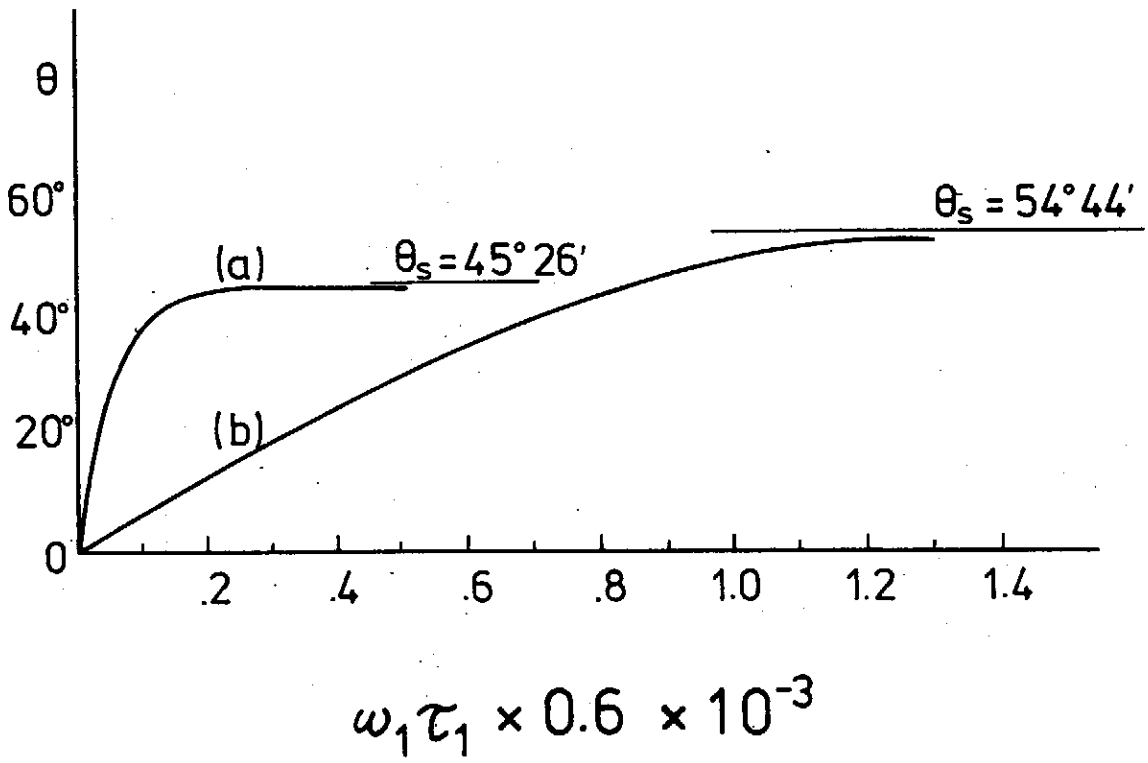

(a) Solution of equation (11), with k = 1

(b) Solution of equation (11), with k = 0

FERROMAGNETIC MULTIFILAMENTARY COMPOSITES PRODUCED BY COLD POWDER METALLURGY PROCESSING

Y. D. Yao

Institute of Physics, Academia Sinica

Taipei, Taiwan, R.O.C.

and

S. Foner

Francis Bitter National Magnet Laboratory,

Massachusetts Institute of Technology,

Cambridge, MA 02139 U.S.A.

Powder-metallurgy-processed multifilamentary Cu-Fe, Cu-Ni and Nb-Ni ferromagnetic composite wires were fabricated with a relatively high coercive field, H_c, at room temperature. Compacts of Cu-36 wt.% Fe, Cu-36 wt.% Ni and Nb-36 wt.% Ni powders were reduced in cross section to produce ferromagnetic multifilamentary materials. Areal reduction ratios of 10^8 for Cu-36 wt.% Fe and 10^4 for Nb-36 wt.% Ni and Cu-36 wt.% Ni resulted in values of $H_c \sim 195$ Oe, 94 Oe and 77 Oe respectively. A final 300° C anneal of the Cu-36 wt.% Fe composite gave $H_c \sim 460$ Oe. The average ferromagnetic fiber diameters are estimated to be 100 Å to 1,000 Å for the Fe fibers and are about 1 μ for the Ni fibers.

The technology for cold powder metallurgy processing of ultrafine fiber multifilamentary superconducting materials was pioneered at the National Magnet Laboratory, MIT in recent years[1-3]. In this letter we present results for powder metallurgy processed multifilamentary Cu-Fe, Cu-Ni and Nb-Ni ferromagnetic composites with a relatively high coercive field, H_c. The values of H_c at room temperature of Cu-Fe samples are comparable to those made by multifilamentary composites of Cu-Fe made by the In Situ process and reported recently[4,5]. In order to achieve the multifilamentary ferromagnetic structure the In Situ process requires that the ferromagnetic phase precipitate out of the melt.

Thus the particular composites are limited by the phase diagram of the starting alloys. As indicated in the super conductor development[1-3], the powder process avoids the limitations of the phase diagram because the powders are physically mixed and processed at low temperatures. Thus multifilamentary materials can be produced over a wide ragne of compositions and there is considerable flexibility of choice of the matrix (which also may be magnetic). The present results show that powder metallurgy processing may be used to fabricate novel magnetic (and non-magnetic) fine fiber composites. In addition, this process can be used for materials which cannot be fabricated by the In Situ process, for example, for Cu-Ni composites.

The procedure we employed followed that developed for superconducting materials[1-3]. Ductile powders of say Cu and a ferromagnetic metal were compacted in a copper tube, and the cross section of the compact was reduced by swaging, rolling, and wire-drawing to produce long submicron ferromagnetic fibers in the Cu-matrix[6]. Starting with 40 μm diameter ferromagnetic powders, an areal reduction ratio of 10^6 would yield elongated ferromagnetic fibers with average diameters of ≅ 400 Å. The fibers are protected from external oxidation by the matrix. An essential requirement is that the powders be ductile. The fabrication approach parallels much of the technology developed for superconducting materials. From a basic point of view this approach permits fabrication of a high density of nearly one-dimensional conductors. (They need not be ferromagnetic or superconducting.) In principle the limits are set by the deformability of the elemental powders. The composition is determined by physical mixing and is not influenced by any phase diagrams of an alloy unless high temperature heat treatments are carried out during the areal reduction.

Copper tubes with ∿ 12.7 mm o.d. and ∿ 11.1 mm i.d. were used as an external jacket to contain the powders. The mixed powders were tapped into the Cu tube, the tube was evacuated, and then the compact was swaged and wire drawn to final size. Using ∿ 100 μm Ni and ∿ 60 μm Nb or Cu powders, we have made a series of powder metallurgy processed filamentary ferromagnetic Cu-Ni and Nb-Ni materials both containing 36 wt.% Ni. Swaging techniques were used for the preliminary elongation, and the remaining deformation to a wire with a final outer diameter of ∿ 0.125 mm was made by wire drawing. Nominal areal reduction ratios, R, of 10^4 were obtained without any intermediate anneals.

Multiple bundling of ≅ 80 μm Fe powders was used to produce very fine Fe fibers.

The first compact of Cu-36 wt.% Fe was swaged in a 12.7 mm o.d. Cu tube down to a 2.5 mm o.d. strand which was then heat treated at 800° C for 2 hours. 14 of these 2.5 mm o.d. strands were bundled in another 12.7 mm o.d. copper tube and swaged to 4 mm o.d. Again an 800° C heat treatment was applied. The copper outside was then etched away. Six of these strands were bundled in a 12.7 mm o.d. copper tube and swaged to 2.5 mm o.d. and heat treated. A 4th and 5th bundling, of 14 strands, reduction to 2.5 mm o.d., and heat treatment was again employed. Finally, the 6th bundling of 14 strands was swaged and wire drawn to 0.125 mm o.d.. The final nominal areal reduction was $R = 4 \times 10^{10}$. However, due to the vacancies between the powders in the first compact copper tube and between the stands of the multiple bundling, we estimated the actual area reduction ratio to be $R \sim 10^8$.

The starting Fe and Ni powders were spherical and made by rotating electrode processing. The Nb matrix was chosen to better match the mechanical properties of Ni. The increase in hardness with areal reduction ratio was examined for each powder (i.e. Cu, Nb, Ni and Fe). To do this, each of the powders were compacted in a separate Cu tube and processed by swaging and drawing. Measurements of the Vickers microhardness H_v versus areal reduction ratio show systematic differences between each element (see Fig. 1). The Fe, Ni and Nb exhibit rapid increase for H_v for areal reductions of 100 or more.

Magnetic measurements were made with a vibrating sample magnetometer[7] at room temperature with the field along the fiber axis. A maximum field of 5000 Oe was applied. Cu-Fe composites with an areal reduction ratio of about 10^8 resulted in $H_c \sim 195$ Oe, whereas pure Fe has an $H_c \sim 0.8$ Oe. Based on the areal reduction, average Fe fiber diameters of about 100 Å are calculated. However, comparing the observed value of H_c with In Situ processed Cu-Fe data of Dublon et.al.[4,5] We estimate Fe fiber diameters of 100 to 1000 Å.

Nb-Ni and Cu-Ni composite wires with an areal reduction ratio of about 10^4 resulted in $H_c \sim 94$ Oe and 77 Oe, respectively, whereas pure Ni has an $H_c \sim 0.7$ Oe. Estimates based on the nominal areal reductions suggest Ni average fiber diameters of about 1 μm.

Plots of H_c versus areal reduction ratio are given in Fig. 2. These data show that the coercive force increases with increasing areal reduction ratio. Fig. 2(a) shows data for Cu-Ni and Nb-Ni. For a same areal reduction, H_c of Nb-Ni is higher than that

of Cu-Ni. This may be due to the fact that Nb is harder than Cu and more nearly matches the the hardness of the Ni powder so that more effective elongation occurs. Areal reduction ratios higher than $\cong 10^4$ were not achieved for the Nb-Ni or Cu-Ni composite wires without breakage. Fig. 2(b) shows H_c as a function of areal reduction ratio for Cu-Fe composite wires. H_c is small for nominal areal reduction ratios lower than 10^4. However, a rapid increase of H_c occurs for $R > 10^6$ and an areal reduction ratio of about 10^8 resulted H_c in the order or $\sim$ 200 Oe.

Hysteresis curves of Cu-36 wt.% Fe with $R = 10^8$ are shown in Fig. 3. Fig. 3a shows the relative magnetization versus magnetizing field, H, prior to the low temperature anneal and Fig. 3b shows the increased H_c when annealed at 300° C for 1 hour. Again this is consistent with the results reported earlier by Dublon et.al.[4,5] who obtained an increase on H_c for In Situ processed Cu-Fe after annealing at 300°C. The microstructure of the cross section of a final-compacted as-drawn Cu-Fe .25 mm diameter composite wire is shown in Fig. 4(a) and (b).

The present results show that the powder metallurgy processing technology (originally developed for fabrication of high performance fine fiber superconductors) can be adapted for fabrication of fine fiber composites, particularly permanent magnet materials with high coercive fields. The final results for Fe in Cu are comparable with that of the In Situ process developed earlier[4,5], but the powder process is not limited by the phase diagram so that various composites can be made of magnetic or nonmagnetic constituents. Examples of Nb-Ni and Cu-Ni are given here. However, the components of the powder process must be ductile. Although extremely large areal reductions were used for the Cu-Fe materials, smaller starting particle sizes would require smaller areal reductions for the same final fiber size.

Comments — Due to the time limitation, the final form of this report did not sent to Dr. S. Foner for approval. Therefore, if any mistake happens, Yao will take the responsibility.

Acknowledgment — The Francis Bitter National Magnet Laboratory is supported by the National Science Foundation. One of us, Y.D. Yao is grateful to the National Science Council of R.O.C. for partial financial support of this work.

REFERENCES

(1) R. FLÜKIGER, R. AKIHAMA, S. FONER, E. J. McNIFF, Jr. and B. B. SCHWARTZ, Appl. Phys. Lett. 35, 810 (1979).

(2) R. AKIHAMA, R. J. MURPHY and S. FONER, Appl. Phys. Lett. 37, 1107 (1980).

(3) For a recent review of the powder and In Situ processing for superconductors, see R. ROBERGE, Chapter 6, Superconductor Materials Science, Metallurgy, Fabrication and Applications, Edited by S. FONER and B. B. SCHWARTZ, Plenum Press (1981).

(4) G. DUBLON, F. HABBAL and J. BEVK, Appl. Phys. Lett. 39, 659 (1981).

(5) G. DUBLON, F. HABBAL and J. L. BELL. J. Appl. Phys. 53, 8335 (1982).

(6) Y. D. YAO and S. FONER, Ann. Rept. National Magnet Lab., M.I.T. (1981-1982).

(7) S. FONER, Rev. Sci. Instr. 30, 548 (1959).

Fig. 1 Nominal areal reduction ratio, R, versus Vickers microhardness, H_v, for compacts of Cu, Nb, Ni or Fe powder.

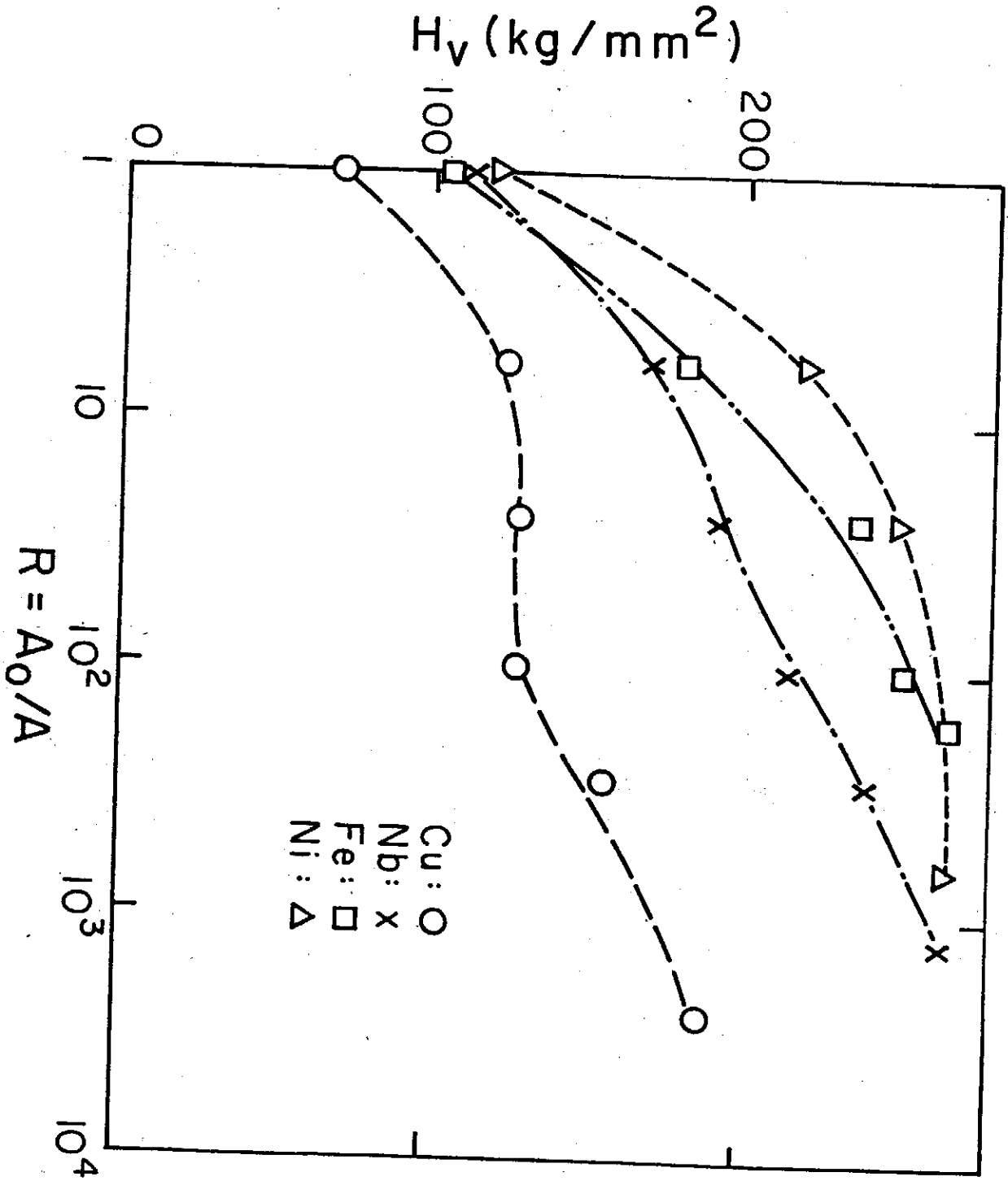

Fig. 2 Coercive force H_c versus areal reduction, R:
a) Cu-36 wt.% and Nb-36 wt.% Ni composites.

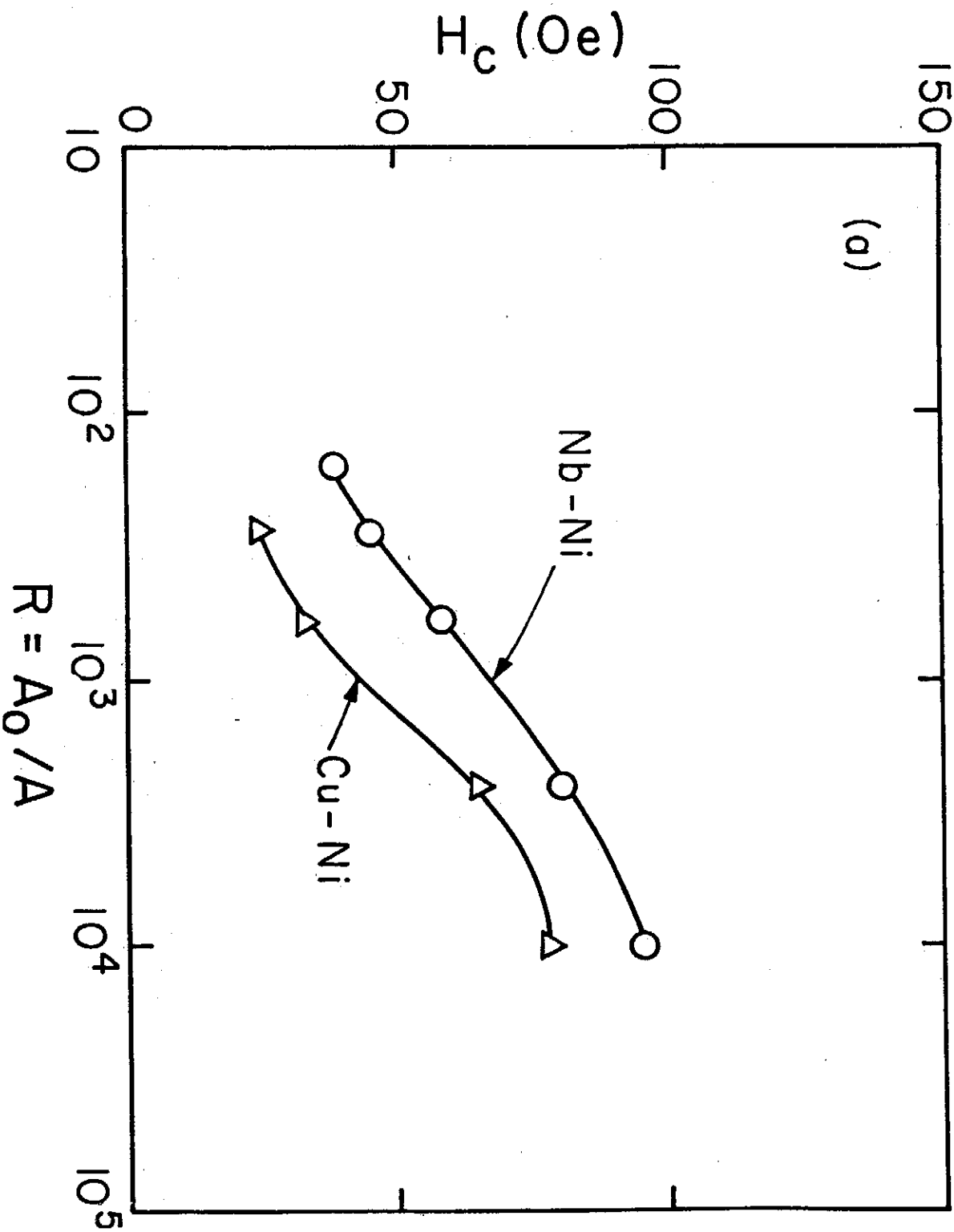

Fig. 2 Coercive force H_c versus areal reduction, R:
b) Cu-36 wt.% Fe composite.

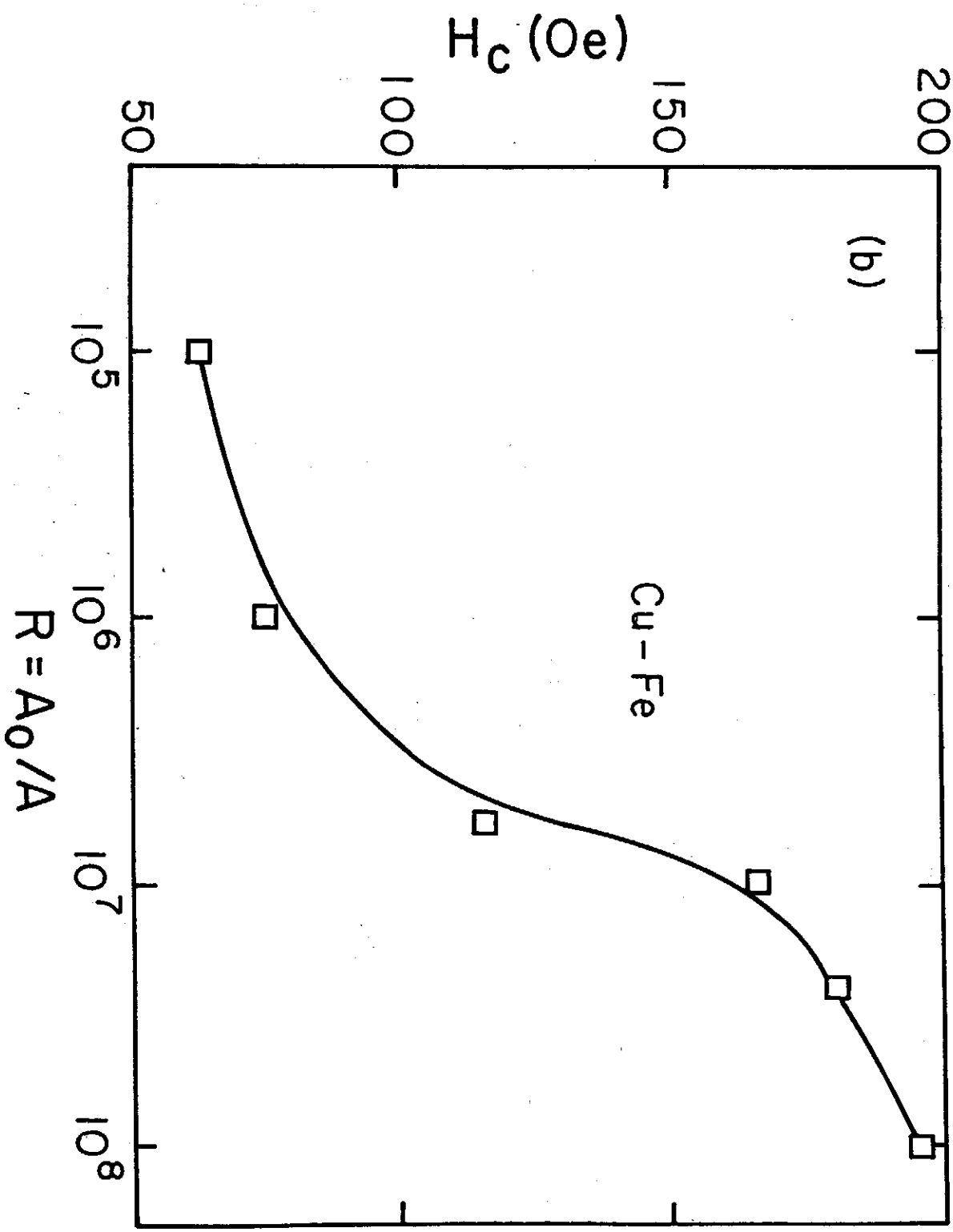

Fig. 3 Relative magnetization versus magnetizing field, H, for Cu-36 wt.% Fe powder processed composite (Fig. 2b, R = 10^8): a) without low temperature final anneal.

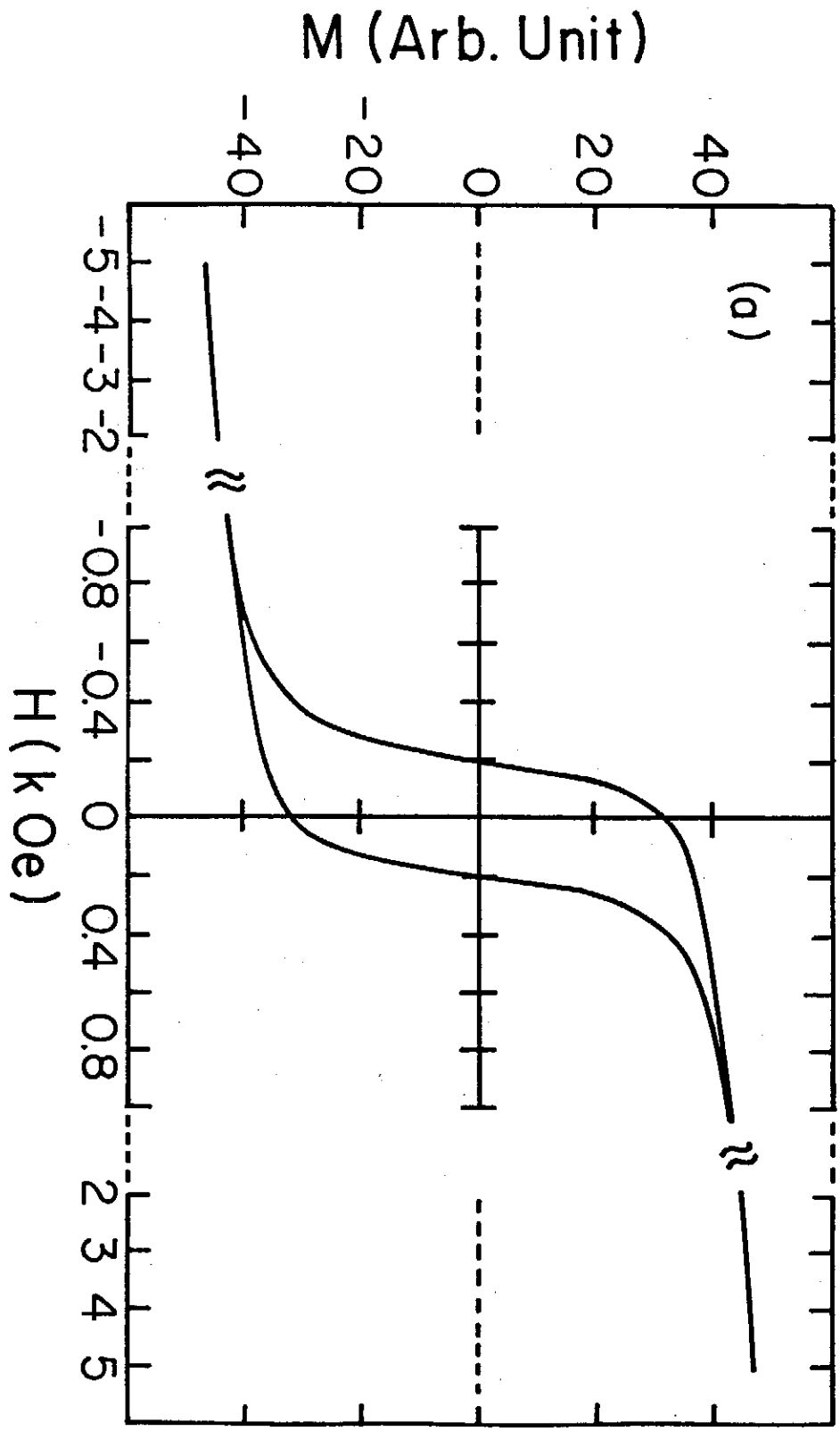

Fig. 3 Relative magnetization versus magnetizing field, H, for Cu-36 wt.% Fe powder processed composite (Fig. 2b, R = 10^8): b) with an additional anneal at 300°C for 1 hour showing increase in H_c to 460 Oe.

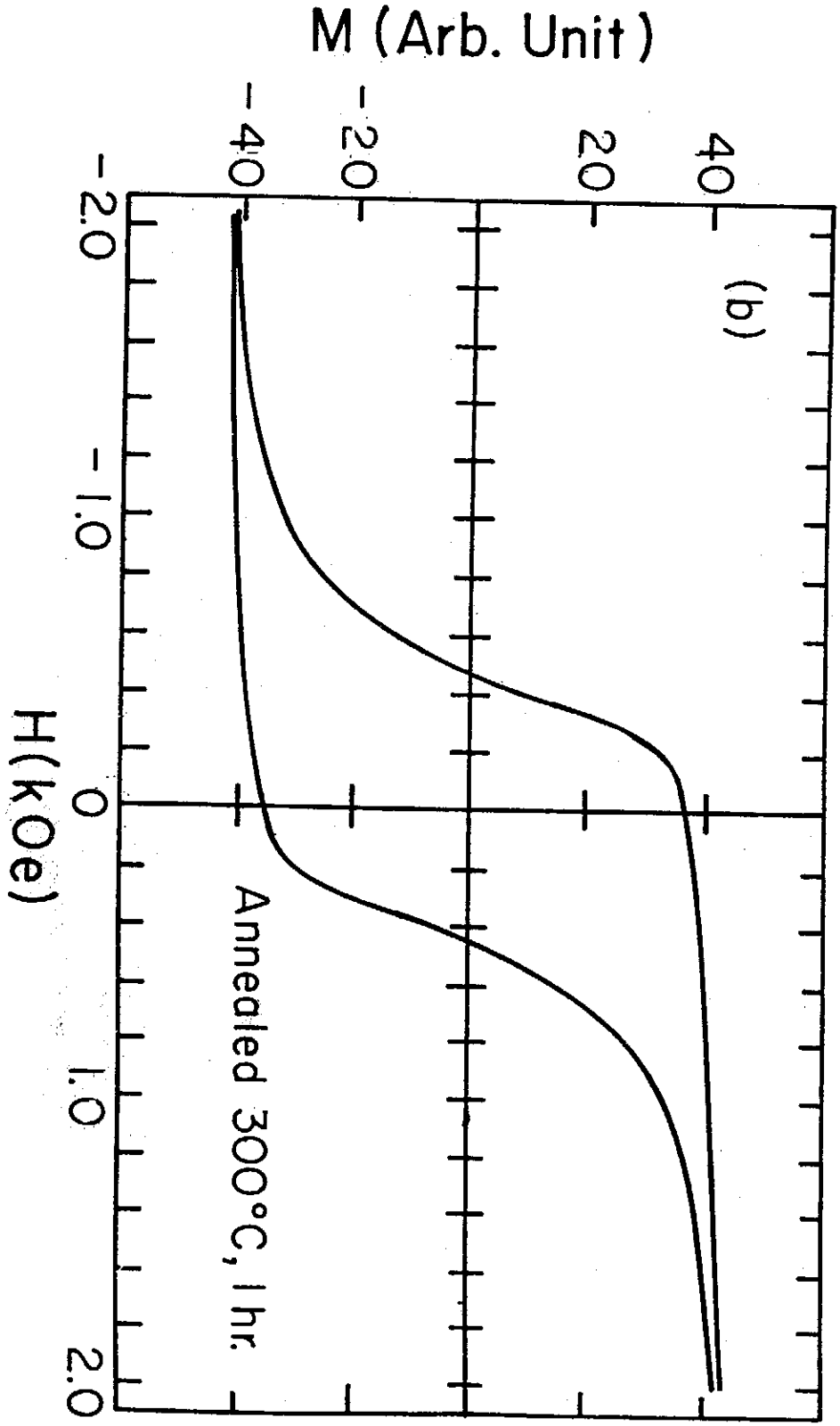

Fig. 4 Micrograph of polished cross section of an as-drawn Cu-Fe 0.25 mm diam. composite wire (a) 500 x

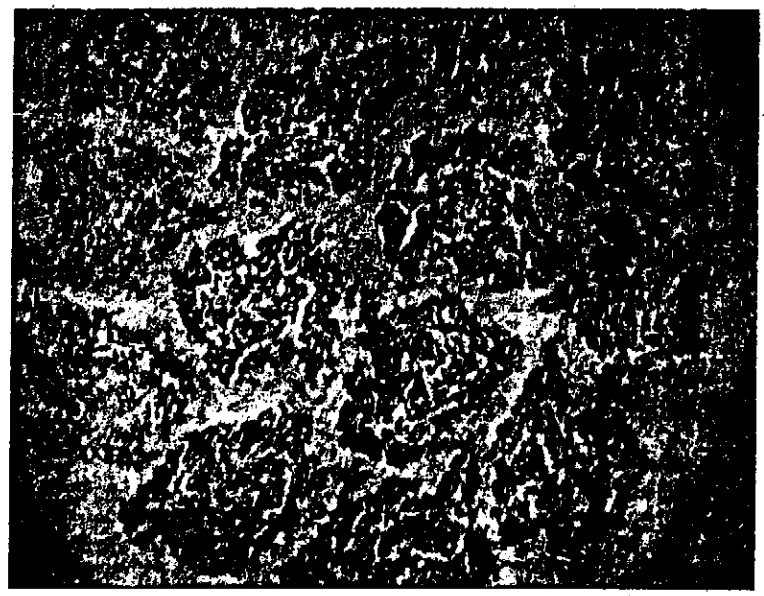

Fig. 4 Micrograph of polished cross section of an as-drawn Cu-Fe 0.25 mm diam. composite wire (b) 1,000 x

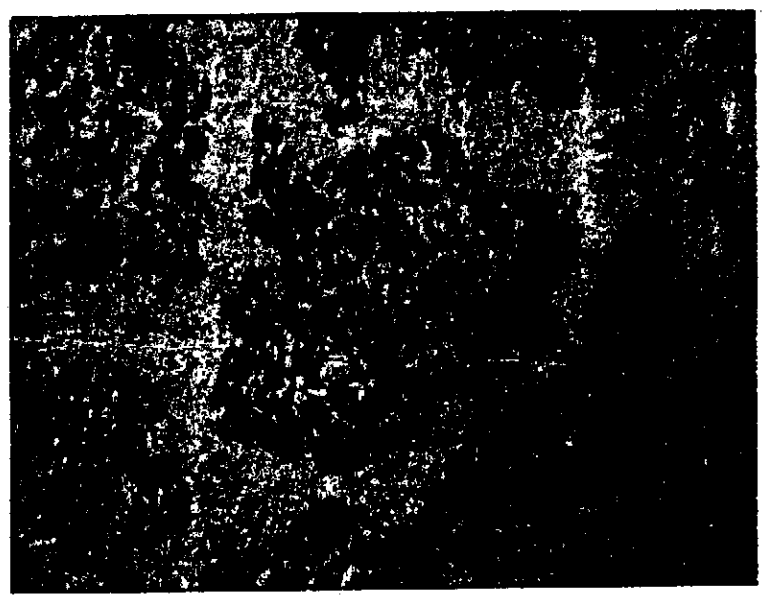

10 μ

On the Stability, Switching Voltage and Transient ON-Characteristics of Amorphous Thin Films

Chun Chiang

Institute of Physics

Academia Sinica

Nankang, Taipei, Taiwan,

R. O. C.

By proposing that two types of reversible configurations co-existing in the film, that the ratio of two configurations is determined by current according to the law of mass action and the electronic energy transfer, that the difference of configurations may be due to phase, bonding state, filament formation, valence alternation pair, etc., mathematical equations can be derived to explain the threshold switching, the time dependence of the threshold voltage, transient ON characteristics and the non-linearity of the conductance.

Switching phenomenon[1] is a very interesting and important phenomenon. Many theories have been proposed for its explainating[2-10], most of them are qualitative and with limited success. Recently, Chiang proposes a switching theory[11, 12] which is able to explain the S-like curve of voltage vs. current, and the time delay phenomena. However, the basic excitation mechanism has not been fully explored. The purpose of this letter is to further discuss this basic excitation mechanism and its related properties such as threshold voltage, nature of switching ON and switching OFF, transient ON characteristics, non-linearity in conductance, etc..

Assuming that there are two configurations (I and II) coexisting in the film which can be transformed to each other by current excitation through a barrier. The mechanisms that the current may excite the configurations are as follows:

(a) The electrons may react with configurations such that

$$n\ e + \text{Configuration I} \longleftrightarrow \text{Configuration II}$$

The direction of the reaction and its transformation is determined by the electron density ρ according to the law of mass action. The electrons may either be consumed, in this case, there is charge storage effect as claimed by Haberland and stiegler[7], or the electrons may simply act as catalysis and are not consumed in the process.

(b) The energy of impact from the electons may excite the configuration.

$$\text{Configuration I} \xrightarrow{\text{energy}} \text{Configuration II}$$

The energy of impact is related to electron velocity v but may not be a simple relationship, since the impact process of electrons in thin films may be quite complicated.

The above two reactions are reversible, decreasing the electron density or its velocity will reverse the direction of the reactions. For generality, we may use f(I) to represent the extent of the above two transformation processes induced by current (remembering that $I = \rho v$). The difference between the two configurations may be due to positional displacement, bonding state (for example, polymer-monomer conversion[12]), valence alternation pair[16], crystalline state, filament formation[17, 18], phase transformation[21], or a combination of these.

Let n_1 and n_2 be the percentage of configuration I and II per unit area respectively ($n_1 + n_2 = 1$), we may write the kinetic equations as follows:

$$\frac{dn_1}{dt} = -A\, n_1\, e^{-[u-E_1-k_1 f_1(I)]/K_b T} + A\, n_2\, e^{-[u-E_2-k_2 f_2(I)]/K_b T}$$
$$\frac{dn_2}{dt} = A\, n_1\, e^{-[u-E_1-k_1 f_1(I)]/K_b T} - A\, n_2\, e^{-[u-E_2-k_2 f_2(I)]/K_b T} \qquad (1)$$

where A, k_1, k_2 are constant, E_1 and E_2 represent the energy of configuration I and II, u the barrier. Let g_1 and g_2 represent the conductivity of configurations I and II, and since they are in parallel, the total conductance G is the mixture of these two conductances, thus

$$G = n_1 \frac{a}{d} g_1 + n_2 \frac{a}{d} g_2 = \frac{a}{d} g_1 + n_2 \frac{a}{d} (g_2 - g_1) \qquad (2)$$

where a is the area and d is the thickness. The above equation applies to the case of filamer formation, since mathematically, we can imagine to divide the filament to many pieces and mix it homogeneously with the surrounding configuration. When the local current density in some area of the film matrix reaches certain value, the matrix is excited to configuration II form and rearranged to form the filament, so that a higher current density may be sustained. Thus the increased current increases the size of the filament, whereas the current density in the filament may not increase much as evidenced by Henisch and Pryor[14] and Perterson and Adler[1 It should also be noted that the filament formation is reversible and thus may or may not be readily observable. Since

$$U_o = IR + I/G \tag{3}$$

(2) and (3) may be transformed to be

$$n_2 = \frac{U_o}{R\frac{a}{d}(g_2-g_1)(U_o-IR)} - \frac{1+\frac{a}{d}g_1 R}{R\frac{a}{d}(g_2-g_1)} \tag{4}$$

Differentiating (4), we obtain

$$\frac{dn_2}{dt} = \frac{U_o}{\frac{a}{d}(g_2-g_1)(U_o-IR)^2}\frac{dI}{dt} \tag{5}$$

From (1), (4) and (5), we obtain

$$\frac{dI}{dt} = \frac{A}{U_o}e^{-\frac{u}{K_bT}}(U_o - IR)\{[U_o - g_2\frac{a}{d}(L + R\,g_2\frac{a}{d})I]\,e^{\frac{E_1+k_1f_1(I)}{K_bT}} + [U_o\,g_1\frac{a}{d} - (1 + R\,g_1\frac{a}{d})I]\,e^{\frac{E_2+k_2f_2(I)}{K_bT}}\} \tag{6}$$

This is the dynamic differential switching equation for amorphous thin films. In the equilibrium state, $\frac{dI}{dt} = 0$, we have

$$U_o = \frac{(1+R\,g_1\frac{a}{d})e^{\frac{E_1+k_1f_1(I)}{K_bT}} + (1+R\,g_1\frac{a}{d})e^{\frac{E_2+k_2f_2(I)}{K_bT}}}{\frac{a}{d}g_2\,e^{\frac{E_1+k_1f_1(I)}{K_bT}} + \frac{a}{d}g_1\,e^{\frac{E_2+k_2f_2(I)}{K_bT}}}\,I \tag{7a}$$

This is the equilibrium switching equation in terms of the applied voltage U_o and the current In terms of voltage U across the sample and the current, we have

$$U = U_o - IR = \frac{e^{\frac{E_1+k_1f_1(I)}{K_bT}} + e^{\frac{E_2+k_2f_2(I)}{K_bT}}}{\frac{a}{d}g_2 e^{\frac{E_1+k_1f_1(I)}{K_bT}} + \frac{a}{d}g_1 e^{\frac{E_2+k_2f_2(I)}{K_bT}}} I \qquad (7b)$$

If there is contact resistance, then U should be replaced by $U-V_b$, where V_b is the electrode contact voltage. (7b) may be ploted as the heavy line in Fig. (1) with the parameter that $(E_2 - E_1)/K_bT = 8$, $(k_2 - k_1)/K_bT = -3 \times 10^3$ ev/A, $ag_1/d = 5 \times 10^{-5}$ ev/A, $ag_2/d = 1.7 \times 10^{-3}$ Ω^{-1} and $V_b = 1$ volt. For simplicity, f(I) is assumed to be $|I|$. (7b) shows three parts, curve I represents the OFF state, curve II represents the ON state and cruve III represents mixture state.

The threshold voltage is the minimum voltage required such that the film can be transformation to the ON state and such that a large current can flow. This threshold voltage may be calculated by differentiating (7b) and let $\frac{dU}{dt} = 0$. The calculation is tedeuous, however, the threshold voltage U_{th} may easily be found from Fig. 1 to be 17.29 volt ($U_{th}' = 18.29$ volt).

If the film is in the ON state and then is interupted for a period of t during which no current passing through the film, then n_1 may be solved from (1) with the initial conditions that $n_1\ (t = 0) = 0$ and $I(\ t = 0) = 0$ to be

$$n_1 = \frac{e^{\frac{E_2}{K_bT}}}{e^{\frac{E_1}{K_bT}} + e^{\frac{E_2}{K_bT}}} \{1 - e^{-[Ae^{-\frac{u-E_1}{K_bT}} + Ae^{-\frac{u-E_2}{K_bT}}]t}\} \qquad (8)$$

From (2), the film now at time t has the conductance

$$G(t) = \frac{a}{d}g_2 + \frac{a}{d}(g_1 - g_2)\frac{e^{\frac{E_2}{K_bT}}}{e^{\frac{E_1}{K_bT}} + e^{\frac{E_2}{K_bT}}} \{1 - e^{-[Ae^{-\frac{u-E_1}{K_bT}} + Ae^{-\frac{u-E_2}{K_bT}}]t}\} \quad (9$$

Since G = I/U, and assuming f(I) = I, the threshold current at t can be obtained by combining (9) and (7b) to be

$$I_{th}(t) = \frac{K_b T}{k_2 - k_1} \ln \frac{\frac{a}{d} g_2 - G(t)}{G(t) - \frac{a}{d} g_1} + \frac{E_1 - E_2}{k_2 - k_1} \tag{10}$$

thus

$$U_{th}(t) = \frac{I_{th}(t)}{G_{th}(t)} = \frac{K_b T}{(k_2 - k_1) G_{th}(t)} \ln \frac{\frac{a}{d} g_2 - G_{th}(t)}{G_{th}(t) - \frac{a}{d} g_1} + \frac{E_1 - E_2}{(k_2 - k_1) G_{th}(t)} \tag{11}$$

Equation (11) together with equation (9) may be ploted in Fig. 2 with the parameter that $A = 10^9 \text{sec}^{-1}$ and $e^{-(u-E_1)/K_b T} = 10^{-8}$.

It might be more instructive to find the threshold voltage $U_{th}(t)$ and threshold current $I_{th}(t)$ graphically. This may be done by finding the intersection point of the equilibrium switching curve of (7b) and conductance curve G(t) (equation (9)).

In Fig. 2, the calcualted voltage drops at a latter time, this is so because G(t) intersects with curve I in Fig.1 at a smaller voltage. However, once the film switches to curve I state, it requires the normal threshold voltage which is 17.29 volt and is indicated as dot line in Fig. 2. Similarly, at early time G(t) intersect with curve II and the voltage increases at a shorter time. However, once the film is in curve II state, it only requires V_{MON} to stay in ON state as indicated by dot line. The V_{MON} in this case is 2.28 volt ($V'_{MON} = V_{MON} + V_b$ = 3.28 volt).

In Fig. 1, the crossed area is the switching area. If the state of the film initially belongs to this area, then the film will eventually switches to the stable ON state indicated as curve II in Fig. 1. The route of switching is determined by the load resistance and the voltage. The dot area is also the switching area, however, if the state of the film initially belongs to this area, then the film will eventually switches to the stable OFF state indicated as curve I in Fig. 1. Curve III is the boundary between these two areas and may be termed metastable state. The other areas are forbiddened areas.

Henish et. al.[8] have observed some intersting result that if a fast pulse is applied in a ON state, a transient ON characteristics (TONC) is observed; if the applied voltage is within certain minimum value V_b, then only very small current exists. This

state is different from the OFF state in the sense that the film can readily be in ON state without going through the switching. They term this as the block ON state. These phenomena can now be explained with the present theory as follows: If the pulse is very fast such that the film is fixed practically in configuration II from and has no time to switch back to configuration I form, then the I-V curve reveals the characteristic properties of configuration II (curve II and the dot line in Fig. 1). The reason that the current is very small when voltage is smaller then V_b is due to the contact resistance and the electric barrier between the electrode and the thin film. Thus when the voltage is small, only very small quantity of current can tunnel through. However the film still consists of entirely configuration II form, thus the film can readily be in ON state without going through the switching process by applying a minimum threshold voltage V_{Mth}, this V_{Mth} may also be termed minimum ON voltage V_{MON}, below which no "stable" ON state can exist. When the applied pulse reverses the direction, the current also reverses. The I-V curve in negative direction is similar to the I-V curve in positive direction and may have some asymmetry if the electrodes are different. This asymmetry is due to the different electrode contact resistance.

Other fast pulse experiment[19] reveals the highly non-linear conductance region around the normal threshold voltage. This can be explained as due to the reason that with the fast pulse, the film is fixed at certain mixture of configurations, thus the conductance is non-linear (region between curve I and curve II in Fig. 1). The conductance in the region between curve II and curve III should also be non-linear under similar conditions, this is indeed revealed by Popescu and Croitoru[20].

The above discussion concerns with threshold switching, namely, the reversible conversion of configuration I and configuration II is mediated by current; by withdrawing the current, the film reverses to the OFF state. However, if the energys of configurations are changed due to environmental change during the switching process, then the equilibrium point is shift such that the film may return to OFF state through another route or remain in the ON state even if the mediated current is completely reduced to zero, then this is the memory switching. Also, for simplicity, f(I) is assumed to be I in the present calculation. However, if there is charge storage effect, f(I) should be $\int I dt$; if there is power consumption, f(I) should be $\int I^2 dt$. Thus threshold switching with slightly different process as well as memory switching can all be incorporated in the same theroretical

frame-work.

In conclusion, by proposing two physically reasonable catagories of configurations co-existing in a film, methematical equations can be derived to explain the threshold switching, time dependence of threshold voltage, block on state, non-linearity in I-V curve, non-symmetry in transient ON characteristics, etc.. The memory switching can also be incorporated within this theory by assuming a change of energy of configurations in switching.

REFERENCES

(1) S. R. OVSHINSKY, Phys. Rev. Lett. 21, 1450 (1968).

(2) H. K. HENISCH, E. A. FAGEN and S. R. OVSHINSKY, J. Non-Cryst. Solids 2, 538 (1970).

(3) H. FRITZSCHE and S. R. OVSHINSKY ,J. Non-Cryst. Solids 2, 393 (1970).

(4) I. LUCAS, J. Non-Cryst. Solids 6, 136 (1971).

(5) M. IIDA and A. HAMADA, Jap. J. Appl. Phys. 10, 224 (1971).

(6) W. VAN ROOSBROECK, Phys. Rev. Lett. 28, 1120 (1972).

(7) D. R. HABERLAND and H. STIEGLER ,J. Non-Cryst. Solids 8-10, 408 (1972).

(8) D. ADLER, H. HENISCH, N. Mott, Rev. Mod. Phys. 50, 209 (1978).

(9) A. WARREN, IEEE Trans. Electron Devices 20, 123 (1973).

(10) K. PETERSEN and D. ADLER, J. Appl. Phys. 47, 256 (1976).

(11) C. CHIANG, Phys. Stat. Sol. (a) 54, 735 (1979).

(12) C. CHIANG, Sol. Stat. Comm. 39, 111 (1981).

(13) R. R. SHANKS, J. Non-Cryst. Solids 2, 504 (1970).

(14) H. K. HENISCH and R. W. PRYOR, Solid State Electronics 14, 765 (1971).

(15) R. W. PRYOR and H. K. HENISCH ,J. Non-Cryst. Solids 7, 181 (1972).

(16) M. KASTNER, D. ADLER, and H. FRITZSCHE, Phys. Rev. Lett. 37, 1504 (1976).

(17) L. A. COWARD, J. Non-Cryst. Solids 6, 107 (1971).

(18) M. SAJI and K. C. KAO, J. Non-Cryst. Solids, 22, 223 (1976).

(19) W. D. BUCKLEY, S. H. HOLMBERG, Solid State Elect. 18, 127 (1975).

(20) C. POPESCU, N. CROITORU, J. Non-Cryst. Solids 8-10, 531 (1972).

(21) P. J. WALSH, R. VOGEL, E. J. EVANS, Phys. Rev. 178, 1274 (1969).

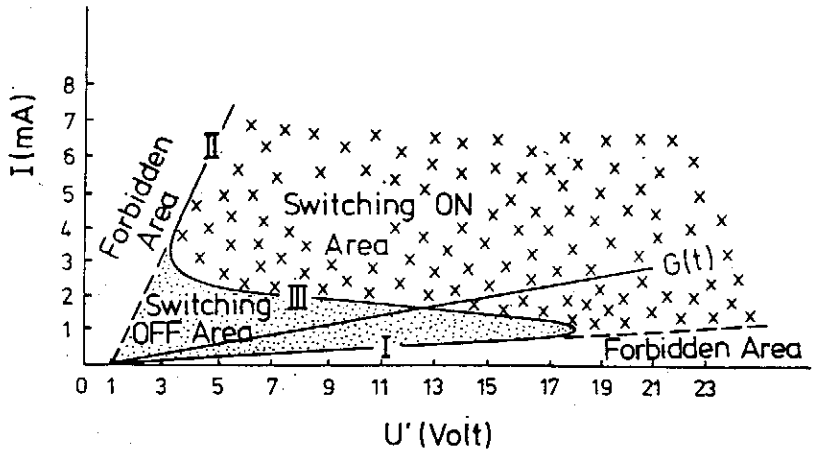
I(mA)
8
7
6
5
4
3
2
1
0 1 3 5 7 9 11 13 15 17 19 21 23
U' (Volt)
Forbidden Area
II
Switching ON Area
G(t)
Switching OFF Area
III
I
Forbidden Area

Fig. 1.

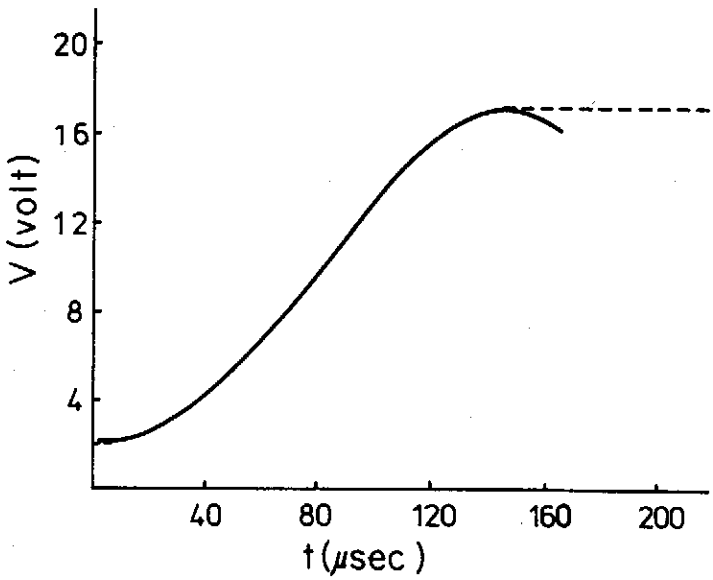
V (volt)
20
16
12
8
4
40
80
120
160
200
t (μsec)

Fig. 2.

MULTIDYON SOLUTIONS IN SU(2) GANGE GROUP

Jiin Chang Shaw

Department of Applied Mathematics, Chio Tung University

Hsinchu, Taiwan, R.O.C.

Jiunn Chuu Chen *

Department of Physics, Cheng Kung University

Tainan, Taiwan, R.O.C.

Recently, Prasad describe a systematic framework for the construction of axially symmetric multimonopole solution of arbitrary topological charge. We found that these solutions can be transformed into axially symmetric multidyon solutions easily. We write down the multidyon solutions in Yang's K-gauge also.

I. INTRODUCTION

Since 'tHooft and Polyakov[1] discovered the solution of one monopole, it has become an interesting problem among physicist whether the solutions of multimonopole exis or not, it is not only a mathematical problem, but also may be related to the origin of t cosmos[2]. Recently the existence of multimonopole solution of arbitrary charge was prov by Taubes[3]. And the explicit form of multimonopole has been written independently by M. K. Prasad[4] and P. Forgács[5] et. al..

Prasad et. al. consider the solutions of monopole in the limit of vanishing Hig potential as a static self-dual Yang-Mills field in 4-dimensional Euclidean space which satisfy the appropriate boundary condition, so that they can use the method of the constr tion of multi-instanton to solve multimonopole problem. In fact, Manton is the first one who uses this method from the CFHW (Corrigan-FAIRLIF-'tHooft-Wilczek) ansatz to rederive the one-monopole solution. This solution is in complex form, but it can be transfomed to real form by a complex gauge transformation. However Manton did not find any new solutio

---

*訪問研究員（國科會補助之寒暑假大專院校教師訪問研究計劃）

which can be made real by a complex gauge transformation.

Based on the "twistor" approach to self-dual Yang-Mills fields developed by Ward[7], Atiyah and Ward[8] proposed a hierarchy of ansätz An, n = 1, 2, ··· , for the construction of all instanton solution. The first ansatz A_1 is the (CFHW) ansatz which is given in terms of spin zero massless free field, i.e., a solution of four dimensional Laplace equation. The ansatz An can be described by certain spin (n-1) massless fields. Atiyah and Ward use the language and techniques of analytic and algebraic geometry. Moreover they did not give any explicit forms beyond the A_2 ansatz. Corrigan, Fairlie, Goddard and Yates[9] gave an explicit construction of all the ansätze Aℓ, ℓ = 1, 2, ··· , which takes a particularly simple form in Yang's[10] R gauge. In R-gauge, the self-dual potentials are described by three functions satisfying a system of second order (non-linear) differential equations. Moreover, Corrigan et. al. have shown that in R-gauge, successive AW ansätze are related by a Bäcklund transformation, which we call BT, for Yang's Equations. For our purpose, a Bäcklund transforamtion is a transformation, usually given by a system of first order differential equations, which generate locally "new" solutions of self-duality equations from old ones. Corrigan et. al., then integrate this BT, to give an independent "elementary" proof that the Aeiyah-Ward ansätze does indeed give solutions of the self-duality equations, and, of course, this give an explicit construction of the Atiyah-Ward ansätze. But Backlund transformation operate on real function can generate a complex one, so that it became a big problem in construction of multimonopole solutions by means of Bäcklund transformation.

Prasad et. al.[11] found that they can construct a complex gauge transformation such that the solutions become real. Especially, after a properly choosing asymptotic behavior (or boundary condition) they found a systematic framework for generating multimonopole solutions.

After the discovery of multimonopole solutions, it is naturally to looking for the solutions of multidyon, we found that the static multidyon solutions can be constructed very easily from the static multimonopole solutions. Just the same as the Julia-Zee[12] dyon solution can be inferred from Bogomolny-Prasad[13] one monopole solution. That is, if the solution of multimonopole can be stated as follows:

$$A_i^{a'}, \quad \phi'^a, \quad A_o{}^a = 0 \qquad (1\text{-}1$$

then the following substitutions

$$A_i^a = A_i^{a'} \quad A_o{}^a = \sinh\gamma\ \phi^{'a}$$
$$\phi^a = \cosh\gamma\ \phi^{'a} \tag{1-2}$$

where $\sinh\gamma = -\frac{e}{q}$ $\cosh\gamma = \frac{\sqrt{q^2+e^2}}{q}$

and q(e) is the magnetic (electric) charge of the dyon, is the multidyon solution.

In this report, we review the self-dual gauge fields theory such as the self-duality eqs. in Yang's R gauge, Bäcklund transformation of those equations and Atiyah-Ward An ansatz in Section II. In section III, we outline the framework for generating multi-monopole solutions, and write down the gauge potential of n-monopole in Yang's $K^{(10)}$ gauge. Finally, we show that the static multidyon problem is equivalent to static multimonopole problem.

II. SELF-DUAL GAUGE FIELDS AND R-GAUGE

(II-A) Self-Dual Equations in Complex Space:

In this report, we restrict ourselves to SU(2) gauge theory, and we use matrix notation for gauge potential etc. defined as

$$A_\mu \equiv \frac{g}{2i}\sigma^a A_\mu{}^a \qquad \mu = 1, 2, 3, 4, \quad a = 1, 2, 3 \tag{2-1}$$

where σ^a are the usual Pauli matrices and g is the coupling constant. Then

$$F_{\mu\nu} \equiv g\cdot\frac{\sigma^a}{2i}F^a_{\mu\nu} = \partial_\mu A_\nu - \partial_\nu A_\mu + [A_\mu, A_\nu] \tag{2-2}$$

when the gauge potentials A_μ^a are real, then the matrix A_μ is traceless and antihermitian However, if the gauge potential A_μ^a are complex, the matrix A_μ is traceless but not anti-hermitian.

Consider an analytic continuation of A_μ into complex space where x_1, x_2, x_3 and x_4 are complex. The self-duality equations in Euclidean space

$$F_{\mu\nu} = \frac{1}{2}\varepsilon_{\mu\nu\rho\sigma}F_{\rho\sigma} \tag{2-3}$$

are valid also in complex space. Define

$$\sqrt{2}\, y = x_1 + i\, x_2 \quad , \qquad \sqrt{2}\, \bar{y} = x_1 - i\, x_2$$
$$\sqrt{2}\, z = x_3 - i\, x_4 \quad , \qquad \sqrt{2}\, \bar{z} = x_3 + i\, x_4 \tag{2-4}$$

$$\sqrt{2}\, Ay = A_1 - i\, A_2 \quad , \qquad \sqrt{2}\, A\bar{y} = A_1 + i\, A_2$$
$$\sqrt{2}\, Az = A_3 + i\, A_4 \quad , \qquad \sqrt{2}\, A\bar{z} = A_3 - i\, A_4 \tag{2-5}$$

Then self duality equation (2-3) reduce to

$$F_{yz} = F\, \bar{y}\, \bar{z} = 0 \tag{2-6a}$$

$$F_{y\bar{y}} + F_{z\bar{z}} = 0 \tag{2-6b}$$

The equation (2-6a) implies that the potentials Ay, Az($A\bar{y}$, $A\bar{z}$) are pure gauge for fixed $\bar{y}$, $\bar{z}$ (y, z), i.e. we can find two 2x2 complex matrices D and $\bar{D}$ such that

$$Ay = D^{-1}\, D,y \quad , \qquad Az = D^{-1}\, D,z$$
$$A\bar{y} = \bar{D}^{-1}\, \bar{D},\bar{y} \quad , \qquad A\bar{z} = \bar{D}^{-1}\, \bar{D},z \tag{2-7}$$

where $D,y \equiv \partial_y D$ etc.

From Eq. (2.7) and since $TrA_\mu = 0$, then we have

$$\det D = \det \bar{D} = 1 \tag{2-8}$$

If we define a matrix J by

$$J \equiv D\, \bar{D}^{-1} \tag{2-9}$$

Clearly det J = 1. The remaining self-duality equation (2-6b) can be written as

$$(J^{-1}\, J,y)\bar{y} + (J^{-1}\, J,z)\bar{z} = 0 \tag{2-10}$$

Now gauge transformations are the following transformations:

$$D \to \bar{V}(\bar{y}, \bar{z})DG \qquad \bar{D} \to V(y, z)\bar{D}\, G \tag{2-11a}$$

$$A_\mu \to G^{-1} A_\mu G + G^{-1}\, G,\mu \tag{2-11b}$$

Under these transformation (2-11a), J transforms as

$$J \to \bar{V}(\bar{y}, \bar{z})\, J\, V^{-1}(y, z) \tag{2-12}$$

Yang has discovered the R-gauge, which is defined by choosing the matrices D and $\bar{D}$ to be lower and upper triangulars respectively, i.e. by

$$D \equiv R \equiv \frac{1}{\sqrt{\phi}} \begin{pmatrix} 1 & 0 \\ \rho & \phi \end{pmatrix} \tag{2-13}$$

$$\bar{D} \equiv \bar{R} \equiv \frac{1}{\sqrt{\phi}} \begin{pmatrix} \phi & -\bar{\rho} \\ 0 & 1 \end{pmatrix} \tag{2-13}$$

where ϕ, ρ and $\bar{\rho}$ are independent complex functions of y, z, $\bar{y}$ and $\bar{z}$. From the definition (2-9) we have

$$J \equiv R\, \bar{R}^{-1} = \frac{1}{\phi} \begin{pmatrix} 1 & \bar{\rho} \\ \rho & \phi^2+\rho\bar{\rho} \end{pmatrix} \tag{2-14}$$

Substitution of (2-14) in (2-9) gives

$$(\partial y \partial \bar{y} + \partial z \partial \bar{z}) \ell n \phi + \frac{\rho_{,y}\, \bar{\rho}_{,\bar{y}} + \rho_{,z}\, \bar{\rho}_{,\bar{z}}}{\phi^2} = 0 \tag{2-15}$$

$$\left(\frac{\rho_{,y}}{\phi^2}\right)_{,\bar{y}} + \left(\frac{\rho_{,z}}{\phi^2}\right)_{,\bar{z}} = 0 \tag{2-15}$$

$$\left(\frac{\bar{\rho}_{,\bar{y}}}{\phi^2}\right)_{,y} + \left(\frac{\bar{\rho}_{,\bar{z}}}{\phi^2}\right)_{,z} = 0 \tag{2-15}$$

The self-duality equations in terms of ϕ, ρ and $\bar{\rho}$. We must remark here we can always parametrize J as in Eq. (2-14), even though we arrived at this via Young's R-gauge. (Since J is an artitrary complex 2x2 matrix function with determinant one)

(II-B) Bäcklund Transformation and Atiyah-Ward's Ansatz

(Lemma 2-1) Let $(\phi, \rho, \bar{\rho})$ be a solution of Eq. (2-15) Then $(\phi^I, \rho^I, \bar{\rho}^I)$ defined by

$$\phi^I = \frac{\phi}{\phi^2 + \rho\bar{\rho}} \quad , \quad \rho^I = \frac{\bar{\rho}}{\phi^2 + \rho\bar{\rho}} \quad , \quad \bar{\rho}^I = \frac{\rho}{\phi^2 + \rho\bar{\rho}} \tag{2-16}$$

is also a solution of (2-15).

(Lemma 2-2) Let $(\phi, \rho, \bar{\rho})$ be a solution of Eq. (2-15). Then $(\phi^B, \rho^B, \bar{\rho}^B)$ defined by

$$\phi^B = \frac{1}{\phi} \tag{2-17a}$$

$$\rho^B{}_{,y} = -\frac{\rho,\bar{z}}{\phi^2} \qquad \phi^B{}_{,z} = \frac{\bar{\rho},\bar{y}}{\phi^2} \tag{2-17b}$$

$$\bar{\rho}^B{}_{,\bar{y}} = \frac{,z}{\phi^2} \qquad \bar{\rho}^B{}_{,\bar{z}} = -\frac{\rho,y}{\phi^2} \tag{2-17c}$$

is also a solution of Eq. (2-15)

Note that $(\phi, \rho, \bar{\rho}) \xrightarrow{\text{II}} (\phi,\rho, \bar{\rho})$

and $(\phi, \rho, \bar{\rho}) \xrightarrow{\text{BB}} (\phi,\rho, \bar{\rho})$

here I^2 and B^2 transformations are trivial transformations. But the composite transformation BI is not, it can produces "locally" new solutions of the self-duality equations from "old" ones. The Bäcklund transformation is the transformation BI. Whick is the I transformation followed by B transforamtion.

(Lemma 2-3) A solution of Eq. (2-15) is given by

$$\rho,y = \phi,\bar{z} \quad , \qquad \rho,z = -\phi,\bar{y} \tag{2-18a}$$

$$\bar{\rho},\bar{y} = \phi, z \quad , \qquad \rho,\bar{z} = -\phi, y \tag{2-18b}$$

$$\phi,y\bar{y} + \phi,z\bar{z} = 0 \tag{2-18c}$$

Eq. (2-18) is the well-known Corrigan-Fairlie-'tHooft-Wilczek (CFHW) ansatz. Note that eq. (2-18c) is the integrability condition of Eqs. (2-18a,b) with the CFHW ansatz, we can define the Atiyah-Ward ansätze An, n = 1, 2, ··· , as

$$A_1 \xrightarrow{\text{BI}} A_2 \xrightarrow{\text{BI}} A_3 \rightarrow \cdots \xrightarrow{\text{BI}} A_n \tag{2-19}$$

Let us denote the functions ϕ, ρ, $\bar{\rho}$ of the An ansatz by ϕ_n, ρ_n, $\bar{\rho}_n$, then $(\phi_n, \rho_n, \bar{\rho}_n)$ is given by $(\phi_1, \rho_1, \bar{\rho}_1) \xrightarrow{(BI)^{n-1}} (\phi_n, \rho_n, \bar{\rho}_n)$ where $(\phi_1, \rho_1, \bar{\rho}_1)$ is a solution of eq. (2-18).

Corrigan, Fairlie, Goddard and Yates[9] has given an explicit construction of ϕ_n, ρ_n, $\bar{\rho}_n$, $n \geq 2$ in terms of "spin (n-1) massless anti-dual linear field". Their solution begins by defining (2n+1) function Δ_k, $-n \leq k \leq n$, which satisfy the following equations:

$$\partial_{\bar{y}}\Delta_k = -\partial_{\bar{z}}\Delta_{k+1} \tag{2-20a}$$

$$\partial_z\Delta_k = \partial_{\bar{y}}\Delta_{k+1} \tag{2-20b}$$

It follows from (2-20) that Δ_k satisfies the free field equation:

$$(\partial_y \partial_{\bar{y}} + \partial_z \partial_{\bar{z}})\, \Delta_k = 0 \tag{2-21}$$

Let us also define for $n \geq 1$

$$D_n = \begin{vmatrix} \Delta_0 & \Delta_{-1} & \cdots\cdots & \Delta_{-n+1} \\ \Delta_1 & \Delta_0 & \cdots\cdots & \Delta_{-n+2} \\ \vdots & \vdots & & \vdots \\ \Delta_{n-1} & \Delta_{n-2} & \cdots\cdots & \Delta_0 \end{vmatrix} \tag{2-22}$$

where $|\cdots|$ denote the determinant. We now state the result of Corrigan et. al..

(Theorem 2-1) The functions ϕ_n, ρ_n, $\bar{\rho}_n$ of the An ansatz is given by

$$\phi_n = \frac{D_n}{D_{n-1}} \tag{2-23a}$$

$$\rho_n = \frac{(-1)^n}{D_{n-1}} \begin{vmatrix} \Delta_{-1} & \Delta_{-2} & \cdots\cdots & \Delta_{-n} \\ \Delta_0 & \Delta_{-1} & \cdots\cdots & \Delta_{-n+1} \\ \vdots & \vdots & & \vdots \\ \Delta_{n-2} & \Delta_{n-3} & & \Delta_{-1} \end{vmatrix} \tag{2-23b}$$

$$\bar{\rho}_n = \frac{(-1)^{n-1}}{D_{n-1}} \begin{vmatrix} \Delta_1 & \Delta_0 & \cdots & \Delta_{-n+2} \\ \Delta_2 & \Delta_1 & & \Delta_{-n+3} \\ \vdots & \vdots & & \vdots \\ \Delta_n & \Delta_{n-1} & & \Delta_1 \end{vmatrix} \tag{2-23c}$$

Proof of this theorem is given in reference (9).

(II-C) The Condition of Real Gauge Potential

When the gauge potential A_μ^a is real and the gauge transformation G is unitary in the real space, then we require

$$\overline{D} \doteq (D^+)^{-1} \tag{2-24}$$

and $$V \doteq (\overline{V^+})^{-1} \tag{2-25}$$

(the symbol $\doteq$ is used for equations valid only for real values of x_1, x_2, x_3, x_4), which implies $J \equiv D\,\bar{D}^{-1} \doteq D \cdot D^{+}$ = a positive definite Hermitian matrix.

But in nomopole problem, BI transformation can't preserve the reality of gauge potential, hence we must consider complex potential and complex gauge transformations even in real space. This leads to the question: given D and $\bar{D}$ or equivalently J, when is it possible to choose a gauge so that the gauge fields are real? Prasad et. al. answer this question with (Theorem 2-2) Given J or D and $\bar{D}$, a necessary and sufficient condition that the gauge potentials are real in some gauge is the existance of an SL (2, C) matrix V (y, z), depending on y and z only, such that $J \cdot V \doteq$ positive definite hermitian matrix.

Furthermore, if V exists then the gauge transformation is given by

$$G\,G^{+} = \bar{D}^{-1}\,V\,(y, x)\,D^{+\,-1} \tag{2-26}$$

In closing this subsection, we remark that in R-gauge the usual reality condition $D \doteq (D^{+})^{-1}$ becomes

$$\phi \doteq \text{real} \quad \text{and} \quad \bar{\rho} \doteq \rho^{*}$$

III. Multimonopole Solution

(III-A) Self-Duality Equations in Euclidean Space and Bogomolny's Equation:

In this subsection, we begin with the simple observation that the self-duality equation (2-3) in Euclidean space

$$\frac{1}{2}\,\epsilon_{ijk4}\,F_{ij} = \frac{1}{2}\,\epsilon_{ijk}\,F_{ij} = F_{k4} = \partial_k\,A_4 + [A_k, A_4] - \partial_4\,A_k$$

becomes identical with the Bogomolny's equations

$$B_k = +\frac{1}{2}\,\epsilon_{ijk}\,F_{ij} = +\,D_k\,\phi \tag{3-1}$$

when $\partial_4 A_\mu = 0$ and the Higgs field ϕ^a is identical to $A_4{}^a$. Since x_4 can be though of as Euclidean "time". We shall use the word "static" in this context to mean independent of the Euclidean time x_4. In what follows we shall restrict the gauge transformations to static both in Euclidean and Mikowski space. Therefore, with the above restriction, the monopole problem becomes identical with the self-dual Yang-Mills fields provided we require suitable

boundary condition.

Therefore we can obtain a multimonopole solution as a solution of the self-duality equation (2-3) which satisfies[14]:

(MI) The potentials are static: $\partial_4 A_\mu = 0$

(MII) In some gauge the potentials A_μ^a are real and smooth i.e. A_μ^a and its derivatives are non-singular.

(MIII) The gauge invariant quantity, the square of the Higgs field $\phi^2 = \phi^a \phi^a = A_4^a A_4^a$ has the asymptotic behavior

$$\phi^2 \xrightarrow[r \to \infty]{} \frac{C^2}{g^2} - \frac{2nC}{g^2}\frac{1}{r} + O(r^{-2}) \quad n = 0, 1, 2, \tag{3-2}$$

Condition (MIII) implies this solution has topological charge n, since the total energy of the monopole in the limit of vanishing Higgs potential is

$$\begin{aligned} E &= \frac{1}{2}\int d^3x\, [B_i^a B_i^a + D_i \phi^a D_i \phi^a] \\ &= \int d^3x\, (B_i^a D_i \phi^a) \\ &= \frac{1}{2}\int \partial_i \partial_i (\phi^2) \\ &= \lim_{\gamma \to \infty} \frac{1}{2}\int r^2 d\Omega \left(\frac{\partial \phi^2}{\partial r}\right) \\ &= \frac{4\pi C}{g^2} \cdot n \\ &= \frac{C}{g} Q^{[17]}. \end{aligned} \tag{3-3}$$

Then magnetic charge $Q = \frac{4\pi}{g} \cdot n$, i.e. the solution is a multimonopole solution with topological charge n.

(III-B) Multimonopole Solution with Axially Symmetry

Let $$\Lambda_o = \sum_{i=1}^{n} \alpha_i \frac{\sinh C R_i}{R_i} \tag{3-4}$$

where $R_i = x_1^2 + x_2^2 + (x_3 - C_i)^2$

and α_i, C_i can be complex, subject to the restriction that Λ_o is real. It is convenient to define

$$\sqrt{2}\ y = x_1 + i\, x_2 = \xi = \rho e^{i\theta} \tag{3-5a}$$

$$\sqrt{2}\,\bar{y} = x_1 - i\,x_2 = \bar{\xi} = \ell e^{-i\theta} \tag{3-5b}$$

i.e. $\quad \ell^2 = x_1^2 + x_2^2 \quad$ etc

Define $\quad \Lambda_k \equiv \bar{y}^{-1}\,\partial_y\,\Lambda_{k+1} \equiv y^{-1}\,\partial\bar{y}\;\Lambda_{k+1} \equiv \ell^{-1}\,\partial\ell\,\Lambda_{k+1}$ (3-6)

Then Λ_{k+1} is given by an (k+1)-fold indefinite integral

$$\Lambda_{k+1} = \int \ell d\ell \cdot \cdot \cdot \cdot \int \ell d\ell\,\Lambda_o \qquad k \geq 0$$

$$= \sum_i \alpha_i \int R_i dR_i \cdot \cdot \cdot \cdot \int R_i dR_i \quad (\frac{\sinh CR_i}{R_i}) \tag{3-7}$$

Note that in defining Λ_k $(1 \leq k \leq n)$ we do not include any integration "constant", which may be any arbitrary function of x_3. We found that

(Lemma 3-1): The functions Δ_k, Δ_{-k} and Δ_o, $1 \leq k \leq n$ defined by

$$\Delta_o = e^{icx_4}\,\Lambda_o$$

$$\Delta_{-k} = (-1)^k\,e^{icx_4}\,\bar{\xi}^{-k}\,(\partial_3 + C)^k\,\Lambda_k \tag{3-8}$$

$$\Delta_k = e^{icx_4}\,\xi^{-k}\,(\partial_3 - C)^k\,\Lambda_k$$

is a solution of (2-20).

And then we can construct $(\phi_n, \rho_n, \bar{\rho}_n)$ by using (2-23) and (3-8) their form are

(Lemma 3-2): The solution constructed above has the form

$$\phi_n = \phi_n\,\ell^{-n}\,e^{icx_4}$$

$$\rho_n = \phi_n\,\bar{\xi}^{-n}\,e^{icx_4} \tag{3-9}$$

$$\bar{\rho}_n = -\,\bar{P}_n\,\xi^{-n}\,e^{icx_4}$$

where ψ_n, P_n, $\bar{P}_n$ are real functions of ℓ and x_3 only. Note that P_n, $\bar{P}_n$ and ϕ_n are in fact defined by eq. (3-9),

We would show these solution constructed from Eq. (3-9) to be a multimonopole with magnetic charge n.

(I) Monopole Charge

(Theorem III-1) Suppose that $(\phi_n, \rho_n, \bar{\rho}_n)$ in eq. (3-9) correspond to the ansatz An. Then the Higgs field for the nth ansatz satisfies

$$\phi_n^2 \equiv (A_4^a A_4^a)_n = \frac{C^2}{g^2} - \sum_{k=1}^{n} \nabla^2 \ell n\, \phi_k \tag{3-10}$$

$$\xrightarrow[r\to\infty]{} \frac{C^2}{g^2} - \frac{2nc}{g^2 r} + O(r^{-2}) \tag{3-11}$$

(II) Static Properties

From eqs. (2-7), (2-13) we have

$$Au = -\frac{1}{2\phi}\begin{pmatrix} \phi, u & 0 \\ -2\rho, u & -\phi, u \end{pmatrix}$$

$$A\bar{u} = \frac{1}{2\phi}\begin{pmatrix} \phi, \bar{u} & -2\bar{\rho}, \bar{u} \\ 0 & -\phi, \bar{u} \end{pmatrix}.$$

It's clear gauge potentials are static from (Lemma 3-2).

(III) The Reality of the Solution

Choose

$$V_n(y, z) = \begin{pmatrix} 0 & (r\xi^n)^{-1} \\ -r\xi^n & 0 \end{pmatrix} \tag{3-12}$$

Then

$$J_n V_n = \begin{pmatrix} \dfrac{r\,\ell^n\,\bar{\rho}_n}{r_n} & \dfrac{\ell^n e^{-icx_4}}{r\xi^n\,\phi_n} \\ -\dfrac{r\,\xi^n\, e^{icx_4}(\phi_n^2 - \rho_n\,\bar{\rho}_n)}{\ell^n \phi_n} & \dfrac{\rho_n}{r\,\ell^n\,\phi_n} \end{pmatrix}$$

Therefore, $J_n V_n$ is hermitian if r is real and

$$r^2\,(P_n \bar{P}_n - \phi_n^2) = 1 \tag{3-13}$$

If Eq. (3-13) is satisfied, the necessary gauge transformation G is given by

$$G_n\, G_n^{+} = \begin{pmatrix} \bar{P}_n & -\phi_n e^{-in\theta} \\ -\phi_n e^{in\theta} & P_n \end{pmatrix} \tag{3-14}$$

Note that a constant factor (real non-zero) in the definition of Λ_o, Δ_k and therefore $(\phi_n, \rho_n, \bar{\rho}_n)$ are multiplied by the same factor, which does not affect potential. Using

this factor, we can always choose

$$r = +1 \qquad \text{in eqs. (3-31) and (3-14) i.e.}$$

$$P_n \bar{P}_n - \phi_n^2 = 1 \tag{3-15}$$

and

$$G_n G_n^+ = \begin{pmatrix} \bar{P}_n & -\phi_n e^{-in\theta} \\ -\phi_n e^{in\theta} & P_n \end{pmatrix} \tag{3-16}$$

Prasad[15] has been shown take the A_n ansatz with

$$\Lambda_o = \sum_{k=1}^{n} \alpha_k \frac{\sinh r_k}{r_k} \tag{3-17a}$$

where

$$r_k^2 = x_1^2 + x_2^2 + (x_3 - z_k)^2 \tag{3-17b}$$

$$z_k = [\frac{(n+1)}{2} - k]\, i\pi \tag{3-17c}$$

$$\alpha_k = \frac{(n-1)!}{(k-1)!(n-k)!} \tag{3-17d}$$

he can obtain a monopole solution of topological charge n, i.e. solution constructed from eq. (3-17) can satisfy eq. (3-13).

(IV) Nonsingular

From eqs. (3-3), (3-10) and (2-23a) the energy density of the A_n ansatz is given by

$$\varepsilon_n = -\frac{1}{g^2} \nabla^2 \nabla^2 \ell n\, (\phi_1\, \phi_2 \cdots \phi_n) \tag{3-18}$$

$$= -\frac{1}{g^2} \nabla^2 \nabla^2 \ell n\, Dn \tag{3-19}$$

Hence the monopole solutions require Dn is never zero. Prasad has shown that there exist solutions which can be nonsingular by arguments[16].

(III-C) Real Solution in Yang's K-gauge[10]:

Yang's K gauge is the gauge which D is a hermitian matrix in eq. (2-7). In this gauge the gauge transformation is

$$G_n^k = \frac{1}{\sqrt{P_n + \bar{P}_n + 2}} \begin{pmatrix} \bar{P}_n+1 & -\phi_n e^{-in\theta} \\ -\phi_n e^{in} & P_n+1 \end{pmatrix}$$

and the gauge potentials are

$$A_1 = (\frac{-V_n}{eS} \sin(n-1)\theta, \ \frac{V_n}{eS} \cos(n-1)\theta, \ \frac{-2M_n}{eS} \sin\theta) \tag{3-21a}$$

$$A_2 = (\frac{-V_n}{eS} \cos(n-1)\theta, \ \frac{-V_n}{eS} \sin(n-1)\theta, \ \frac{2M_n}{eS} \cos\theta) \tag{3-21b}$$

$$A_3 = (\frac{-(W_n+C\phi_n)}{eS} \sin n\theta, \ \frac{(W_n+C\phi_n)}{eS} \cos n\theta, \ 0) \tag{3-21c}$$

$$A_4 = (\frac{(W_n-C\phi_n)}{eS} \cos n\theta, \ \frac{(W_n-C\phi_n)}{eS} \sin n\theta, \ \frac{-2N_n}{eS}) = \phi \tag{3-21d}$$

where
$$S = P_n + \bar{P}_n + 2 \tag{3-21e}$$

$$M_n = \frac{S}{2} \partial_\ell (\ell n - \frac{\phi_n}{S}) - \frac{S}{2} \frac{n}{\ell} \tag{3-21f}$$

$$V_n = \frac{(1+\bar{P}_n) \partial_\ell P_n - (1+P_n) \partial_\ell \bar{P}_n}{\phi_n} \tag{3-21g}$$

$$N_n = \frac{S}{2} \partial_3 [\underline{n}(\frac{\phi_n}{S})] - \frac{C}{2} (\bar{P}_n - P_n) \tag{3-21h}$$

$$W_n = \frac{(1+\bar{P}_n) \partial_3 P_n - (1+P_n) \partial_3 \bar{P}_n}{\phi_n} - \frac{C}{\phi_n} (1+P_n)(1+\bar{P}_n) \tag{3-21i}$$

If we let

$$\Lambda_o = \frac{\sinh cr}{r} \tag{3-22a}$$

then we can get

$$P_1 = \cosh cr + \frac{x_3}{r} \sinh cr \tag{3-22b}$$

$$\bar{P}_1 = \cosh cr - \frac{x_3}{r} \sinh cr \tag{3-22c}$$

$$\psi_1 = \frac{\ell}{r} \sinh cr \tag{3-33d}$$

Substituting eq. (3-22) into (3-21), we can get the Bogomolny-Prasad exact one monopole solution

$$A_i^a = \frac{1}{g}\,\varepsilon_{aij}\,\frac{x_j}{r^2}\left[1 - \frac{cr}{\sinh cr}\right] \tag{3-23a}$$

$$A_4^a = \phi^a = \frac{1}{g}\,\frac{x_a}{r^2}\left[1 - cr\coth cr\right] \tag{3-23b}$$

IV. MULTIDYON SOLUTIONS

The total energy of the SU(2) gauge theory with a Higgs triplet in the limit of vanishing Higgs potential can be written as[17]

$$E = \int d^3x\left[\frac{1}{4}F_{ij}^a F_{ij}^a + \frac{1}{2}D_i\phi_a D_i\phi_a + \frac{1}{2}F_{0i}^a F_{0i}^a + \frac{1}{2}D_0\phi_a D_0\phi_a\right] \tag{4-1}$$

If we assume A_o^a and ϕ^a are parallel in group space, so that $D_0\phi^a = 0$ for static field. Then eq. (4-1) can be written

$$E = \int d^3x\left[\frac{1}{4}(F_{ij}^a - \cos\alpha\,\varepsilon_{ijn}D_n\phi_a)^2 + \frac{1}{2}(F_{0n}^a - \sin\alpha\,D_n\phi_a)^2 + \sin\alpha\,\partial_n k_n \mp \cos\alpha\,\partial_n I_n\right] \tag{4-2}$$

where

$$\partial_n I_n = \frac{1}{2}\varepsilon_{ijn}F_{ij}^n D_n\phi_a = \partial_n\left(\frac{1}{2}\varepsilon_{ijn}F_{ij}^a\phi_a\right) = \partial_n(B_n^a\phi_a)$$

$$\partial_n K_n = F_{0n}^a D_n\phi_a = \partial_n(F_{0n}^a\phi_a) = \partial_n(E_n^a\phi_a)$$

Define physical magnetic field and electric field as follows:

$$B_n = B_n^a\hat{\phi}_a \tag{4-3}$$

$$E_n = E_n^a\hat{\phi}_a \tag{4-4}$$

Then

$$\int d^3x\,\partial_n I_n = \int d\Omega\,\{r^2[\hat{r}_n B_n\phi]_{r=\infty}\} = \frac{C}{g}(q) \tag{4-5}$$

$$\int d^3x\,\partial_n K_n = \int d\Omega\,\{r^2[\hat{r}_n B_n\phi]_{r=\infty}\} = \frac{C}{g}(e) \tag{4-6}$$

where

$$q \equiv \int d\Omega\,[r^2\hat{r}_n B_n]_{r=\infty} \tag{4-7}$$

$$e \equiv \int d\Omega\,[r^2\hat{r}_n E_n]_{r=\infty} \tag{4-8}$$

If we let $$F^a_{ij} = \cos\alpha\ \varepsilon_{ijn}\ D_n\ \phi_a \tag{4-9}$$

$$F^a_{0n} = \sin\alpha\ D_n\ \phi_a \tag{4-10}$$

and choose α as follows

$$\sin\alpha = \frac{e}{\sqrt{q^2+e^2}}\ ,\quad \cos\alpha = \frac{q}{\sqrt{q^2+e^2}} \tag{4-11}$$

then we get the minimum total energy

$$E = \frac{C}{g}\sqrt{q^2+e^2} \tag{4-12}$$

Hence if gauge potential satisfy the generalized Bogomolny's condition i.e. eqs. (4-9) and (4-10), and $A_o{}^a$ parallel with ϕ^a in group space, then we have minimum total energy. Furthermore if we assume

$$A_o{}^a = -\sin\alpha\ \phi_a \tag{4-13}$$

then eq. (4-10) can be satisfied trivially. This leaves eq. (4-9), which can now be written

$$q\ F^a_{0n} = \frac{1}{2}\varepsilon_{ijn}\ e\ F^a_{ij} \tag{4-14}$$

Now we can take eqs. (4-13) and (4-14) as equations of multidyon, since its solutions satisfy the field equations

$$\partial^\nu F^a_{\mu\nu} = e\ \ \varepsilon_{abc}\ \ [F^b_{\mu\nu}\ A_c{}^\nu - (D_\mu\phi_b)\phi_c] \tag{4-15}$$

$$\partial^\mu D_\mu \phi_a = e\ \varepsilon_{abc}\ (D_\mu\phi_b)A^\mu_c \tag{4-16}$$

automatically and its solutions possess electric and magnetic charge.

We found that if we let

$$A^a_o = \sinh\gamma\ \phi'^a \tag{4-17a}$$

$$\phi^a = \cosh\gamma\ \phi'^a \tag{4-17b}$$

where $$\sinh\gamma = -\frac{e}{q} \qquad \cosh\gamma = \frac{1}{q}\sqrt{q^2+e^2}$$

then eq. (4-14) can be reduced to

$$B_n^a = \frac{1}{2}\varepsilon_{ijn} F_{ij}^a = \frac{q}{e} F_{0n}^a$$

$$= \frac{-1}{\sinh\gamma}\left[\partial_o A_n^a - \partial_n A_o^a + e\,\varepsilon_{abc} A_o^b A_n^c\right]$$

$$= D_n \phi'^a$$

which is the Bogomolny's condition.

From eqs. (4-17a) and (4-17b), we can get

$$A_o^a = -\sin\alpha\ \phi_a$$

This tell us the problem to find multidyon solutions is equivalent to find multimonopole solutions. That is if

$$A_i^{a'}\ ,\ \phi^{a'}\ ,\ A_o^{a'} = 0$$

represents the solution of multimonopole, then these functions

$$A_i^a = A_i^{a'}$$

$$A_o^a = \sinh\gamma\ \phi^{a'}$$

$$\phi^a = \cosh\gamma\ \phi^{a'}$$

are the corresponding multidyon solutions.

Hence we can easily write the multidyon solutions in Yang's K-gauge from Eqs. (1-2) and (3-21)

$$A_1 = \left(-\frac{V_n}{eS}\sin(n-1)\theta,\ \frac{V_n}{eS}\cos(n-1)\theta,\ \frac{-2M_n}{eS}\sin\theta\right) \tag{4-18a}$$

$$A_2 = \left(-\frac{V_n}{eS}\cos(n-1)\theta,\ \frac{-V_n}{eS}\sin(n-1)\theta,\ \frac{2M_n}{eS}\cos\theta\right) \tag{4-18b}$$

$$A_3 = \left(-\frac{(W_n+c\phi_n)}{eS}\sin n\theta,\ \frac{(W_n+c\phi_n)}{eS}\cos n\theta,\ 0\right) \tag{4-18c}$$

$$A_4 = \left(-\sinh\gamma\frac{(W_n-c\phi_n)}{eS}\cos n\theta,\ -\sinh\gamma\frac{(W_n-c\phi_n)}{eS}\sin n\theta,\ 2\sinh\gamma\frac{N_n}{eS}\right) \tag{4-18d}$$

$$\phi = (-\cosh\gamma \frac{(W_n - c\phi_n)}{eS} \cos n\theta,\ -\cosh\gamma \frac{(W_n - c\phi_n)}{eS} \sin n\theta,$$

$$2\cosh\gamma \frac{N_n}{e}) \qquad (4\text{-}18e)$$

where S, V_n, M_n, W_n, ϕ_n are defined in eqs. (3-21) and (3-9). When n=1, we get the Julia-Zee dyon[17] solution from eqs. (3-23) and (1-2).

REFERENCE

(1) G. 'tHOOFT, Nucl. Phys. B79, 276 (1974).
A. M. POLYAKOV, JETP Lett. 20, 194 (1974).

(2) P. LANGACKER, SLAC-PUB-2544 June (1980).

(3) C. H. TAUBES, Commu. Math. Phys. to be published.

(4) M. K. PRASAD, "Exact Yang-Mills-Higgs Monopole Solutions of Arbitrary Topological Charge" to be published in Comm. Math. Phys.

(5) P. FORGACS, Z. HORVATH, and L. PALLA "Soliton Theoretical Framework for enerating Multimonopoles" KFKI preprint-1981-21.

(6) E. F. CORRIGAN and D. B. FAIRLIE, Phys. Lett 67B, 69 (1977); G.'tHooft unpublished
F. WILCZEK, Quark Confinement and Field Theory, ed. D. STUMP and D. WEINGARTEN, JOHN WILEY, NY 1977.

(7) R. S. WARD, Phys. Lett. 61A, 81 (1977).

(8) M. F. ATIYAH and R. S. WARD, Comm. Math. Phys. 55, 117 (1977).

(9) E. F. CORRIGAN, D. B. FAIRLIE, P. GODDARD and R. G. YATES, Phys. Lett. 72B, 354 (1978), and Comm. Math. Phys. 58, 223 (1978).

(10) C. N. YANG, Phys. Rev. Lett. 38, 1377 (1977).

(11) M. K. PRASAD; A. SINHA and LING-LIE CHAU WANG: "A Systematic Framework for generating Multi-monopole Solutions" ITP-SB-80-73.

(12) JULIA, B., and A. ZEE, Phys. Rev. D11, 2227 (1975).

(13) M. K. PRASAD and C. M. SOMMERFELD, Phys. Rev. Lett. 35, 760 (1975).
E. B. BOGOMOL'NYI, Sov. J. Nucl. Phys. 24, 449 (1976).

(14) See reference 11

(15) See reference 12

(16) M. K. PRASAD and P. ROSSI: "Construction of Exact Multi monopole Solutions".

(17) A. Actor: Rev. Mod. Phys. 51, 461 (1979).

FORCE CONSTANT MODEL OF CRYSTALLINE HI IN ITS LOW TEMPERATURE PHASE

Chia-Nan Chang

Department of Electronic Engineering and Technology

National Taiwan Institute of Technology, Taipei, R.O.C.

and

Wan-Sun Tse

Institute of Physics, Academia Sinica,

Nankang, Taipei, Taiwan, R.O.C.

Lattice dynamics of crystalline HI in phase III is studied by using the Born-Von Kármán force constant model with five different kinds of interatomic force constants and the results are compared to observed zone centre ($\vec{k} = 0$) frequencies (Raman & I.R.).

Solid HI forms an interesting molecular crystals, in common with HCl and HBr, has three phase[1,2]. Phase I and II are isomorphous to those of HCl and HBr in which the hydrogen atoms are disorded and the unit cell has 4 molecules in both phases. In the low temperature phase III, the hydrogens are fully ordered. In HCl, HBr and HF, the molecules form planar zig-zag chains. There are 2 molecules per primitive unit cell and the space group is C_{2v}^{12}[3]. For HI, however, although the structure has not been completely determined, it is known that the unit cell is larger, with 8 or more molecules per primitive unit cell, and groups of 4 molecules form hydrogen-bonded squares[4,5]. The point group of this pseudomolecule $(HI)_4$ is C_{4h} and standard group theoretical techniques shows that the external modes corresponding to pure translations and rotations are of (Au + Eu) and (Ag + Eg) species respectively. It also shows that the Ag, Bg and Eu species involve motions within the molecular plane while Au, Bu and Eg are species involving out-of-plane motions. The activities of the fundamentals, except pure translations and rotations, are as follow:

Raman active modes: 3Ag + 4Bg + Eg

Infrared active modes: Au + 3Eu

Inactive modes: 2Bu

In this paper, a simple model of crystalline HI has been developed using the ydrogen bonded squares described in reference 4 as the basic building blocks of the structure. he planar square consists of four molecules as shown in Figure 1. The z-axis corresponds to he crystallographic z-axis. In this model, interactions between atoms in different squares ere ignored and interatomic interactions within each square were described by the four force onstants as indicated in Figure 1. The fifth, δ, represents a bending constant, giving a estoring force proportional to the perpendicular displacement of a hydrogen atom from the ine between adjacent iodine. Assuming the Axially-symmetric force constants[6], α, β, δ etween each atom to its first and second-nearest neighbours, and the central force onstants[7] γ, ε between each atom to its third and fourth neighbours, the equations of otion for the eight independent atoms in the x, y and z directions, relating the five nteracting force constants, establish a 24×24 dynamical matrix. The length parameters a nolecular bond) and b (hydrogen bond) were obtained from the literatures[1,8]. All force onstants were then adjusted to give optimum agreement between the observed[8] and the alculated frequencies. This involved diagonalization of the dynamical matrix on a VAX 1/780 computer using the Jacobi rotation method. The eigenvectors were also found and ese allowed assignments of the observed frequencies to be made.

Some physical arguments, as follows, are used to assist in the determination of ome of the force constants. (a) The stretching frequencies of HI in the planar structure lmost totally depend on combinations of the force constants α and β. The appropriate alue of β is obtained by fitting the external in-plane translational frequencies due to ne fact that the molecules HI translate in the plane is determined mostly by β as seen in igure 1. In turn a value of α can be found and checked against the gas phase value[9].) The splitting of the internal stretching frequencies and the lattice librational equencies within the plane depend mostly on γ and combination of γ, δ and ε respectively.) The out-of-plane libration depend on δ since only the δ force constant is involved in ne z-direction.

The optimized values of the force constants and a comparison of the observed and alculated frequencies are listed in Table 1. Since coupling between squares of $(HI)_4$ is eglected, the number of calculated eigenvalues is less than the number of observed equencies, and so some of the latter were grouped, as indicated. From Table 1, it is en that the stretching, in-plane librational and in-plane translational modes are quite

well fitted, because the in-plane motions are less likely to be significantly influenced by the inter-square forces. The agreement is not as good for the out-of-plane librations, which is due to the neglect of inter-planar forces between squares. Note that the pure translational and rotational modes are not identically equal to zero because of the round-off errors produced during the diagonalization procedure. If inter-planar forces were induced, additional low frequency modes would occur, as well as further splittings of the higher frequency modes.

The model adopted in this calculation for solid HI shows generally good agreement between the observed and calculated frequencies suggesting that the forces between molecules in different squares are much smaller that those between nearest neighbours in the same square. A comprehensive lattice dynamical analysis and assignment of all of the observed features will not be possible until the crystal structure is more completely determined.

References

(1) F. A. MAUER, C. J. KEFFER, R. B. REEVES, and D. W. ROBINSON, J. Chem. Phys. 42, 1465 (1965).

(2) K. K. KOBAYASHI, E. HANAMURA, and F. SHISIDO, Phys. Lett. 28A, 718 (1969).

(3) J. E. VESSEL and B. H. TORRIE, Can. J. Phys. 55, 592 (1977).

(4) E. SANDOR and J. H. CLARK, Acta, Cryst., 28A, 5188 (1972).

(5) E. SANDOR, Private Communication.

(6) N. WAKABAYASHI and R. M. NICKLOW, Neutron Scattering and Lattice Dynamics of Material with Layered Structures in "Material Science", Vol. 2, Addison-Wesley Publishing Company, 413 (1979).

(7) A. A. MARADUDIN, E. W. MONTROLL, G. H. WEISS and I. P. IPATOUA, Theory of Lattice Dynamics in the Harmonic Approximation, Academic Press, New York 14, (1971).

(8) A. ANDERSON, B. H. TORRIE and W. S. TSE, J. Raman Spect., 8, 213 (1979).

(9) G. HERZBERG, Spectra of Diatomic Molecules, D. Van Nostraud, Princeton, 540 (1950).

Table 1. Experimental (Ref. 8) and calculated frequencies (cm^{-1}) for solid HI.

Frequencies (cm^{-1}) Observed	Calculated	Activity	Assignment
—	0.24	—	Eu, Au } $T(HI)_4$
—	0.03	—	
—	0.02	—	Eg, Ag } $L(HI)_4$
—	0.24	—	
—	0.006	—	Bu o/p T
26, 30	15	R	Bg
48, 59	54	IR	Eu } i/p T
55	54.5, 56	R	Ag, Bg
	174		Bu
136, 169.5, 188.5	174.5	R	Eg } o/p L
207	175	IR	Au
235.5	231	R	Bg
253	256	IR	Eu } i/p L
254, 334, 374	340.5	R	Ag
2108	2114	R	Ag
2125.5	2121.5	IR	Eu } i/p S
2129	2129	R	Bg

Optimized force constants: $\alpha = 2.525\times10^5$ dynes cm^{-1}
$\beta = 0.111\times10^5$ dynes cm^{-1}
$\gamma = 2100$ dynes cm^{-1}
$\delta = 1800$ dynes cm^{-1}
$\varepsilon = 600$ dynes cm^{-1}

R - Raman active; IR - Infrared active; o/p - out of plane
i/p - in plane; L - libration; T - translation; S - stretching.

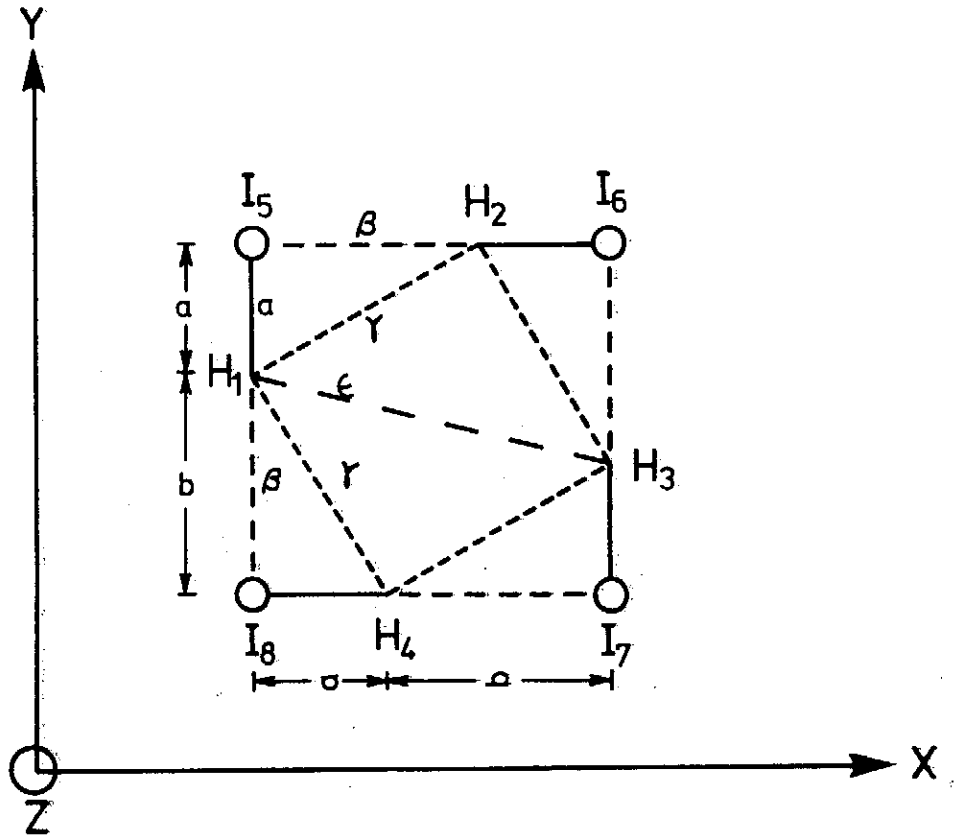

Figure 1. Geometry of the force constant model for solid HI (Phase III)

a = 1.604 Å

b = 2.626 Å

LATTICE VIBRATIONS OF SOLID HYDROFLUORIDE ACID

Wan-Sun Tse

Institute of Physics, Academia Sinica

Nankang, Taipei, Taiwan, R.O.C.

and

Chia-Nan Chang

Department of Electronic Engineering and Technology

National Taiwan Institute of Technology, Taipei, R.O.C.

Lattice dynamics calculations on the solid hydrofluoride acid are presented. It is found that a six interatomic force constants using the Born-Von Karman model is capable of giving acceptable values of the zone center frequencies.

I. INTRODUCTION

Solid hydrofluoric acid is an interesting example of a simple molecular crystals which has been the subject of several experimental[1-5] and theoretical studies[6-8]. There are no known phase transitions in the solid state, and the crystal structure is ordered orthorhombic with space group C_{2v}^{12} ($Bb2_1m$)[9] forming the hydrogen-bonded zig-zag chains, which is characteristic of all members of the hydrogen halide family at low temperatures, except for HI-DI. There are two molecules in the primitive unit cell and neighbouring zig-zag chains are parallel, resulting in a polar structure. The three dimensional structure of those zig-zag chains is shown in Figure 1.

From the correlation diagram[2] we know that the lattice and stretching vibrations for $\vec{k}=0$ of this crystal is classified into twelve non-degenerate normal modes in accordance with their symmetries. There are three translational ($A_1+B_1+A_2$) and four librational modes ($A_1+B_1+A_2+B_2$) corresponding to the external motions of rigid molecules. There are also two stretching modes (A_1+B_1). In this paper, we describe lattice dynamics calculations based on the Born-Von Karman model, using the harmonic approximation. Parameters are

adjusted to attempt to interpret those normal modes of vibrations obtained from spectroscopic techniques[1] in terms of such a simple force constant model.

II. LATTICE DYNAMICAL MODEL

The calculation of phonon frequencies requires a detailed knowledge of the potential function Φ for the crystal. Within the harmonic approximation the potential energy of the three dimensional zig-zag chain crystal can be written as

$$\Phi = \Phi_o + \sum_{\ell,k,\alpha} \Phi_\alpha(^{\ell}_{k})\, u_\alpha(^{\ell}_{k}) + \frac{1}{2} \sum_{\ell,k,\alpha} \Phi_{\alpha\beta}(^{\ell;\ell'}_{k;k'})\, u_\beta(^{\ell'}_{k'})\, u_\alpha(^{\ell}_{k}) \tag{1}$$

where $\vec{u}_\alpha(^{\ell}_{k})$ is the α-th component of the displacement of the ℓ-th one of the k-kind atom. When the differentials are evaluated at the equilibrium the equations of motions are then

$$M_k\, u_\alpha(^{\ell}_{k}) = - \sum_{\ell';k';\beta} \Phi_{\alpha\beta}(^{\ell;\ell'}_{k;k'}) u_\beta(^{\ell'}_{k'}) \tag{2}$$

The lattice dynamical calculations then follow a standard procedure and we can obtain the mass reduced dynamical matrix whose elements are given by:

$$D_{\alpha\beta}(^{\ell;\ell'}_{k;k'}|\vec{k}) = \frac{1}{\sqrt{M_k M_{k'}}} \sum_{\substack{\ell' \\ k'}} \Phi_{\alpha\beta}(^{\ell;\ell'}_{k;k'}) \times e^{-i\vec{k}\cdot[\vec{r}(^{\ell}_{k}) - \vec{r}(^{\ell'}_{k'})]}$$

The eigenvalues of the dynamical matrix D are the squared frequencies of the phonons, $\omega^2(k)$, and the matrix which diagonalises D is the matrix of phonon eigenvectors. The problem of obtaining the phonon frequencies and eigenvectors at long wavelength limit, $\vec{k}<<1$, then consists of constructing D and diagonalising it.

In this three dimensional interacting model, interaction between adjacent zig-zag chains were considered to their nearest neighbors. The model is outlined in Fig. 1 where all the force constants are shown. We limit the range of interaction of each hydrogen atom and fluorine atom to their fourth-nearest neighbors in each planar zig-zag chain structure. Assuming both the central force constants α, β and axially symmetry angular force constant[10] δ between each atom to its first and second nearest neighbors. (Since there are strong covalent bond and hydrogen bond between them), while only central force constants γ, ε, η between each atom to its further nearest neighbors, we have the

following dynamical matrixes of interaction for the four atoms in one unit cell. (expressed in dyadic forms).

Let $P = a^2+b^2+2ab\sin\theta$ $\quad X = (a^2+b^2)(1+\sin^2\theta)+4ab\sin\theta$

$Q = (a+b)^2+2a(a+b)\sin\theta+a^2$ $\quad V = a+(a+b)\sin\theta$

$U = (a+b)+a\sin\theta$ $\quad R = d^2+b^2-2bd\sin\theta+c^2$

$W = 2ab\cos\theta+(a^2+b^2)\sin\theta\cos\theta$

$$\Phi\begin{pmatrix}(0,0,0)\\0\\F\end{pmatrix};\begin{pmatrix}(0,0,0)\\0\\F\end{pmatrix} = \Phi\begin{pmatrix}(0,0,0)\\0\\F\end{pmatrix};\begin{pmatrix}(0,0,0)\\0\\H\end{pmatrix}$$

$$= -\left[(\hat{i}\hat{i}+\hat{k}\hat{k})\,\delta\left(\frac{a}{a+b}\right)+\hat{j}\hat{j}\,(\alpha)\right]$$

$$\Phi\begin{pmatrix}(0,0,0)\\0\\H\end{pmatrix};\begin{pmatrix}(0,0,0)\\1\\F\end{pmatrix} = \Phi\begin{pmatrix}(0,0,0)\\1\\F\end{pmatrix};\begin{pmatrix}(0,0,0)\\0\\H\end{pmatrix}$$

$$= -\left[(\hat{i}\hat{i}+\hat{k}\hat{k})\,\delta\left(\frac{a}{a+b}\right)+\hat{j}\hat{j}\,(\beta)\right]$$

$$\Phi\begin{pmatrix}(0,0,0)\\0\\H\end{pmatrix};\begin{pmatrix}(0,0,0)\\1\\H\end{pmatrix} = \Phi\begin{pmatrix}(0,0,0)\\1\\H\end{pmatrix};\begin{pmatrix}(0,0,0)\\0\\H\end{pmatrix}$$

$$= -\left(\frac{\gamma}{p}\right)\left[\hat{i}\hat{i}\,(a^2+b^2)\cos^2\theta+\hat{j}\hat{j}\,(x)-(\hat{i}\hat{j}+\hat{j}\hat{i})(W)\right]$$

$$\Phi\begin{pmatrix}(0,0,0)\\0\\H\end{pmatrix};\begin{pmatrix}(0,0,\pm1)\\1\\F\end{pmatrix} = \Phi\begin{pmatrix}(0,0,0)\\1\\F\end{pmatrix};\begin{pmatrix}(0,0,\pm1)\\0\\H\end{pmatrix}$$

$$= -\frac{\eta}{R}\left[\hat{i}\hat{i}(d^2\cos^2\theta)+\hat{j}\hat{j}\left(\frac{d}{2}-b\right)^2+\hat{k}\hat{k}(c^2)+(\hat{i}\hat{j}+\hat{j}\hat{i})(d)\right.$$

$$\left.\cdot\left(\frac{d}{2}-b\right)\cos\theta\pm(\hat{i}\hat{k}+\hat{k}\hat{i})(c)(d)\cos\theta\pm(\hat{j}\hat{k}+\hat{k}\hat{j})(c)\left(\frac{d}{2}-b\right)\right]$$

$$\Phi\begin{pmatrix}(0,0,0)\\0\\H\end{pmatrix};\begin{pmatrix}(1,1,0)\\1\\F\end{pmatrix} = \Phi\begin{pmatrix}(0,0,0)\\1\\F\end{pmatrix};\begin{pmatrix}(-1,-1,0)\\0\\H\end{pmatrix}$$

$$= -\left[\hat{i}\hat{i}(\varepsilon)\left(\frac{(a+b)^2}{Q}\right)\cos^2\theta+\hat{j}\hat{j}(\varepsilon)\left(\frac{V^2}{Q}\right)-(\hat{i}\hat{j}+\hat{j}\hat{i})(\varepsilon)\left(\frac{V}{Q}\right)(a+b)\cos\theta\right]$$

$$\Phi\begin{pmatrix}(0,0,0)\\1\\H\end{pmatrix};\begin{pmatrix}(0,0,0)\\1\\F\end{pmatrix} = \Phi\begin{pmatrix}(0,0,0)\\1\\F\end{pmatrix};\begin{pmatrix}(0,0,0)\\1\\H\end{pmatrix}$$

$$= -\left[\hat{i}\hat{i}\left(\alpha\cos^2\theta+\delta\left(\frac{b}{a+b}\right)\sin^2\theta\right) + \hat{j}\hat{j}\left(\alpha\sin^2\theta+\delta\left(\frac{b}{a+b}\right)\cos^2\theta\right)\right.$$

$$\left. + \hat{k}\hat{k}\ \delta\left(\frac{b}{a+b}\right)\right]$$

$$\Phi\left(\begin{matrix}(0,0,0)\\ 1\\ H\end{matrix}\ ;\ \begin{matrix}(-1,-1,\pm\bar{1})\\ 0\\ F\end{matrix}\right) = \Phi\left(\begin{matrix}(0,0,0)\\ 0\\ F\end{matrix}\ ;\ \begin{matrix}(1,1,\pm 1)\\ 1\\ H\end{matrix}\right)$$

$$= -\frac{\eta}{R}\left[\hat{i}\hat{i}(d-b)^2\cos^2\theta + \hat{j}\hat{j}(d+b)^2\sin^2\theta + \hat{k}\hat{k}(c^2)\right.$$

$$+ (\hat{i}\hat{j}+\hat{j}\hat{i})\left(\frac{1}{2}\right)(d^2-b^2)\sin 2\theta$$

$$\pm (\hat{i}\hat{k}+\hat{k}\hat{i})(c)(b-d)\cos\theta$$

$$\left.\pm (\hat{j}\hat{k}+\hat{k}\hat{j})(c)(b+d)\sin\theta\right]$$

$$\Phi\left(\begin{matrix}(0,0,0)\\ 1\\ H\end{matrix}\ ;\ \begin{matrix}(-1,-1,0)\\ 0\\ F\end{matrix}\right) = \Phi\left(\begin{matrix}(0,0,0)\\ 0\\ F\end{matrix}\ ;\ \begin{matrix}(1,1,0)\\ 1\\ H\end{matrix}\right)$$

$$= -\left[\hat{i}\hat{i}\left(\beta\cos^2\theta+\delta\left(\frac{a}{a+b}\right)\sin^2\theta\right) + \hat{j}\hat{j}\left(\beta\sin^2\theta+\delta\left(\frac{a}{a+b}\right)\cos^2\theta\right)\right.$$

$$\left. + \hat{k}\hat{k}\left(\frac{\delta a}{a+b}\right) - (\hat{i}\hat{j}+\hat{j}\hat{i})\left(\frac{1}{2}\right)\left(\beta - \frac{\delta a}{a+b}\right)\sin 2\theta\right]$$

Here different superscript (i,j,k) in each interaction matrix represents the different unit-cell at various position as shown in Figure 1. The distances corresponding to each force constant and the structural properties[7] are follow:

α : 0.97 Å	a = 0.97 Å
β : 1.53 Å	b = 1.53 Å
γ : 2.183 Å	c = 1.71 Å
η : 2.9024 Å	d = 2.70 Å
ε : 3.101 Å	θ = 30°

All other matrixes that are not listed are zero matrixes.

III. Results And Discussion

The equations of motion for the four independent atoms in the x, y and z directions, relating the six interacting constants, establish a 12×12 dynamical matrix as discussed in previous section. All force constants were then adjusted to give a good fit of the observed Brillouin zone centre mode frequencies determined from available Raman[1] and infrared[2] data with the calculated frequencies. The calculations involved diagonalization of the dynamical matrix on a VAX 11/780 computer using the Jacobi rotation method and the assignment of the symmetry of each mode was made by studying the transformation properties of the eigenvectors of the dynamical matrix and compared with experimental values.

The optimized values of the force constants and the results of the calculations as compared with the experimental values are summarized in Table 1. The calculated translational mode frequencies for two of the three modes (A_1 and B_1) are in good agreement with those from experiments. The calculated low frequency A_2 translational mode differs by a 49% deviation from the experimental value (85 cm^{-1} compared with 57 cm^{-1}). However, this is a much better result compared with the previous two-dimensional model calculations on hydrogen halide[8] (121.5 cm^{-1} compared with 57 cm^{-1}) because in this three-dimensional model inter-planar forces are included. This surprisingly low frequency for such a light molecule (the comparable modes for HCl and HBr are at 61 and 45 cm^{-1} respectively) is an indication of rather weak interplanar forces. From Table 1, it is interesting to note that the A_1 librational model frequency only differs by a 1.6% deviation compared with a 21% deviation using rigid molecular Lennard-Jones potential calculation[6] and 9.16% deviation using planar zig-zag chain model[8]. Besides, the two stretching (A_1 and B_1), B_1 in plane librational and two out-of-plane librational modes (A_1 and B_1) are quite well fitted. The overall agreement between the calculated and observed frequencies are good (average deviation ≈ 9%). Note that the acoustic modes are not identically equal to zero because of the round-off errors produced during the diagonalization procedure.

The three dimentional model adopted in this calculation is reasonably successful in lattice dynamics calculation of solid HF and shows good overall fitting between the observed and calculated frequencies. The optimized force constants indicate that the

forces between molecules in different chains and different planes are much smaller than those between nearest neighbours in the same linear chain.

V. REFERENCES

(1) A. ANDERSON, B. H. TORRIE and W. S. TSE, Chem. Phys. Lett. 70, 300 (1980).

(2) W. S. TSE, A. ANDERSON and B. H. TORRIE, Chin. J. Phys. No. 1,2, 20, 56 (1982).

(3) M. L. N. SASTRI and D. F. HORNIG, J. Chem. Phys. 39, 3497 (1963).

(4) J. S. KITTELBERGER and D. F. HORNIG, J. Chem. Phys. 46, 3099 (1967).

(5) P. A. GIGVERE and N. ZENGIN, Can. J. Chem. 36, 1013 (1958).

(6) W. S. TSE, A ANDERSON and J. W. LEECH, Chin. J. Phys. No. 1,2, 20, 49 (1982).

(7) A. AXMANN, W. BIEM, P. BORSCH, F. HOBFELD and H. STILLER, Dis. Faraday So.c (GB), No. 48, 69 (1969).

(8) C. N. CHANG, W. S. TSE and C. LI, To be published.

(9) M. W. JOHNSON, E. SANDOR and E. ARZI, Acta. Cryst. B31, 1998 (1975).

(10) N. WAKABAYASHI and R. M. NICKLOW. "Neutron Scattering and Lattice Dynamics of Material with Layered Structures in "Material Science", Vol. 2, Addison-Wesly Publishing Company, 413 (1979).

Table 1. Observed and calculated lattice vibrations of solid hydrofluoride acid.

Assignment		Observed[1] Frequencies (cm^{-1}) (Raman) 18K	Calculated
A_1	Acoustic	0	0.073
B_1	Acoustic	0	0.225
B_2	Acoustic	0	0.371
A_2	(o/p)T	57	85
A_1	(i/p)T	187.5	198
B_1	(i/p)T	363.5	324
A_2	(o/p)L	548.5	528.5
B_2	(o/p)L	569.5	535
A_1	(i/p)T	742	730
B_1	(i/p)T	943	998.5
A_1	(i/p)S	3045.5	3090.5
B_1	(i/p)S	3386	3305.5

Force constants for HF (10^5 dyn/cm)

α	4.970	δ	0.040
β	0.405	ε	0.055
γ	0.290	η	0.175

o/p, out of plane; i/p, in plane; L, libration; T, translation; S, stretching.

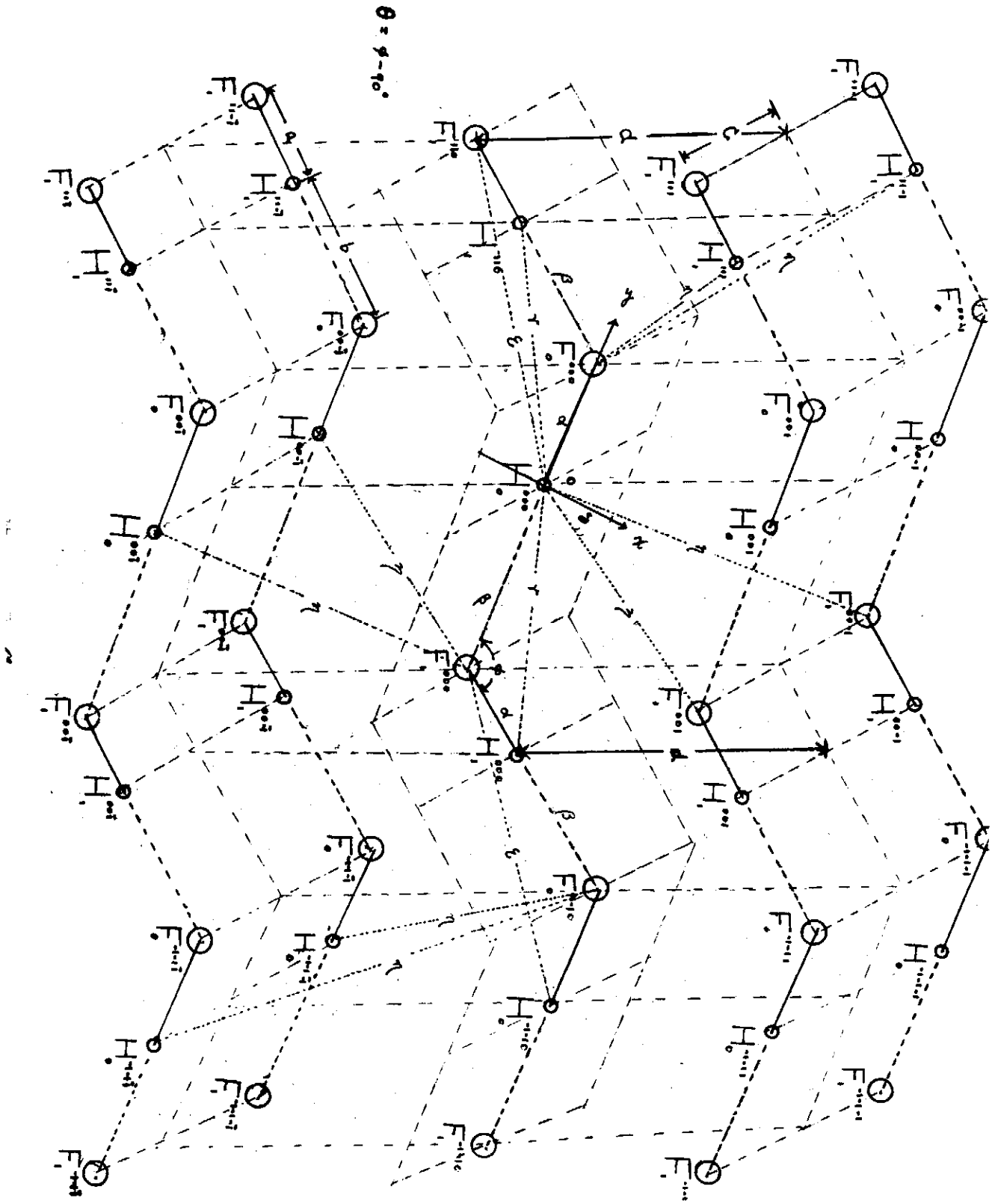

Figure 1. The three dimensional structure and force constants of solid hydrofluoride acid.

LATTICE DYNAMICS OF THE HYDROGEN HALIDE CRYSTALS

Chia-Nan Chang

Department of Electronic Engineering and Technology

National Taiwan Institute of Technology, Taipei, R.O.C.

and

Wan-Sun Tse, Li Chang

Institute of Physics, Academia Sinica

Nankang, Taipei, Taiwan, R.O.C.

A lattice dynamical model for three of the four hydrogen halide molecular crystals in their low temperature phase III has been investigated by using the Born-Von Karman model with different interatomic force constants and the results are compared to observed zone centre ($\vec{k} = 0$) frequencies (Raman). This simple model is also used to estimate those hydrogen bond strengths in different crystals.

I. INTRODUCTION

Solid HCl, HBr and HF form an interesting group of isomorphic molecular crystals which has been the subject of several experimental and theoretical studies. The phase temperature diagram for the hydrogen and deuterium halide is shown in figure 1. HCl and HBr have 3 solid phases. Phase I and II show orientational disorder, while phase III is order. In HF the intermolecular binding is stronger than in the other hydrohalides. Molecular aggregates form in the gas phase[1]. In constrast to the other two halides, there is no phase transition in the solid phase, the molecules condense directly into a structure, which corresponds to the low temperature structure of HCl and HBr. In this low temperature phase, the crystals have ordered orthorhombic structures[2,3,4].

The molecules form planar zig-zag hydrogen-bonded chains, with two molecules in the primitive unit cell on sites of C_s symmetry forming space group C_{2v}^{12} ($Bb2_1m$). The structural properties of those zig-zag chain are listed in Table 1.

Standard group theoretical techniques shows that there are three translational ($A_1 + B_1 + A_2$) and four librational modes ($A_1 + B_1 + A_2 + B_2$) corresponding to the external motions of rigid molecules. There are also two stretching modes ($A_1 + B_1$). All of the nine optically active modes are active in Raman scattering and, except for two A_2 modes, are also active in infrared absorption. It is the aim of this work to attempt to interpret these normal modes of vibrations obtained from spectroscopic techniques (5,6,7) in terms of such a simple force constant model and to estimate those hydrogen bond strengths in those three crystals.

II. Model Calculation

Assuming that the vibrational motions of each atom in the zig-zag chain are harmonic, the equations of motion of the ℓ^{th} one of the k- kind atom are

$$M_k \ddot{u}_\alpha(^{\ell}_{k}) = - \sum_{\ell',k',\beta} \phi_{\alpha\beta}(^{\ell}_{k} ; ^{\ell'}_{k'}) u_\beta(^{\ell'}_{k'}) \tag{1}$$

where $\phi_{\alpha\beta}(^{\ell}_{k};^{\ell'}_{k'})$ is the negative of the force exerted in the α-direction on the atom $(^{\ell}_{k})$ when the atom $(^{\ell'}_{k'})$ is displaced a unit distance in the β-direction, all other atoms being kept at their equilibrium position.

If we choose, as a solution to equation (1), a function of the travelling-wave form

$$u_\alpha(^{\ell}_{k}) = (M_k)^{-\frac{1}{2}} u_{\alpha o}(^{\ell}_{k}) \, e^{i(\vec{q}\cdot\vec{r}(^{\ell}_{k})-\omega t)} \tag{2}$$

We find that

$$\omega^2 u_{\alpha o}(^{\ell}_{k}) = \sum_{k',\ell',\beta} (M_k M_{k'})^{-\frac{1}{2}} \phi_{\alpha\beta}(^{\ell}_{k};^{\ell'}_{k'}) \, e^{-i\vec{q}\cdot(\vec{r}(^{\ell}_{k})-\vec{r}(^{\ell'}_{k'})} \, u_{\beta o}(^{\ell'}_{k'}) \tag{3}$$

In the long wave length limit, i.e. $\vec{q}\cdot(\vec{r}(^{\ell}_{k})-\vec{r}(^{\ell'}_{k'}) \ll 1$, and for nontrivial solution of (3), i.e. $u_{\beta o}(^{\ell'}_{k'}) \neq 0$, we have the following secular equation

$$\left| (M_k M_{k'})^{-\frac{1}{2}} \sum_{\ell',k',\beta} \phi_{\alpha\beta}(^{\ell}_{k} ; ^{\ell'}_{k'}) - \omega^2 \delta_{\alpha\sigma}\delta_{kk'} \right| = 0 \tag{4}$$

In this planar chain model, interaction between adjacent zig-zag chains were ignored if compared with intramolecular forces. The model is outlined in Figure 2 where all the force constants are shown. We limit the range of interaction of each hydrogen atom and halogen atom to their fourth-nearest neighbors in each planar zig-zag chain

structure. Assuming the axially-symmetric force constant[8], α, β, δ between each atom to its first and second nearest neighbors, and the central force constant[9] γ, ε between each atom to its third and fourth nearest neighbors, we have the following matrix of force constar between various pairs of atoms.

Let $P = a^2 + b^2 + 2ab\sin\theta$ $\quad X = (a^2 + b^2)(1 + \sin^2\theta) + 4ab\sin\theta$

$Q = (a+b)^2 + 2a(a+b)\sin\theta + a^2$ $\quad V = (a) + (a+b)\sin\theta$

$U = (a+b) + a\sin\theta$ $\quad N = F, Cl, or Br$

$W = 2ab\cos\theta + (a^2+b^2)\sin\theta\cos\theta$

$$\phi\left(\begin{smallmatrix}0,1\\H;H\end{smallmatrix}\right) = \phi\left(\begin{smallmatrix}1,0\\H;H\end{smallmatrix}\right) = \left(-\frac{\gamma}{p}\right)\begin{vmatrix}(a^2+b^2)\cos^2\theta & -W & 0\\ -W & +X & 0\\ 0 & 0 & 0\end{vmatrix}$$

$$\phi\left(\begin{smallmatrix}0,0\\H;N\end{smallmatrix}\right) = \phi\left(\begin{smallmatrix}0,0\\N;H\end{smallmatrix}\right) = \begin{vmatrix}-\delta\left(\frac{b}{a+b}\right) & 0 & 0\\ 0 & -\alpha & 0\\ 0 & 0 & -\delta\left(\frac{b}{a+b}\right)\end{vmatrix}$$

$$\phi\left(\begin{smallmatrix}0,1\\H;N\end{smallmatrix}\right) = \phi\left(\begin{smallmatrix}1,0\\N;H\end{smallmatrix}\right) = \begin{vmatrix}\left(-\delta\left(\frac{a}{a+b}\right) - \frac{\varepsilon}{Q}(a+b)^2\cos^2\theta\right) & \frac{\varepsilon}{Q}(V)(a+b)\cos\theta & 0\\ \frac{\varepsilon}{Q}(a+b)(V)\cos\theta & -\frac{\varepsilon}{Q}(V)^2 - \beta & 0\\ 0 & 0 & -\delta\left(\frac{a}{a+b}\right)\end{vmatrix}$$

$$\phi\left(\begin{smallmatrix}0,0\\H;H\end{smallmatrix}\right) = \begin{vmatrix}\left(\frac{\gamma}{p}(a^2+b^2)+\frac{\varepsilon}{Q}(a+b)^2\right)\cos^2\theta+\delta & -\frac{\gamma}{p}(W) - \frac{\varepsilon}{Q}(V)(a+b)\cos\theta & 0\\ -\frac{\gamma}{p}(W) - \frac{\varepsilon}{Q}(V)(a+b)\cos\theta & +\alpha+\beta+\frac{\gamma}{p}(X) + \frac{\varepsilon}{Q}(V)^2 & 0\\ 0 & 0 & \delta\end{vmatrix}$$

$$\phi\left(\begin{smallmatrix}1,0\\H;N\end{smallmatrix}\right) = \phi\left(\begin{smallmatrix}0,1\\N;H\end{smallmatrix}\right) = \begin{vmatrix}-\left(\beta + \frac{\varepsilon a^2}{Q}\cos^2\theta - \delta\left(\frac{a}{a+b}\right)\sin^2\theta\right) & \frac{1}{2}\left(\beta - \delta\frac{a}{a+b}\right)\sin 2\theta + \frac{\varepsilon}{Q}(a\cos\theta)(U) & 0\\ \frac{1}{2}\left(\beta - \delta\frac{a}{a+b}\right)\sin 2\theta + \frac{\varepsilon}{Q}(a\cos\theta)(U) & -\beta\sin^2\theta - \frac{\delta a}{(a+b)}\cos^2\theta - \frac{\varepsilon}{Q}(U)^2 & 0\\ 0 & 0 & -\delta\left(\frac{a}{a+b}\right)\end{vmatrix}$$

$$\phi\left(\begin{smallmatrix}1,1\\H;N\end{smallmatrix}\right) = \phi\left(\begin{smallmatrix}1,1\\N;H\end{smallmatrix}\right) = \begin{vmatrix}-\alpha\cos^2\theta - \delta\left(\frac{b}{a+b}\right)\sin^2\theta & \frac{1}{2}\left(\alpha - \delta\frac{b}{(a+b)}\right)\sin 2\theta & 0\\ \frac{1}{2}\left(\alpha - \delta\frac{b}{(a+b)}\right)\sin 2\theta & -\alpha\sin^2\theta - \delta\left(\frac{b}{a+b}\right)\cos^2\theta & 0\\ 0 & 0 & -\delta\left(\frac{b}{a+b}\right)\end{vmatrix}$$

$$\phi\left(\begin{smallmatrix}1\\H\end{smallmatrix};\begin{smallmatrix}1\\H\end{smallmatrix}\right) = \begin{vmatrix} [(\alpha+\beta)+\frac{\gamma}{p}(a^2+b^2)+\frac{\varepsilon}{Q}a^2]\cos^2\theta+\delta\sin^2\theta & [\tfrac{1}{2}(\delta-\alpha-\beta)\sin2\theta-\frac{\varepsilon}{Q}(U)(a\cos\theta)-(\frac{\gamma}{p})(W)] \\ \tfrac{1}{2}(\delta-\beta-\alpha)\sin2\theta-\frac{\varepsilon}{Q}(U)(a\cos\theta)-\frac{\gamma}{p}(W) & (\alpha+\beta)\sin^2\theta+\delta\cos^2\theta+\frac{\varepsilon}{Q}(U)^2+\frac{\gamma}{p}(X) \\ 0 & 0 \end{vmatrix}$$

$$\phi\left(\begin{smallmatrix}0\\N_o\end{smallmatrix};\begin{smallmatrix}0\\N_o\end{smallmatrix}\right) = \begin{vmatrix} \delta(\frac{b+a\sin^2\theta}{a+b})+(\beta+\frac{\varepsilon}{Q}a^2)\cos^2\theta & -\tfrac{1}{2}(\beta-\delta\frac{a}{a+b})\sin2\theta-\frac{\varepsilon U}{Q}(a\cos\theta) & 0 \\ -\tfrac{1}{2}(\beta-\delta\frac{a}{a+b})\sin2\theta-\frac{\varepsilon U}{Q}(a\cos\theta) & (\alpha+\beta\sin^2\theta)+\frac{\varepsilon}{Q}(U)^2+\delta(\frac{a}{a+b})\cos^2\theta & 0 \\ 0 & 0 & \delta \end{vmatrix}$$

$$\left(\begin{smallmatrix}0\\N_1\end{smallmatrix};\begin{smallmatrix}0\\N_1\end{smallmatrix}\right) = \begin{vmatrix} \frac{\delta}{(a+b)}(a+b\sin^2\theta)+(\alpha+\frac{\varepsilon}{Q}(a+b)^2)\cos^2\theta & -\tfrac{1}{2}(\alpha-\delta\frac{b}{a+b})\sin2\theta-\frac{\varepsilon}{Q}(a+b)(V)\cos\theta & 0 \\ -\tfrac{1}{2}(\alpha-\delta\frac{b}{a+b})\sin2\theta-\frac{\varepsilon}{Q}(a+b)(V)\cos\theta & \beta+\delta(\frac{b}{a+b})\cos^2\theta+\frac{\varepsilon}{Q}(V)^2+\alpha\sin^2\theta & 0 \\ 0 & 0 & \delta \end{vmatrix}$$

All other matrixes that are not listed are zero matrixes. In the long wavelength limit, q 0, we have the following 12×12 symmetric secular equation with $A_{ij} = A_{ji}$

$$\begin{vmatrix} (A_{11}-\omega^2 I) & A_{12} & A_{13} & A_{14} \\ A_{21} & (A_{22}-\omega^2 I) & A_{23} & A_{24} \\ A_{31} & A_{32} & (A_{33}-\omega^2 I) & A_{34} \\ A_{41} & A_{42} & A_{43} & (A_{44}-\omega^2 I) \end{vmatrix} = 0 \qquad (6)$$

where $A_{ij} = \frac{1}{M_H}\phi\left(\begin{smallmatrix}i\\H\end{smallmatrix};\begin{smallmatrix}j\\H\end{smallmatrix}\right)$ is an 3×3 matrix with $1 \le i, j \le 2$

$A_{ij} = \frac{1}{M_N}\phi\left(\begin{smallmatrix}i\\N\end{smallmatrix};\begin{smallmatrix}j\\N\end{smallmatrix}\right)$ is an 3 3 matrix with $3 \le i, j \le 4$.

(N = F, Cl, or Br)

$A_{ij} = \frac{1}{\sqrt{M_H M_N}}\phi\left(\begin{smallmatrix}i\\H\end{smallmatrix};\begin{smallmatrix}j\\N\end{smallmatrix}\right)$ is an 3×3 matrix with $1 \le i \le 2$, $3 \le j \le 4$

The elements in each diagonal submatrix of equation (6) are defined as follow

$$(A_{ii}-\omega^2 I)_{\alpha\beta} = \frac{1}{M_k}\phi_{\alpha\beta}\left(\begin{smallmatrix}i\\k\end{smallmatrix};\begin{smallmatrix}i\\k\end{smallmatrix}\right) - \omega^2\delta_{\alpha\beta} \qquad k = N \text{ or } H$$

The equations of motion for the four independent atoms in the x, y and z directi relating the five interacting force constants, are set up and a 12×12 dynamical matrix is estiblished as discussed above. This is diagonalized on an VAX 11/780 computer using the

Jacobi rotation method, and the eigenvalues (giving normal mode frequencies) and eigenvectors (atomic amplitudes) are calculated. Since the in-plane motions are less likely to be significally influenced by inter-chain forces, the force constants are varied to give a best fit with these frequencies. The optimized values of the force constants and a comparison of the observed and calculated frequencies are listed in Table 2. In Figure 3 the vibrational displacements for $\vec{k} = 0$ in-plane and out-of-plane motions of HF, HCl and HBr (same structure) are reported qualitatively.

III. Discussion and Conclusions

Some physical arguments are used to assist in the determination of some of the force constants:

(1) The stretching frequencies mostly depend on combination of the force constant α and β. The appropriate value of β is obtained by fitting the external inplane translational frequencies due to the fact that the molecules (HBr, HCl or HF) translate in the plane is determined chiefly by β as seen in Fig. 2.

(2) The splitting of the internal stretching frequencies depends on γ.

(3) The lattice librational frequencies within the zig-zag plane depend on the combination of γ, δ and ε.

(4) The out-of-plane libration depend on δ since only the δ force constant is involved in the z direction.

From Table 2, it is seen that the stretching, in-plane librational and in-plane translational modes are quite well fitted. The agreement is not as good for the out-of-plane librations, which is due to the fact that only a δ bending force constant is introduced. Note that the pure translational modes are not identically equal to zero because of the round-off errors produced during the diagonalization procedure. The optimized force constants show some interesting trends:

(1) α, representing the molecular bond, for HCl and HBr differs from its gas phase value by -12 or -13% while the change is nearly -44% for HF.

(2) β, representing the hydrogen bond, is much larger for HF than it is for HCl and HBr which is consistent with the large changes mentioned above for α, i.e. production of a strong hydrogen bond weakens the molecular bond between the hydrogen and fluorine.

(3) γ, δ and ε again have much larger values for HF than for the other hydrogen halides

reflecting the strong bonding between molecules.

The model adopted in these calculations for solid HCl, HBr and HF shows generally good agreement between the observed and calculated frequencies suggesting that the forces between molecules in different chains are much smaller than those between nearest neighbours in the same linear chain. A completely acceptable model, however, is unlikely until a satisfactory representation of the hydrogen bonds is found.

REFERENCES

(1) GMELIN, HANDBUCH DER ANORG. Chem., Eng-Bd., 5 (1959).

(2) E. SANDOR and R.F.C. FARROW, Nature, 213, 171 (1967).

(3) E. SANDOR and M. W. JOHNSON, Nature, 217, 541 (1968).

(4) M. W. JOHNSON, E. SANDOR and E. ARZI, Acta, Cryst. B31, 1998 (1975).

(5) A. ANDERSON ,B. H. TORRIE and W. S. TSE, Chem. Phys. Lett. 70, 300 (1980).

(6) J. E. VESSEL and B. H. TORRIE, Can. J. Phys. 55, 592 (1977).

(7) T. S. SUN and A. ANDERSON, Chem. Phys. Lett. 17, 104 (1972).

(8) N. WAKABAYASHI and R. M. NICKLOW. Neutron scattering and lattice dynamics of material with layered structures in "Materials Science", Vol. 2, Addison-Wesly Publishing Company, 413 (1979).

(9) A. A. MARADUDIN, E. W. MONTROLL, G. H. WEISS and I. P. IPATOVA, "Theory of Lattice Dynamics in the Harmonic Approximation", Academic Press, New York, 14 (1971).

Table 1.

Properties of the phase III crystals

	HF(4.2K)	HCl (77.4K)	HBr (84K)
Molecular Bond Length a (Å)	0.97	1.275	1.414
Hydrogen Bond Length b (Å)	1.53	2.413	2.513
Angle (ϕ) ($\theta = \phi - 90^\circ$)	120.1°	$93^\circ 31'$	$91^\circ 48'$

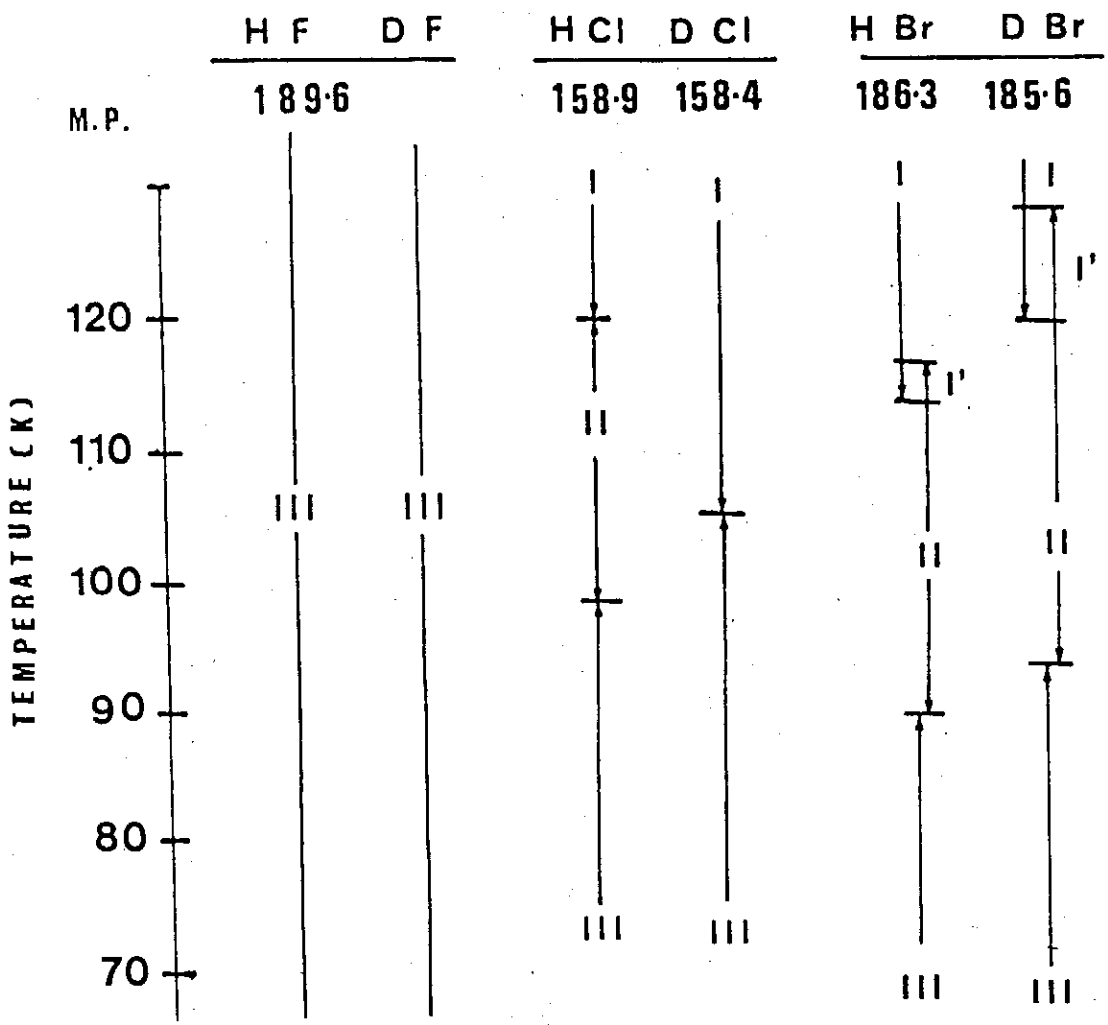

Figure 1. Phase-temperature diagram for the crystalline HF, HCl and HBr.

Table 2. Calculated frequencies and force constants for solid HF, HCl, HBr, in phase III (cm^{-1})

Assignment		HF		HCl		HBr	
		Cal	Exp	Cal	Exp	Cal	Exp
Acoustic	A_1	0.08	0	0.07	0	0.09	0
	B_1	0.22	0	0.71	0	0.95	0
	B_2	0.37	0	0.75	0	0.97	0
(o/p)T	A_2	121.5	57	28.5	61.0	18	45.0
(i/p)T	A_1	199	187.5	94	88.5	65	61.0
(i/p)T	B_1	334	363.5	103.5	114	69.5	75.5
(o/p)L	A_2	543	548.5	178	141.5	165.5	147
(o/p)L	B_2	556.5	569.5	180	223	166.5	209
(i/p)L	A_1	674.5	742	300	336	272	297
(i/p)L	B_1	950	943	444	409	393	376
(i/p)S	A_1	3089	3045.5	2706.5	2697	2399	2395
(i/p)S	B_1	3313	3386	2728	2741.5	2417	2431

Optimized force constants: (in units of 10^5 dyne/cm)

	HF	HCl	HBr
α	4.970	4.135	3.273
β	0.345	0.095	0.102
γ	0.30	0.040	0.029
δ	0.175	0.0188	0.0163
ε	0.160	0.032	0.027

o/p, out of plane; i/p, in plane; L, libration; T, translation; S, stretch.

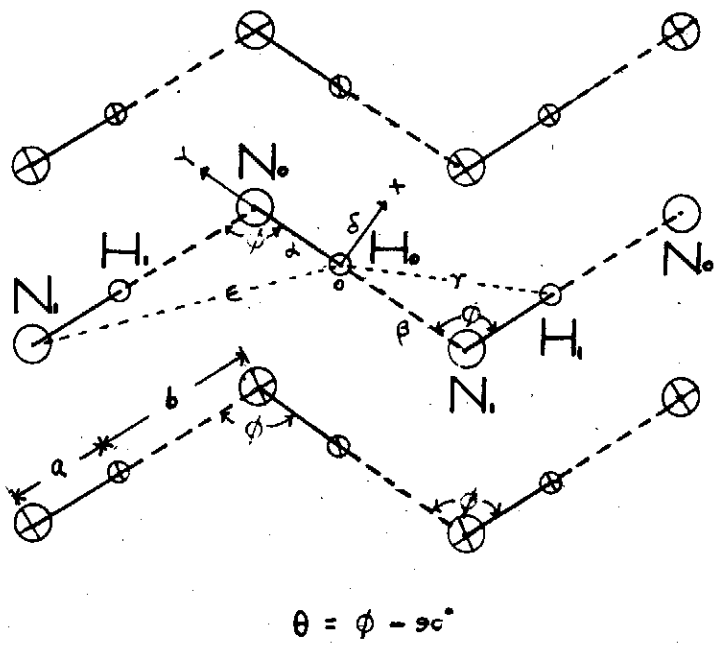

Figure 2. Geometry and force constants of phase III solid HF, HCl and HBr adopted in the calculations described in this paper. Empty circles are atoms in the plane z=0, the circles with crosses inside are atoms in different plane parallel to z=0.

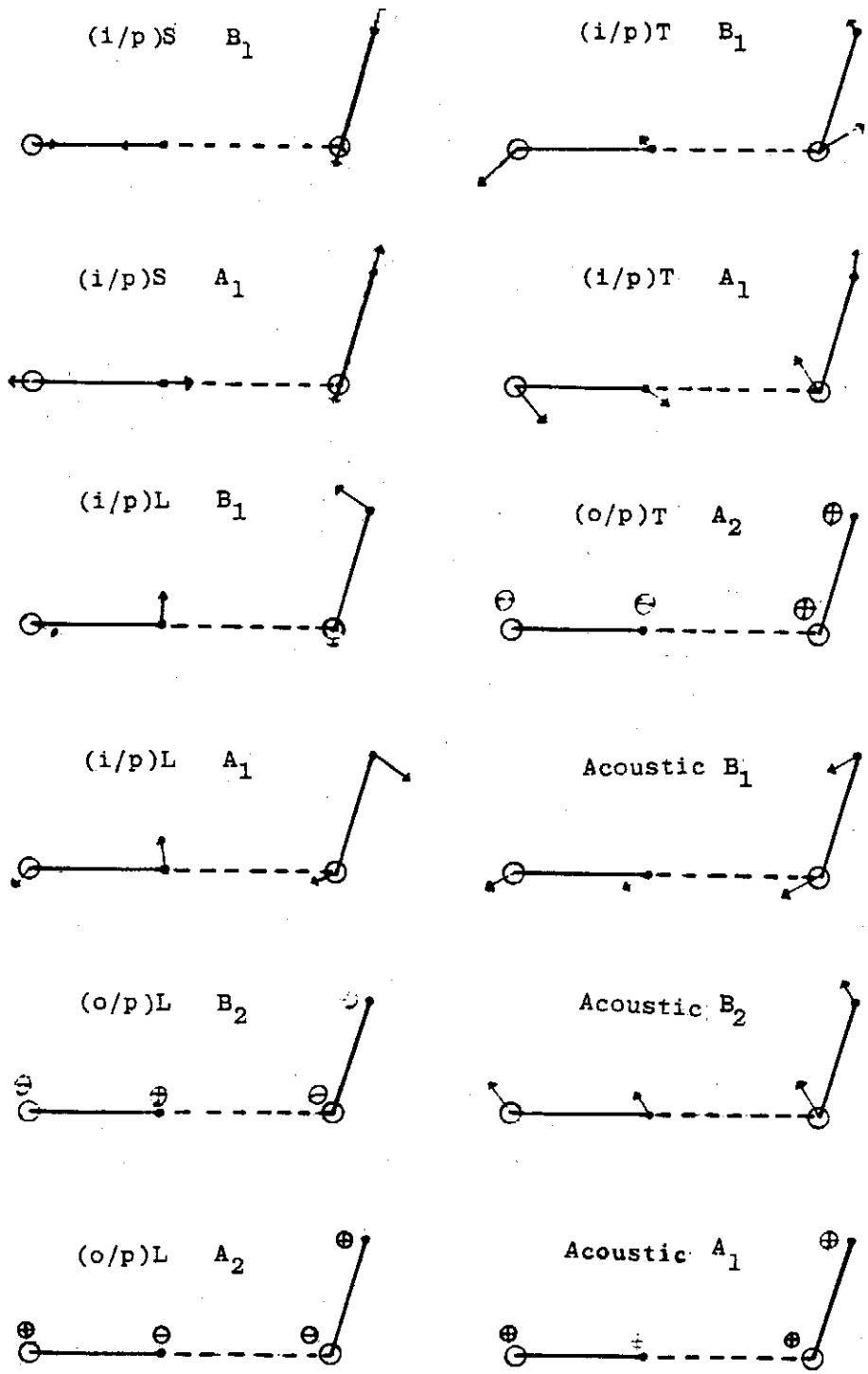

Figure 3. Zone centre normal modes of a single chain of solid HF, HCl and HBr derived from a five-parameter force constant model.

Impulsively Started Viscous Flow Over A Rotating Circular Cylinder

Lai-Chen Chien and Ching-Shang Chen

Institute of Physics, Academia Sinica

Taipei, Taiwan, 115,

Republic of China

The impulsively started flow of an incompressible viscous fluid over a circular cylinder with circulation is studied. Because of the impulsively start, there is a singularit at time zero plus. The accurate solution in the neighborhood of the singularity by the matche asymptotic expansion to the second order is extended to the third order. Then the viscous layer considered analytic solutions are employed as initial conditions for numerical integration to obtain the solutions for larger time. The finite difference scheme adapted for the vorticity equation is the hopscotch method and that for the Poisson equation is the direct method. The time development of the flow properties, lift and moment coefficients are obtained and plotted.

I. Introduction

Investigation on the flow over a rotating cylinder has been carried out by a number of scholars for over a century. It is well known that the life induced by a stream of inviscid fluid perpendicular to a rotating cylinder is $\rho U_\infty \Gamma$, where U_∞ and Γ are free stream velocity and circulation respectively. As reviewed by Swanson[1], the existing literature on the Magnus effect is investigated. However, the theoretical understanding is not yet very complete in investigating the flow properties, and in predicting the lift over the cylinder because of the great difficulty encountered in the problem.

Viscosity effect plays an important role in the problem of an impulsively started flow over a rotating circular cylinder. The impulsively start flow will induce an infinite acceleration at the very beginning of the motion. And there exists a

singularity at the time of zero plus. The accurate solution in the neighborhood of the singularity can be obtained either by developing an analytic solution or a series soluti for small time[2]. The computation can then be continued with the aid of suitable numer method[3].

In this study, the viscous layer considered analytic solution for the flow fie obtained by the inner-outer expansion to the second order by Wang[4] is extended further the third order as initial condition for numerical solution. The hopscotch method[5] is described to integrate the vorticity equation. And the Poisson equation relating the stream function and vorticity is solved by direct method. The time development of the f properties such as flow patterns, vorticity distribution over the cylinder surface, the lift and moment coefficients are obtained.

II. FORMULATION

Consider a circular cylinder of radius r_o has been rotating in a viscous fluid And an impulsive cross flow with constant velocity U_∞ in the direction of the front stagr point is applied (Figure 1). We assume that the fluid properties are constants and the body force is negligible. The Navier-Stokes equations for the fluid motion can be expre in the form of vorticity equation

$$\frac{\partial \omega}{\partial T} + \frac{1}{r}\left[\frac{\partial \psi}{\partial \theta}\frac{\partial \omega}{\partial r} - \frac{\partial \psi}{\partial r}\frac{\partial \omega}{\partial \theta}\right] = \frac{1}{Re}\left[\frac{\partial^2 \omega}{\partial r^2} + \frac{1}{r}\frac{\partial \omega}{\partial r} + \frac{1}{r^2}\frac{\partial^2 \omega}{\partial \theta^2}\right]$$

where the terms have been normalized using radius of the cylinder, and the velocity of t free stream. The Reynolds number is defined by $Re = U_\infty r_o/\nu$, in which ν is the kinematic viscosity. Vorticity and the stream function are related by the Poisson equation

$$\frac{\partial^2 \psi}{\partial r^2} + \frac{1}{r}\frac{\partial \psi}{\partial r} + \frac{1}{r^2}\frac{\partial^2 \psi}{\partial \theta^2} = \omega \ .$$

The velocity components in the radial and tangential directions are defined as

$$u_r = -\frac{1}{r}\frac{\partial \psi}{\partial \theta} \ , \ u_\theta = \frac{\partial \psi}{\partial r} \ .$$

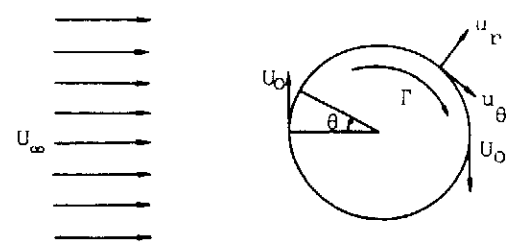

Fig. 1. Polar coordinate system.

Since it is desirable to haye a finer mesh near the surface of the cylinder and coaser ones far away, modified polar coordinates system is used to study this problem,

$$\xi = \ln r \text{ , and } \theta = \theta \tag{4}$$

The above defining equations then can be rewritten as

$$\exp(2\xi)\frac{\partial\omega}{\partial T} + \frac{\partial\psi}{\partial\theta}\frac{\partial\omega}{\partial\xi} - \frac{\partial\psi}{\partial\xi}\frac{\partial\omega}{\partial\theta} = \frac{1}{Re}\left(\frac{\partial^2\omega}{\partial\xi^2} + \frac{\partial^2\omega}{\partial\theta^2}\right) \tag{5}$$

$$\frac{\partial^2\psi}{\partial\xi^2} + \frac{\partial^2\psi}{\partial\theta^2} = \exp(2\xi)\omega \tag{6}$$

$$u_r = -\exp(-\xi)\frac{\partial\psi}{\partial\theta} \tag{7a}$$

$$u_\theta = +\exp(-\xi)\frac{\partial\psi}{\partial\xi} \tag{7b}$$

The nonslip condition at the cylinder surface gives the boundary conditions

$$\psi = 0,\ u_\theta = \frac{\partial\psi}{\partial\xi} = \beta, \text{ when } \xi = 0, \tag{8}$$

where constant β is the ratio between the peripheral velocity U_o and the free stream velocity U_∞. The boundary condition for vorticity at the surface can be directly derived from equation (6), and non-slip condition (8). Using central difference for space derivative, equation (6) becomes

$$\omega_{iw} = \frac{\psi_{iw+1} + \psi_{iw-1} - 2\psi_{iw}}{\Delta\xi^2} + \frac{\psi_{i+1w} + \psi_{i-1w} - 2\psi_{iw}}{\Delta\theta^2} \tag{9}$$

where subscript w refers grid point on the wall and i, the i-th grid in the θ direction. The factor, $\exp(2\xi)$, is equal to 1 at the cylinder surface. The second term on the right hand side vanishes since ψ is a constant along the surface of the cylinder. Furthermore, equation (8) implies

$$u_\theta = \frac{\psi_{iw+1} - \psi_{iw-1}}{2\Delta\xi} = \beta \tag{10}$$

$$\psi_{iw-1} = \psi_{iw+1} - 2\Delta\xi\beta. \tag{11}$$

Thus, the vorticity on the surface of the cylinder is

$$\omega_{iw} = \frac{2(\psi_{iw,1} - \Delta\xi\beta)}{\Delta\xi^2} \tag{12}$$

The flow far away from the cylinder is irrotational. The boundary conditions at far field are

$$\psi = \beta \ln r + r\sin\theta, \tag{13}$$

$$\omega = 0 . \tag{14}$$

III. NUMERICAL METHODS

Let n denote the number of time steps and ΔT the size of time increment. The scheme for advancing the solution from time $n\Delta T$ to time $(n+1)\Delta T$ consists of calculating new values of the vorticity, $\omega_{i,j}^{n+1}$ at all grid points via the vorticity equation (5) by finite-difference approximation, with the boundary conditions, the values of vorticity $\omega_{i,j}^{n}$ and the stream function $\psi_{i,j}^{n}$ from the previous time step.

The treatment of the partial differential equation of parabolic type is generally performed using explicit or implicit finite-difference method. Hopscotch method developed by Gourlay[5], is 3 to 4 times as fast, per computational step, as Peacemen-Rachford alternating direction implicit method. The scheme was also adopted by investigators in recent study on fluid dynamics[6]. The efficient numerical method is employed to solve the vorticity equations.

Hopscotch method is used to compute the vorticity at the new time step. The method divides each time step into two sweeps of the mesh. In the first and subsequent odd-number time steps, the points with i+j equal to odd are calculated based on the current values of neighboring points. For vorticity equation (5), the new values of vorticity are given by

$$\omega_{i,j}^{n+1} = \omega_{i,j}^{n} + \Delta T \exp(-2\xi_{i,j})\Big[-\frac{\psi_{i+1,j}^{n} - \psi_{i-1,j}^{n}}{2\Delta\theta}\,\frac{\omega_{i,j+1}^{n} - \omega_{i,j-1}^{n}}{2\Delta\xi} + \frac{\psi_{i,j+1}^{n} - \psi_{i,j-1}^{n}}{2\Delta\xi}\,\frac{\omega_{i+1,j}^{n} - \omega_{i-1,j}^{n}}{2\Delta\theta}\Big] + \frac{1}{Re}\Big[\frac{\omega_{i+1,j}^{n} + \omega_{i-1,j}^{n} - 2\omega_{i,j}^{n}}{\Delta\theta^{2}} + \frac{\omega_{i,j+1}^{n} + \omega_{i,j-1}^{n} - 2\omega_{i,j}^{n}}{\Delta\xi^{2}}\Big],$$

$$\text{for } j+i = \text{odd} \tag{15a}$$

For the second sweep at the same time level, the points (i+j) equal to even are calculated using the new values of the neighboring points obtained in the first sweep:

$$\omega_{i,j}^{n+1} = \omega_{i,j}^{n} + \Delta T \exp(-2\xi_{i,j})\left[-\frac{\psi_{i+1,j}^{n} - \psi_{i-1j}^{n}}{2\Delta\theta}\frac{\omega_{ij+1}^{n+1} - \omega_{ij-1}^{n+1}}{2\Delta\xi} + \frac{\psi_{i,j+1}^{n} - \psi_{i,j-1}^{n}}{2\Delta\xi}\right.$$

$$\left.\frac{\omega_{i+1,j}^{n+1} - \omega_{i-1,j}^{n+1}}{2\Delta\theta}\right] + \frac{1}{Re}\left[\frac{\omega_{i+1,j}^{n+1} + \omega_{i-1,j}^{n+1} - 2\omega_{i,j}^{n+1}}{\Delta\theta^2} - \frac{\omega_{i,j+1}^{n+1} - \omega_{i,j-1}^{n+1} - \omega_{i,j}^{n+1}}{\Delta\xi^2}\right],$$

for i+j = even (15

The first sweep consists of forward-time-central-space differencing for (i+j) odd, while the second sweep is fully implicit in the sense that the new values are reguired at (i, j), (i±1, j), and (i, j±1), but this implicitness involves no simultaneous algebraic solutions.

During the past ten years, one of the significant trends in computational fluid dynamics is the usage of direct methods to solve the Poisson's equation. It has become increasing popular to solve equation by direct than iterative methods Temperton[7]. New values of stream function are computed for all grid points by using central finite differe approximation of the Poisson equation (6), boundary conditions and the new values of vorticity. The numerical method for solving the elliptic equation is the accurate directe method proposed by Ogura[8].

V. Initial Conditions and Computational Procedure

The numerical solution of the problem considered is an initial-boundary value problem. Besides the boundary conditions described in above section, the initial values of stream function and vorticity distribution over the field considered must be known in order to carry out the numerical integration.

The stream function over the flow field for small time was obtained by Wang[4] by the method of asymptotic expansion to second order. Although his work is conceptually sound, he did not carryout enough terms in expansion to describe the flow properties accurately. In this study, we extend the solution obtained by Wang[4] using the method of asymptotic expansion to the third order. The tangential velocity is

$$u_\theta = \partial\psi(r, \theta, t)/\partial r = \beta/r + \{1 + 1/r^2 - 2\,\mathrm{erfc}\eta + 4\sqrt{T/(\pi Re)}\,[1/r^2 + 3\sqrt{\pi}/2\eta\mathrm{erfc}\eta$$
$$- \exp(-\eta^2)\}\sin\theta + 4T\{f(\eta)\sin\theta + \beta[\eta/\sqrt{\pi}\,\exp(-\eta^2) - \eta^2\,\mathrm{erfc}\eta]\}\cos\theta$$
$$- 4T\sqrt{T/\pi Re}\,\{2(4\sqrt{2}/3 - 1 - 4/9\pi)(1/r^3 - 1)\sin2\theta + [(1/r^2 - 1)/3 -$$
$$2\sqrt{\pi}I(\eta)]\beta\cos\theta\} + 8T^2[2\beta^2F(\eta) + N(\eta)\cos^2\theta + G(\eta)\sin^2\theta] + T/Re\,[1/r^2 -$$
$$(16\eta^2 + 1)\,\mathrm{erfc}\eta + 13/\sqrt{\pi}\eta\,\exp(-\eta^2)]\sin\theta + 16\beta^2T^2K(\eta) + 4T\sqrt{T/Re}\,L(\eta)\sin2\theta$$
$$+ 8\beta T^2M(\eta)\cos2\theta \qquad (1$$

where $\eta = (r - 1)/2\sqrt{\alpha t}$ is the stretched variable, and $f(\eta)$, $F(\eta)$, $G(\eta)$, $I(\eta)$, $K(\eta)$, $L(\eta)$ and $M(\eta)$ are polynomial of error function and exponential function.

Integrating the above equation, one gets the stream function. By equation (2) we have values of vorticity at every interior grid point for the given Reynolds number and time.

Numerical integration of equations (5) and (6), carried out according to the following steps:

(1) Time is stepped by ΔT and new values of vorticity are computed from equation (15).

(2) The new values of stream function ψ using direct method.

(3) Compute the values of the vorticity on the cylinder surface using equation (9).

The above procedure is repeated for subsequent time steps.

VI. Computational Results

Comparing analytic solution with numerical solution, we find the flow patterns are very similar to each other at $T < 0.5$. The values of stream function of the analytic solution agree with numerical one to three significant figures for $T < 0.2$. The case of Re=100, β=1, the initial conditions for the computation are the stream function and vorticity at T=0.01 obtained from analytic solution. Because the analytic solution only valid for $Re \gg 1$ and $T \ll 1$. We plotted the flow patterns of analytic solution at T=0.01 and T=0.2 only (Figure 2a, 2b). At T=0.01, the effect of viscosity is still little, the flow pattern is symmetry and is very similar to that of potential flow. As

time increasing the flow pattern will not symmetry any more because of viscosity and rotation of the cylinder.

At T=0 plus, the velocity discontinuity at the cylinder surface creates infinite vorticity at the cylinder surface. As time increasing, the vorticity of the cylinder surface continuously diffuses into the flow field and the vorticity at the cylinder surface decreases with time. We can see the diffusion of surface vorticity in Figure 3. The surface vorticity distributions at T=0.1, 0.2, 0.3 also have been plotted. We may see from Figure 3 and 4 that the streamlines of the upper part doesn't obviously change when time increases. While the streamlines of the lower part gradually been pressed and leaving the cylinder for the sake of viscosity and rotation of the cylinder.

The flow patterns for larger time are obtained by numerical integration, and are shown in Figure 4 at T=5.0 and 10. The vorticity diffuses away from the boundary. The change of surface vorticity distribution at the cylinder surface at moderate time is shown in Figure 3b. The surface vorticity decreases and diffused with time, and the difference of surface vorticity between T=5 and T=10 is very small.

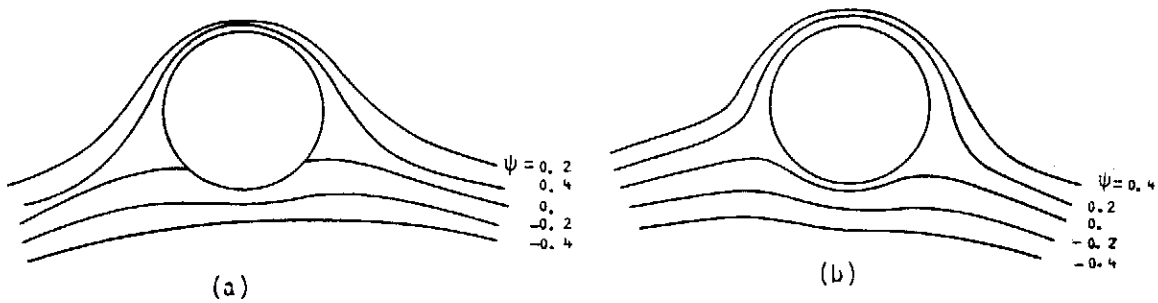

Figure 2. Flow pattern at Re=100, β=1 for (a) T=0.01, (b) T=0.2 (Analytic solution).

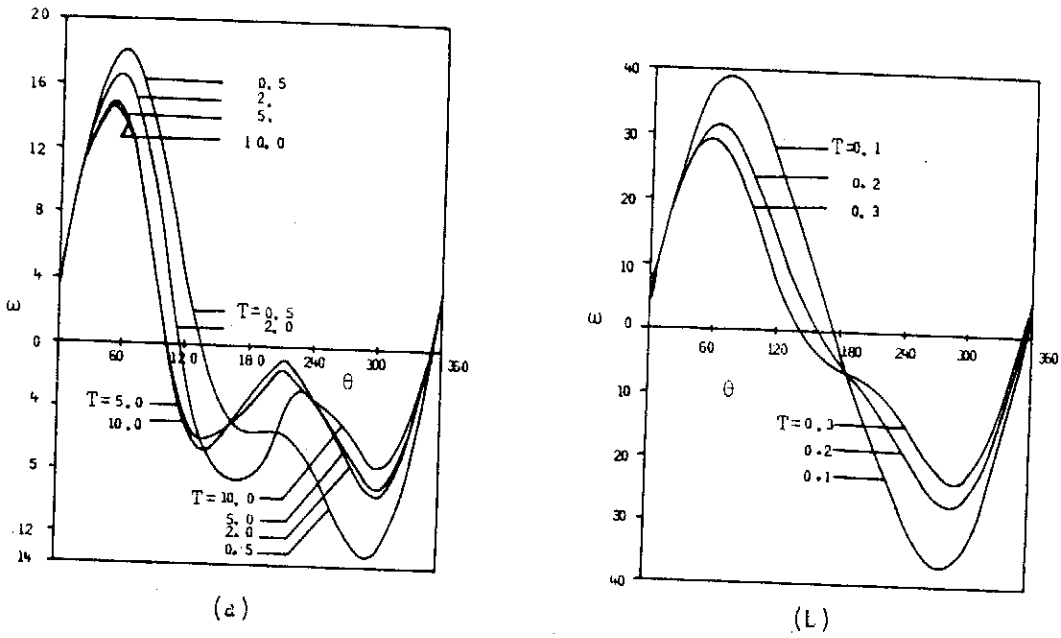

Figure 3. Vorticity distribution on the cylinder surface at Re=100, β=1, (a) small time (analytic solution), (b) moderate time (numerical solution).

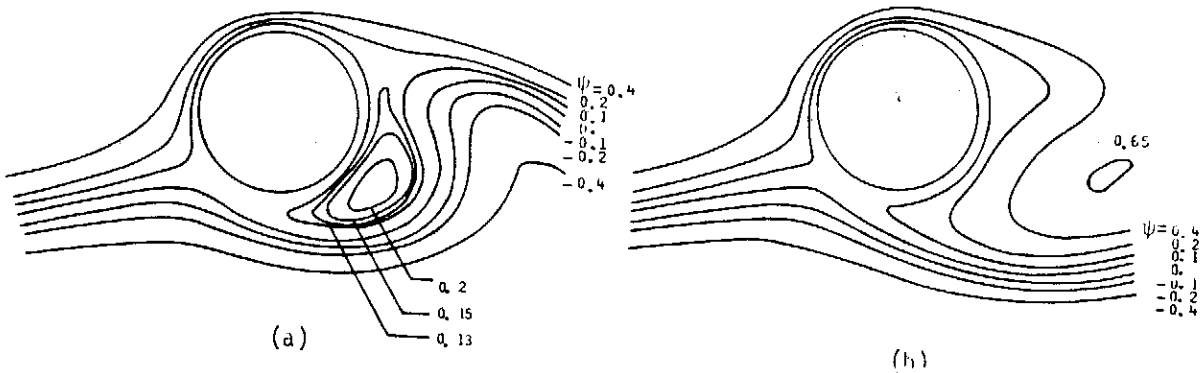

Figure 4. Flow pattern at Re=100, β=1 for (a) T=5.0, (b) T=10.

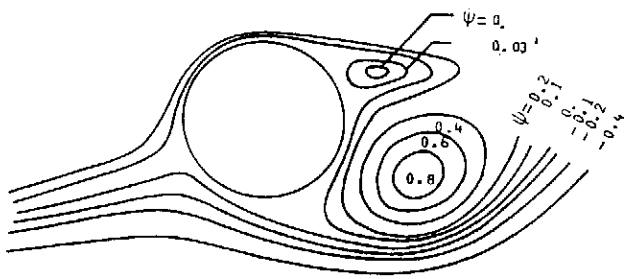

Figure 5. Flow pattern at Re=500, β=1 for T=10.0.

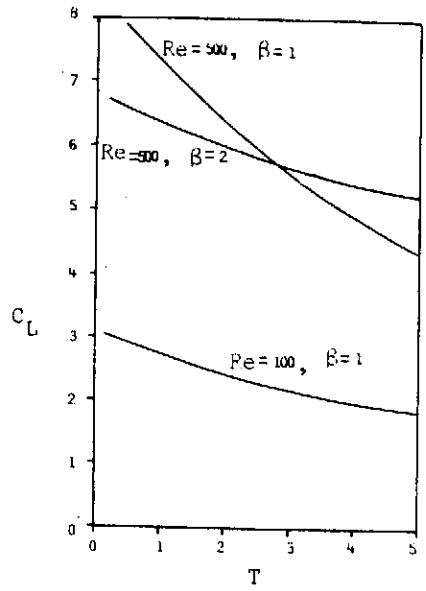

Figure 6. Lift coefficient.

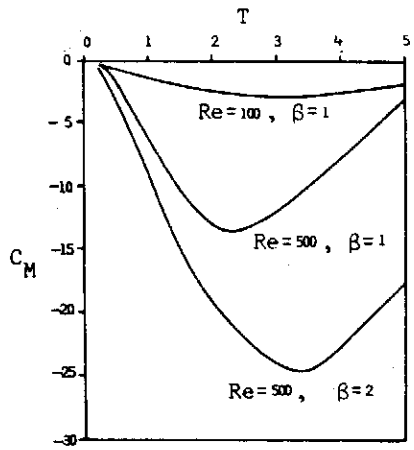

Figure 7. Moment coefficient.

The developments of flow pattern of Re=500, β=1 at T=10 is shown in Figure 5. The streamline is of the same direction of the rotation of the cylinder at the upper part of the cylinder, while the streamlines at the lower part have opposite direction with the rotation of the cylinder and will be decelerated and disturbed the flow. We can see that the lower and right parts of the flow pattern have larger change. The flow is decelerated and loses their kinetic energy in the region of $\pi<\theta<3\pi/2$. Due to losing kinetic energy, the region may create bubble than other parts. The bubble than other parts. The bubble shifts up to the region of $\pi/2<\theta<\pi$ and has influence on the flow pattern. Compare the flow pattern of Re=500, β=1 and Re=100, β=1. We find their development have the same trend, but

Re=100, β=1 develops earlier than Re=500, β=1. Due to larger viscosity of Re=100.

The lift and moment coefficient are calculated by the following formulas

$$C_L = C_{LS} + C_{LP}$$

$$= \frac{1}{Re}\int_0^{2\pi} (\omega)_{r_0}\cos\theta d\theta - \frac{1}{Re}\int_0^{2\pi} (\frac{\partial\omega}{\partial r})_{r_0}\cos\theta d\theta \qquad (17)$$

$$C_M = \int_0^{2\pi} (\omega)_{r_0}\, d\theta \qquad (18)$$

The lift and moment coefficients for various cases are shown in Figure 6 and 7 respectively. The lift coefficient decreases monotonically. For smaller Reynolds number, Re=100, it have a stable value of C_L=1.9 at T greater than 5. Whilst for greater Renolds number, the time history of C_L is of the same trend but reaches the stable values at larger time.

Figure 7 shows the time change of the moent coefficient. All the cases have the same tendency. It decreases gradually reaches a minimum value, then increases again.

VII. REFERENCES

(1) W. M. SWAMSON, Trans. ASME, J. Basic Eng., 83, 461-470, 1964.

(2) U. CRANK, "The Methematics of Diffusion" Clarendon Press, Oxford, 1975.

(3) H. SCHLICHTING, "Boundary Layer Theory" McGraw Hill, New York, 1979.

(4) C. Y. WANG, Private Communication.

(5) A. R. Gourlay, J. Inst. Math. Appl., 6, 375-390, 1970.

(6) J. B. GREENBERG, AIAA J., 20, 1064-1070, 1982.

(7) C. TEMPERTON, J. Comp. Phys., 31, 1-20, 1979.

(8) M. Ogura, J. Met. Soc. Japan., 47, 319-323, 1969.

MODIFIED DIFFERENTIAL QUARATURE METHOD FOR NUMERICAL SOLUTION OF PRIMITIVE EQUATIONS

Lai-Chen Chien

Institute of Physics, Academia Sinica

Taipei, Taiwan, 115, R.O.C.

A multiple-level primitive equation model in σ-coordinate is designed to study the Atmospheric motion during the outburst of the cold air. A new numerical algorithm based on a combination of the modified differential quarature method with the rational Runge-Kutta time integration scheme is devised to solve the prognostic equations. Comparing with the predicted fields prepared by explicit method and hopscotch method, we found satisfactory agreement for the fields forecasted by the new explicit method. The method developed test runs for 24h shows that the new method is a stable, efficient and accurate scheme.

I. INTRODUCTION

Many important phenomena arising in atmospheric dynamics are governed by a system of nonlinear partial differential equations. Analytic solutions for these equations are seldom known for the practical problems. Therefore, the numerical solution is an obvious approach. Various different numerical techniques have been proposed and developed.

Although the primitive equations are simpler and involve fewer approximations than the filtered equations, the presence of gravity waves requires a much smaller time step to avoid computational instability with explicit integration schemes. Otherwise the small time step is of little advantage or perhaps even harmful insofar as meteorological waves are concerned, and it is certainly expensive in terms of computer time. As a consequence, there has been considerable effort to prevent the stability requirement. Marchuk (1965) introduced a differencing scheme which treated the gravity waves implicitly

and permitting a much larger time step. Kwizak and Robert (1971), successfully applie semi-implicit differencing method to a barotropic 500 mb forecast which allowed a computational saving of factors up to three compared to conventional explicit method. Sh afterwards, the same method was applied to three-dimensional baroclinic models. Gerri McPherson and Scolnik (1973) developed the semi-implicit differencing equations using Shuman's semi-momentum differencing technique for National Meteorological Center six-layer primitive equations model. Robert, Henderson and Turnbull (1972), Bourke (1974) Gauntlett, Leslie, McGregor and Hincksman (1978), Campana (1979) have reported similar experimental success of semi-implicit concepts to integrate the models using a larger step.

Although the important developments have been made in implicit and its relat methods, their computer time per time step, as well as their complexity, is still larg than that of the explicit methods. It is the reason why the new explicit methods, su as hopscotch (Chien, 1979) splicit explicit (Gadd, 1978), explicit-multiple-time-step method (Chao, 1982) was developed recently. If one could devise a new explicit method that possesses the property of unconditional stability, the method would have immense practical importance. The present investigation describes such a investigation.

The newly developed numerical scheme consists of the modified differential quarature method combined with a rational Runge-Kutta time integration scheme (Wambecq 1978). In modified differential quarature method, spatial derivatives are approximate by a weighted sum of the values of unknown function at properly chosen neighborhing po to generate a set of ordinary differential equations in time. And then the set of ordi differential equations is solved by using an rational Runge-Kutta time integration sch It has been proved that the method is computationally explicit and unconditional stable for some classes of parabolic partial differential equations.

The newly method is applied to numerical weather prediction in this study. In order to consider orographic effect in numerical weather prediction, primitive equat model in σ-coordinate is adopted to study the atmospheric motion. The new numerical scheme is tried to integrate the equations over the East Asia Aera to obtain the accura results by increasing time step. The forecasts have been made for real data in Mei-Yu season using time step up to thirty minutes. For comparison, the twenty-four hour

predicted geopotential field pattern agrees with that of four-level primitive equation model in P-coordinate (Chien, 1980).

II. DESCRIPTION OF THE MODEL

In this investigation we consider forecasts generated by a four-level primitive equation model. The sigma (σ) coordinate system has been chosen for the model investigated (Figure 1). The vertical coordinate σ is defined with respect to pressure P by

$$\sigma = \frac{P - P_T}{P_S - P_T} = \frac{P - P_T}{\pi} \tag{2-1}$$

where P_T is the constant pressure at the top of the model and P_S is the variable pressure at the surface. In sigma coordinate, the lower boundary condition will always apply exactly at σ=1.

The independent variables are time t, coordinate distances east x, north y and vertical σ. Assuming the model atmosphere to be a perfect gas, we express the hydrostatic equation as

$$\frac{\partial \phi}{\partial \ln \sigma} = -R\,T \tag{2-2}$$

where R is the gas constant and ϕ is the geopotential. The prognostic equations for the east and north wind velocity u, v, virtual temperature θ, water vapor q are of the form

$$\frac{d\psi}{dt} = \frac{\partial \psi}{\partial t} + \vec{V}_3 \cdot \nabla\psi \tag{2-3}$$

where ψ is any of the prognostic variables. The local, advective and material changes are $\partial\psi/\partial t$, $\vec{V}_3 \cdot \nabla\psi$ and $d\psi/dt$, respectively.

The material derivatives may be expressible in terms of basic variables using the following governing equations.

(a) Momentum equations

$$\frac{\partial(\pi u)}{\partial t} = -\frac{\partial(\pi uu)}{\partial x} - \frac{\partial(\pi vu)}{\partial y} - \frac{\partial(\pi \dot{\sigma} u)}{\partial \sigma} + fv\pi - \pi\frac{\partial \phi}{\partial x} + \pi F_x \tag{2-4}$$

$$\frac{\partial(\pi v)}{\partial t} = -\frac{\partial(\pi uv)}{\partial x} - \frac{\partial(\pi vv)}{\partial y} - \frac{\partial(\pi \dot{\sigma} v)}{\partial \sigma} - fu - \frac{\partial \phi}{\partial y} + \pi F_y \tag{2-5}$$

where f is the Coriolis parameter and F_x, F_y, the friction terms.

(b) Continuity equations

$$\frac{\partial \pi}{\partial t} = - \frac{\partial(\pi u)}{\partial x} - \frac{\partial(\pi v)}{\partial y} - \frac{\partial(\pi \dot{\sigma})}{\partial \sigma} \quad . \tag{2-6}$$

(c) Thermal equaton

$$\frac{\partial(\pi\theta)}{\partial t} = - \frac{\partial(\pi u\theta)}{\partial x} - \frac{\partial(\pi v\theta)}{\partial y} - \frac{\partial(\pi\dot{\sigma}\theta)}{\partial \sigma} + \pi \frac{dQ}{dt} \quad , \tag{2-7}$$

where dQ/dt is diabatic heating or cooling rate per unit time and per unit mass,

(d) Specific humidity equation

$$\frac{\partial(\pi q)}{\partial t} = - \frac{\partial(\pi uq)}{\partial x} - \frac{\partial(\pi vq)}{\partial y} - \frac{\partial(\pi\dot{\sigma}q)}{\partial \sigma} - \frac{\pi}{L} \frac{dQ}{dt} \quad , \tag{2-8}$$

where L represent the latent heat of condensation.

The relations between thermodynamic variable (σ,θ) and the usual pressure (P,T) are

$$\pi = C_p \left(\frac{P}{P_s}\right)^{R/C_p} \quad ; \quad \theta = T^* \left(\frac{P_s}{P}\right)^{R/C_p} \quad ; \quad \pi\theta = C_p T^* \tag{2-9}$$

The virtual temperature T* includes the effect of water vapor on the specific heat at constant pressure C_p and R so that constants for dry air can be used throughout with little modification

$$T^* = (1 + 0.61\, q)\, T \quad . \tag{2-10}$$

By differentiation of equation (1), we have the relationship between vertical P-velocity ω and $\dot{\sigma}$

$$\omega = \sigma \frac{\partial \pi}{\partial t} + u \frac{\partial \pi}{\partial x} + v \frac{\partial \pi}{\partial y} + \pi\dot{\sigma}. \tag{2-11}$$

The set of governing equations permits a variety of responses (gravity waves, inertial waves, Rossby Waves) to a variety of forcing mechanisms, e.g. orography, convection, radiation, boundary layer processes. A significant amount of the forcing comes about within the model domain but lateral boundary conditions must provide for at least large scale forcing from outside the domain. The condition must permit internally excited waves to pass out of the domain without abnormal reflection back into the domain.

The time dependent porous sponge conditions (Perkey and Kreitzberg, 1976) are

applied to the tendency after linear extrapolation to the boundary tendencies at the two interior points. For example, the prognostic variable ψ at n+1 time step and grid point (i,j) is computed from the previous time step value and its tendency

$$\psi_{ij}^{n+1} = \psi_{ij}^{n} + W_{ij} \left(\frac{\partial \psi}{\partial t}\right)_{ij}^{n} \Delta t \tag{2-12}$$

The tendencies at the three outmost rows are multiplied by 0.4 (outmost row), 0.7 (first interior row), and 0.9 (second interior row), respectively. The boundary conditions allow the waves to propagate out of the region.

The vertical σ-velocity $\dot{\sigma}$ will always vanish at the ground even in the presence of the sloping orograph. Therefore, the lower boundary condition in σ-coordinate system is $\dot{\sigma} = 0$ at $\sigma = 1$. Whilst the upper boundary $\sigma = 0$ is $\dot{\sigma} = 0$.

The friction force in momentum equation (2-4) and (2-5), diabatic heating term in energy equation (2-8) and humidity equation (2-9) are fully described in previous study (Chien and Wang, 1979).

III. INITIAL DATE

The atmosphere between the earth's surface and 200 mb is divided into four layers bounded by sigma surfaces, Figure 1. The basic input data for the numerical experiment are difined on constant pressure surfaces. They are the wind, geopotential and temperature at 850, 700, 500, 300 and 200 mb plus the sea-level pressure and wind derived from sea level pressure. These data are balanced on the constant pressure surface with balance equation for nondivergent flow and interpolated to the sigma surfaces.

The balance equation

$$\nabla^2 \phi = f \nabla^2 \psi + \frac{\partial f}{\partial y} \frac{\partial \psi}{\partial y} - 2\left(\frac{\partial^2 \psi}{\partial x \partial y} \frac{\partial^2 \psi}{\partial x \partial y} - \frac{\partial^2 \psi}{\partial x^2} - \frac{\partial^2 \psi}{\partial y^2}\right) \tag{3-1}$$

is solved to obtain the stream function. The horizontal wind is represented by the stream function for non-divergent flow

$$u = -\frac{\partial \psi}{\partial y} \quad \text{and} \quad v = \frac{\partial \psi}{\partial x} \tag{3-2}$$

The boundary condition for Eq. (3-1) is that geopotential is given on the boundary. The method to solve Eq. (3-1) is relaxation procedure (Shuman, 1957).

The method for computing the stream function is obtained by solving the equation

$$\nabla^2\psi = \frac{\partial v}{\partial x} - \frac{\partial u}{\partial y} , \tag{3-3}$$

with the boundary condition

$$\frac{\partial \psi}{\partial \sigma} = v_n - \frac{\partial \chi}{\partial n} , \tag{3-4}$$

where χ is the potential function for irrotational flow, n refers to the outward normal to the boundary and S is directed along the boundary. The potential function is computed from

$$\nabla^2\chi = \frac{\partial u}{\partial x} + \frac{\partial v}{\partial y} , \tag{3-5}$$

The boundary condition for Eq. (3-5) is $\chi = 0$, and these places all of the potential flow in the region into stream function. The horizontal wind velocity components u and v are related to the stream function ψ and velocity potential in the following manner,

$$u = -\frac{\partial \psi}{\partial y} + \frac{\partial \chi}{\partial x} \tag{3-6}$$

$$v = \frac{\partial \psi}{\partial x} + \frac{\partial \chi}{\partial y} \tag{3-7}$$

The balanced geopotential and wind velocity are interpolated to σ surface following the procedure of Shuman and Hovermale (1968).

The geopotential height at σ-surface is obtained by interpolation from P-surface data,

$$d_{\sigma k} = \alpha_k - \beta_k \ln P_k + \gamma(\ln P_k)^2 \tag{3-8}$$

where α_k, β_k and γ_k are determined by the geopotential heigh ϕ_{k-1}, ϕ_k and ϕ_{k+1} at P_{k-1}, P_k and P_{k+1} surfaces respectively.

By equation (3-8) and the surface heigh z_s, one can compute the surface pressure P_s

$$\ln P_s = 2(\alpha - z_s)/[\beta + \sqrt{\beta^2 - 4\gamma(\alpha - z_s)}] \tag{3-9}$$

The temperature field at the pressure surface is derived from geopotential heigh by making the use of hydrostatic equation

$$T = (\phi_U - \phi_L)/[R \ln(P_L/P_U)] \tag{3-10}$$

where ϕ_U and ϕ_L are the geopotential heigh of the neighboring upper and lower pressure level. And the temperature field at σ surface is then obtained by making the use of interpolation formula

$$(T\sigma)_k = \alpha_k - \beta_k \ln P_k + \gamma_k(\ln P_k)^2 \tag{3-11}$$

The specific huminity is assumed proportional to the square of the pressure

$$q_k = a P_k^2 + b \tag{3-12}$$

where a and b are constants. By the difference of temperature and dew point temperature, T_d can be estimated. Using the formula, we have

$$q_k = \frac{6220}{P_k} \exp [20.33X - 22.3816X^2 - 0.50464] , \tag{3-13}$$

$$X = (T_d - 273.2)/273.2 , \tag{3-14}$$

and can compute the specific huminity at the sea surface and the constant pressure levels. Comparing the values obtained from eqs (3-12) and (3-13), we get the constants a and b for each level. Then, the specific huminity at σ surface is evaluated by interpolation.

IV. INTEGRATION SCHEMES

As presented by Shuman and Hovermal (1968), and later investigators, the primitive equations were transformed into difference equations containning a great deal of horizontal average. For example, the momentum equation (2-4) was written as (Shuman and Hovermal, 1968)

$$\overline{\pi u}^t_t = -[\bar{m}^{xy}(\overline{\pi u u_x}^{xy} + \overline{\pi v u_y}^{xy} + \bar{\pi}^{xy}_y \bar{\phi}^x_y) - \overline{\pi\dot{\sigma}u}^{xy} + \overline{fv\pi}^{xy} + \pi F_x]^{xy} , \tag{4-1}$$

where differencing and averaging are represented as

$$\bar{u}^x_{i,j} = (u_{i+1,j} + u_{i-1,j})/2 \tag{4-2}$$

and

$$(u_{i,j})_x = (u_{i+1,j} - u_{i-1,j})/2\Delta x \tag{4-3}$$

for the velocity at point (i,j). The excess averaging on the terms might upset the balance the prognostic equations. Gerrity and McPherson (1971) have successfully used the unaverag velocity components in coriolis terms to preserve a reasonable geostraphic balance. And th was also attamped in semi-implicit model (Campana, 1974). The momentum equation (2-4) is written as

$$\overline{\pi u}^{t} = - \bar{m}^{xy} \left(\overline{\pi u u_x}^{xy} + \overline{\pi v u_y}^{xy} + \bar{\pi}^{xy} \bar{\phi}_y^{x} - \overline{\pi \dot{\sigma} u}^{xy} + \overline{\pi v f}^{xy} + F_x \right) . \qquad (4\text{-}4)$$

Similarly, y-compoment momentum equation (2-5), continuity equation (2-6). Thermal equatic (2-7) and humidity equation (2-8) are transformed into the similar forms.

For time difference, $\partial u_{i,j}/\partial t$ is

$$(u_{i,j})_{t} = (u_{i,j}^{n+\frac{1}{2}} - u_{i,j}^{n-\frac{1}{2}})/\Delta t . \qquad (4\text{-}5)$$

and the term $\bar{u}_t^t$ is

$$(\bar{u}_{i,j}^{t})_t = (u_{i,j}^{n+1} - u_{i,j}^{n-1})/2\Delta t , \qquad (4\text{-}6)$$

where the superscript n is the index for time step index. The time derivative is a simple centered-difference approximation of second order accuracy.

In this study, a newly developed numerical scheme, combination of the modified differential quarature method for space differentiation and rational Runge-Kutta time integration scheme (Wambecq, 1978), is adopted to integrate the prognostic equations.

Consider the prognostic variable $u(x,y,\sigma,t)$ be a function of sufficiently smooth. For simplicity, we consider the differentiation of u in x-direction by modified differentia quarature method. The space differentiation is approximated by

$$\frac{\partial u_i(t)}{\partial x} \cong \sum_{j=1}^{N} a_{ij} u_i(t) , \quad i = 1, 2, \cdots , N. \qquad (4\text{-}7)$$

And the second-order derivative can be expressed by

$$\frac{\partial^2 u_i(t)}{\partial x^2} \cong \sum_{j=1}^{N} b_{ij} u_j(t) , \qquad (4\text{-}8)$$

where $b_{ij} = \sum_{k=1}^{N} a_{ik} a_{kj}$. The approximation relations (4-7) and (4-8) used to evalute the values of derivatives of u at the nearest M points centered around x_i. Therefore the relat can be rewritten as

$$\frac{\partial u_i(t)}{\partial x} \cong \sum_{j=1}^{M} a_j \, u_{i+j-\alpha}(t) = D_M(u_i) \tag{4-9}$$

$$\frac{\partial^2 u_i(t)}{\partial x^2} \cong \sum_{j=1}^{M} b_j \, u_{i+j-\alpha}(t) = D_M^2(u_i) \tag{4-10}$$

where $a_j = a_{\alpha j}$, $b_j = b_{\alpha j}$ and $\alpha = (M + 1)/2$.

The coefficient a_{ij} is chosen similar to Lagrangian interpolation of the form

$$\phi_j(x) = \pi(x)/[(x - x_j)\pi'(x_j)] \tag{4-11}$$

where $\pi(x)$ is a polynomial of degree N

$$\pi(x) = (x - x_1)(x - x_2) \cdots (x - x_N) \tag{4-12}$$

If the values of u(x) are known at N points, $x = x_1, x_2, \cdots x_N$, a polynomial $\tilde{p}(t)$ of degree N-1, $\tilde{u}(x)$ coincided with u(x) at these points, can be written as

$$\tilde{u}(x) = \sum_{j=1}^{N} \phi_j(x) u(x_j) \tag{4-13}$$

By differentiating Eq. (4-13) with respect to x, we have

$$\tilde{u}'(x) = \sum_{j=1}^{N} \phi'_j(x) u(x_j) \tag{4-14}$$

Using the relation Eq. (4-7) to be exact for $\tilde{u}(x) = u(x)$, we have

$$a_{ij} = \pi'(x_i)/[(x_i - x_j)\pi'(x_j)], \text{ for } i = j \tag{4-15}$$

For i=j, using the ℓ'hospital's rule, one gets

$$a_{ij} = \pi''(x_j)/[2\pi'(x_j)] \tag{4-16}$$

By Eqs. (4-15) and (4-16), the coefficients a_j and b_j in Eqs. (4-9) and (4-10) are determine

Now we have the space derivatives of the quantities diagnostic variables. Eqs. (2-4) to (2-8) will be changed into the set of ordinary differential equations in time. For example, eq. (2-4) can be written as

$$(\pi u)'_{ij}(t) = -D_M(u,v,\theta)_{ij} \tag{4-17}$$

or in matrix form

$$\vec{U}' = \vec{F}(\vec{U}, \vec{V}, \vec{\theta}) \tag{4-18}$$

where the prime denotes differentiation with respect to time. Eq. (4-18) is solved by rational Runge-Kutta time integration, and is expressed as

$$\vec{g}_1 = \Delta t\, \vec{F}(\vec{U}, \vec{V}, \vec{\theta}) \tag{4-19a}$$

$$\vec{g}_2 = \Delta t\, \vec{F}\,(\vec{U}^n + C_2\vec{g}_1) \tag{4-19b}$$

$$\vec{U}^{n+1} = \vec{U}^n + [2\vec{g}_1(\vec{g}_1, \vec{g}_3) - \vec{g}_3(\vec{g}_1, \vec{g}_1)]/(\vec{g}_3, \vec{g}_3) \tag{4-19c}$$

where $\vec{g}_3 = b_1\vec{g}_1 + b_2\vec{g}_2$, $b_1+b_2=1$, and $(\vec{g}_1, \vec{g}_3)$, the scalar predict of $\vec{g}_1$ and $\vec{g}_3$.

Similarly, the other prognostic equation can also be integrated by the method described above.

V. NUMERICAL EXPERIMENT

In order to consider the orographic effect in numerical weather pridiction, σ-coordinate is adopted in this investigation. The information levels for meteorological elements are shown in Figure 1.

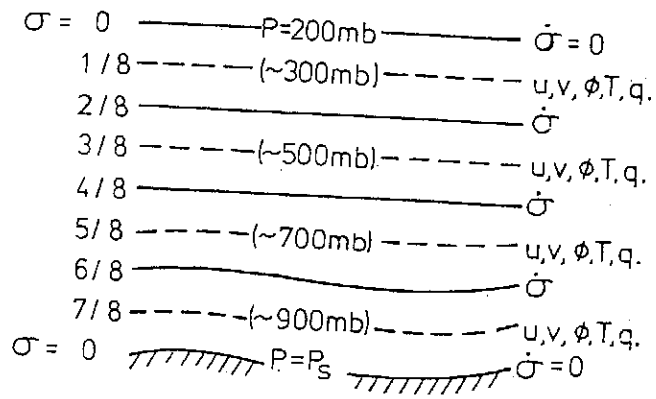

Figure 1. Vertical grid structure.

The synoptic situation of 00GTM 27 January, 1978 is used as initial conditions for numerical experiment. Meteorological elements are read from the grid points of the synoptic charts and then are balanced by the method described at the section 4.

Figure 2 showed the surface chart of 00GTM 27 January, 1978. The low pressure located at 95°-100°E, 25°-30°N. The cold front extended from 110°E, 30°N southwestward to the low center. The high pressure presided over 70°-80°E, 50 -55°N. After twenty-four hours, the front moves eastward. The front extended from 120°E, 30°N to the low center located at 100°E, 20°N.

The upper atmosphere patterns are similar to that of the surface for the initial conditions, Figure 3 through figure 6 are the geopotential pattern and temperature distritution for 700 mb at 00GTM 27 January, 1978. The pattern is not so complicate compare with that of the surface. Above 500 mb, no huminity is considered.

In order to test the accuracy of the method incoporated in this investigation, a preliminary study is made using one level primitive equation model to predict the atmospheric motion with the same initial condition in this study (Chien, 1983). No heat source considered in the preliminary study, the forecasted front moved slower than the actual situation. But the atmospheric pattern, geopotential at 500 mb are exactly coincide with that of forecasted by explicit method (Shuman and Hovermal, 1968). The numerical experimen indicated that the heat sources play an important role in the atmospheric motion during the outburst of the cold air.

A twenty-four hour forecast was produced using the method of combination of modified differential quarature for space differentiation and rational Runge-Kutta time integration with time increment of ten minutes. The twenty-four hour forecast of geopotential and temperature fields are shown in Figure 7 through Figure 10. They are similar to those produced by the explicit method with time increment of six minutes. The front extended from 110°E, 35°N to 100°E, 26°N for 500 mb. It almost coincided with the actual front position.

Then, we adopted the new method with the same initial and boundary conditions except the integration time steps are increased by double the predicted geopotential and temperature fields show no difference for three significant figures compared with that produced by time increment with ten minutes.

Furthermore, the numerical experiment was carried out with larger integration time increment with thirty minutes. This is the same with that used by semi-implicit.

method (Campana, 1974). The predicted fields agree with those produced by integration time increment of ten minutes.

VI. Conclusion and Recommendation

The newly developed numerical method, based on the combination of modified differential quarature method and rational Runge-Kutta time integration scheme, is applied to four-level primitive equation model. It is fully explicit, requires no matrix inversion, and is stable at much larger time step than the usual explicit method. In this investigation the atmospheric motion during the outburst of the cold air is investigated to demonstrated the accuracy and efficiency of the proposed algorithm. For comparison, numerical experiments were made for the same initial and boundary conditions by applying both explicit method and present scheme with triple and quadruple time increment during the time integration. The computation results show that twenty-four hour predicted geopotential and temperature field agree excelly to three significant figures in both methods.

Recently, some efficiency and high order accuracy numerical schemes (Brown and Campana, 1978; Campana, 1979; Chao, 1982; Gadd, 1978) are developed and applied to numerical weather prediction. It is encouraged to compare the proposed algorithm with those hewly developed numerical methods for accuracy an efficiency.

References

(1) W. BOURKE, Month. Weath. Rev., 102, 687-701 (1974).

(2) J. A. BROUN, and K. CAMPANA, Mon. Wea. Rev., 106, 1125-1136, (1978).

(3) K. CAMPANA , NOAA Tech. Memo. NWS NMC-54, 22 (1974).

(4) K. A. CAMPANA, Month. Weath. Rev., 107, 363-376, (1979).

(5) W. C. CHAO, Mon. Wea. Rev., 110, 1603-1617, (1982).

(6) L. C. CHIEN and C. T. WANG, Proc. Natl. Sci. Coun. ROC. 3, 356-363, (1979).

(7) L. C. CHIEN ,Ann. Rept. Inst. Phys. Acad. Sin., 10, 115-127 (1980).

(8) L. C. CHIEN ,Atm. Sci., 8, 19-25, (1981).

(9) L. C. CHIEN ,Atm. Sci., 10, 39-44, (1983).

(10) A. J. GADD, Quart. J. Roy. Met. Soc., 104, 569-582, (1978).

(11) D. J. GAUNTETT, L. M. LESLIE ,J. L. McGREGOR, and D. R. HINCKSMAN, Quart. J. R. Met. Soc., 104, 103-117, (1978).

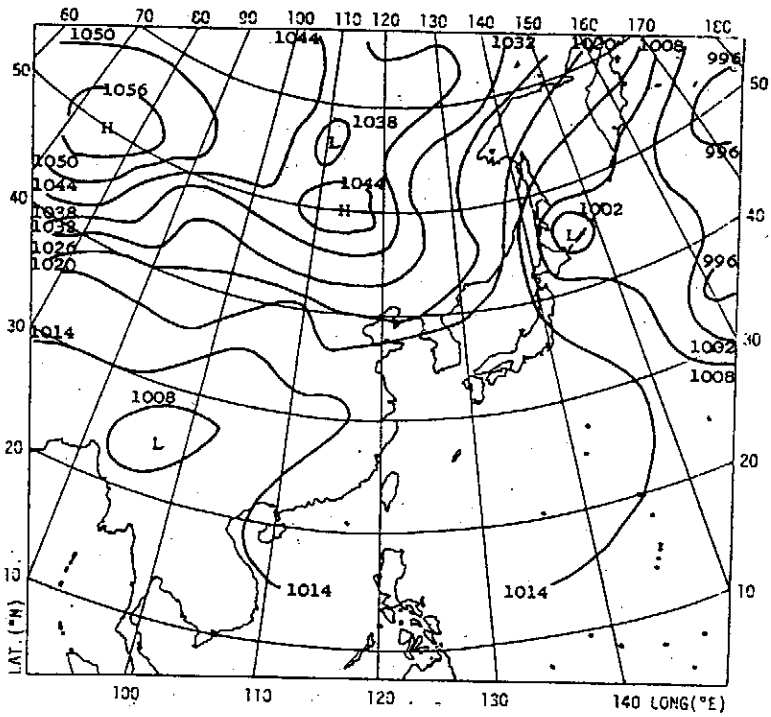

Fig. 2. Surface pressure at 00GTM January 27, 1978.

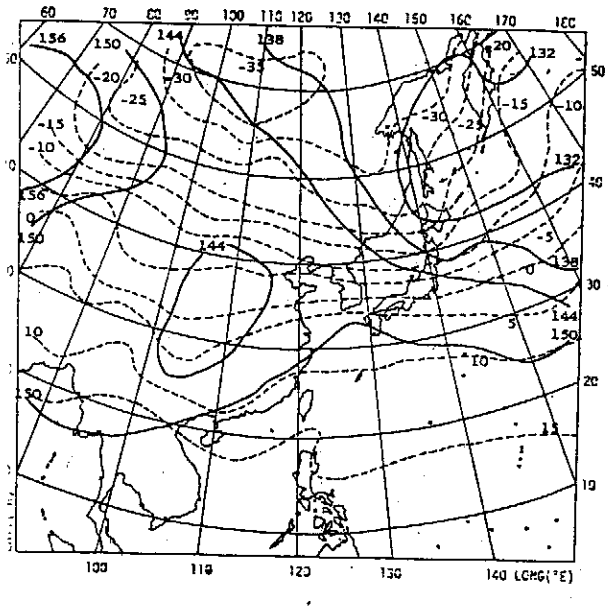

Fig. 3. 850 mb geopotential (m) (solid line) and temperature (°C) (dash line) for 00GTM 27 January 1978.

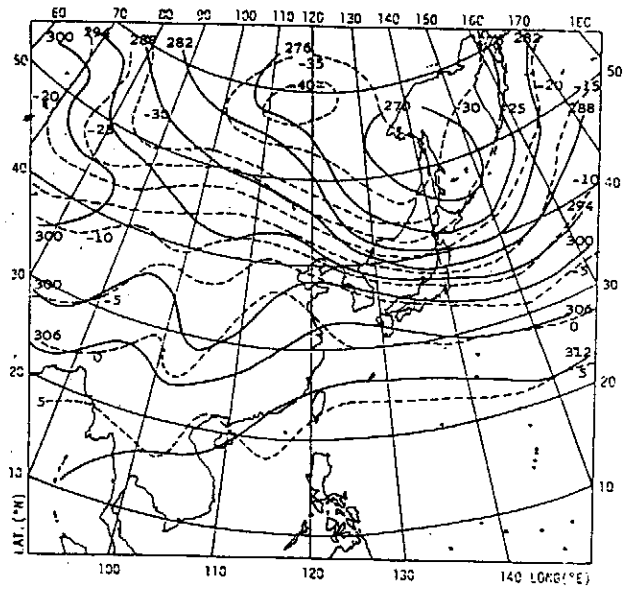

Fig. 4. 700 mb geopotential (m) (solid line) and temperature (°C) (dash line) for 00GTM 27 January 1978.

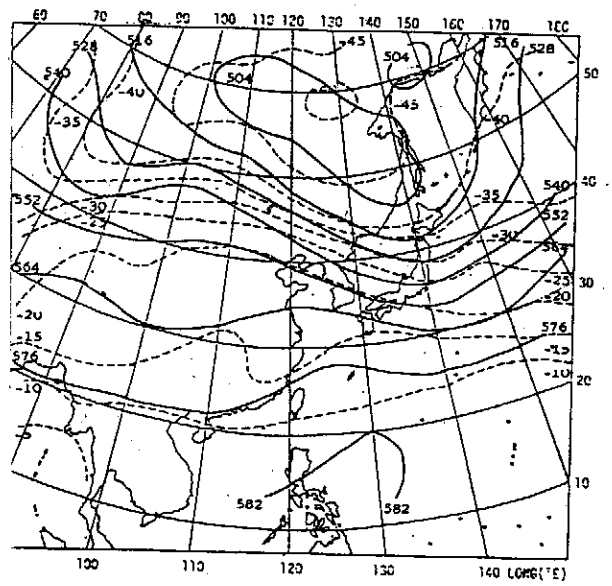

Fig. 5. 500 mb geopotential (m) (solid line) and temperature (°C) (dash line) for 00GTM 27 January 1978.

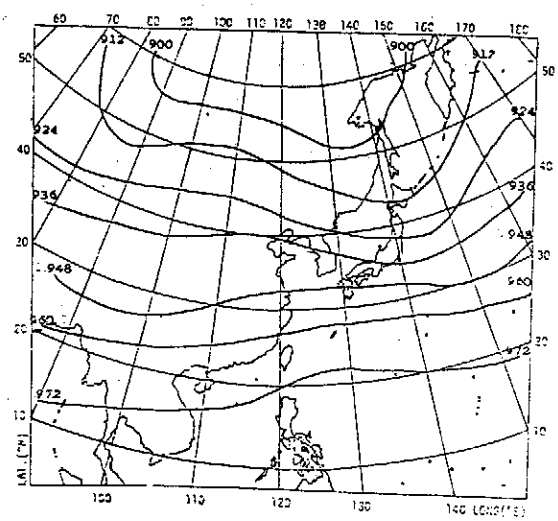

Fig. 6. 300 mb geopotential (m) (solid line) and temperature (°C) (dash line) for 00GTM 27 January 1978.

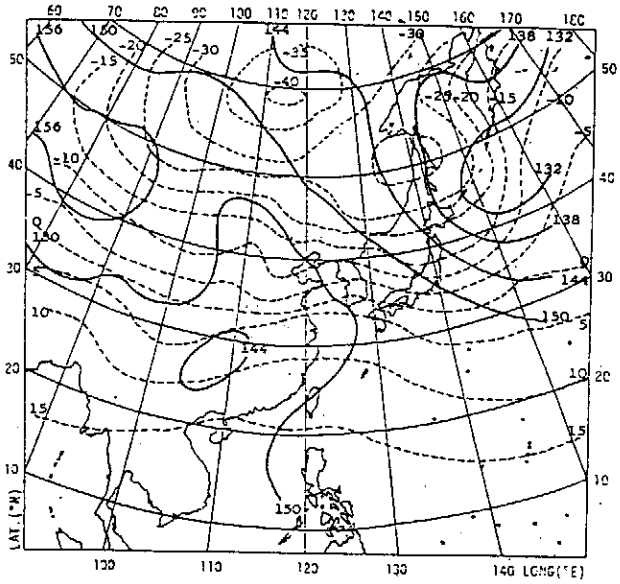

Fig. 7. 24-hour forecast 850 mb geopotential (m) (solid line) and temperature (°C) (dash line) from 27 January 1978 data.

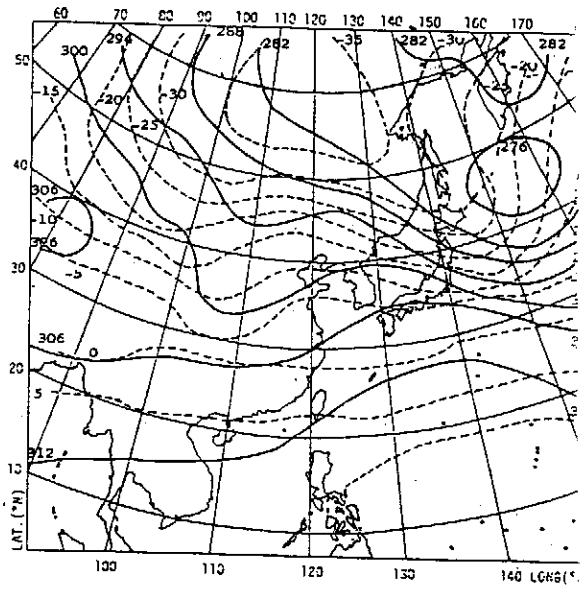

Fig. 8. 24-hour forecast 700 mb geopotential (m) (solid line) and temperature (°C) (dash line) from 27 January 1978 data

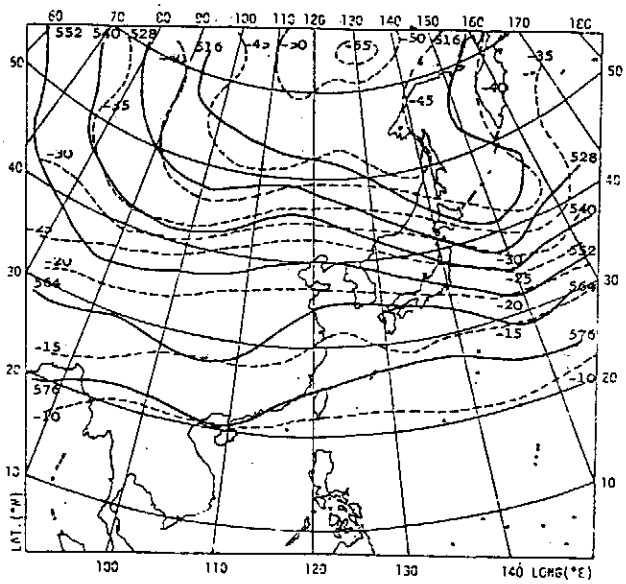

Fig. 9. 24-hour forecast 500 mb geopotential (m) (solid line) and temperature, (°C) (dash line) from 27 January 1978 data.

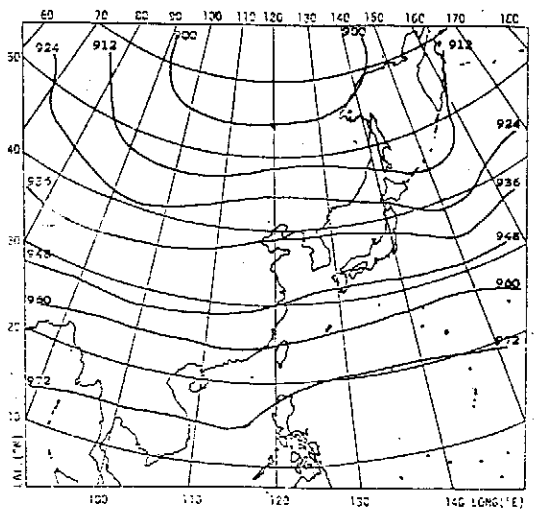

Fig. 10. 24-hour forecast 300 mb geopoten (m) (solid line) and temperature (dash line) from 27 January 1978

修正空間微分法在數值天氣預報上之應用

簡　來　成

中央研究院物理研究所

摘　要

以修正 quarature 空間微分法與 rational Runge-Kutta 所組成的新數值方法，解 σ 座標四層原始方程式模式，以探討寒潮爆發期間東亞地區之大氣運動。此計算方法雖然顯函程式，但其積分時間增量可與隱函法比擬。並且已爲數學上證實解拋物線型偏微分方程爲無條件穩定。爲確定其正確性，先以一般的微方法與顯函法六分鐘時間增量積分預報二十四小時後的天氣形勢，再以此法，用相同的原始與邊界條件用本文的方法積分，時間增量放大三倍，四倍，二十四小時後之重力位與溫度場與顯函法預報者有效數字三位相同，可見準確度可靠，計算程序經濟。

小型質子加速器之研製

程 斌 陳志遠
陳明壽 江紀成 王建萬
中央研究院物理研究所

小型質子加速器在現今科技上佔重要地位，對於材料研究、放射元素之研究，醫療、原子核物理之研究以及訓練人才均爲所需。國內從事此類研究工作者不多，有鑑及此特從根做起，亦即從離子加速器之各個單元開始研製。它的各個單元可分爲㈠離子源㈡加速及聚焦部份㈢質譜分析部份㈣高壓供應部份㈤眞空及冷却系統㈥控制部份。以上各部份執行研製時，盡量使用國產品材料以減少對國外之依賴。技術更求百分之百自立。小型加速器之研製是一項基本的研究工作。

㈠冷陰極離子源研製

根據以上目標逐步展開研究工作，第一要研究“離子源”，國內離子源之研製，核能研究所有R.F.型離子源，其輸出電流大約在1.5 MA左右，台大亦有Nelson-Type之離子源，其輸出電流亦不大，故而本研究採冷陰極型式者開始研製，在稍爲犧牲能量分析度一點之情況下，它是可望有較大輸出者。本實驗室有數年之操作離子源之工作經驗，每逢離子源發生故障，在現有的技術情況下修復之希望極少。故在從事此一研究時，力求減少故障以及修理方便作爲重點之一。

(A)冷陰極離子源之工作原理

冷陰極離子源之設計在一直圓筒的容器內置以電極，兩端爲陰極，中間某部份爲陽極，整個容器內維持甚低之氣壓（工作氣體），正負極間施以數千伏特之電壓使之放電產生電漿，另由一外施磁場，沿軸線方向，兩端較強，使電子作往返運動，不達器壁以增加碰撞機會產生更多之離子，在軸線末端開一細孔附近加一電極並施以吸引電壓，使離子逸出以便下級聚焦、加速之用。

冷陰極之釋放電子詳情仍不爲所知，但一經釋放有活力之電子，即可使之行較長之路徑（旋轉）以增加對於工作氣體之碰撞機會，產生很多的離子。於是

$$N_+ = \frac{J_- \; P \; L \; Se}{e} \qquad \cdots\cdots(1)$$

(1)式中N_+爲每秒鐘每平方公分產生之離子數，這些離子是因電流密度爲J_-之電流（安培/公分^2）通過距離爲L（公分）氣壓爲p（Torr）之情況下所產生。

S_e 爲von Engel (1965)[1] 之氣體電離係數，如圖㈠所示。

一個電子當具有W_e 之能量在氣體中進行時在未變成壽終電子之前（能量交盡）所能行走之平均距離。

$$R_e(\text{公分}) = (1.4 \times 10^{-7}) \frac{TW_e}{PM} \quad \cdots\cdots(2)$$

(2)式中T爲溫度（°K）P 爲氣壓（Torr）M爲氣體之分子量，但W_e須大於2000 eV。

電子之碰撞氣體電離交能量之方式是依電離之程度而計算的。

$$S_e = a(W_e - eV_i) \quad \cdots\cdots(3)$$

式中W_e爲電子之動能eV_i爲氣體電離所需之能量，a爲與氣體有關之常數。圖㈡即其電離程度與所需之能量情形。

(B)熱陰極及冷陰極之放電特性

利用電子在氣體中碰撞以產生離子的方法較有效的有兩種，其一爲熱陰極，另一則爲冷陰極，但二者之特性大概類似；即使含在一陰極及一陽極之間的氣體由電弧之放電，而產生離子對又稱之爲電離。陰極之放射電子可由外施電壓將陰極加熱，或者工作啟動後由陽極區返回之離子轟擊陰極表面，提升溫度而維持電子之繹放，進而維持整個放電狀況。在陰陽極之間所加之電壓產生一空間電荷限制區〔參閱圖㈢〕。此區是一薄層，侷限於陰極之附近，並且外施之電壓實際上却有效的跨於此一薄層的兩邊。電子在此區域中加速進入電漿區使氣體電離造成更多的離子及二次放射電子。所具活動力較弱的離子向陰極方向進行，於是在此一薄層區中就有兩種相對方向之電流流動著。假如氣壓不太高，從陰極射出之電子就進入此一薄層區再進入電漿區。此時這一空間電荷之薄層就扮演著導通二極管之陽極工作一樣，於是由Child- Langmuir[2] 方程式可以求此等雙方向之電流

$$\text{電子流密度 } J_- = \sqrt{\frac{2e}{M_e}} \cdot \frac{V_d^{3/2}}{9\pi d_s^2} \quad \cdots\cdots(3)$$

$$\text{離子流密度 } J_+ = \sqrt{\frac{2e}{M_i}} \cdot \frac{V_d^{3/2}}{9\pi d_s^2} \quad \cdots\cdots(4)$$

上兩式中V_d爲空間電荷薄層之電壓降，d_s表示薄層之厚度（假定是平面的）故兩電流之比

$$\frac{J_-}{J_+} = \sqrt{\frac{M_i}{M_e}} \quad \cdots\cdots(5)$$

從公式(5)可知電子流密度比離子流密度約大200倍，陰極空間電之薄層爲電子所構成。陽極之薄層由離子所構成。這兩種薄層都能加速電子及離子（各扮陰極及陽極），有一極小部份的慢速離子和電子，重新組合（Recombination）可以在陰極附近察覺到它發出的微光（Cathode glow）。圖㈢(a)中所示熱陰極放電者之電位及電場分佈情形，在兩電極薄層區之電位分佈表示出空間一電荷一限制放射之標準特性。電場在薄層之中央爲最大，而在電漿區內電場爲零。電位之分佈在空間電荷區爲一變化之曲線，電漿區爲一常數，此種方式之電子流密度通常爲1 A/cm² 。圖㈢(b)爲冷陰極電弧放寬（arc）之情形，在兩電極處之電場非常高，在電漿區之電場爲一常數。電位之分佈則兩端各爲 V_d

及 V_s 爲快速升起之電位，與熱陰極者大不相同。此種冷陰放電之特性仍不甚詳；據稱這種放電是陰極表面受到甚強之電場而放射電子，這種電子流常由陰極某一局部表面開始然後遍及整個表面。這種冷陰極之放電，倘若在氣壓甚高之時可能有極高之電流密度產生，約爲 10^6 安培/平方公分。上述兩種熱冷陰極在氣體中放電，陰極薄層之電位降約爲 10 至 20 V。電漿之濃度通常約爲 $10^{12} \sim 10^{14}$ 個離子每立方公分，對於中性原子來說相當要有 10^{-5} 至 10^{-3} Torr 之氣壓下之濃度。公式(3)表示能從空間電荷層所取之最大電子流密度。若無外加加熱之來源，則電弧中之正離子流必須提供轟擊陰極以釋放 J-電子流的離子流，這種 J-電子流又電離中性氣體 。對於上述之離子流公式(4)所表者爲最大值，但若外加一軸向磁場使電子旋轉增加碰撞機會，可以增多離子數。詳細之分析可參閱 Spitzer氏(1956)[3] 荷電體之運動。

(C)本設計冷陰極離子源的幾個重要數據

1. 磁場係電磁式而非永久磁鐵，且須製造一" potential well "須精密計算，激磁電壓應于可變且極穩定。大約的磁場強度在 1K guass 左右，電子之旋轉半徑應小於 1 公分。

2. 離子源之軸心有一細的出孔，由耐高溫之金屬爲之，口徑約爲 3 mm 。已採用鉭金屬。因爲離子之密度高達每立方厘米 10^{14} 左右。

3. 冷却：由於電弧的 3kv × 100 mA之電力全部消耗於短短之 5 公分×直徑 5 公分之筒內，且向右集中，故須于以週邊中空散熱，以 Freon-113 帶出熱量。

4. 饋氣系統目前採用 Pd leak 。加熱時對於氫多孔而饋氣。

(二)加速與聚焦部份

(A)離子由離子源經由引極(extractor) 加以聚焦再加速至所需之能量備用。

Langmuir (1937) 之最大離子射束電流爲

$$J_m = \frac{J_o e V^2 \theta^2}{K T_s} = \frac{J_o V_o \theta^2}{T_s / 116000} \quad \cdots\cdots(6)$$

參閱圖四，原來之離子流密度爲 J_o，經過理想之聚焦及加速而趨於一點時之最大離子流密度公式(6)，稱爲 Langmuir 極限值。由於實際上射束含有高溫的粒子不完全受聚焦等約束，必不能同時到達於一點，故

$$E_i = \frac{J_s}{J_m} \quad \cdots\cdots(7)$$

式中 J_s 爲實際上能集中於一點之電流密度。圖五爲電流密度因受熱散射部份之影響情形。E_i 爲效率。

(B)離子源之引極(extractor)

離子源內發生之離子爲欲使之引出並加速，都希望有較細而高濃度的離子射束，投射於某一點，沿途不使散開或損失。於是離子經過的每一點都要考慮，在設計引極時應把握離子一光學性質之要點當設計一電子槍或離子槍時，有一個重要的比值稱爲 P 的應用公式

$$P=\frac{I_0}{V_a^{3/2}}=\frac{5.45\times10^{-8}}{\sqrt{M}}\cdot\frac{A}{d^2}\quad\left(\frac{\text{安培}}{\text{伏特}}\right)\qquad\cdots\cdots(8)$$

(8)式中I_0爲射束電流，V_a爲引極之電壓 。此公式P 值常與幾何形狀有關。對於離子，(8)式之應用也可以像普通電子槍的應用情形相似。電子槍中假定兩個金屬平面，其間隔爲d ，截面爲A ，兩極間施以電壓V_a，內部充滿空間電荷的導電情況下工作（M爲離子之質量）。今日之電子槍一般多沿用 Pierce 氏於1940 年所提供之方法，祇是特別加以修正應用而已。在此特舉 Pierce[4] 氏之技巧如下圖(七)所示。圖中爲一完整之兩平面形成有空間電荷之二極管，左片爲離子發射區，右邊爲引極或加速陽極，由於兩表面均勻對稱，離子之活動以完全有層次之方式流動，亦即各成直線跨過此二極管。假定在此二極管當中作二條虛線（如圖所示），當作離子槍，同理自此槍中射出之離子亦呈層次之方式流動。但是射束之內外邊緣界面沿途均應等電位。因此Pierce 氏指出此種槍外之離子區可由一電極擔任之，此極又稱爲射束形成極或曰聚焦電極。假如設計適當則槍外區之邊界電場對於射束邊緣有較佳之邊界條件，能使射束離子源亦爲直線之軌跡。若電子槍非爲平板，亦可由類比方式接近之。

Pierce 氏槍之主要目的是如何使聚焦電極作成適當之形狀造成之電場以迫使離子成直線進行，參閱圖(七)以易了解，若離子在引極細孔處的動量擾亂情形不計，則沿著離子流行徑的電位分佈如圖(七)中之A 曲線，若離子流去掉，則電位分佈如B 曲線。離子流限制在虛線以內的就是曲線A ，在其位就是B之分佈情況。這種離子流的兩邊界面上的電位分佈差別意謂著電力線必須重新分佈以求跨越那二條虛線，如此即產生橫亙的電場分量使得離子流之區域膨脹，亦即不再循著理想之直線途徑。因此聚焦電極之設計主要就是算出一種表面，它的帶電能強迫電力線沿著離子流邊界成平行分佈，這種情況可如圖(七)(b)之下半邊所示。Pierce 氏槍之數學計算，他假定除上述之理想二極管外，並以保守電場，及不計各種熱速度等，由Poisson 方程式

$$\frac{d^2V}{dz^2}=\frac{J}{\varepsilon_0(2nv)^{1/2}}\qquad\cdots\cdots(9)$$

沿途以

$$\frac{dV}{dx}=\frac{dV}{dy}=0\qquad\cdots\cdots(10)$$

式中電位V之解由$V=0$，$z=0$，在$z=0$時，$\frac{dV}{dz}=0$，

$$V=A_z^{4/3}\qquad\cdots\cdots(11)$$ 式中

$$A=\left(\frac{9J}{4\varepsilon_0(2n)^{1/2}}\right)^{1/2}\qquad\cdots\cdots(12)$$

公式（11）與（12）爲理想二極管電位分佈公式又稱爲Langmuir and Blodgett (1924)[5] 分佈公式。

由公式（11）與（12）可得電流密度

$$J = \frac{5.45 \times 10^{-8}}{\sqrt{M}} \cdot \frac{V_a^{3/2}}{d^2} \qquad \frac{\text{安培}}{\text{平方公分}} \qquad \cdots\cdots(13)$$

此一電流垂直朝向平板作直線之流動，這種情形唯有在所行之距離不太長且須在公式(10)及(11)之保證情形下才能維持。公式(10)表示沒有能使射束邊緣正交處升高電場的空間電荷存在。公式(11)則表示射束之沿途貼近的內外交邊電位都是同樣的。離子射束內流動區之電位分佈可由Poisson方程式解決，而射束以外的電位分佈已由Laplace方程式求得，Pierce氏得Laplace方程之解：

$$V = A(Z^2 + Y^2)^{2/3} \cos\left(\frac{4}{3} \tan^{-1} \frac{Y}{Z}\right) \qquad \cdots\cdots(13)$$

由(13)式可以看出它的零等電位發生於一直線上，此線通過$z = 0$並與射束邊緣形成$\left(\frac{4}{3} \cdot \frac{\pi}{2}\right)$之角度。亦即意謂用一個電極做成零等位線之形狀連接於離子源之電位，也就是射束外邊界面之電位。這一電極稱爲聚焦電極，此一電極之設計爲電子槍或離子槍所必須。

(C)電子槍或離子槍細孔之透鏡效應

上面曾談到離子槍之設計使離子流成理想的直線路徑由一個平面朝引極平面進行。當離子經過引極之細孔時由於電場之電力線在此爲終止之點，離子受到此種橫向力線之影響即有發散之趨勢，見圖(八)。假如引極細孔之口徑遠小於離子源與引極間之距離時，此種偏向之軌跡就像光學上一透鏡所造成的效應一樣，它的焦距可由Pavisson-Calbick (1931及1932)[6]方程式定出，此一透鏡對於圓柱體形細孔之焦距爲

$$f = \frac{4V_a}{E_2 - E_g} \qquad \cdots\cdots(14)$$

式中V_a爲引極電壓，E_g及E_2爲軸向之電場，各爲引極平面內外之強度。此一公式之來由係因徑向及軸向電場對通過細孔離子之作用因其動量之改變而導出(Klemperr 1953)，假如$E_2 = 0$，離子束即進入一無電場區。則透鏡之效應永爲散，見圖(八)(b)〔從上式知道球面散焦效應並未考慮，因f與r無關〕。於是離子從此一圓柱體形細孔離開時之斜率

$$\tan\gamma = \frac{-r_0}{f} = \frac{r_0 E_g}{4V_a} = \frac{r_0}{3L} \qquad \cdots\cdots(15)$$

式中r_0爲離子束在引極平面處之半徑，L爲離子源與引極間之距離。上式$E_g = \frac{4}{3} V_a / L$係由公式(11)之應用代入，$E_g$即爲引極處電位之斜率。

公式(14)之焦距尚可作收斂射束時初步約略計算之用。

$$E_g(a) = \left(\frac{dV}{dr}\right)_{r=r_a} = \frac{4}{3} \frac{V_a}{\alpha_a r_a} \left(\frac{d\alpha}{d\gamma}\right)_a \qquad \cdots\cdots(16)$$

〔式中$\alpha = \gamma - 0.3\gamma^2 + 0.075\gamma^3 - 0.001432\gamma^4$　而$r = \ell n(r/r_c)$爲Langmuir及Blodgett以同心圓作二極管所發展之參數，並且得一公式$V/V_a = (-\alpha/-\alpha_a)^{4/3}$。〕

以$E_2 = 0$，其焦距已知，因此當$r = r_a$處彎曲通過細孔之角

$$\theta - \gamma = \tan^{-1}\left(\frac{r_a}{f}\right) = \tan^{-1}\left[\frac{\sin\theta}{3\alpha_a}\left(\frac{d\alpha}{d\gamma}\right)\right]_a \quad \cdots\cdots(17)$$

從公式(17)則鑽出之射束之斜率爲

$$\left(\frac{dr}{dz}\right)_a = \tan\left\{\theta - \tan^{-1}\left[\frac{\sin\theta}{3\alpha_a}\left(\frac{d\alpha}{d\gamma}\right)\right]_a\right\} \quad \cdots\cdots(18)$$

公式(17)也可能是正角，意卽從引極出去變爲發散，相當於作用於透鏡之輸出動量高於輸入收斂射束之動量。

另外在引極之後，增加一個電極，使其電位爲V_f比V_a更負（更高）或者介於離子源與引極間之電位，故又可減速。因此稱此爲"加速－減速電極"。參閱圖(八)(a)。在引極出孔邊之電場$E_2 = -(V_a - V_f)/s$於是公式(14)對於這種直圓筒離子槍則變爲

$$f = \frac{-4L}{\left[1 - V_f/V_a\right]L/S + 4/3} \quad \cdots\cdots(19)$$

由公式(19)可見V_f/V_a大於1時爲"加速—加速"情形它的焦距減短，則離開引極細孔之射束更爲發散，那是因爲在細孔中之電場相抵消以致射束離開細孔後毫無偏向。不過對再好之聚焦通過最後一個孔口之後因進入無電場區，必終將散焦。Pierce槍之一切上述對於強力射束均應修正方能正確使用。

離子射束對於聚焦，加速之另一種方便之計算法

對於離子射束中任意一束，可以將物平面（object plane）和像平面（Image plane）相關位置及動量表示成

$$r_i = a_{11}\, r_o + a_{12}\sqrt{V_o}\, r_o'$$

$$\sqrt{V_i}\, r_i' = a_{21}\, r_o + a_{22}\sqrt{V_o}\, r_o'$$

其中r和r′分別表示橫向之r平面的位置及斜率。而$\sqrt{V}\,r'$正比於橫向的動量。

這樣兩個平面之間的關係就像線性方程式，我們用矩陣符號M表轉換矩陣

$$\begin{pmatrix} r_i \\ \sqrt{V_i}\, r_i' \end{pmatrix} = \begin{pmatrix} a_{11} & a_{12} \\ a_{21} & a_{22} \end{pmatrix} \begin{pmatrix} r_o \\ \sqrt{V_o}\, r_o' \end{pmatrix} = M \begin{pmatrix} r_o \\ \sqrt{V_o}\, r_o' \end{pmatrix} \quad \cdots\cdots(20)$$

如果是由第K個和第一個平面之間的轉換矩陣可以表示成這些轉換矩陣之相乘積

$$\begin{pmatrix} r_i' \\ \sqrt{V_i}\, r_i' \end{pmatrix} = M_{KL} \cdots M_{34} M_{23} M_{12} \begin{pmatrix} r_o \\ \sqrt{V_o}\, r_o' \end{pmatrix}$$

在轉換矩陣中的元素a_{11}表示放大倍率。a_{21}可以代表焦距（$a_{21} = -\sqrt{V_o}/f_o$），而離子射束是收斂（當$a_{12} < 0$）或者發散（$a_{12} > 0$）由a_{12}決定。根據轉換矩陣的特性，其行列式值須等於1，故$a_{11}\, a_{22} - a_{12}\, a_{21} = 1$。

設使離子射束在兩個平面中間，電位差V，距離d而成直線的軌跡，我們可寫成

$$\begin{pmatrix} r_i \\ \sqrt{V}\, r_i' \end{pmatrix} = \begin{pmatrix} 1 & \ell/\sqrt{V} \\ 0 & 1 \end{pmatrix} \begin{pmatrix} r_o \\ \sqrt{V}\, r_o' \end{pmatrix} \quad \cdots\cdots (21)$$

若在主平面突然改變方向，如圖九。

轉換矩陣也是很簡單的型式

$$\begin{pmatrix} 1 & 0 \\ -1/f & 1 \end{pmatrix}$$

對於單孔透鏡，我們可由Davisson-Calbick薄透鏡近似法得知，焦距爲 $4V/(E_2-E_1)$ 由此得知此轉換矩陣爲

$$M = \begin{pmatrix} 1 & 0 \\ \dfrac{E_1-E_2}{4\sqrt{V}} & 1 \end{pmatrix}$$

再考慮雙孔透鏡，我們可以想像成三個部份之組合，如圖十所示。參考單孔透鏡之轉換矩陣，在孔外面 $E=0$ 而在兩孔之間

$E=(V_2-V_1)/d$，因此

$$M_{12} = \begin{pmatrix} 1 & 0 \\ \dfrac{V_1-V_2}{4d\sqrt{V_1}} & 1 \end{pmatrix}, \quad M_{34} = \begin{pmatrix} 1 & 0 \\ \dfrac{V_2-V_1}{4d\sqrt{V_2}} & 1 \end{pmatrix}, \quad M_{23} = \begin{pmatrix} 1 & \dfrac{2d}{\sqrt{V_1}+\sqrt{V_2}} \\ 0 & 1 \end{pmatrix}$$

$$\begin{pmatrix} r_4 \\ \sqrt{V_2}\, r_4' \end{pmatrix} = M_{34}\, M_{23}\, M_{12} \begin{pmatrix} r_1 \\ \sqrt{V_1}\, r_1' \end{pmatrix} = M_{14} \begin{pmatrix} r_1 \\ \sqrt{V_1}\, r_1' \end{pmatrix},$$

$$M_{14} = \begin{pmatrix} \dfrac{3\sqrt{V_1}-\sqrt{V_2}}{2\sqrt{V_1}} & \dfrac{2d}{\sqrt{V_1}+\sqrt{V_2}} \\ \dfrac{3(V_2-V_1)}{8d} \quad \dfrac{\sqrt{V_1}-\sqrt{V_2}}{\sqrt{V_1 V_2}} & \dfrac{3\sqrt{V_2}-\sqrt{V_1}}{2\sqrt{V_2}} \end{pmatrix} \quad \cdots\cdots (22)$$

安折透鏡如圖十一所示，可看成二組雙孔透鏡之組合，我們可很容易的由已知雙孔透鏡之轉換矩陣相乘而得到安折透鏡的轉換矩陣 M_E

$$M_E = \begin{pmatrix} \dfrac{3\sqrt{V_2}-\sqrt{V_1}}{2\sqrt{V_2}} & \dfrac{2d}{\sqrt{V_1}+\sqrt{V_2}} \\ \dfrac{3}{8}\dfrac{(V_1-V_2)}{d} \cdot \dfrac{(\sqrt{V_2}-\sqrt{V_1}}{\sqrt{V_1 V_2}} & \dfrac{3\sqrt{V_1}-\sqrt{V_2}}{2\sqrt{V_1}} \end{pmatrix} \times$$

$$\begin{pmatrix} \dfrac{3\sqrt{V_1}-\sqrt{V_2}}{2\sqrt{V_1}} & \dfrac{2d}{\sqrt{V_1}+\sqrt{V_2}} \\ \dfrac{3}{8}\dfrac{(V_2-V_1)}{d} \cdot \dfrac{(\sqrt{V_1}-\sqrt{V_2}}{\sqrt{V_1 V_2}} & \dfrac{3\sqrt{V_2}-\sqrt{V_1}}{2\sqrt{V_2}} \end{pmatrix}$$

$$= \begin{pmatrix} \frac{16\sqrt{V_1V_2} - 6V_1 - 6V_2}{4\sqrt{V_1V_2}} & \frac{2d}{\sqrt{V_1}+\sqrt{V_2}} \cdot \frac{3\sqrt{V_2}-\sqrt{V_1}}{\sqrt{V_2}} \\ \frac{3}{8}\frac{V_1V_2}{d}\frac{(\sqrt{V_2}-\sqrt{V_1}}{\sqrt{V_1V_2}}\frac{(3\sqrt{V_1}-\sqrt{V_2}}{\sqrt{V_1}} & \frac{16\sqrt{V_1V_2} - 6V_1 - 6V_2}{4\sqrt{V_1V_2}} \end{pmatrix} \quad \cdots\cdots(23)$$

如果我們希望離子射束經過透鏡只有轉彎，這樣對於安折透鏡之轉換矩陣中元素 a_{12} 必須爲 0，

$\frac{2d}{\sqrt{V_1}+\sqrt{V_2}} \quad \frac{3\sqrt{V_2}-\sqrt{V_1}}{\sqrt{V_2}} = 0$ 即 $V_1 = 9\ V_2$，那麼必然有 $a_{11} = a_{22} = \frac{16\sqrt{V_1V_2} - 6V_1 - 6V_2}{4\sqrt{V_1V_2}} = 1$，且 $a_{21} = -\sqrt{V_1}/f$ 可求出 $f = \frac{9}{16}d$

當 $d = 10$ cm 則 $f \approx 5.63$ cm

一種質量分離器，利用電場和磁場互相正交以及當離子進入後因非平衡力使得粒子有不同的速度，這種稱作 E × B 分離器。我們利用這種方式來選擇直線通過的離子，當其有不同的質量和速度時就有不同的偏斜，此直線通過的特性也就是 E × B 分離器常被利用在離子射束系統之原因，如圖十二所示。

我們考慮在分離器內電場和磁場是均勻的且是常數值與 x 和 z 無關，則離子運動方程式

$$m\ddot{x} = eE_x - e\dot{z}B_y \quad \cdots\cdots(24)$$

$$m\ddot{x} = e\dot{x}B_y \quad \cdots\cdots(25)$$

$$m\ddot{y} = 0 \quad \cdots\cdots(26)$$

將任意 x 在 z 軸上速度用 V_z 表示，當 $x = 0$ 時爲 V_{z_0}，我們可先解出 (25) 式利用當 $x = 0$ 時，$\dot{z} = V_{z_0}$，求出積分常數代入 (24) 式。

得到

$$\ddot{y} = 0 \quad \cdots\cdots(27)7$$

$$\ddot{x} + W_c^2 x = \eta E_x - \eta B_y V_{z_0} \equiv K \quad \cdots\cdots(28)$$

其中 $W_c = \eta B$，$\eta = |e/m|$。

K 值我們可改寫成在特殊的 E，B 及 V_{z_0} 中得到平衡，這些量我們稱作 E_0，B_0 和 V_0 而 E_0/B_0 值決定特殊速度 V_0 則 $K = \eta E_0/V_0$。

假使軌跡斜率 $\frac{dx}{dz} = x'$ 而 $x'^2 \ll 1$，則 (28) 式可換成新的變數

$$x'' + \beta^2 x = \frac{K}{V_{z_0}^2}, \quad \beta = W_c/V_{z_0}$$

可解出

$$x = \frac{K}{W_c^2}(1 - \cos\beta z) + x_0\cos\beta z + \frac{x_0'}{\beta}\sin\beta z \quad \cdots\cdots(29)$$

我們亦可改寫軌跡和它的導數之方程式，在分離器全長 $z = L$ m，得到

$$X_L = X_o \cos\beta L_m + \frac{X_o}{\beta} \sin\beta L_m + \frac{\eta E \delta V}{W_c^2 V_o} \left(1 - \cos\beta L_m \right)$$

$$X_L' = X_o' \cos\beta L_m + \frac{\eta E_o \delta V}{V_o^2 W_c} \sin\beta L_m - \beta X_o \sin\beta L_m$$

$$\delta V = V_o - V_{zo}$$

其中 X_o 和 X_o' 都是在 $z = 0$ 時的位置和斜率。

我們上面的關係得出他們的轉換矩陣

$$\begin{pmatrix} X_L \\ X_L' \end{pmatrix} = \begin{pmatrix} \cos\beta L_m & L_m \left(\frac{\sin\beta L_m}{\beta L_m} \right) \\ -\beta \sin\beta L_m & \cos\beta L_m \end{pmatrix} \begin{pmatrix} X_o \\ X_o' \end{pmatrix} + \frac{\delta V}{V_o} \begin{pmatrix} \frac{\eta E}{W_c^2} \left(1 - \cos\beta L_m \right) \\ \frac{\eta E_o}{V_o W_c} \sin\beta L_m \end{pmatrix} \quad \cdots\cdots (30)$$

對於 y 軸，軌跡速度分量平行於磁場，離子在 yz 平面漂移只與 y' 有關，

$$\begin{pmatrix} y_L \\ y_L' \end{pmatrix} = \begin{pmatrix} 1 & L_m \\ 0 & 1 \end{pmatrix} \begin{pmatrix} y_o \\ y_o' \end{pmatrix} \quad \cdots\cdots (31)$$

假使我們調節電磁場，而使得特定的離子（質量爲 m_o 速度爲 V_o）沿著軸前進而不偏斜，而質量不同（$m_o \pm \delta m$）的離子在出去時之斜率（用 $\frac{\delta m}{m} = -\frac{\delta V}{2V_o}$）得到

$$X_L' = \frac{1}{2} \frac{\delta m}{m_o} \sin \frac{E_o L_m}{2V_o} \quad \cdots\cdots (32)$$

對於小的 $\frac{E_o L_m}{2V_o}$ 值，亦即分離器能力較小

$$X_L' \approx \frac{\delta m}{m_o} \frac{E_o L_m}{4V_o} \quad \cdots\cdots (33)$$

在漂移距離 L_d 質量爲 $m_o + \delta m$ 的離子，離開中心軸距離爲

$$\triangle X = L_d X_L' + X_L - \frac{\delta m}{m} \frac{E_o L_m}{4V_o} \left(\frac{L_m}{2} + L_d \right) = \frac{1}{2} \frac{\delta m}{m} \beta L_m \left(\frac{L_m}{2} + L_d \right) \quad \cdots\cdots (34)$$

假使 $\frac{\delta m}{m}$ 不遠小於 1，則可用下列等式

$$\triangle X = \left(\sqrt{\frac{m_o}{m_o + \delta m}} - 1 \right) \left\{ L_d \sin \frac{E_o L_m}{2V_o} + L_m \frac{1 - \cos\left(\frac{E_o L_m}{2V_o} \right)}{\frac{E_o L_m}{2V_o}} \right\} \quad \cdots\cdots (35)$$

Annual Report of the Institute of Physics, Academia Sinica, Vol. 12, 1982

安折透鏡(Einzel Lens)

Einzel 透鏡是一種單一電位方式之"離子一光學"元件，各種散焦失眞都很小，由於它能一面聚集一面保持能量不變而廣被採用。這種設備是因爲它的射束輸出與輸入特性在改變加速電壓時均不改變，輸入不影響離子源之能量，輸出進入加速級亦無影響。如圖(九)(a)V_2 可大於或小於 V_1 並且對於中心電極之大部份電壓數值均呈收斂之射束。但若 V_2 與 V_1 反極性，且 V_2/V_1 之比值大於 1/10 時，此一Einzel 透鏡會成爲一反射鏡，將輸入之離子反射。圖十三所示爲一實際離子加速系統，其最左爲離子源，第一爲引極，第二爲安折鏡之中間電極，它與左右構成安折之組合。第三個電極爲一連串電極之組合，稱爲恒電位梯度加速電極，每個單極間電位差都相等。它的輸入與安折組合間之匹配並不甚嚴格。從圖中曲線可以看出離子射束有兩個最大值呈現於靶上，套筒電極(中心電極)上的兩種電壓 2 KV 及 12 KV就是產生兩最大電流值之主要因素。也就是說安折透鏡可以工作於加速或減速兩種區域。本計劃之研究系統即採安折直圓筒形狀之組合，其後離子束即進入無電場區(drift tube)直達到靶。或增加一個 E × B 質量分析級將所需之離子選擇通過再到靶子。工作時安折中心電極與左右兩電極保持相同之位同一步調升降，以保持良好之聚焦情況。安折中心電成爲套筒以防止離子束射穿絕緣體而破壞眞空。

200 KeV 小型加速器之高低壓系統，此一系統爲目前所設計實用系統。

高壓電供給系統一爲了節省空間及重量，本設計採用高週率 20 KH_z 方波，可以配合非常輕巧的 ferrite core 用來升高電壓，祇要鐵心之窗口夠大能夠容納絕緣程度 200 KV 以上之絕緣材料，就可作此用途。故這種絕緣變壓器體積極小。

以上用兩組變壓器即能達 80 KV 4 mA 而對地之絕緣計算的 200KV 強度耐壓。

另一組合供應離子源之電弧電壓，激磁電流，以及 Pd leak 之加熱電流。最後尙須供應 2 — 50 KV 之極電壓。這四種電壓電流均須自零變化至最大，並且都在 200 KV 之電位上工作，故提供此一電力供應之辦法極爲精密，本研究中改良傳統方法可以節省大量之空間及重量，正在逐步解決之中。

眞空系統：離子源處之工作氣體氣壓通常約在 $10^{-5}\ \tau$ 到 $10^{-3}\ \tau$ 之間，若氣壓稍高，在射束之中將產生可觀之中性原子分量，它會影響靶的壽命是應避免的。整個眞空平常應維持在 $10^{-8}\ \tau$ 以上，本系統採用 Ion Pump。由於整個體積不大，故採用 140 升 / 秒之抽氣量者擔任。談到眞空，必須要有耐心及細心之人、經過訓練及經驗的人才適應。故本系統爲自製問題特別多，訓練眞空人才至爲恰當。

冷却系統：在超高電位上離子源之冷却愼防漏電，水氣應極力避免。本系統採用 Freon — 113 冷却，另一端在一水槽中散熱即採雙循環系統散熱。

安　全：整個高壓區做有防護罩，地線多點通地。自動跳開及洩放電裝置，沿控制線途徑上均置會高壓浪潮宣洩間隙，以保障工作人員之安全。

X - ray 之防護：電壓在 90 KV 以上即應避免。

參 考 文 獻

1. Von Engel, A. Ionized Gases (Oxford U-p England 1965).
2. Langmuir. D. B. proc. IRE. 25, 977 1937.
3. Spitzer L. Physics of Fully Jonized Gases (Interscience, New York, 1965), p.3.
4. Pierce, J. R. Theory and Pesign of Elestron Beam 2nd ed. (VON Nostrand, New York 1954).
5. Langmuir I., and D. Blodgett, Phys. Rev 24, 49 (1924).
6. Davisson. G. J. and C. J. Calbick, Phys. Rev. 38, 585(1931); 42, 580(1932).

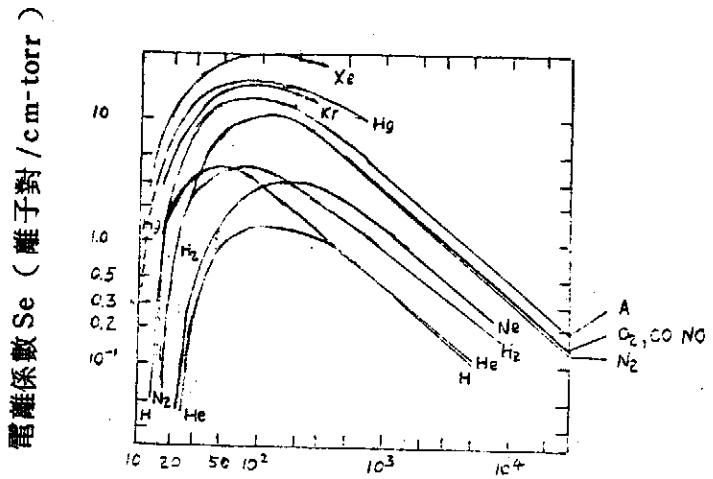
電離係數Se（離子對/cm-torr）
10
1.0
0.5
0.3
0.2
10^{-1}
Xe
Kr
Hg
H_2
Ne
H_2
He
H
A
O_2, CO NO
N_2
N_2
H
He
10
20
50
10^2
10^3
10^4
電子能量We（eV）

圖一

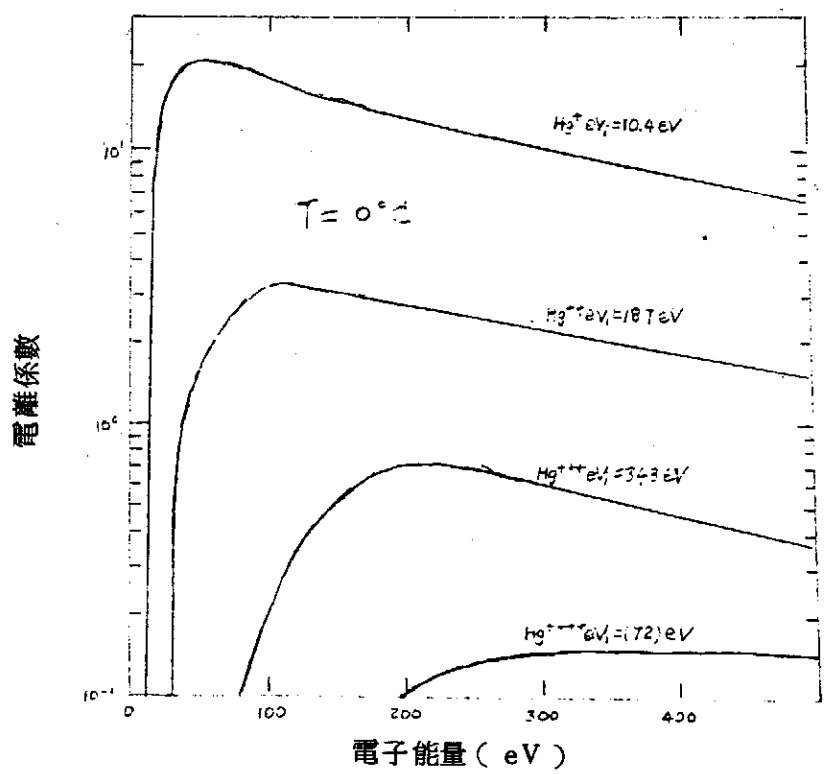
電離係數
10^1
10^0
10^{-1}
H_2^+ eV$_i$=10.4 eV
T= 0°C
Hg^+ eV$_i$=18.7 eV
Hg^{++} eV$_i$=34.3 eV
Hg^{+++} eV$_i$=(72) eV
0
100
200
300
400
電子能量（eV）

圖二

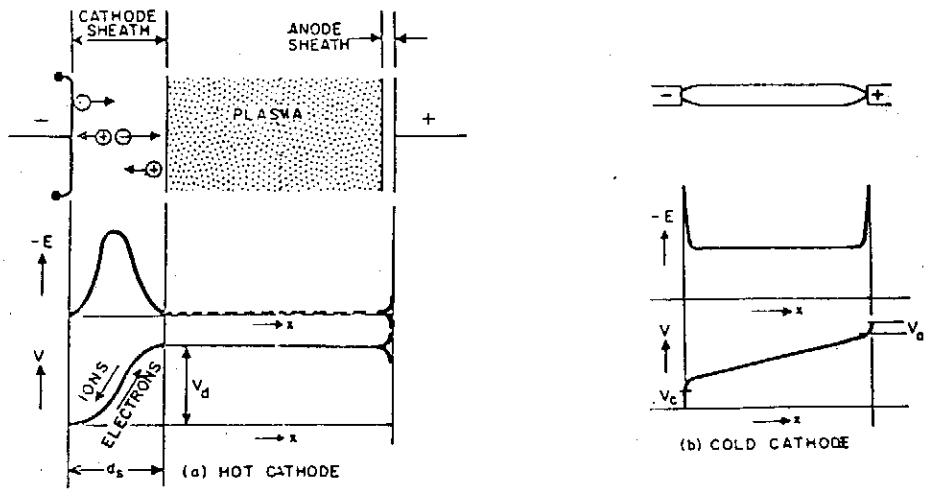
CATHODE SHEATH
ANODE SHEATH
PLASMA
-E
V
IONS
ELECTRONS
V_d
d_s
(a) HOT CATHODE
-E
V
V_a
V_c
(b) COLD CATHODE

圖三

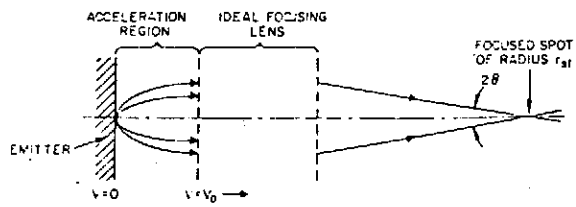
ACCELERATION REGION
IDEAL FOCUSING LENS
FOCUSED SPOT OF RADIUS r_{sf}
2θ
EMITTER
V=0
V=V₀

圖四

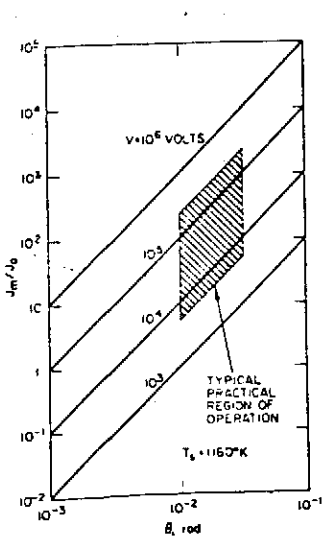
V=10⁶ VOLTS
TYPICAL PRACTICAL REGION OF OPERATION
T_e = 11600°K
J_m/J_0
B, rad

圖五

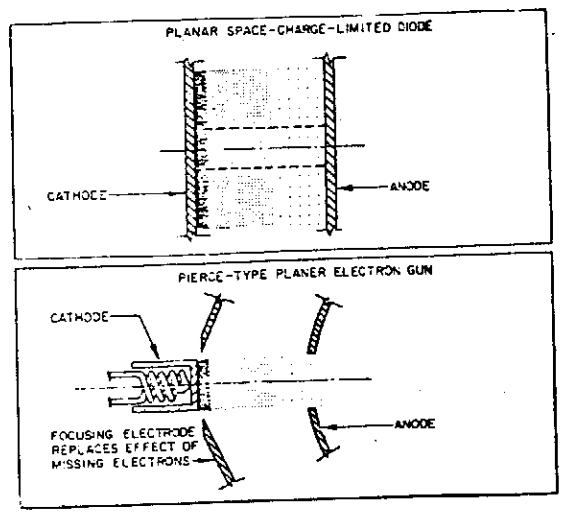
PLANAR SPACE-CHARGE-LIMITED DIODE
CATHODE
ANODE
PIERCE-TYPE PLANER ELECTRON GUN
CATHODE
FOCUSING ELECTRODE REPLACES EFFECT OF MISSING ELECTRONS
ANODE

圖六

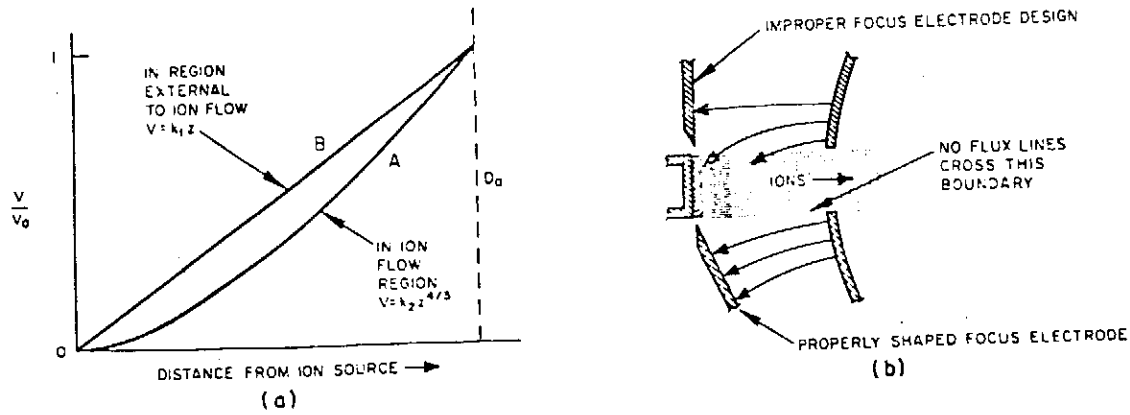
IN REGION EXTERNAL TO ION FLOW
B
A
IN ION FLOW REGION
DISTANCE FROM ION SOURCE
(a)
IMPROPER FOCUS ELECTRODE DESIGN
NO FLUX LINES CROSS THIS BOUNDARY
IONS
PROPERLY SHAPED FOCUS ELECTRODE
(b)

圖 七

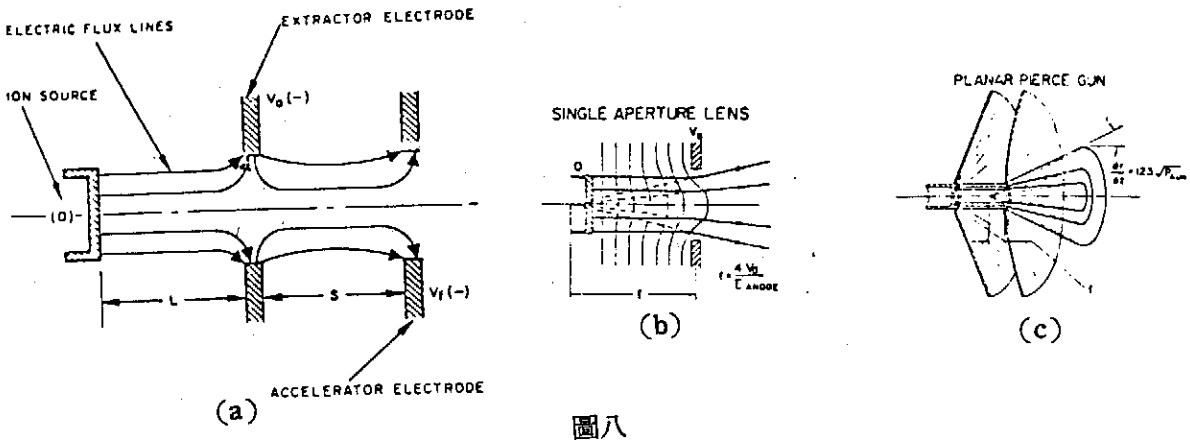
ELECTRIC FLUX LINES
EXTRACTOR ELECTRODE
ION SOURCE
ACCELERATOR ELECTRODE
(a)
SINGLE APERTURE LENS
(b)
PLANAR PIERCE GUN
(c)

圖八

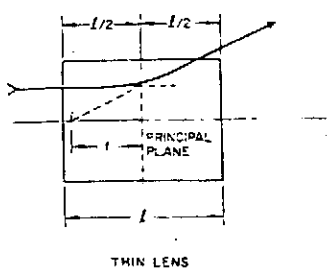
PRINCIPAL PLANE
THIN LENS

圖九

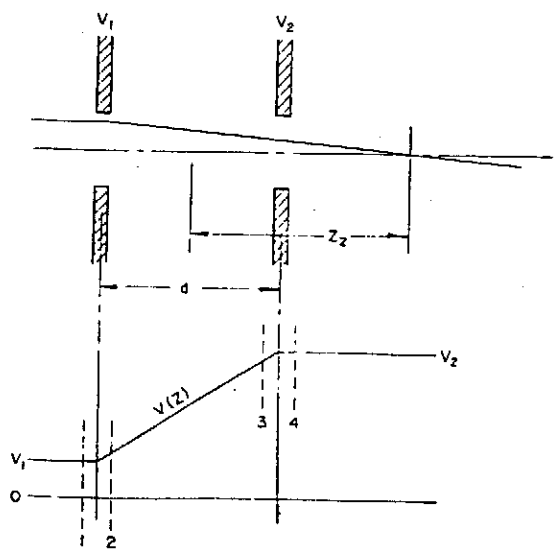
V(z)
1
2
3
4

圖十

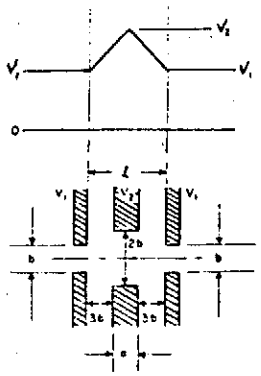

圖十一

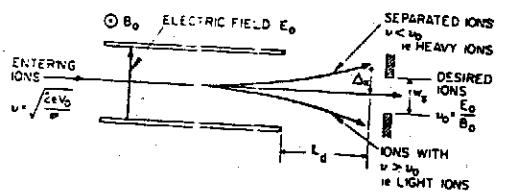
MAGNETIC POLE PIECE
ELECTRIC PLATE
ENTERING IONS

ELECTRIC FIELD E_0
SEPARATED IONS
HEAVY IONS
ENTERING IONS
DESIRED IONS
IONS WITH
LIGHT IONS

圖十二

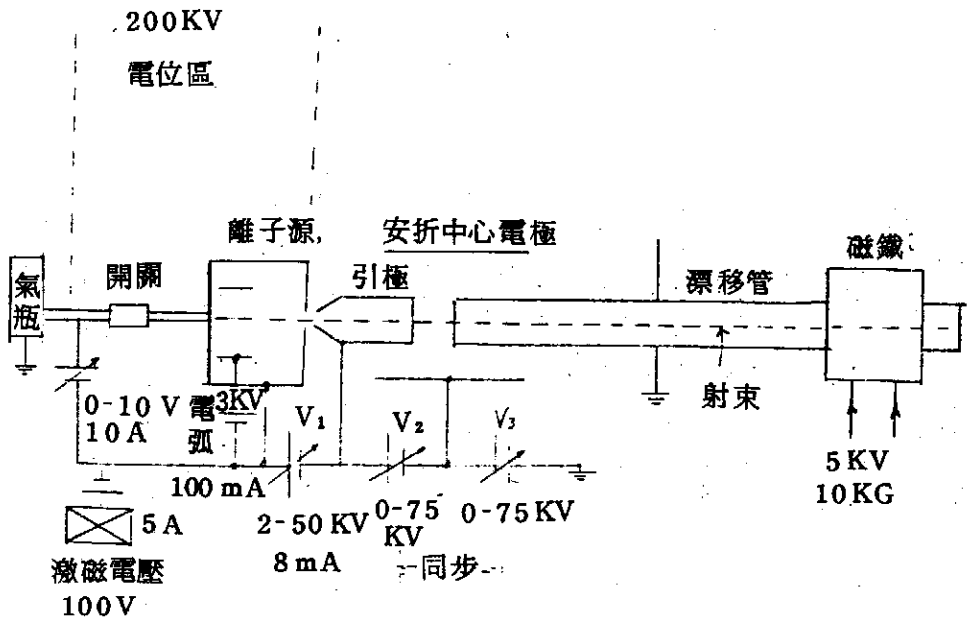
200KV
電位區
離子源
安折中心電極
磁鐵
氣瓶
開關
引極
漂移管
射束
0-10 V 電
10 A
3KV
弧
V_1
V_2
V_3
100 mA
5 A
2-50 KV
8 mA
0-75 KV
0-75 KV
同步
5 KV
10 KG
激磁電壓
100 V

圖十三

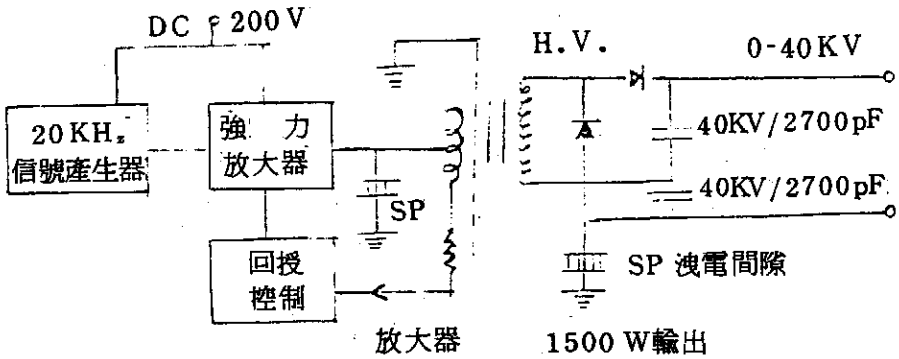
DC 200V
20KHz
信號產生器
強 力
放大器
SP
回授
控制
放大器
H.V.
0-40KV
40KV/2700pF
40KV/2700pF
SP 洩電間隙
1500 W輸出

圖十四

密度層變流通過障礙體受阻的數值研究

黃榮鑑　蔣修德
中央研究院物理研究所

摘　要

本文經由連續方程式、內維一史托克運動方程及密度擴散方程式，利用數值分析以變向隱式法（alternative direction implicit scheme）的差分方法建立數值模式，探討二維密度層變流體通過半橢圓之柱體及半圓柱體等障礙物時背面波之形成及流場流況的變化情形。引生的流場變化分三區（即形成於障礙體上游的阻滯區，形成於障礙體下游之分離區以及上述二區外之場內區）分別加以研討。

結果顯示背面波的形成及發展受流場的密度福祿數F、雷諾數R及障礙體的高寬比ε所影響。F值減小將使分離區的發展受到壓抑，背面波的發展也將加快，容易造成流場的不穩定，並且使阻滯區向上游延伸。ε小的障礙體，分離區不容易形成，背面波的發展也較快，同時流況受R值的影響相當明顯。減小ε及R值，阻滯區的長度將增長，但並不十分明顯，而R值及ε值的增加將促使近分離區的發展，有助於流場的穩定。

壹、緒　言

地球表面的流體如大氣、海洋等，由於受日光的照射及重力的作用，其密度皆隨高度的增加而減小，呈穩定的層變性質。在層變流場中若遭受擾動，由於重力的作用將產生內重力波，如大氣中的山岳波即爲其例之一。當密度層變流體通過一障礙體時，在其前方將形成阻滯區。而在障礙體後方所形成的分離區則將因密度較大之流體的沉降作用而受壓抑，同時在流場中也將由於內重力波的存在，在某些情況下波狀的流線可能發展爲旋螺而呈不穩定。層變流場中由於受重力、慣性力及粘滯力的同時作用而使流場的特性與密度均勻流場不同，層變的情形越明顯其性質的差異也越大。

有關層變流通過障礙物的理論探討，如Hwang（1982）文中所引述，早期以Long的無黏滯性假設的研究最爲卓然。其他學者在這方面的研究也多以此模式爲出發點，較著名的有：Jones（1970）以反轉法（Inverse method）求解層變流體流經一階狀障礙物的流況；Drazin & Moore（1967）以繞射理論（Diffraction Theory）計算流體通過Dipole及垂直薄壁的流況；Miles（1968 a，b

，1968）以變分略解法（Variational Approximation method）求解流體通過各種不同形狀障礙物的流況，並說明其阻力係數及流況穩定之臨界條件。

近期在數值方面，Lin & Apelt（1972）曾考慮粘帶性以計算層變流通過垂直薄壁的流況；Furukawa（1973）計算了層變流體通過三角形障礙物的流況，但在障礙物面上令其旋量（vorticity）爲零，因此不會發生流線分離的情形；Haussling（1977）使用了二種適合芮維一史托克運動方程式的特殊流速分佈以作爲上下游之邊界條件，然後計算橢圓形障礙物的流況，其文中所採用的密度福祿數（Densimetric Froude number）較本文爲大，故流況始終處於穩定狀況（Stable state）之下。而他所謂的旋螺（rotor）尺度甚小，似乎是因流線分離所產生的 bubble ，而非眞正由重力波扭曲過度的流線所產生。此外 Orville（1968）也在三角形障礙物上令其旋量爲零，再加上熱力（Thermodynamic）的考慮來計算與說明雲的生成與發展。

本文由連續方程式、運動方程式及擴散方程式，利用變向隱示法的數值方法以研討二維密度層變流通過半圓形、半橢圓形（包括高橢圓及扁橢圓）柱體時背面波的形成與發展以及流場流態的變化情形。本文爲基本現象之探討模擬氣流通過山脈受阻所發生的效應，對於背面波的發展，片狀雲層越過山脈後的現象，飛航路線的擇定均極具參考價值。

貳、控制方程式

在密度梯度、動力粘滯係數及擴散係數爲常數之二維密度層變平流中，經由波氏近似（Boussinesq Approximation），則控制密度層變流通過障礙體之流場的連續方程式、運動方程式及密度擴散方程式可寫爲：

$$\nabla \cdot \vec{u}' = 0 \tag{1}$$

$$\frac{D\vec{u}'}{Dt'} = \frac{-1}{\rho_0'} \nabla p' + \frac{\rho'}{\rho_0'} \vec{g} + \nu \nabla^2 \vec{u}' \tag{2}$$

$$\frac{D\rho'}{Dt'} = D_m \nabla^2 \rho' \tag{3}$$

式中撇號表示具有因次之變數，$\vec{u}'$ 爲流速，ρ' 爲密度，ρ_0' 爲參考密度，p' 爲壓力及 ν 爲流體的動力黏滯係數，D_m 爲流體的擴散係數。

爲分析方便起見，將(2)式取其旋度以消去其壓力項，並由連續方程式定義流線函數，將流線函數和流速的關係式代入旋量之定義式，則可得旋量方程式及流線函數－旋量關係式爲：

$$\frac{D\vec{\zeta}'}{Dt'} = \frac{1}{\rho_0'} \nabla \times (\rho' \vec{g}') + \nu' \nabla^2 \vec{\zeta}' \tag{4}$$

$$\nabla^2 \phi' = -\zeta' \tag{5}$$

式中 $\vec{\zeta}' = -\nabla \times \vec{u}'$，爲旋量（Vorticity），$\phi'$ 爲流線函數。ϕ' 在不同座標之定義如下：

(1)在扁橢圓柱體中取橢圓座標（ α' ，β' ）與直角座標（ x′ ，y′ ）之關係爲：

$$x' = A' \cosh \alpha' \cos \beta' \quad , \quad y' = A' \sinh \alpha' \sin \beta'$$

則連續方程式(1)可寫成

$$\frac{\partial H' u_{\alpha}'}{\partial \alpha'} + \frac{\partial H' u_{\beta}'}{\partial \beta'} = 0$$

因而定義流函數滿足上式爲

$$u_{\alpha}' = \frac{1}{H'} \frac{\partial \psi'}{\partial \beta'} \quad , \quad u_{\beta}' = -\frac{1}{H'} \frac{\partial \psi'}{\partial \alpha'}$$

式中，A′ 爲橢圓之焦距，$H' = A' (\sinh^2 \alpha' + \sin^2 \beta')^{1/2}$ ，爲座標轉換因子。

(2)在高橢圓柱體中，橢圓座標（ α' ，β' ）與（ x′ ，y′ ）之關係取爲：

$$x' = A' \sinh \alpha' \cos \beta' \quad , \quad y' = A' \cosh \alpha' \sin \beta'$$

則由連續方程式可定義流函數爲

$$u_{\alpha}' = \frac{1}{H'} \frac{\partial \psi'}{\partial \beta'} \quad , \quad u_{\beta}' = -\frac{1}{H'} \frac{\partial \psi'}{\partial \alpha'}$$

座標轉換因子，$H' = A' (\sinh^2 \alpha' + \cos^2 \beta')^{1/2}$ 。

(3)在圓柱體時，取圓柱座標（ γ' ，θ' ）與（ x′ ，y′ ）之關係爲：

$$x' = \gamma' \cos \theta' \quad , \quad y' = \gamma' \sin \theta'$$

則定義流函數 ψ' 爲：

$$u_{\gamma}' = \frac{1}{\gamma'} \frac{\partial \psi'}{\partial \theta'} \quad , \quad u_{\theta}' = -\frac{\partial \psi'}{\partial \gamma'}$$

上列方程式(3)、(4)及(5)式爲探討密度層變流通過障礙體受阻之流場變化的控制方程式，爲簡化數值分析，將控制方程式無因次化。各座標系統之無因次參數定義如下：

(1)扁橢圓柱體障礙物

取橢圓柱體焦距A′，上游遠方之水平流速U′及 $\Delta \rho' = \rho_0' - \rho_a'$ 分別爲特性長度、速度及密度，以定義下列無因次變數：

$$\alpha = \alpha' \quad , \quad \beta = \beta' \quad , \quad t = t' / (A' / U')$$

$$u_{\alpha} = u_{\alpha}' / U' \quad , \quad u_{\beta} = u_{\beta}' / U' \quad , \quad \psi = \psi' / U' A' \qquad (6)$$

$$\zeta = \zeta' / (U' / A') \quad , \quad \rho = (\rho' - \rho_0') / \Delta \rho'$$

經無因次化後，扁橢圓柱體流場之控制方程式可寫爲

$$h^2 \frac{D\zeta}{Dt} = \frac{1}{R} \left(\frac{\partial^2 \zeta}{\partial \alpha^2} + \frac{\partial^2 \zeta}{\partial \beta^2} \right) + \frac{1}{F^2} \left(\cosh \alpha \sin \beta \frac{\partial \rho}{\partial \beta} - \sinh \alpha \cos \beta \frac{\partial \rho}{\partial \alpha} \right) \cdots (7)$$

$$\nabla^2 \psi = -\zeta \qquad (8)$$

$$h^2 \frac{D\rho}{Dt} = \frac{1}{RS_c} \left(\frac{\partial^2 \rho}{\partial \alpha^2} + \frac{\partial^2 \rho}{\partial \beta^2} \right) \qquad (9)$$

式中，$\frac{D}{Dt} = \frac{\partial}{\partial t} + \vec{v} \cdot \nabla$ ，$u_{\alpha} = \frac{1}{h} \frac{\partial \psi}{\partial \beta}$ ，$u_{\beta} = -\frac{1}{h} \frac{\partial \psi}{\partial \alpha}$ ，$h = (\sinh^2 \alpha + \sin^2 \beta)^{1/2}$ ，

$R = U'A' / \nu$ 爲雷諾數（ Reynolds number ），$F^2 = U'^2 / g'A'$ 爲密度福祿數（ densimetric Froude number ）及 $S_c = \nu / D_m$ 爲史密斯數（ Schmidt number ）。

(2)高橢圓柱體障礙物

高橢圓柱體流場中之無因次參數的定義與扁橢圓形障礙物相同，控制方程式經無因次化後可寫爲：

$$h^2 \frac{D\zeta}{Dt} = \frac{1}{R}\left(\frac{\partial^2 \zeta}{\partial \alpha^2} + \frac{\partial^2 \zeta}{\partial \beta^2}\right) + \frac{1}{F^2}\left(\sinh \alpha \sin \beta \frac{\partial \rho}{\partial \alpha} - \cosh \alpha \cos \beta \frac{\partial \rho}{\partial \beta}\right) \tag{10}$$

$$\nabla^2 \phi = -\zeta \tag{11}$$

$$h^2 \frac{D\rho}{Dt} = \frac{1}{RS_c}\left(\frac{\partial^2 \rho}{\partial \alpha^2} + \frac{\partial^2 \rho}{\partial \beta^2}\right) \tag{12}$$

式中，$h = (\sinh^2 \alpha + \cos^2 \beta)^{1/2}$ 。座標（ α ， β ）在扁高橢圓柱體流場之座標如圖一所示。

(3)圓柱體障礙物

層變流通過圓柱體障礙物的流場，取障礙體半徑 a 爲特性長度，各無因次參數之定義爲：

$$r = r' / a \quad , \quad \theta = \theta' \quad , \quad t = t' / (a / U')$$

$$u_r = u_r' / U' \quad , \quad u_\theta = u_\theta' / U' \quad , \quad \phi = \phi' / (U' a') \tag{13}$$

$$\zeta = \zeta' / (U' / a') \quad 及 \quad \rho = (\rho' - \rho_0') / \Delta\rho'$$

將控制方程式(4)、(5)及(3)式無因次化後可寫爲：

$$\frac{D\zeta}{Dt} = \frac{1}{R}\left[\frac{1}{r}\frac{\partial}{\partial r}\left(r \frac{\partial \zeta}{\partial r}\right) + \frac{1}{r^2}\frac{\partial^2 \zeta}{\partial \theta^2}\right] + \frac{1}{F^2}\left(-\cos\theta \frac{\partial \rho}{\partial r} + \frac{\sin\theta}{r}\frac{\partial \rho}{\partial \theta}\right) \tag{14}$$

$$\nabla^2 \phi = -\zeta \tag{15}$$

$$\frac{D\rho}{Dt} = \frac{1}{RS_c}\frac{1}{r}\left[\frac{\partial}{\partial r}\left(r \frac{\partial \rho}{\partial r}\right) + \frac{1}{r}\frac{\partial^2 \rho}{\partial \theta^2}\right] \tag{16}$$

式中，$u_r = \frac{1}{r}\frac{\partial \phi}{\partial \theta}$ ， $u_\theta = -\frac{\partial \phi}{\partial r}$ ， $R = \frac{U'a}{\nu}$ ， $F^2 = \frac{U'^2}{(g'a)}$ 。

基於運算方便，將柱面座標（ r ， θ ）經下列的轉換成直角不等比座標（ α ， β ）。其關係式爲：

$$r = e^{\pi\alpha} \quad , \quad \theta = \pi\beta \tag{17}$$

$$h^2 \frac{D\zeta}{Dt} = \frac{1}{R}\left(\frac{\partial^2 \zeta}{\partial \alpha^2} + \frac{\partial^2 \zeta}{\partial \beta^2}\right) + \frac{h}{F^2}\left(-\cos \pi\beta \frac{\partial \rho}{\partial \alpha} + \sin \pi\beta \frac{\partial \rho}{\partial \beta}\right) \tag{18}$$

$$\frac{\partial^2 \phi}{\partial \alpha^2} + \frac{\partial^2 \phi}{\partial \beta^2} = -h^2 \zeta \tag{19}$$

$$h^2 \frac{D\rho}{Dt} = \frac{1}{RS_c}\left(\frac{\partial^2 \rho}{\partial \alpha^2} + \frac{\partial^2 \rho}{\partial \beta^2}\right) \tag{20}$$

式中，$h=\pi e^{\pi\alpha}$ ，$u_r=\frac{1}{h}\frac{\partial\psi}{\partial\beta}$ 及 $u_\theta=-\frac{1}{h}\frac{\partial\psi}{\partial\alpha}$ 。

參、數值解析

基本方程式經前述之無因次化及座標轉換後，流場之控制方程式(7)～(9)，(10)～(12)及(18)～(20)均具同一形式，可整理歸納爲：

$$h^2\frac{\partial\zeta}{\partial t}+\frac{\partial\psi}{\partial\beta}\frac{\partial\zeta}{\partial\alpha}-\frac{\partial\psi}{\partial\alpha}\frac{\partial\zeta}{\partial\beta}=\frac{1}{R}\left(\frac{\partial^2\zeta}{\partial\alpha^2}+\frac{\partial^2\zeta}{\partial\beta^2}\right)+\frac{1}{F^2}\left(C_1\frac{\partial\rho}{\partial\beta}-C_2\frac{\partial\rho}{\partial\alpha}\right) \quad (21)$$

$$\frac{\partial^2\psi}{\partial\alpha^2}+\frac{\partial^2\psi}{\partial\beta^2}=-h^2\zeta \quad (22)$$

$$h^2\frac{\partial\rho}{\partial t}+\frac{\partial\psi}{\partial\beta}\frac{\partial\rho}{\partial\alpha}-\frac{\partial\psi}{\partial\alpha}\frac{\partial\rho}{\partial\beta}=\frac{1}{RS_c}\left(\frac{\partial^2\rho}{\partial\alpha^2}+\frac{\partial^2\rho}{\partial\beta^2}\right) \quad (23)$$

及 $$u_\alpha=\frac{1}{h}\frac{\partial\psi}{\partial\beta}\ ,\quad u_\beta=-\frac{1}{h}\frac{\partial\psi}{\partial\alpha} \quad (24)$$

式中，當障礙物形狀爲扁橢圓柱體時

$$h=(\sinh^2\alpha+\sin^2\beta)^{1/2}\ ,\ C_1=\cosh\alpha\sin\beta\ ,\ C_2=\sinh\alpha\cos\beta$$

高橢圓柱體時

$$h=(\sinh^2\alpha+\cos^2\beta)^{1/2}\ ,\ C_1=\sinh\alpha\sin\beta\ ,\ C_2=\cosh\alpha\cos\beta$$

圓柱體障礙物時

$$h=\pi e^{\pi\alpha}\ ,\ C_1=h\sin\pi\beta\ ,\ C_2=h\cos\pi\beta$$

以有限差分法求解上述方程式之數值解析，對空間之變化採用中心差分，對時間變化則以前進差分，並運用變向隱式之雙向掃描原則將偏微分方程式化爲差分方程式如下：

$$\frac{h^2}{\Delta t/2}\rho_{i,j}^{n+1}+\frac{\psi_{i+1,j}-\psi_{i-1,j}}{2\Delta\beta}\cdot\frac{\rho_{i,j+1}^{n+1}-\rho_{i,j-1}^{n+1}}{2\Delta\alpha}$$

$$-\frac{1}{RS_c}\left(\frac{\rho_{i,j+1}^{n+1}-2\rho_{i,j}^{n+1}+\rho_{i,j-1}^{n+1}}{\Delta\alpha^2}\right)$$

$$=\frac{\psi_{i,j+1}^{n}-\psi_{i,j-1}^{n}}{2\Delta\alpha}\cdot\frac{\rho_{i+1,j}^{n}-\rho_{i-1,j}^{n}}{2\Delta\beta}+\frac{1}{RS_c}\left(\frac{\rho_{i+1,j}^{n}-2\rho_{i,j}^{n}+\rho_{i-1,j}^{n}}{\Delta\beta^2}\right)$$

$$+\frac{h^2}{\Delta t/2}\rho_{i,j}^{n} \quad (25)$$

$$\frac{h^2}{\Delta t/2}\rho^{n+1}_{i,j} - \frac{\psi^n_{i,j+1}-\psi^n_{i,j-1}}{2\Delta\alpha}\,\frac{\rho^{n+1}_{i+1,j}-\rho^{n+1}_{i-1,j}}{2\Delta\beta} - \frac{1}{RS_c}\left(\frac{\rho^{n+1}_{i+1,j}-2\rho^{n+1}_{i,j}+\rho^{n+1}_{i-1,j}}{\Delta\beta^2}\right)$$
$$= -\frac{\psi^n_{i+1,j}-\psi^n_{i-1,j}}{2\Delta\beta}\,\frac{\rho^n_{i,j+1}-\rho^n_{i,j-1}}{2\Delta\alpha} + \frac{1}{RS_c}\left(\frac{\rho^n_{i,j+1}-2\rho^n_{i,j}+\rho^n_{i,j-1}}{\Delta\alpha^2}\right) + \frac{h^2}{\Delta t/2}\rho^n_{i,j} \tag{26}$$

$$\frac{h^2}{\Delta t/2}\zeta^{n+1}_{i,j} + \frac{\psi^n_{i+1,j}-\psi^n_{i-1,j}}{2\Delta\beta}\,\frac{\zeta^{n+1}_{i,j+1}-\zeta^{n+1}_{i,j-1}}{2\Delta\alpha} - \frac{1}{R}\left(\frac{\zeta^{n+1}_{i,j+1}-2\zeta^{n+1}_{i,j}+\zeta^{n+1}_{i,j-1}}{\Delta\alpha^2}\right)$$
$$= \frac{\psi^n_{i,j+1}-\psi^n_{i,j-1}}{2\Delta\alpha}\,\frac{\zeta^n_{i+1,j}-\zeta^n_{i-1,j}}{2\Delta\beta} + \frac{1}{R}\left(\frac{\zeta^n_{i+1,j}-2\zeta^n_{i,j}+\zeta^n_{i-1,j}}{\Delta\beta^2}\right) + \frac{h^2}{\Delta t/2}\zeta^n_{i,j} + \frac{1}{F^2}\left(-C_2\,\frac{\rho^{n+1}_{i,j+1}-\rho^{n+1}_{i,j-1}}{2\Delta\alpha} + C_1\,\frac{\rho^{n+1}_{i+1,j}-\rho^{n+1}_{i-1,j}}{2\Delta\beta}\right) \tag{27}$$

$$\frac{h^2}{\Delta t/2}\zeta^{n+1}_{i,j} - \frac{\psi^n_{i,j+1}-\psi^n_{i,j-1}}{2\Delta\alpha}\,\frac{\zeta^{n+1}_{i+1,j}-\zeta^{n+1}_{i-1,j}}{2\Delta\beta} - \frac{1}{R}\left(\frac{\zeta^{n+1}_{i,j+1}-2\zeta^{n+1}_{i,j}+\zeta^{n+1}_{i,j-1}}{\Delta\beta^2}\right)$$
$$= -\frac{\psi^n_{i+1,j}-\psi^n_{i-1,j}}{2\Delta\beta}\,\frac{\zeta^n_{i,j+1}-\zeta^n_{i,j-1}}{2\Delta\alpha} + \frac{1}{R}\left(\frac{\zeta^n_{i,j+1}-2\zeta^n_{i,j}+\zeta^n_{i,j-1}}{\Delta\alpha^2}\right) + \frac{h^2}{\Delta t/2}\zeta^n_{i,j} + \frac{1}{F^2}\left(-C_2\,\frac{\rho^{n+1}_{i,j+1}-\rho^{n+1}_{i,j-1}}{2\Delta\alpha} + C_1\,\frac{\rho^{n+1}_{i+1,j}-\rho^{n+1}_{i-1,j}}{2\Delta\beta}\right) \tag{28}$$

$$\psi^{n+1}_{i,j} = \psi^n_{i,j} + \frac{\omega_1}{2(1+m_1^2)}\left[\psi^n_{i,j+1}+\psi^n_{i,j-1}+m_1^2\psi^n_{i+1,j}+m_1^2\psi^{n+1}_{i-1,j} - 2(1+m_1^2)\psi^n_{i,j} + h^2\Delta\alpha^2\zeta^{n+1}_{i,j}\right] \tag{29}$$

$$\psi^{n+1}_{i,j} = \psi^n_{i,j} + \frac{\omega_2}{2(1+m_1^2)}\left[\psi^n_{i+1,j}+\psi^{n+1}_{i-1,j}+m_2^2\psi^n_{i,j+1}+m_2^2\psi^{n+1}_{i,j-1} - 2(1+m_2^2)\psi^n_{i,j} + h^2\Delta\beta^2\zeta^{n+1}_{i,j}\right] \tag{30}$$

$$u_\alpha = (\psi^{n+1}_{i+1,j} - \psi^{n+1}_{i-1,j}) / 2h\Delta\beta$$
$$u_\beta = (\psi^{n+1}_{i,j+1} - \psi^{n+1}_{i,j-1}) / 2h\Delta\alpha \quad (31)$$

上列式中 n 爲時間之增量，i 表 β 向之格點，j 表 α 向之格點。由於擴散及旋量方程式(23)，及(21)皆爲拋物線形方程式，利用變向隱示法採用雙向掃瞄法，將擴散方程式及旋量方程有限差分化，故各有兩式分別爲(25)、(26)、(27)及(28)式。流線函數—旋量關係式(22)爲卜松形方程式，除採用 SOR 方法加速其收斂外，又混合以變向隱示法之概念以雙向掃瞄之，此式經展開後列如(29)及(30)兩式，式中之 ω_1 及 ω_2 爲加速收斂之係數介乎 1 、 2 之間，取其值爲 1.8 。此外，$m_1 = \Delta\beta / \Delta\alpha$ ，$m_2 = \Delta\alpha / \Delta\beta$ ，流速則由(24)式展開得如(31)。

肆、起始條件，邊界條件及數值運算程序

流線函數之起始條件由勢能流(potential flow)決定，密度起始條件爲 $\rho = -\psi$ ，旋量之起使條件除在障礙體表面外，各處皆爲零。

流場之邊界條件如圖一所示，就其邊界位置分別列述如下：

(1)在障礙體表面 ABC 上(對應於橢圓柱體之 α_0 ，圓形柱體之 $\alpha_0 = 0$)，$\psi_{i,1} = 0$ ，$\rho_{i,1} = 0$ ，$(u_\alpha)_{i,1} = 0$ ，表面上之旋量 $\zeta_{i,1}$ 可由 $\psi_{i,2}$ 與 $\psi_{i,3}$ 以泰勒級數分別對 $\psi_{i,1}$ 展開至三次項，化簡得之，即

$$\zeta_{i,1} = -\frac{1}{h^2}\frac{8\psi_{i,2} - \psi_{i,3}}{2\Delta\alpha^2} \quad (32)$$

(2)在二側渠床上，AE及CD (對應於橢圓柱體之 $\beta = 0$ 及 π ，圓形柱體之 $\beta = 0$ 及 1)，$\psi = 0$ ，$\rho = 0$ 及 $\zeta = 0$ 。

(3)在離障礙體無窮遠處FED上， $\alpha \to \infty$ ，$\zeta = 0$ ，密度及流函數皆爲起始條件之數值。

起始條件及邊界條件決定後，控制方程式之求解由下列步驟經數值差分法之方程式寫成電腦程式後，利用高速電子計算機解出。(1)由流函數之拉普拉方程式解出勢能流流場。(2)利用起始條件由擴散方程式(25)與(26)分別對 α 及 β 雙向掃瞄以得出新時段的密度值 ρ^{n+1} 。(3)由(32)式求得在障礙體表面上之旋量，ζ 值。(4)解旋量方程式(27)及(28)分別對 α 及 β 方向雙向掃瞄，加入邊界條件求得新時段的旋量 ζ^{n+1} 。(5)由求得之旋量 ζ^{n+1} 代入流函數—旋量關係式(29)及(30)，利用 SOR 法循序收斂以求得該新時段的流函數 ψ^{n+1} ，收斂之是否完成，則由是滿足下式爲判斷依據。

$$ABS[(\psi^{n+1}_{i,j} - \psi^{n}_{i,j}) / \psi^{n}_{i,j}] \leq 0.005 \quad (33)$$

(6)新時段之速度則由(31)式求得。(7)重複步驟(2)至(6)以求解在各個不同時段流場的變數值。

在(25)～(28)式之運算中，其係數矩陣除主軸及兩側有值外，其餘皆爲零，故可化爲一維矩陣解之。本文對三種形狀的障礙體分別取 $\varepsilon = 0.5$ (半扁橢圓)， 1.0 (半圓形) 及 2.0 (半高橢圓) 的流場進行數值計算。各種形狀障礙體的 α_0 ， $\Delta\beta$ 及 $\Delta\alpha$ 列如下表：

ε	α_{max}	α_0	$\Delta\alpha$	$\Delta\beta$
0.5	5	0.5493	5 / 60	π / 30
1.0	1.6	0	1.6 / 60	1 / 30
2.0	5	0.5493	5 / 60	π / 30

計算中時間增量 Δt 的選取並未固定，其變化如下：

$$\Delta t = \begin{cases} 0.005 & , \quad t = 0 \\ 2 \times \Delta t_f & 0 < t < 0.2 \\ 0.2 & t > 0.2 \end{cases}$$

式中 Δt_f 爲前一時段所用之 Δt 。時間的增量 Δt ，曾取 0.01 、0.02 、0.05 、0.1 及 0.2 比較，發現當 $t > 0.2$ 後以 $\Delta t = 0.2$ 其誤差尙可容忍。

伍、結果與討論

爲印證本文數值模式計算之準確性，將密度福祿數 F 趨近一很大值，以探討密度均勻流體流過一圓柱體障礙物之流場變化。將計算所得結果與 Honji & Taneda (1972) 之實驗結果及 Son & Hanratty (1969) ，Collins & Dennis (1973) 等之數值結果比較以驗證本文數值模式之準確性。圖㈡、圖㈢及圖㈣所示分別爲障礙體表面渦度分佈，分離區長度及分離點位置之比較，結果顯示本文之數值計算所得與前人之實驗和計算結果甚爲吻合。

二維密度層變流通過半橢圓柱體及半圓形柱體受阻的流場分析，經系列數值計算結果，就阻滯區、分離區以及場內區分別研討其發展情形以及密度福祿數 F 、雷諾數 R 和障礙體形狀 ε 對流場產生的影響。

(1)阻滯區

層變流越過一障礙體時，在 F 值較小 (密度層變梯度較大) 的情況下，由於流體所具有的慣性力不足於克服黏滯力及重力，有部分流體儲滯於臨近障礙體的上游方，而不隨主流向下游流動，形成一阻滯區。圖㈤所示爲層變流，$F = 0.48$ 通過半圓柱體時，數值計算所得的流場流線變化情形。在障礙體之上游面形成一阻滯區，下游面形成一近分離區及一遠分離區，場內區之流線則形成波狀變化的背面波。這個現象與實驗所得的流場甚爲吻合。

阻滯區的形成可從流場中渦度分佈的情形加以說明，障礙體表面由於粘滯性所生的負渦度 (順時針方向) 藉擴散項向流場中擴散，而密度梯度項，$\partial\rho / \partial x$ ，在障礙物上游，因流體越過阻礙體時爬升之故，同一高程上右邊流體密度較左邊爲大，因而滋生逆時針方向之正渦度，而使渦度在障礙體上游面產生正渦度之區域而形成阻滯區。阻滯區流體之流速很小，數值計算結果顯示此區內的流速在 10^{-2} 大小次序左右。阻滯區的形成爲密度層變流中的特性之一。F 值小，$\frac{1}{F^2}\frac{\partial\rho}{\partial x}$ 所引生之正渦度自然較强，因而阻滯區比較容易形成。F 值對於阻滯區之形成與發展的影響，可由圖㈥結果顯示。一般而言，F 值小之流場阻滯區較易發生，且阻滯區長度較長，最大分離點 (θ_{max}) 較快發生

，其值亦較F大者爲高，如圖(七)及(八)所示。

阻滯區之形成與發展受R及ε之影響比受F之影響小得多，如圖(九)及(十)所示，R值的增大將使流體的慣性力增大，障礙體表面的負渦度增强，因而影響阻滯區之形成與發展。ε值小的障礙體因其前沿到頂點的距離較長，坡度較緩，$|\partial\rho/\partial x|$較小，因此衍生之正渦度也較弱，阻滯區之分離點較$\varepsilon$值大者爲低，但並不顯著，數值之計算結果示如圖(十一)及(十二)。

(2)分離區

流體通過障礙物後流域突然擴大，部分動能無法立即轉換爲壓能，遂在障礙體下游側引生了流線的分離而形成分離區，在層變流場中，因背面波形成的影響，而有多個分離區的形成。定義緊靠障礙物之分離區爲近區，其餘爲遠區。層變流場中，當流體越過障礙體下降後，在同高程上，右邊流體密度較左邊爲小，因而$\partial\rho/\partial x$引生順時針向之負渦度而壓抑了近分離區的形成，使分離區的時間延後，尺度也小很多，分離點的位置亦較低。

圖(十三)所示爲$\varepsilon=1$的障礙體在不同F及R的流場中分離區的形成與發展情形。在$R=100$及$F=0.6$的算例，$t=8$時近區開始發生，然尺度甚小，孤懸在15°左右而不與底床接觸，此種現象在Haussling（1977）的計算中也曾發生。此近區逐漸增長而在$t=10$時與底床相接，此時一反時針轉動之小漩渦則被鎖在接角處。$t=11$時遠分離區發生，近區則繼續增大；$t=12$時，反時針轉動之小漩渦被大漩渦給消噬。$t=15$時近區之分離點提高至30°，而其遠區之長度則達2.65單位。(b)圖爲$R=100$，$F=0.48$之算例，$t=7$時遠區先發生；$t=11$時近區出現，遠區則繼續增大。若與前算例比較，當可知F小時，其近區之尺度較小，又因遠區發生在內重力波之波峯下，因此可以知道F小時其內重力波之波長較小，振幅較大較易引生遠區。(c)圖爲$R=200$，$F=0.48$之算例，$t=5$時近區發生，孤懸於20°左右，$t=6$時遠區發生，$t=9$時孤懸之近區與底床相接，在接角處有一逆轉之小漩渦。$t=13$時第二遠區發生，此時近區之分離點最高約在37°左右，之後逐漸下降；$t=14$時近區，第一遠區與第二遠區相連成爲一極大的分離區，在第一遠區之下產生另一逆轉之漩渦，除近區分離點下降外，各區普遍成長，而在$t=15$時其成長並未有停止的趨勢，此時相連之分離區到達7.6單位。若與前算例比較可知R值對分離區影響極大，R值大者不僅分離點位置較高，且在發生分離區後又較易連成一極大之分離區。由於分離區發生之位置大略相同，故可知R值對內重力波之波長影響不大。

圖(十四)及(十五)爲分離區的發展受障礙體形狀ε，不同的情形。ε大的障礙體由於形狀突出，較易導致流線的分離；ε小者則較不易引生分離區，但其受層作用的影響且較ε大者爲大。分離點的位置以ε大者較高，分離區長度也較長。另外，ε大的流場由於流體越過障礙體後的沉降力較强，阻礙了遠分離區向上游的擴展，因而遠區的發展以ε小者爲速。

(3)場內區

場內區是指除去阻滯與分離兩區外的流場區域。本區討論背面波之形成與發展、渦度的變化以及障礙體上方之水平流速和渦量等。圖(十六)及圖(十七)分別表示$R=100$，$F=0.6$及$R=200$，$F=0.46$流場流過扁橢圓及圓形柱體時背面形成及流線變化情形。流況的變化由初始條件之勢能流，隨着時間增

加，由於密度層變所產生之旋量作用，使上爬流線之旋量趨向順時針旋轉，而下落流線之旋量趨向反時針旋轉，因而產生背面波。波形流線將隨時間變化的發展而有逐漸扭曲的趨勢。分離區的形成和發展，將吸收場內區之部分動能，而使波形的扭曲再趨緩和。由於流線之扭曲由密度層變所引起，當分離區的形成及發展不足於減緩背面波波形之扭曲，則扭曲區域將形成一旋螺（ rotor ）。有關旋螺之特性詳見 Hwang（ 1982 ）之實驗研究。

背面波之形成與發展受密度層變所影響，F 值小者波形之形成與發展較快，流況較爲不穩定。如上述分離區的存在一方面消耗了主流之部分能量，一方面則加長了流體越過障礙體之後沉降的水平距離，而使 $\partial\rho / \partial x$ 減小而有助於流場的穩定。F 值小者將壓抑分離區之形成和發展，同時其本身的重力浮昇作用也較明顯，使波形流線較易扭曲成不穩定。數值計算的結果顯示 R 值增加將導致分離區的形成，此現象以 ε 小者最爲明顯，ε 小的障礙體較不易引生流線的分離，當 R 值增加形成分離區後，背面波的流線扭曲易趨於穩定；ε 大的障礙體因分離區較易發生所以流況的穩定性受 R 值的影響，不如 ε 小者爲明顯。

圖(六)係將流線與等旋量線畫在一起之情形，圖中顯示旋量爲零之處爲流線之反曲點，圖(七)爲其等密密度線分佈，圖(八)及(九)係對應圖(六)算例層變流通過不同形狀之橢圓柱體，旋量分佈的變化情形。圖中顯示場內區零渦度旋量線的變化，因時間的增加而有所變化，圖(十)爲層變流通過不同橢圓柱體之渦旋量分佈，因而顯見背面波的波長係隨高程及時間的不同而變化。另外由圖中可看出背面波的發展以 F 小時爲速，F 小者旋量之絕對值較大，亦即其流線會有較劇烈之扭曲，此外，旋量爲零之線相隔較近，亦即說明流線之波長較短。

圖(十一)(a)爲由數值計算所繪出在障礙物垂直上方之水平流速隨時間的變化，起始流速值僅有一相對極大（以下簡稱極大）值，在障礙物面上，其值爲 2 ，隨高度增加其流速趨近於 1 。t = 5 時，有二個極大，一個極小。t = 10 時，增爲三個極大，二個極小，t = 15 時，極大極小之數目不變。各極值，除第一極大（自下方算起）外，皆自上方發生後逐漸往下方移動且趨近一固定值，且在此固定值左右跳動。R 值對此水平流速的影響不很顯著，故不加以比較。圖中(六)顯示 F 值小者，其極值個數較多，極值與極值之間距也較小，此外，第一極大也較 F 值大者爲大。因而在層變流受阻的流場中可以看出在障礙體上方有一近似射流的現象發生，其速度隨着密度梯度的增大（ F 值小）而增大。圖(十一)(c)爲障礙體形狀對頂點上方水平向流速的影響。ε 小者因其表面黏滯性的影響較大，最大速度發生的位置較高，其值也較小，流速分佈的振動情形則無顯著的差別。

圖(十二)爲幾個算例在障礙物表面上之旋量大小，折線以下與折線以上之比例尺，爲了較明確的顯示旋量的差異而略有不同。左方顯示阻滯區內之旋量隨 F 之變化較大，停滯點的位置隨 R 、F 之增加而有降低之趨勢。右方分離點似乎不受 F 之影響，分離區內之旋量受 R 值影響較大，唯在接角處所產生之第二漩渦的強度因 F 值減小而加大。在 90° 附近旋量有一極大值，R 值愈大其值愈大，且發生之點較近上游方；F 值愈小其值愈大，且發生之點較近下游。

圖(十三)爲障礙物上的旋量隨時間的變化情形。圖中顯示左側阻滯區內之旋量隨時間增加而減少，停滯點則逐漸降低。90° 左右之極值似隨時間作一漸弱之振盪現象，發生極值之位置則漸向上游移動。

分離區之旋量隨時間漸增，分離點也同樣隨時間昇高。角區之旋量也似乎有一漸弱的振盪現象。

陸、結　　論

本文以有限差分法求解密度層變流通過半橢圓及半圓柱體之流場變化，經由一連串的計算結果，獲致下列之結論：

(1)阻滯區的發展以F爲主要影響因素，R值及ε值的大小，影響並不明顯。阻滯區內之流速很小，約在10^{-2}次序左右，其停滯點隨R值之增加而降低，F值的減小而昇高。阻滯區長度隨F值之增加而減小。

(2)分離區可分爲近區與遠區，F值小者將壓抑分離區的發展，而ε及R值的增加，則有助於近區的形成。遠區的發展則以F小、ε小及R大時發展較速。

(3)背面波的形成與發展受密度層變影響甚大，F值小之流場，其波長較小，波形流線之扭曲較大易於形成旋螺之不穩定流況。R值增加將使流況較趨穩定，ε值小者流況之穩定性受R值影響較大。

(4)障礙體上方的水平流速，其最大流速以F小者較大，發生的位置也較低，振盪也較劇。ε小者的障礙體最大流速較小，流速分佈的振動情形受R及ε值之影響並不顯著。

參考文獻

1. Collins, W. M. & S. C. R. Dennis 1973: Flow past an impulsively started circular cylinder, J. Fluid Mech., Vol. 60, Part 1, 105-127.
2. Drazin, P. G. and D. W. Moore, 1967: Steady two-dimensional flow of fluid of variable density over an obstacle. J. Fluid Mech. 28, 353-370.
3. Furakawa, J. 1973: Numerical experiments of the airflow over mountain. I. Uniform current with constant static stability. J. Meteor. Soc. Japan, 6, 400-418.
4. Haussling, H. J. 1977: Viscos flows of stably stratified fluids over barrier. J. Atmos. Sci. 34, 589-602.
5. Hwang. R. R. & S. W. Jang, 1982: Laboratory study on the two-dimensional flows of stratified fluide over barriers, J. of the Chinese Institute of Engineers, Vol. 5, No.3, pp.13-18.
6. Jones, O. K. 1970: The flow of a stratified fluid over a vertical step, Tellus 12, 481-492.
7. Lin, J. T. and Apelt, C. J. 1972: Stratified flow over a vertical barrier, Lecture Notes in Physics, 19, 176-183.
8. Long, R. R. 1953-1955: Some aspects of the flow of stratified fluids. I. II. III., Tellus 5, 42-48; 6, 97-115; 7, 341-357.
9. Miles, J. W. 1968-1969: Lee waves in a stratified flow. Part I. II. III. IV., J. Fluid Mech. 32, 547-567; 33, 803-814; 35, 481-496; 35, 497-525.
10. Orville, H. D. 1968: Ambient with effects on the initiation and development of cumulus clouds over mountain, J. Atmos. Sci. 25, 385-403.

11. Son, J. S. & T. J. Hanratty 1969: Numerical solution of flow around a cylinder, J. Fluid Mech., Vol. 35, Part 2, 369-386.
12. Turner, J. S. 1973: Buoyant Effects in Fluids, Cambridge Press.
13. Yih. C. S. 1980: Stratified Flows, Academic Press.

NUMERICAL COMPUTATION ON VISCOUS FLOW OF STABLY STRATIFIED FLUIDS OVER OBSTACLES

Robert R. Hwang and S. D. Chiang

Numerical techniques of ADI method for integrating the time-dependent Navier-Stokes equations, which have proven useful in the study of homogeneous viscous flows, have been extended in this study to investigate the flows of stably stratified viscous fluids over a ridge of semi-elliptical cylinder of infinite length with the different ratio of height to half-width of the obstacle. Various properties of the flow field and the characteristics of the lee waves formulated are investigated.

Results show that the stratification tends to encourage the development of overturning flow regions on the upstream slope (blocking effect) and downstream from the ridge. Lee waves produced for viscous flows of stratified fluid past over obstacles depend on the internal Froude number and the Reynolds number of the flow, and the aspect ratio (i.e. the ratio of height to half-width) of the obstacle to some extent. The existences of upstream influence and the flow seperation induced by the obstacle have a great effect on the development of the lee-wave field for cases of small value of internal Froude number

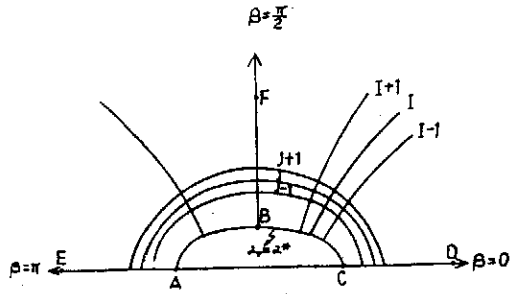

(a)扁橢圓座標

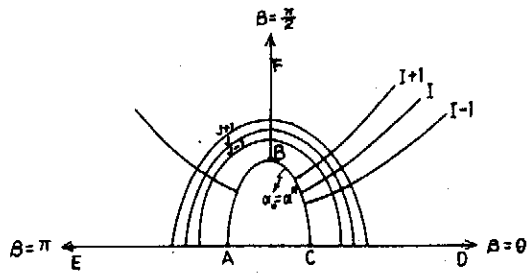

(b)高橢圓座標

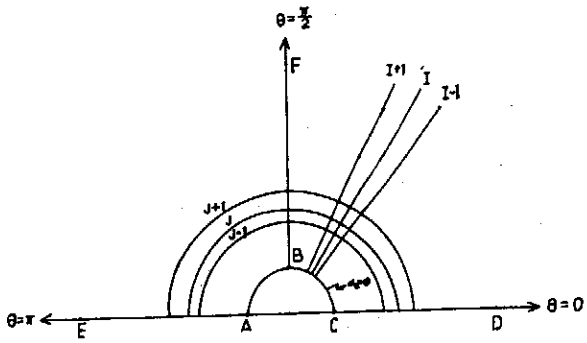

(c)極座標

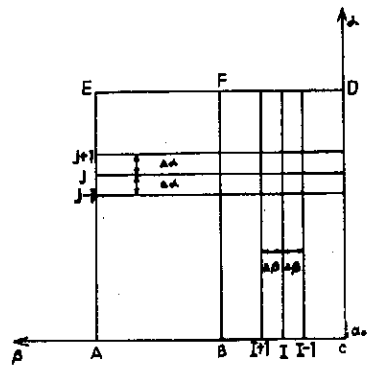

(d)轉換後座標 (a)、(b)、(c)經轉換後均轉換爲(d)

圖一 座標轉換示意圖

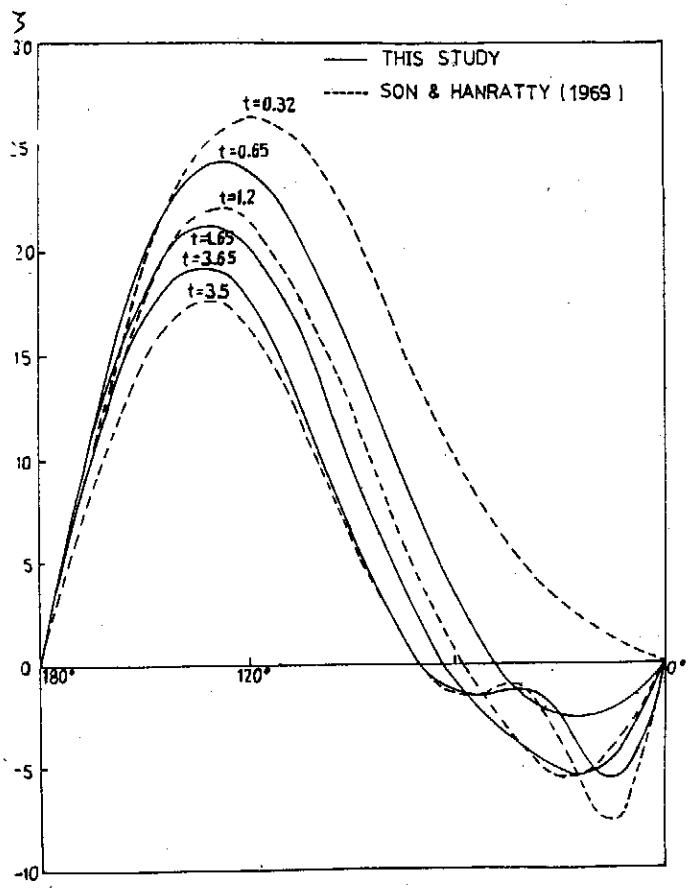

圖二、表面張力之比較 $\epsilon = 1.0$ 、$R = 100$

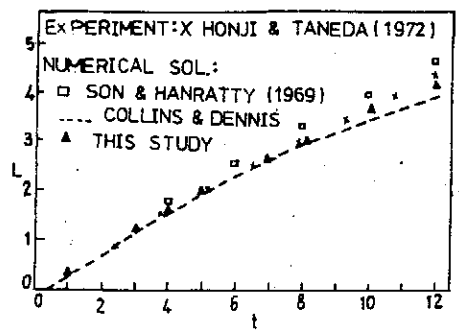

圖三、分離區長度之比較 $\epsilon = 1.0$ 、$R = 100$

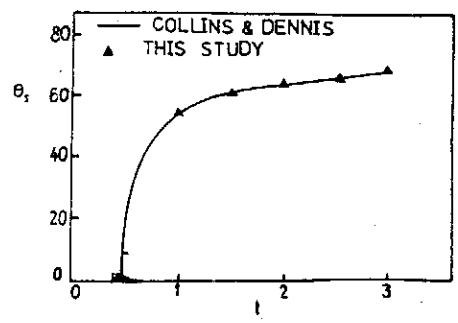

圖四、分離點之比較 $\epsilon = 1.0$ 、$R = 100$

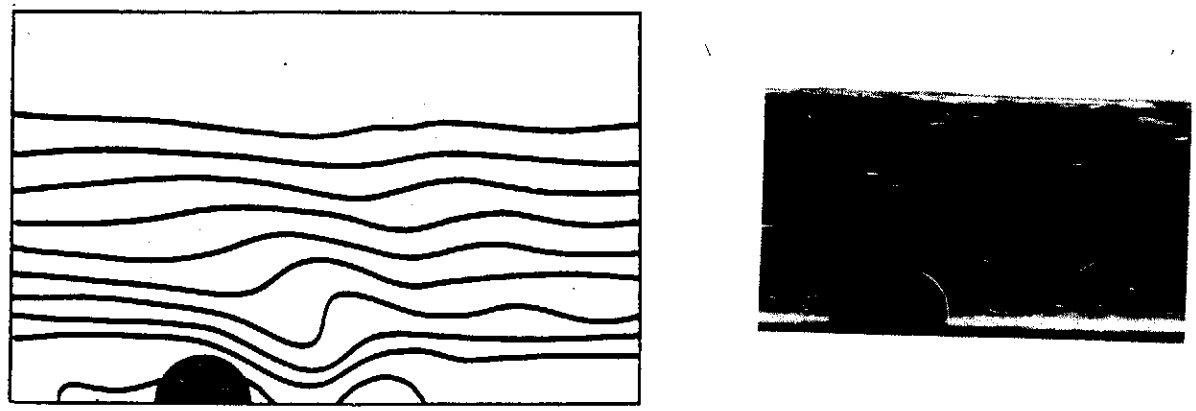

圖五　密度管變流通過障礙體的流況示意

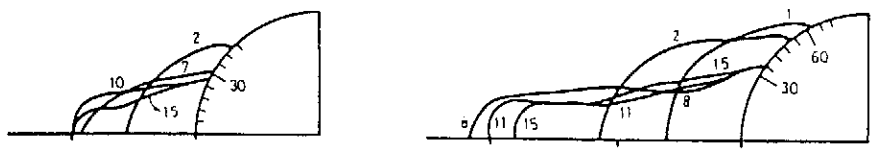

(a) R=100 F=0.60　　(b) R=100 F=0.48

圖六　阻滯區之形成與發展

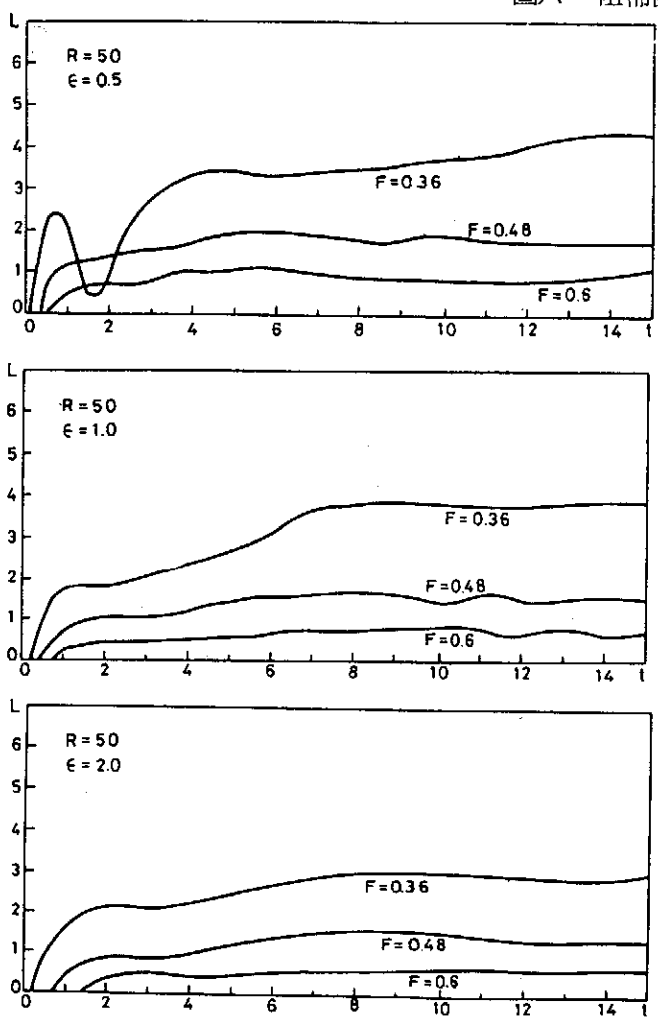

圖七　阻滯區長度受F值之影響

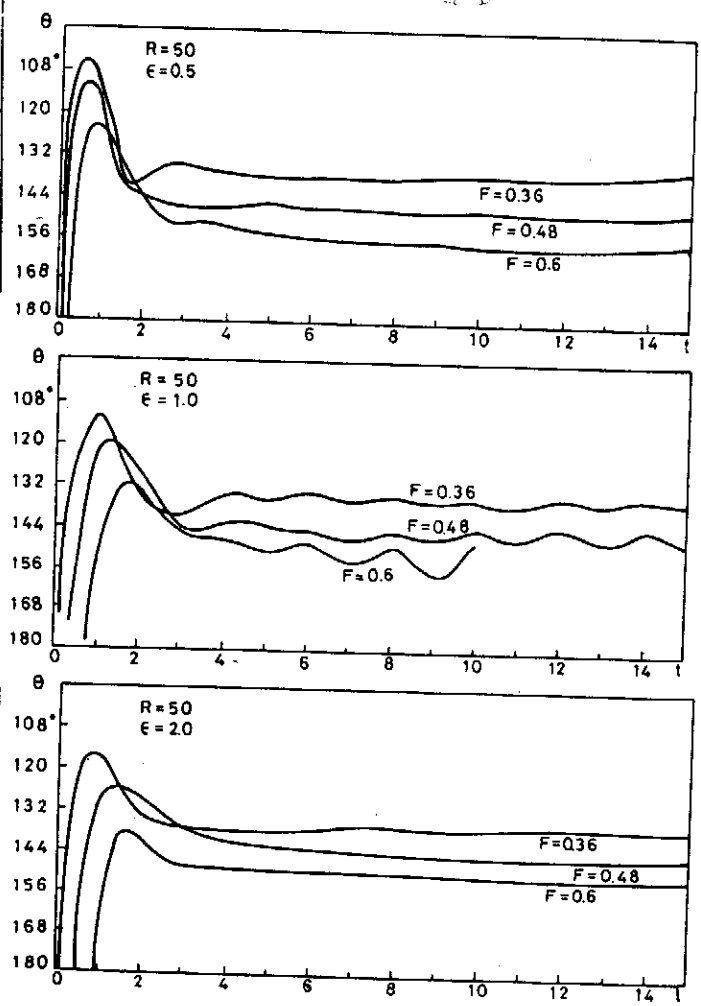

圖八　阻滯區分離點受F值之影響

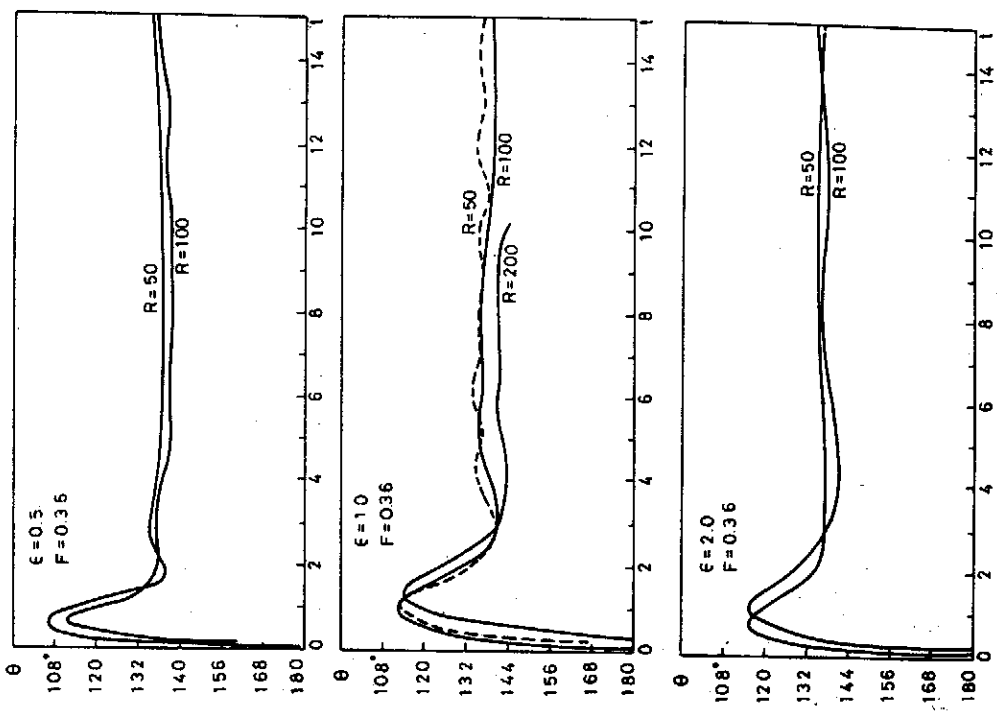

圖十　阻滯區分離點受 R 值之影響

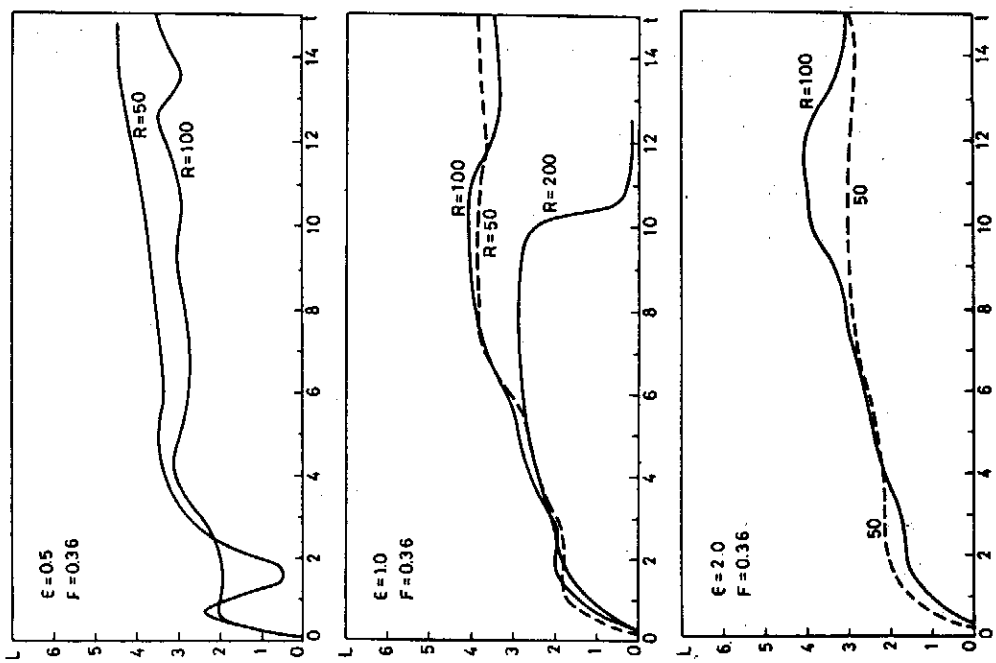

圖九　阻滯區長度受 R 值之影響

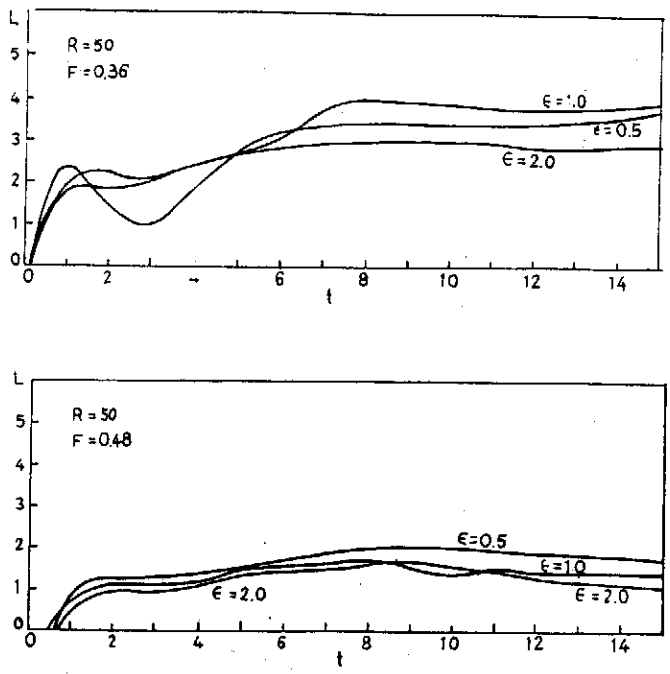

圖十一　阻滯區長度受障礙體形狀之影響

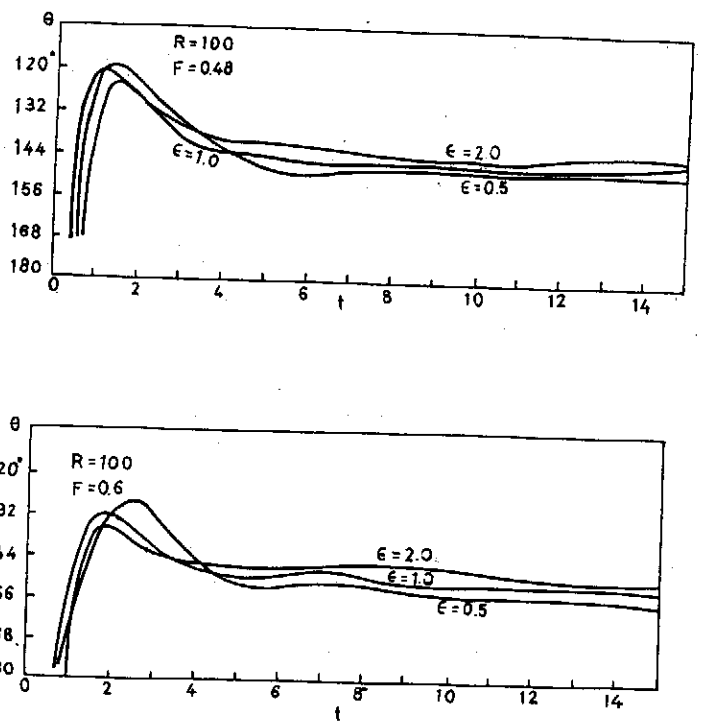

圖十二　阻滯區分離點受障礙體形狀之影響

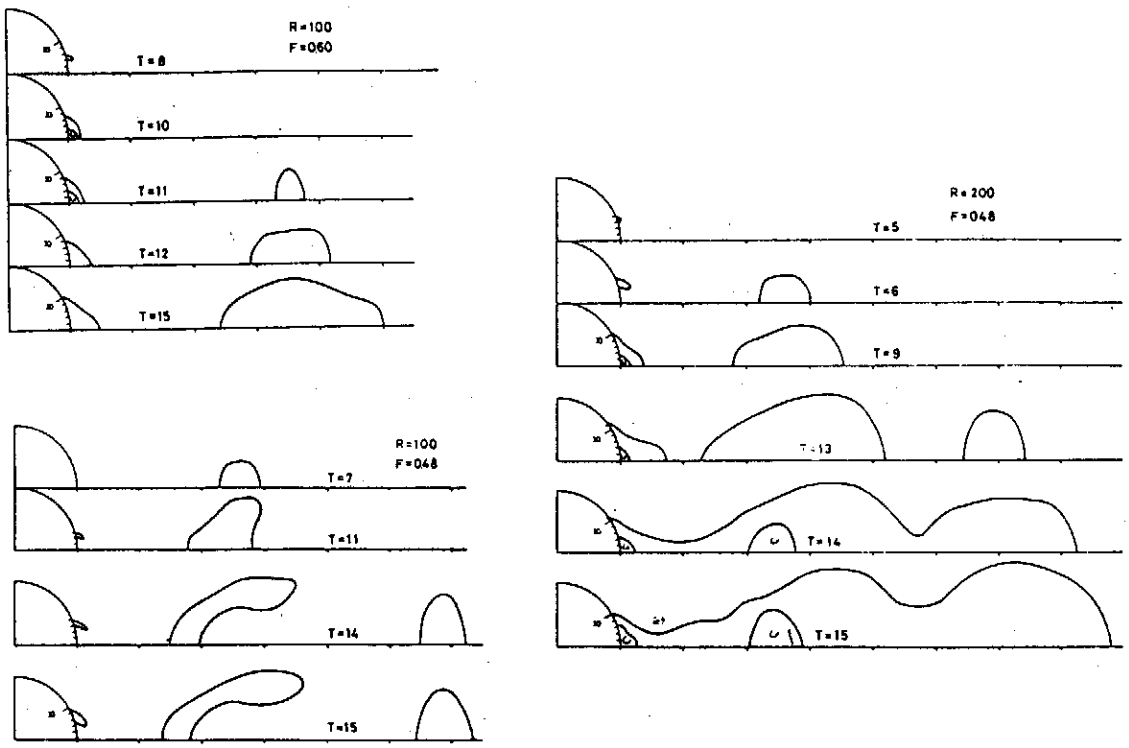

圖　分離區之比較

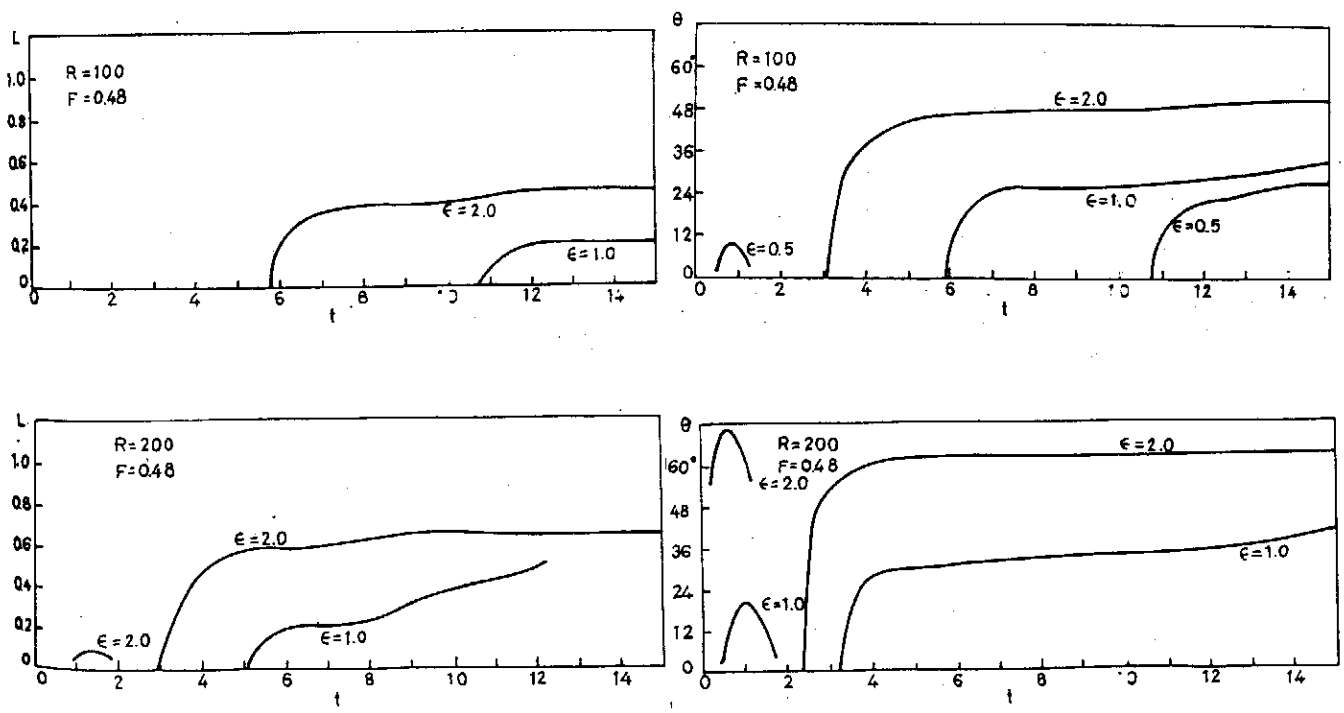

圖十四　分離區長度受障礙體形狀之影響

圖十五　分離區分離點受障礙體形狀之影響

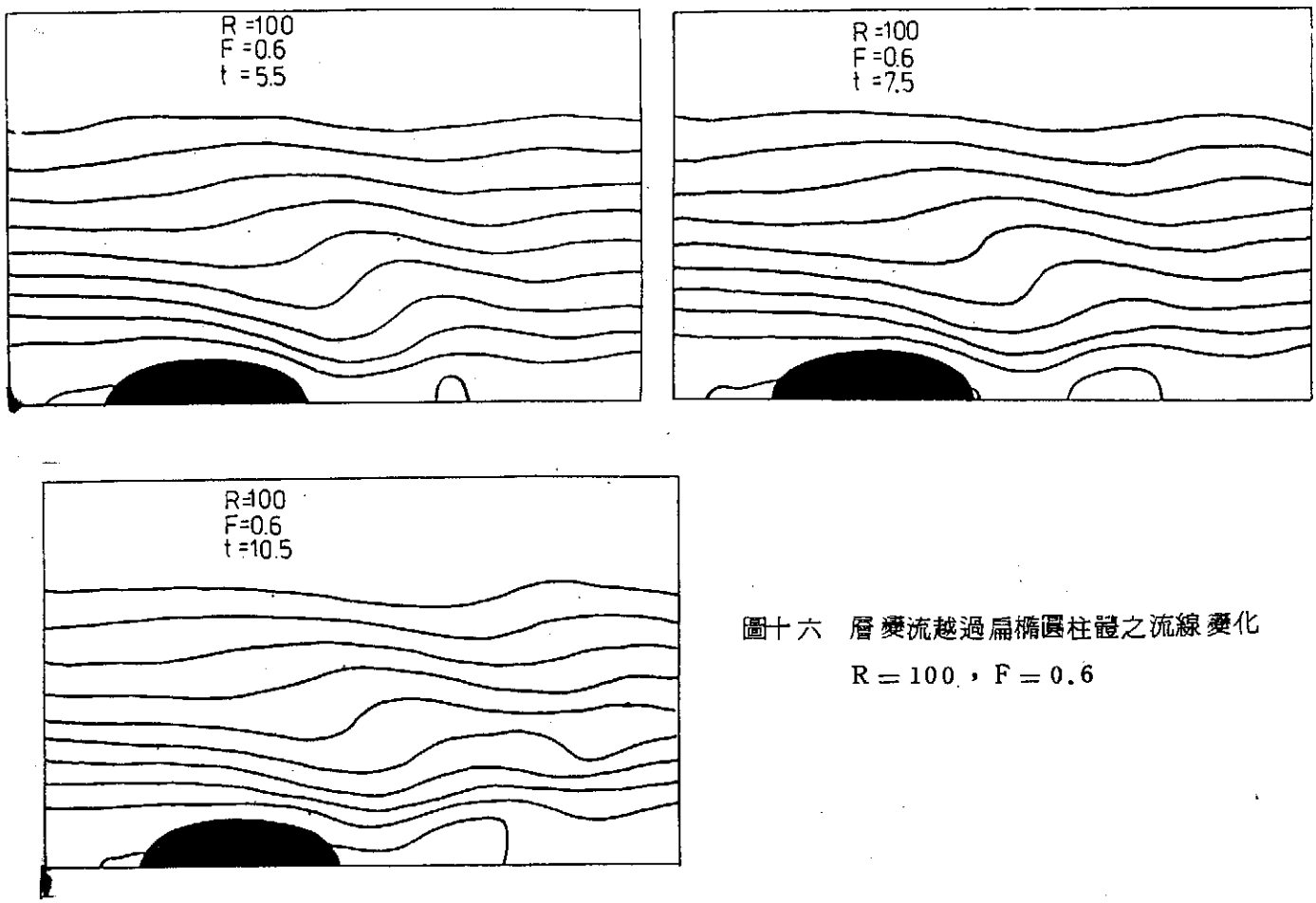

圖十六　層變流越過扁橢圓柱體之流線變化
R = 100 , F = 0.6

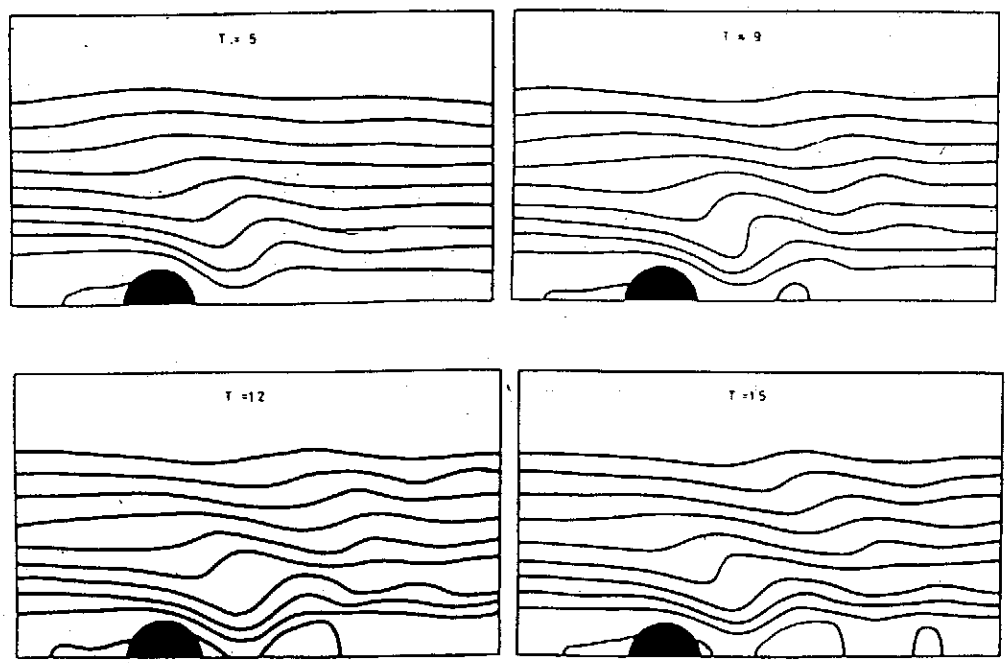

圖十七　層變流越過圓柱體之流線變化
R = 100 , F = 0.48

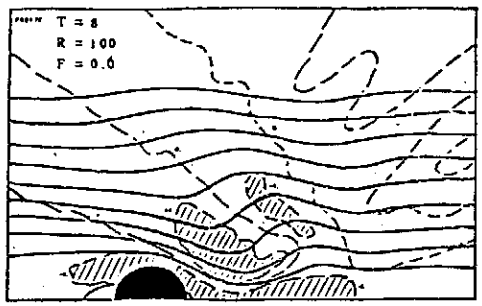

圖十八　渦旋量與流線之關係

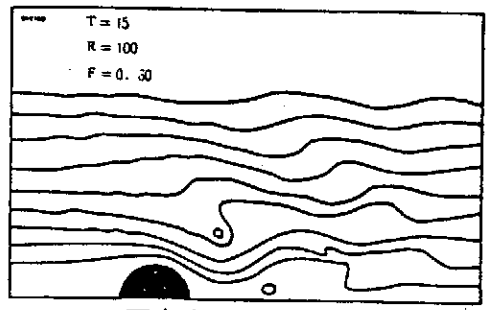

圖十九　等密度線圖

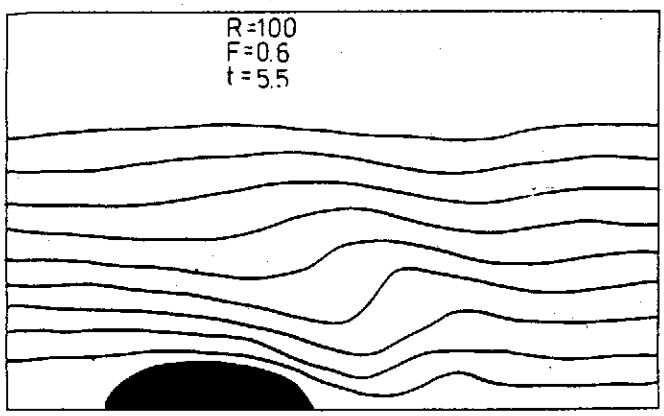

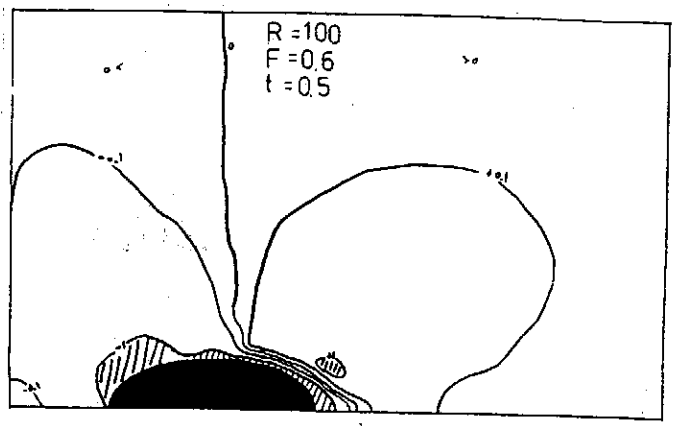

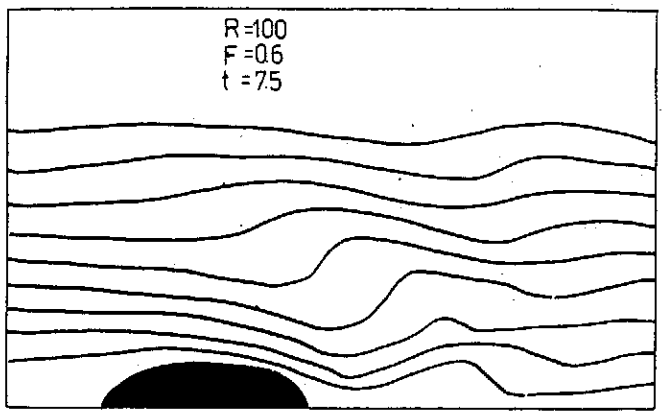

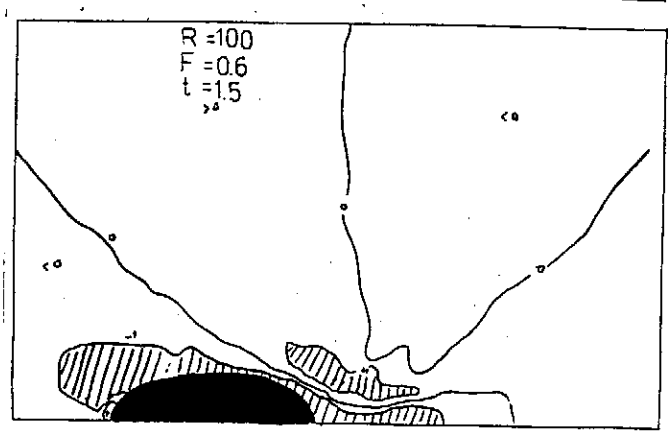

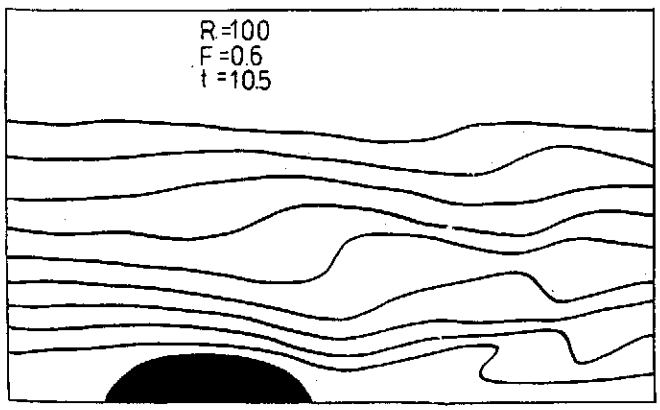

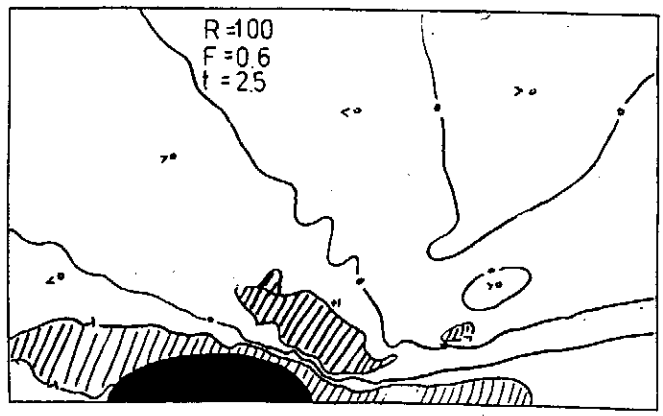

圖二十　相對應於圖十六流場之等密度線變化

圖二十一　相對應於圖十六流場之渦旋量變化

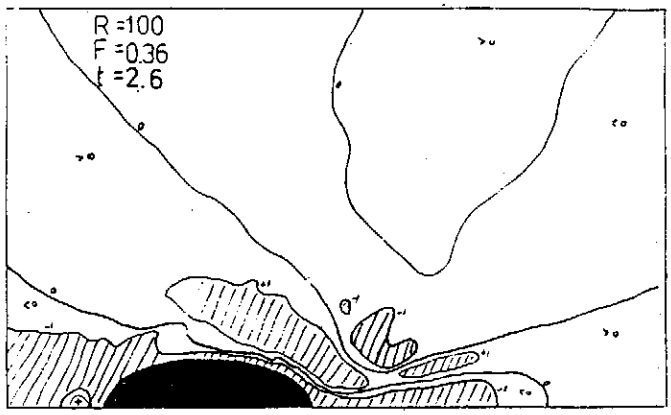

(a)

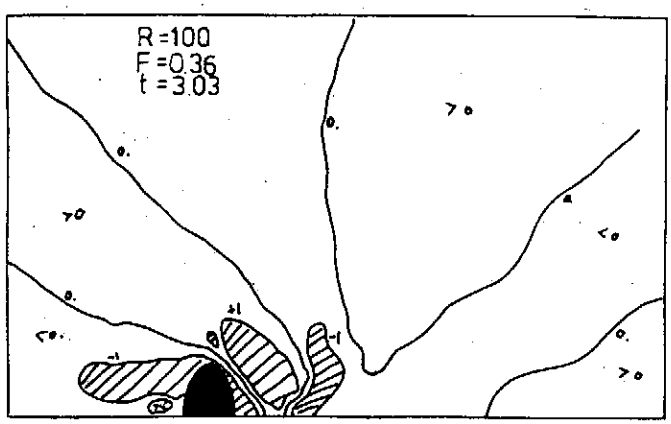

(b)

圖二十二　不同形狀之橢圓柱體流場之渦旋量分佈

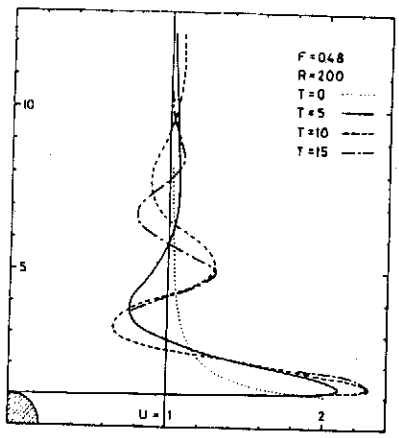

(a)

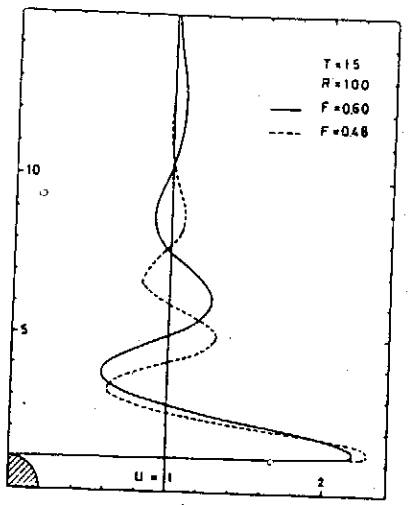

(b)

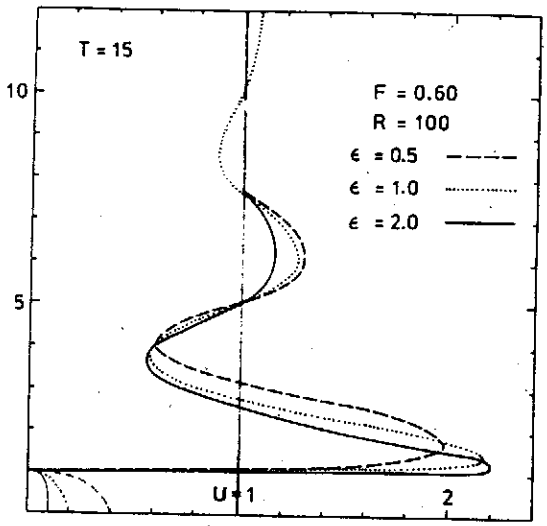

(c)

圖二十三　障礙體頂點上方水平流度之分佈

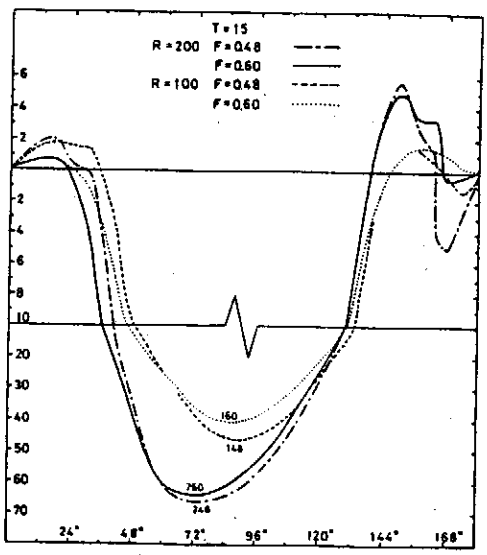

圖二十四　障礙體表面渦旋量之比較，$\epsilon = 1$

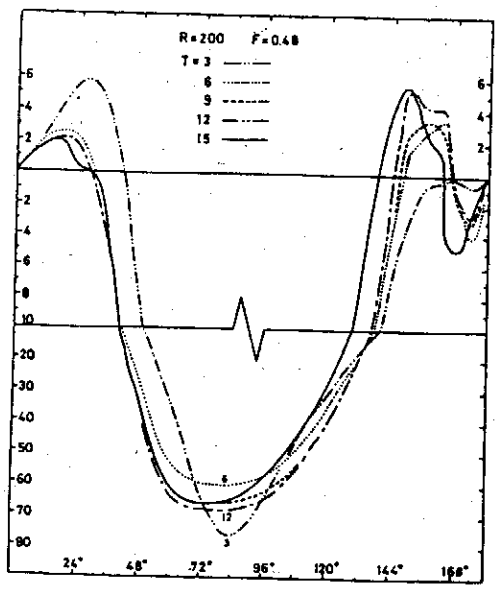

圖二十五　表面渦旋量隨時間之變化，$\epsilon = 1$

垂直浮昇射流在靜止密度層變水域中之浮昇與混合研究

蔡 西 銘

中原大學土木水利工程系

黃榮鑑 王德忠

中央研究院物理研究所

ABSTRACT

The use of submerge outfalls to return sewage and heated water into the ocean has been practiced by many coastal cities around the world. The disposal of waste matter through submarine jets subjects to the mechanical effects of the jet momentum and buoyancy. This study is devised to predict the rise and the development of trubulent buoyant jets discharged to quiescent stratified ambients in both of experimental and theoretical approaches.

In the laboratory experiments, a filling salt solution process is designed to generate a linearly density-stratified ambient and a photographic technique is used to trace the development of the flow. Based on the dimensional analysis, the height of rise is obtained in terms of the initial momentum and the buoyancy of jet, and the stratification of the surrounding environment from correlating a substantial series of experimental data of laboratory study. From the experimental results, an integral approach using a variable entrainment coefficient deduced from the incorporation of the mass conservation into the kinetic energy conservation is monitored and works to predict the gross feature of a buoyant jet discharged vertically into stratified ambients numerically. This study is then to obtain a simple formula-form for the jet-rise and the dilution in terms of the discharge configurations at the source and the stratifications of the surrounding environment.

壹、前 言

近年來，由於工業急速發展，都市人口之激增，使得工業及家庭廢水的排除量大增而使原有之廢水處理廠不敷應用，處理廠的擴建又因其他因素的影響使得擴建速度無法與廢水排除量的增加速度相配合。從工程觀點而言，將這些廢水充分處理，自屬可能，然所費甚鉅，即使先進國家亦難採行，於是，對於濱海城市，如何利用廣大的海洋水域來幫助稀釋及淨化廢水，已成爲各國環境流體力學家們

竭力研究之項目，多年來研究的結果均一致認爲如能把污水處理廠與海洋放流的措施組合起來，對於污水的排除與環境污染的控制將是一個有效而經濟的系統。

典型的海洋放流措施爲包括一延伸入海的管路，廢水經此管道到達另一端之出水口。放流出水口多設在海面下40～60公尺左右。經初級或二級處理之廢水沿管路到達另一端之出水口排入海域，藉排放的動量與周遭海水混合而逐漸稀釋。雖然有些人反對海洋放流，反對理由是會污染海洋。但是，如果海洋放流口設計得當，使排除後污水在海域中充分的稀釋及控制其浮昇之高度，則海洋放流是不會造成污染問題的。故海洋放流問題之探討，不僅具有學術性亦具有實用性。

由於日照的影響，將使海水在深度方向產生密度的變化，使海洋水域成一密度層變的關係。當污水上昇並與周遭海水混合時，因受這層變影響，將使其停滯於水面下某一層，而無法達到海面。此經由放流管多孔放流口排除污水之力學特性與浮昇射流之流場相似，因此瞭解浮昇射流在密度層變水域中之擴散與混合特性，對於海洋放流之設計是相當需要的。

根據驅動力量之性質，射流可分爲三類：

1. 動量射流（Moment Jet）：射流與環境水域之密度相似，驅動力量主要來自射流的啟始動量。
2. 浮流（Plume）：浮流之啟始動量甚微，驅動力量主要來自射流與環境水域之密度或溫度差異所產生之浮力。
3. 浮昇射流（Buoyant Jet）：兼具啟始動量與浮力作用之射流。

射流理論之探討，始於Albertson等氏[1]對均勻環境水域之研究，由純動量射流之實驗顯示，二維及三維軸對稱射流之橫斷面速度分佈極近似高氏分佈，其捲增係數經測定分別爲$\alpha_{j_2}=0.068$及$\alpha_r=0.057$；在純浮流的實驗中，Rouse等氏[2]發現捲增係數亦爲一常數，其在二維及三維軸對稱射流之值分別爲$\alpha_{p_2}=0.16$及$\alpha_{pr}=0.085$，且發現橫斷面密度差亦呈高氏分佈，其與速度分佈間存在一散佈比（spreading ratio）λ之關係，亦經Fan and Brooks二氏[3]分別取定爲$\lambda_2=0.9$及$\lambda_r=1.16$；浮昇射流之理論探討以Morton等氏[4]爲先驅，隨後Abraham氏[5]，Fan氏[6]及Fan and Brooks二氏[3]等繼之。多數之研究皆對射流之捲增概念作出假設，引用Taylor氏[7]之「捲增速度與射流中心速度成正比」的概念，並假設橫斷面之速度與密度差分佈爲高氏分佈，在Boussineq近似條件下對連續方程，運動方程和浮量方程作斷面積分，得出一常微分方程組，經由起始條件則可求得一些所要之物理量，如軸中心速度、密度差、稀釋率及射流軌跡等等。

由前人實驗可見α_{p_2}較α_{j_2}大二倍以上，α_{pr}較α_{jr}大約45％，因此一浮昇射流從出口附近之似射流演化至最後之似浮流過程中，捲增係數不應爲一不變之常數。在均勻環境水域中，List & Imberger二氏[8]及Kotsovinos & List二氏[9]等從因次分析及實驗之數據推斷，浮昇射流之捲增係數應爲局部密度Froude數的函數，至於，在密度層變的環境水域，有關浮昇射流之擴散與混合特性的研究文獻，甚爲稀少。黃等氏[10]以實驗及理論數值計算，探討垂直二維浮昇射流的擴散性，並導出捲增係數與局部密度Froude數之關係式，又由實驗測得散佈比（λ_2）之值介於1.10與1.40之間，而以1.30居多數，Tsai & Hwang二氏[11]在其對圓形浮昇射流之數值探討中運用動量方程及動能量方程導出捲增係數與局部密度Froude數成一線性關係，Fan and Brooks二氏[3]在其數值分析

中，對於捲增係數假定爲一常數，其實，浮昇射流由流出口附近之似射流至射流寬度擴增，射流中心速度降低至某一程度時的似浮流，捲增係數應擔任一演化性的角色，而假定捲增係數爲一常數，應屬不合理。

黃等式[10]及 Tsai & Hwang 二氏[11]導出密度層變環境水域中，二維及圓形浮昇射流的捲增係數應包含兩部份，分別是與紊流特性有關的捲增量α_1，及由浮昇效應引起的捲增量α_2，但α_1逕取前人對均勻環境水域的實驗值$\alpha_{js}=0.068$及$\alpha_{jr}=0.057$似有待商榷。本文嘗試以質量、動量、動能量及浮量守恒，利用斷面積分法，設定速度與密度差剖面呈高氏分佈，由捲增觀念導出一常微分方程組以探討一垂直浮昇射流排入密度層變的環境水域中的一些特性。而與紊流特性有關的捲增量α_1則經由實驗測出其浮昇高度，配合理論之分析反覆運算以定出。利用因次分析的方法尋出浮昇高度及停滯點稀釋率與其它變數之關係，由實驗結果及理論之分析分別求得二維及圓形射流浮昇高度及停滯點之稀釋率與射流排放條件和水域層變因子之關係式，便以供工程設計應用之參考。

貳、基本假設與理論基礎

基本假設如下：

1. 流場流體爲非壓縮性流體。
2. 環境水域之密度爲線性層變者。
3. 射流斷面的速度及密度差分佈近似於常態分佈。
4. 射流爲定常態完全發展之紊流。
5. 採Boussinesq近似法　即流場中局部密度與參考密度之差異量甚小，在浮量中，此差異量予以保留，而在慣性量中則予捨棄。

由上述基本假設，則密度層變流中浮昇射流流場之控制方程式可寫爲：

$$\frac{\partial}{\partial x}(uy^a)+\frac{\partial}{\partial y}(vy^a)=0 \quad \cdots\cdots(1)$$

$$\frac{\partial}{\partial x}(u^2y^a)+\frac{\partial}{\partial y}(uvy^a)=\frac{\rho_2-\overline{\rho}}{\rho_1}gy^a+\frac{1}{\rho_1}\frac{\partial}{\partial y}(\tau_{xy}y^a) \quad \cdots\cdots(2)$$

$$\frac{\partial}{\partial x}(u(\rho_1-\overline{\rho})y^a)+\frac{\partial}{\partial y}(v(\rho_1-\overline{\rho})y^a)=\frac{\partial}{\partial y}(y^a(\overline{v'\rho'})) \quad \cdots\cdots(3)$$

式中，若爲二維浮昇射流時，$a=0$；若爲三維軸對稱浮昇射流時，$a=1$，$y=r$。其中$\overline{u}$及$\overline{v}$爲x－向及y－（或r－）向之時間平均速度，v'及ρ'分別爲速度和密度對時間平均量之變量，ρ_1爲射流放流口處環境水域之密度，ζ_a爲環境水域流體密度，$\overline{\rho}$爲任何點之時間平均局部流體速度。g爲重力加速度。(2)式中之剪應力（τ_{xy}）爲雷諾玆剪應力定義如下：

$$\tau_{xy}=-\rho\overline{u'v'} \quad \cdots\cdots(4)$$

將上述(1)，(2)及(3)式對射流斷面積分可得射流質量通率、動量通率及浮量通率方程式如下：

$$\frac{d}{dx}\left[\int_0^\infty 2u(\pi y)^a dy\right] = 2(\pi b_u)^a V_e \quad \cdots\cdots(5)$$

$$\frac{d}{dx}\left[\int_0^\infty 2u^2(\pi y)^a dy\right] = \int_0^\infty 2g\frac{\rho_a-\overline{\rho}}{\rho_1}(\pi y)^a dy \quad \cdots\cdots(6)$$

$$\frac{d}{dx}\left[\int_0^\infty 2(\rho_1-\overline{\rho})u(\pi y)^a dy\right] = 2(\pi b_u)^a(\rho_1-\rho_2)V_e \quad \cdots\cdots(7)$$

式中 b_u 爲速度剖面特性長度，V_e 爲捲增速度。

對於捲增速度 V_e，吾人採用 Taylor 氏 [7] 之假設，亦即捲增速度與射流中心速度成正比。

$$V_e = \alpha \overline{U}_m \quad \cdots\cdots(8)$$

式中 α 爲捲增係數，$\overline{U}_m$ 爲射流中心速度，基於假設及射流的實驗結果證實，射流斷面的速度及密度差分佈近似於常態分佈，因此令

$$u(x,y) = \overline{U}_m(x)\exp(-y^2/b_u^2) \quad \cdots\cdots(9)$$

$$\rho_a(x) - \overline{\rho}(x,y) = (\rho_a(x)-\rho_m(x))\exp(-y^2/b_d^2) \quad \cdots\cdots(10)$$

式中，若爲三維軸對稱浮昇射流時，$y=r$，$u(x,y)$ 及 $\overline{\rho}(x,y)$ 分別爲流場速度及密度，$\overline{U}_m(x)=u(x,0)$，$\rho_m(x)=\rho(x,0)$ 分別爲射流中心速度及中心密度，b_d 爲密度差剖面特性長度，同時定義散佈比 $\lambda = b_d(x)/b_u(x)$ 爲一常數。

將(8)—(10)三式及散佈比之定義代入(5)—(7)式，則可導出密度層變水域中浮昇射流之基本控制方程組如下：

$$\frac{d}{dx}(b_u^{a+1}\overline{U}_m) = 2(\sqrt{\pi})^{a-1}\alpha b_u^a \overline{U}_m \quad \cdots\cdots(11)$$

$$\frac{d}{dx}(b_u^{a+1}\overline{U}_m^2) = (\sqrt{2}\lambda b_u)^{a+1} g\frac{\rho_a-\rho_m}{\rho_1} \quad \cdots\cdots(12)$$

$$\frac{d}{dx}(b_u^{a+1}\overline{U}_m(\rho_a-\rho_m)) = \left(\frac{\sqrt{1+\lambda^2}}{\lambda}\right)^{a+1} b_u^{a+1}\overline{U}_m\frac{d\rho_a}{dx} \quad \cdots\cdots(13)$$

式中 $d\rho_a/dx$ 爲環境水域之密度梯度。

(11)—(13)式亦可化爲：

$$b_u\frac{d\overline{U}_m}{dx} + (2^a\overline{U}_m)\frac{db_u}{dx} = 2(\sqrt{\pi})^{a-1}\alpha\overline{U}_m \quad \cdots\cdots(14)$$

$$(2^{1-a}b_u\overline{U}_m)\frac{d\overline{U}_m}{dx} + \overline{U}_m^2\frac{db_u}{dx} = (\sqrt{2})^{1-a}(\lambda)^{a+1}b_u g\frac{\rho_a-\rho_m}{\rho_1} \quad \cdots\cdots(15)$$

$$(b_u(\rho_a-\rho_m))\frac{d\overline{U}_m}{dx} + (2^a\overline{U}_m(\rho_a-\rho_m))\frac{db_u}{dx} + (b_u\overline{U}_m)\frac{d(\rho_a-\rho_m)}{dx}$$

$$= \left(\frac{\sqrt{1+\lambda^2}}{\lambda}\right)^{a+1} b_u\overline{U}_m\frac{d\rho_a}{dx} \quad \cdots\cdots(16)$$

由上式基本控制方程組可知其所涉及之變數計有五個，即 b_u，$\overline{U}_m$，$(\rho_a-\rho_m)$，α 及 λ，而方程式只有三個，若已知捲增係數 α 及散佈比 λ，配合邊界條件，則可解得射流各斷面之中心速度 $\overline{U}_m$，中心密度 ρ_m 及速度剖面特性長度 b_u 等物理量之關係。

如上所述捲增係數爲利用捲增概念探討浮昇射流的重要參數，對於浮昇射流的捲增係數，若直接給予一通用常數，則顯然與實際情況不符，本文由動能量之守恒進行探討，將(4)式代入(2)式遍乘 u，並對射流斷面予以積分以得動能量之關係式：

$$\frac{de(x)}{dx}=\int_0^\infty guy^a\frac{\rho_a-\overline{\rho}}{\rho_1}dy-\int_0^\infty\frac{1}{\rho_1}y^a(-\rho\overline{u'v'})\frac{\partial u}{\partial y}dy \quad\cdots\cdots(17)$$

式中 $e(x)=\frac{1}{2}\int_0^\infty u^3y^a\,dy$ 爲動能量通率。(17) 式中之最後一項爲射流中由於紊流的產生所損失的能量。而一般對雷諾玆剪應力之處理亦假設其具動力相似性且與射流中心速度 $\overline{U}_m$ 有如下之關係：

$$-\rho\overline{u'v'}=\rho_1\overline{U}_m^2h(y/b_u) \quad\cdots\cdots(18)$$

式中 $h(y/b_u)$ 爲雷諾玆剪應力之分佈函數，由下段之推導，可知其與捲增係數存在一簡單之關係。

將 (18) 式代入 (17) 式，則 (17) 式可化爲：

$$\frac{d}{dx}(\overline{U}_m^3b_u^{a+1})=2\left(\frac{\sqrt{3}\lambda b_u}{\sqrt{1+\lambda^2}}\right)^{a+1}g\overline{U}_m\frac{\rho_a-\rho_m}{\rho_1}+4(\sqrt{3})^{a+1}(\sqrt{\pi})^{a-1}\overline{U}_m^3b_u^aI \quad\cdots\cdots(19)$$

式中 $I=\int_0^\infty 2\eta^{a+1}e^{-\eta^2}h(\eta)d\eta$；$\eta=y/b_u$

由 (12) 式與 (19) 式的關係可得：

$$\frac{d}{dx}(\overline{U}_mb_u^{a+1})=2\left[\left(\sqrt{\frac{\lambda^2(2\lambda^2-1)}{1+\lambda^2}}\,b_u\right)^{a+1}g\frac{\rho_a-\rho_m}{\zeta_1\overline{U}_m}\right.$$
$$\left.-2(\sqrt{3})^{a+1}(\sqrt{\pi})^{a-1}\overline{U}_mb_u^aI\right] \quad\cdots\cdots(20)$$

比較 (11) 式及 (20) 式可得捲增係數

$$\alpha=\alpha_1+\alpha_2/F_L^2 \quad\cdots\cdots(21)$$

式中 $F_L=\frac{\overline{U}_m}{\sqrt{\frac{\rho_a-\rho_m}{\rho_1}gb_u}}$ 爲沿軸心之局部密度 Froude 數，常數 $\alpha_1=-2(\sqrt{3})^{a+1}I$ 及

$$\alpha_2=\left(\sqrt{\frac{\lambda^2(2\lambda^2-1)}{1+\lambda^2}}\right)^{a+1}(\sqrt{\pi})^{1-a}$$

由 (21) 式得知，對浮昇射流而言，其捲增係數不爲一常數，而係與反局部密度 Froude 數成線性關係，式中 α_1 爲與紊流特性有關之積分參數，α_2 爲浮昇作用之影響因子。

叁、數值解析與因次分析

3－1 數值解析

控制密度層變環境水域浮昇射流的基本方程組如(14)－(16)式所述，若給定捲增係數α及散佈比λ，配合邊界條件，則可進行數值演算。

在均勻環境水域中，Kotsovinos 氏[12]對二維浮昇射流實驗證明散佈比與驅動力性質無關，即不論是在動量射流或純浮流中，散佈比保持常數。List & Imberger 二氏[8]則由因次分析推定λ值應爲局部密度Froude數及該點對射流出口之張角的函數。至於密度層變環境水域中之λ值，研究文獻甚少，黃等式[10]曾以二維之浮昇射流實驗測定λ值，發現其值甚爲紛亂，多介於1.10至1.40之間，而以1.30居多數，無法尋出其與各參數間之關係。Fox 氏[13]以數值試驗發現，λ值對於捲增量之影響遠小於α_1值。至於三維之圓形射流，Hirst 氏[14]認爲在純浮流範圍，$\lambda_p = 1.16$，在動量射流範圍，$\lambda_j = 1.11$，惟於動量射流，由於其局部密度Froude 數較大，λ值對於計算各物理量之影響甚小，因此，不論純浮流或動量射流，可據以選定$\lambda = 1.16$進行演算。

對於捲增量的計算，由(21)式知，捲增係數應包括兩項，其一爲與紊流特性有關之積分參數α_1，另一爲浮昇作用之影響因子α_2。若散佈比λ值已知，則α_2即可求算。而由紊流特性引起的捲增係數α_1迄今尚無定論，因α_1與積分參數I有關故必須先知道雷諾玆剪應力分佈函數h(η)方能得知，然而有關密度層變水域中浮昇射流之h(η)函數迄今尚無足夠資料可得。黃等氏[10]曾以理論推導發現，α_1僅與h(η)及速度剖面分佈函數有關，因此據以推定α_1值可純粹由動量之作用決定，而與浮量無關。Albertson 等氏[1]在均勻環境水域中，對純動量射流所作的實驗中求得二維浮昇射流$\alpha_1 = 0.068$，而三維圓形浮昇射流$\alpha_1 = 0.057$。以均勻環境水域測得之捲增係數用於密度層變環境水域似有待商榷，故α_1值之決定，實有必要另以實驗測出其浮昇高度，再配合理論之分析決定之。

數值之計算如散佈比λ及與紊流特性有關之捲增係數α_1爲已知時，則控制密度層變環境水域之垂直浮昇射流的常微分方程組，只要輸入啟始條件，如射流出口之尺寸b_o，啟始速度U_o，射流出口密度ρ_o，射流出口處環境水域密度ρ_1及環境水域密度梯度$d\rho_a/dx$，利用Runge－Kutta 階式法作數值分析，經由Hp-3000 電子計算機可解出各斷面有關之物理量的數值計算，及質量通率μ，動量通率m，浮量通率β及稀釋率$\overline{\mu}_T$等如下：

$$\mu(x) = \sqrt{\pi}\,(2\sqrt{\pi})^{-a}\,\overline{U}_m\,b_u^{a+1} \qquad (22)$$

$$m(x) = \sqrt{\frac{\pi}{2}}\,(2\sqrt{2\pi})^{-a}\,\overline{U}_m^2\,b_u^{a+1} \qquad (23)$$

$$\beta(x) = \sqrt{\pi}\,(2\sqrt{\pi})^{-a}\left(\overline{U}_m(\rho_a-\rho_m)\left(\frac{\lambda b_u}{\sqrt{1+\lambda^2}}\right)^{a+1} + \overline{U}_m(\rho_1-\rho_a)b_u^{a+1}\right) \qquad (24)$$

$$\overline{\mu}_T = \frac{\overline{U}_m}{U_o} \left(\frac{b_u}{b_o} \right)^{a+1} \quad \cdots\cdots (25)$$

3－2 因次分析

應用海洋放流措施排放污水，最重要的問題在於控制污染物經放流口排放後與環境水域的調混所能達到的浮昇高度及停滯點的稀釋率。就工程觀點而言，浮昇射流上昇之高度及此停滯點的稀釋率爲工程設計之依據，又爲界定動量射流、浮昇射流及浮流的範圍，乃有必要找出一有效之參數，今以因次分析方法尋出浮昇高度及停滯點稀釋率與其它變數間之關係。

在密度層變環境水域下，浮昇射流同時受到動量及浮量的影響，故浮昇高度X_T與下列參數有關：

$$X_T = f(m_o , \beta_o , g\varepsilon') \quad \cdots\cdots (26)$$

式中$m_o = U_o^2 b_o^{a+1}$：啟始動量通率，$\beta_o = g' U_o b_o^{a+1}$：啟始浮量通率，$\varepsilon'(x)$ 指垂直方向之密度梯度，定義爲$\varepsilon'(x) = -\frac{1}{\rho_1} \frac{d\rho_a}{dx}$ 及 $g' = \frac{\rho_1 - \rho_o}{\rho_1} g$：有效重力加速度。

以因次分析法，可得無因次參數式關係如下：

$$\zeta_T = F_1 (N) \quad \cdots\cdots (27)$$

式中 $\zeta_T = X_T m_o^{(a-4)/4} \beta_o^{(4-a)/6} = \frac{X_T}{b_o} F_o^{(a-4)/3}$ ， $N = m_o^2 \beta_o^{-2} g\varepsilon' = F_o^2 S_o^{-1}$ ，

其中 $F_o = \frac{U_o}{\sqrt{\frac{\Delta\rho_o}{\rho_1} g b_o}}$：啟始密度Froude 數，$S_o = \frac{\Delta\rho_o}{b_o} / (-\frac{d\rho_a}{dx})$：密度層變參數，$\Delta\rho_o$

$= \rho_1 - \rho_0$：啟始密度差。

考慮動量射流的情況下，浮量之作用可忽略不計，則(26)式可改寫如下：

$$h_M = f_1 (m_o , g\varepsilon') \quad \cdots\cdots (28)$$

式中h_M：動量射流的浮昇高度

經因次分析結果可得：

$$h_M \sim (m_o / (g\varepsilon'))^{1/(a+3)} \quad \cdots\cdots (29)$$

考慮浮流的情況下，動量之作用可忽略不計，則(26)式改寫如下：

$$h_B = f_2 (\beta_o , g\varepsilon') \quad \cdots\cdots (30)$$

式中h_B：浮流的浮昇高度

經因次分析結果可得：

$$h_B \sim \beta_o^{1/(3+a)} (g\varepsilon')^{(a-4)/8} \quad \cdots\cdots (31)$$

由(27)式知無因次參數N之定義爲$N = F_o^2 S_o^{-1}$，其物理意義爲啟始密度Froude 數愈大或密度層變參數愈小者，流況愈趨近動量射流，反之則愈趨近浮流。應用此無因次參數N之定義，吾人可得浮昇高度之近似函數關係如下：

$$\zeta_T = d_p N^{(a-4)/8} \quad , N \ll 1 \text{（似浮流）} \quad \cdots\cdots (32)$$

$$\zeta_T = d_j N^{-1/(a+3)} \quad , N \gg 1 \text{（似動量射流）} \quad \cdots\cdots (33)$$

式中 d_p =浮流停滯高度係數，d_j =動量射流停滯高度係數。

同理亦可求得停滯點質量通率關係如下：

$$\overline{\mu}_T = F_2(N) \quad \cdots\cdots (34)$$

式中 $\overline{\mu}_T = \frac{\mu_T}{\mu_o} F_o^{-(a+2)/3}$ ，μ_o：啟始質量通率，$\overline{\mu}_T$：比質量通率之無因次參數，μ_T：停滯點質量通率。

及其近似函數關係如下：

$$\overline{\mu}_T = e_p N^{-(a+4)/8} \quad , N \ll 1 \text{（似浮流）} \quad \cdots\cdots (35)$$

$$\overline{\mu}_T = e_j N^{-(a+2)/12} \quad , N \gg 1 \text{（似動量射流）} \quad \cdots\cdots (36)$$

式中 e_p =浮流稀釋率係數，e_j =動量射流稀釋率係數。

由以上之因次分析得知，浮流、浮昇射流與動量射流之浮昇高度及停滯點之質量通率均爲無因次參數N的函數，由N的定義亦可作爲判別三種流況之有效參數。

四、實驗裝置及過程

密度層變水域中，垂直二維浮昇射流的實驗裝置如圖一所示。實驗水槽（$178^{cm} \times 20^{cm} \times 85^{cm}$）爲壓克力水槽，其中央下端有一矩形控制盒（$20^{cm} \times 19.5^{cm} \times 9.5^{cm}$），水流由定頭抽水機在管路中經流量計後導入控制盒，由控制盒上方一寬 2^{mm} 隙縫射入填製密度層變之實驗水槽，而水槽兩端各設置一溢流槽排除水槽內之溢流水量以維持實驗水槽中之水位高度，水槽上、下各置光箱一個，以 Nikon F2 照相機置於試驗斷面之前攝取流場之變化。實驗過程以不同濃度之鹽水，由底層填加，每層 5^{cm} 由下而上，預先決定密度層變梯度，填加不同含鹽量的鹽水計16層，而鹽水密度 ρ 與含鹽量 S_a 間之換算係採用 Knudsen 氏的簡易公式

$$\rho = 1 + (-0.093 + 0.8149 S_a - 0.000482 S_a^2 + 0.0000068 S_a^3) \times 10^{-3}$$

式中 S_a 爲每千克溶液含鹽之克數。水槽中鹽水之填加約需時6小時完成，填妥之鹽水，由於各層間的密度差異，在不受擾動下，因分子運動的作用，將導致上下層間密度差的漸趨緩和，其時間約需24～36小時，水槽中之水域將呈線性分佈的密度層變，實驗前以電導計由上而下測得各高程之電導度與標準鹽水溶液電導度與密度曲線之關係，可得水槽中之水域密度變化情形，其結果顯示，密度變化呈線性分佈，如圖二。將經處理後比重介於1.00～1.05，直徑0.05～0.5^{mm} 之白色微小顆粒緩緩撒入通過射口之平面，由於顆粒之大小不同，遂可懸浮在各層面中，俟顆粒呈現靜止狀態，便可開始進行實驗，開啟閥門，決定流量，光箱之光源使得經處理後之微小顆粒清晰可見，若以ASA 400膠捲，f.11 速度½ sec 則流場之變化軌跡可由照相機攝取。部份流場相片如圖三、圖四所示。而實驗數據如表一。

密度層變水域中，垂直圓形浮昇射流的實驗裝置如圖一所示。實驗水槽（ $90^{cm} \times 90^{cm} \times 50^{cm}$ ）爲壓克力方形水槽，其上緣四週設有溢流槽，可供溢水排除，上端置一光箱，下端中央處設有活動射口，係由高 3.2^{cm} 之壓克力螺絲構成，螺絲上緣鑽有垂直小孔，隨實驗之需要可抽換不同螺絲而得到不同口徑之射口。實驗過程與二維射流時相同，實驗水槽計分爲 10 層，每層 5^{cm} 分別填加不同密度之鹽水，填加及導致上、下層間密度差趨緩和時間與二維射流時間相同，實驗前以電導計量測結果顯示其水槽中之水域密度層變亦呈線性分佈，如圖五所示，將經處理後之白色微小顆粒撒入通過射口之平面，俟顆粒呈靜止狀態後，將水源打入定水頭裝置，俟水流穩定後，便可開始進行實驗，打開水閥由流量測定處可得啟始流量，而其流場之變化軌跡可由照相機攝取。部份流場相片如圖六、圖七所示，實驗數據如表二。圖八所示爲浮昇高度與時間變化的關係。當開啟閥門後，照相機每隔十秒拍照一張，一分半後關閉閥門，由圖顯示，射流已進入穩定狀態，此時，浮昇高度變異的範圍甚小，而浮昇高度之認定，本文係取進入穩定狀態後各點之平均值。

伍、結果與討論

本文基本假設係假設射流爲完全發展之紊流，然而射流伊始，靠起始動量使周遭靜止流體與射流產生混合及對流作用，流況成長層（ Zone of Flow Establishment ）於焉成立，在此層內，紊流混合層沿射流中心軸逐漸成長，最後吞沒勢心層，而變成流況完全建立層（ Zone of Established Flow ），如圖九所示。故實驗數據必須針對流況成長層作適當之修正才能與數值解作比較。本文二維及三維軸對稱修正值分別依 Fan and Brooks 二氏 [3] 及 Daily and Harleman 二氏 [16] 建議，其流況成長層長度分別爲射口寬度的 5.2 倍及射口直徑的 7 倍。

參閱圖九，假設原始射流出口 O′ 與修正射流出口 O 之間浮力效應可忽略，則沿射流進行方向，其動量應守恒。

$$\int_0^{\infty} 2\rho u^2 (\pi y)^2 dy = \rho U_o^2 (\frac{\pi}{4} D)^2 D$$

應用動力相似之假設及 Boussinesq 近似法可得

$$b_o = \sqrt{\frac{2}{\pi}} \quad (\frac{\sqrt{\pi}}{2})^2 D$$

式中 b_o：修正後之啟始速度剖面特性長度

D ：原始射口寬度或直徑

同理，在 O 及 O′ 之間，浮量應守恒

$$\int_0^{\infty} 2\Delta\rho_o u (\pi y)^2 dy = \Delta\rho_o' U_o (\frac{\pi}{4} D)^2 D$$

式中 $\Delta\rho_o$：在修正射口處，周遭流場與射流中心密度差異量。

$\Delta\rho_o'$ ：在原始射口處，周遭流場與射流中心密度差異量。

應用動力相似之假設及Boussinesq近似法可得

$$\Delta\rho_0 = \left(\sqrt{\frac{1+\lambda^2}{2\lambda^2}}\right)^{a+1}\Delta\rho_0'$$

表三及表四爲經修正後之垂直二維及圓形浮昇射流在密度層變水域中的實驗數據。

本文在理論計算方面，利用斷面積分法來探討垂直浮昇射流在密度層變水域中的紊流物理變量，爲了閉合問題，在速度剖面與密度差異剖面分佈中引入兩個參數；捲增係數α及散佈比λ。流體的捲增係數由引入的動能量守恒關係導出一與反局部密度Froude數成線性的關係式，散佈比入及捲增係數中與紊流特性有關之積分參數α_1可由實驗及理論之計算而得，將捲增係數α及散佈比λ代入控制方程組由啟始條件即可進行數值計算。

散佈比λ值之設定，於二維浮昇射流中，本文逕取黃等氏[10]之實驗結果，$\lambda = 1.30$；而於三維圓形浮昇射流中，王等氏[15]發現，散佈比λ值之選定，對數值計算之影響不大，依Fan and Brooks二氏[3]及Hirst氏[14]建議，本文取定$\lambda = 1.16$。至於捲增係數中與紊流特性有關之積分參數α_1的決定，本文利用實驗中之一系列變化排放條件及水域密度層變所測得之浮昇高度，由理論分析之計算，反覆校正模式中捲增係數之參數α_1使計算所得之浮昇高度與實驗中射流的浮昇高度相同，遵此決定捲增係數中與紊流特性有關之積分參數α_1，用以探討垂直浮昇射流在密度層變水域中的物理特性。二維浮昇射流的實驗中，由於排放條件之限制，較不適用於動量射流及浮流，故本文只針對浮昇射流加以探討，而三維圓形浮昇射流之探討除利用本文之實驗值外，並包括前人之實驗值一併分析之。其所得結果如下：

二維浮昇射流中：

浮昇射流　$\alpha_1 = 0.075 \pm 0.013$ ……(37)

三維浮昇射流中：

浮　流　$\alpha_1 = 0.064 \pm 0.004$ ……(38)

浮昇射流　$\alpha_1 = 0.059 \pm 0.012$ ……(39)

動量射流　$\alpha_1 = 0.039 \pm 0.004$ ……(40)

圖十及圖十一爲浮昇射流在密度層變參數S_0相同情況下，不同啟始密度Froude數F_0對射流中心速度及中心密度差在縱向上衰減情形。從圖中吾人可發現在S_0相同條件下，F_0愈大，其啟始動量愈大，相對地，在出口附近射流之中心速度亦大，故引發之捲增量愈多，擴展亦快，而可得較遠之浮昇高度、較快速的中心速度衰退及促使軸中心的密度差有較大的衰退情形。

浮昇射流在其上昇及調混過程中，由於水域的密度層變關係，密度沿射流方向漸減，致使浮量沿射流方向漸減，當射流上昇到某一高度，浮量由正而零再轉爲負，此時射流中的密度較兩邊的環境水域爲大，此後射流由於動量的存在雖仍有一段距離之上昇，但是，由負浮量產生之指向環境水域之負捲增速度在射流未上昇到最高點前，終將超越由紊流應力所衍生者，此時負值的捲增量將使射流內的流體流向環境水域，因而有橫向之擴散。

圖十二及圖十三爲浮昇射流在啟始密度Froude數F_0相同情況下，不同密度層變參數S_0對射流

中心速度及中心密度差在縱向上衰減情形。從圖中吾人可發現在F_o相同條件下，S_o愈大，其性質愈近於浮流。反之。當密度層變參數S_o較小時，環境水域的密度梯度較大，中心密度差很容易由正轉爲負，換言之，其受負浮力作用之影響早於S_o較大者，致使射流中心速度減少，因此導致浮昇高度之降低。由此可知，浮昇射流在發展過程中，動量與浮量相互競爭的一般性。

圖十及圖十五所示分別爲二維及三維垂直浮昇射流之浮昇高度與流況無因次參數N之關係，運用迴歸分析法，吾人可得各種流況下，無因次參數ζ_T與N值之關係式，式中之冪次與因次分析所得之近似函數關係式之冪次均相互之吻合。其結果如下：

二維浮昇射流時：

浮昇射流　$\zeta_T = 3.00\ N^{-0.41}$ ……(41)

三維圓形浮昇射流時：

浮　流　$\zeta_T = 2.75\ N^{-3/8}$ ……(42)

浮昇射流　$\zeta_T = 3.04\ N^{-0.277}$ ……(43)

動量射流　$\zeta_T = 2.78\ N^{-1/4}$ ……(44)

應用以上各式前，必須先判斷射流的種類，然而根據定義，眞正之浮流與動量射流並不存在，故爲切合實際應用，根據圖上顯示，吾人建議：

浮　流　$N < 0.1$ ……(45)

浮昇射流　$0.1 \leq N \leq 10$ ……(46)

動量射流　$N > 10$ ……(47)

圖十六及圖十七所示分別爲二維及三維浮昇射流中，停滯點稀釋率與無因次參數N之關係，以數值結果運用迴歸分析法，吾人亦可得各種流況下，無因次參數$\overline{\mu}_T$與N值之關係式，式中之冪次與因次分析所得之近似函數關係式之冪次相互比較，亦知相互的吻合，其結果如下：

二維浮昇射流時：

浮昇射流　$\overline{\mu}_T = 0.77\ N^{-0.44}$ ……(48)

三維浮昇射流時：

浮　流　$\overline{\mu}_T = 0.84\ N^{-5/8}$ ……(49)

浮昇射流　$\overline{\mu}_T = 0.83\ N^{-0.6}$ ……(50)

動量射流　$\overline{\mu}_T = 0.32\ N^{-1/4}$ ……(51)

陸、結　論

浮昇射流在其上昇及調混過程中，由於水域的密度層變關係，當其射流上昇到某一高度，浮量由正而零再轉爲負值，此時射流中的密度較兩邊的環境水域爲大，此後射流由於動量的存在雖仍有一段距離之上昇，但是，由負浮量產生之捲增速度分量在射流未上昇到最高點前，終將超越由紊流應力所衍生者，此時負值的捲增量將使射流內的流體流向環境水域，因而有橫向之擴散。本文爲對於一垂直

浮昇射流在密度層變的環境水域中的擴散現象及流況作數值分析，並以實驗值相互比較印證。

獲得下列結果：

1. 本文直接由基本方程組的動能量守恒導出捲增係數與射流軸中心的反局部密度Froude 數成正比的關係，較前人逕予設定一通用常數合理。
2. 爲判別射流種類，以因次分析及實驗值導出無因次參數N值與流況之關係如(45)～(47) 三式所示。
3. 由紊流特性影響之捲增係數α_1，其值應與均勻環境水域之捲增係數有別。本文經由實驗測出其浮昇高度，再配合理論分析定出不同射流種類亦有不同之相對α_1值，如(37)～(40)四式所示，俾供參考。
4. 對於射流浮昇高度，停滯點稀釋率與無因次參數N值之關係，本文由實驗資料及數值計算運用迴歸分析法分別得出其簡單的關係式，如(41)～(44)及(48)～(51)等式，以供工程設計應用時之參考。

參考文獻

1. Ablertson, M. L., Dai, Y. B., Jensen, R. A. & Rouse, H., "Diffusion of Submerged Jets," Trans. ASCE, Vol. 115, pp.639-664. (1950).
2. Rouse, H., Yih, C. S. & Humphreys, H. W., "Gravitational Convection from a Boundary Source," Tellas 4, pp.201-210 (1952).
3. Fan, L. N. & Brooks, N. H., "Numerical Solutions of Turbulent Buoyant Jet problems," Report KH-R-18, Calif. Inst. Tech. Pasadena. Calif. (1969).
4. Morton. B., Taylor, G. I. & Turner, J. S., "Turbulent Gravitational Convection from Maintained and Instantaneous Sources," Proc. Royal Society, Vol. A234, pp.1-23 (1956).
5. Abraham, G., "Jet Diffusion in Stagnant Ambient Fluid," Delft Hydraulics Lab. Publ. No. 29, (1963).
6. Fan, L. N., "Turbulent Buoyant Jets Into Stratified or Flowing Ambient Fluid," Report KH-R-15, Calif. Inst. Tech. Pasadena. Calif. (1967).
7. Taylor, G. I., "Flow Indused by Jets," J. Aero/Space Science, Vol.25, pp.464-465 (1958).
8. List, E. J. & Imberger, J., "Turbulent Entrainment in Buoyant Jets and Plumes," ASCE, J. of Hy. Div., HY9, pp.1461-1474 (1973).
9. Kotsovinos, N. E. & List, E. J., "Plane Turbulent Buoyant Jets, Part 1. Integral Properties," J. of Fluid Mech., Vol. 81, pp.25-44 (1977).
10. 黃榮鑑、傅忠申、王燦汶，"密度層變流中的擴散及其在海洋放流之應用"，土木水利季刊第五卷第三期，十九頁～三十二頁(民國六十七年)。
11. Tsai, S. M. & Hwang, R. R., "A Turbulent Buoyant Round Jet Into a Stably Stratified Fluid," Proc. 5th Conf. on Theo. & Appl. Mech. R.O.C. Dec. (1981).
12. Kotsovinos, N. E., "A Study of the Entrainment and Turbulence in a Plane Buoyant Jet," Report KH-R-32, Calif, Inst. Tech. Pasadena. Calif. (1976).
13. Fox. D. G., "Forced Plume in a stratified Fluid," J. of Geophysical Research, Vol. 75, pp.6818-

6835 (1970).

14. Hirst, E., "Buoyant Jets Discharged to Quiescent Stratified Ambient," J. of Geophysical Research, Vol. 76, pp.7375-7384 (1971).
15. 王德忠、蔡西銘、黃榮鑑，"密度層變流中圓形浮昇射流之實驗研究，"第六屆海洋工程研討會 39－1～18 頁（民國七十一年）。
16. Daily, J. W. & Harleman, D. R. F., "Fluid Dynamics," Addison-Wesley Publ. Company. Inc. (1966).
17. Crawford, T. V. & Leonard, A. S., "Observations of Buoyant Plumes in Calm Stably Stratified Air," J. of Appl. Meteorol., Vol.1, pp.251-256 (1962).
18. Abraham, G. & Eysink, W. D., "Jets Issuing into Fluid with a Density Gradient," J. of Hydraul. Res. pp.145-175 (1969).

表一　二維浮昇射流原始實驗數據

Run No.	D(cm)	U_o(cm/s)	ρ_i'(g/cm³)	$\Delta\rho_0'$(g/cm³)	$\frac{d\rho_a}{dx}$(10^{-4}g/cm³)	X_f(cm)
1	0.2	25.16	1.015	0.015	-2.5	22.6
2	0.2	38.60	1.015	0.015	-2.5	29.6
3	0.2	32.54	1.0145	0.0145	-2.0	25.4
4	0.2	44.25	1.0145	0.0145	-2.0	35.0
5	0.2	52.96	1.0145	0.0145	-2.0	40.1
6	0.2	20.75	1.018	0.018	-3.0	17.6
7	0.2	32.54	1.018	0.018	-3.0	23.4
8	0.2	44.25	1.018	0.018	-3.0	30.6
9	0.2	52.96	1.018	0.018	-3.0	34.0
10	0.2	62.46	1.018	0.018	-3.0	37.0
11	0.2	17.20	1.025	0.025	-4.0	15.0
12	0.2	20.75	1.025	0.025	-4.0	18.2
13	0.2	32.54	1.025	0.025	-4.0	23.0
14	0.2	44.25	1.025	0.025	-4.0	28.0
15	0.2	52.96	1.025	0.025	-4.0	31.0
16	0.2	62.46	1.025	0.025	-4.0	34.0
17	0.2	70.53	1.025	0.025	-4.0	35.8
18	0.2	20.75	1.020	0.020	-1.0	38.0
19	0.2	32.54	1.020	0.020	-1.0	47.0
20	0.2	44.25	1.020	0.020	-1.0	50.0
21	0.2	13.31	1.025	0.025	-4.0	12.7
22	0.2	44.25	1.025	0.025	-4.0	27.0
23	0.2	52.96	1.025	0.025	-4.0	30.0
24	0.2	62.46	1.025	0.025	-4.0	33.4
25	0.2	17.20	1.025	0.025	-2.0	24.0
26	0.2	20.75	1.025	0.025	-2.0	29.5
27	0.2	32.54	1.025	0.025	-2.0	38.0

表二 圓形浮昇射流原始實驗數據

Run No.	D(cm)	U_o(cm/s)	ρ_1(g/cm³)	$\triangle\rho_o'$(g/cm³)	$\frac{d\rho_a}{dx}$(10^{-4}g/cm)	X_T'(cm)
1	0.52	4.68	1.0082	0.0082	-0.322	16.70
2	0.52	7.19	1.0101	0.0101	-1.14	16.63
3	0.52	8.76	1.0090	0.0090	-0.836	18.60
4	0.52	9.46	1.0134	0.0134	-1.85	14.32
5	0.52	10.86	1.0091	0.0091	-0.735	21.68
6	0.52	9.53	1.0084	0.0084	-0.869	15.00
7	0.52	10.86	1.0094	0.0094	-1.02	20.09
8	0.52	11.72	1.0096	0.0096	-1.09	20.20
9	0.52	17.97	1.0085	0.0085	-0.505	25.88
10	0.52	14.88	1.0091	0.0091	-0.971	23.98
11	0.52	14.69	1.0178	0.0178	-4.15	14.38
12	0.52	19.79	1.0096	0.0096	-1.07	26.50
13	0.52	21.04	1.0088	0.0088	-0.85	25.17
14	0.52	25.39	1.0140	0.0140	-1.95	19.91
15	0.52	26.24	1.0093	0.0093	-0.83	31.67
16	0.52	30.94	1.0081	0.0081	-0.82	31.15
17	0.52	40.09	1.0079	0.0079	-0.745	36.23
18	0.52	45.58	1.0180	0.0180	-4.17	25.00
19	0.33	52.92	1.0094	0.0094	-1.02	30.10
20	0.33	58.05	1.0090	0.0090	-0.837	31.70
21	0.33	61.64	1.0140	0.0140	-1.88	25.38
22	0.33	55.88	1.0091	0.0091	-1.01	27.15
23	0.33	68.73	1.0182	0.0182	-3.64	23.98
24	0.52	74.66	1.0175	0.0175	-3.93	31.83
25	0.52	91.04	1.0135	0.0135	-1.75	39.16
26	0.33	94.21	1.0138	0.0138	-1.87	33.41
27	0.33	114.97	1.0132	0.0132	-1.70	36.33
28	0.52	105.60	1.0159	0.0159	-3.05	37.10
29	0.33	126.88	1.0180	0.0180	-3.60	32.05
30	0.52	150.27	1.0177	0.0177	-3.50	40.86
31	0.33	233.51	1.0183	0.0183	-3.61	40.43

表三　二維浮昇射流修正後實驗數據

Run No.	b_o(cm)	U_o(cm/s)	ρ_1(g/cm³)	$\Delta\rho_o$(g/cm³)	F_o	S_o	N	$\frac{X_T}{b_o}$	ζ_T
1	0.16	25.16	1.0147	0.0134	17.48	335	0.912	134.75	2.97
2	0.16	38.60	1.0147	0.0134	26.82	335	2.147	178.50	2.22
3	0.16	32.54	1.0143	0.0129	23.04	403.125	1.317	152.25	2.32
4	0.16	44.25	1.0143	0.0129	31.33	403.125	2.435	212.25	2.15
5	0.16	52.96	1.0143	0.0129	37.50	403.125	3.488	244.126	1.94
6	0.16	20.75	1.0177	0.0161	13.17	335.42	0.517	103.50	3.33
7	0.16	32.54	1.0177	0.0161	20.66	335.42	1.273	139.75	2.47
8	0.16	44.25	1.0177	0.0161	28.10	335.42	2.354	184.75	2.16
9	0.16	52.96	1.0177	0.0161	33.63	335.42	3.372	206.00	1.90
10	0.16	62.46	1.0177	0.0161	39.66	335.42	4.689	224.75	1.66
11	0.16	17.20	1.0246	0.0223	9.31	348.44	0.249	87.25	4.45
12	0.16	20.75	1.0246	0.0223	11.23	348.44	0.362	107.25	4.26
13	0.16	32.54	1.0246	0.0223	17.61	348.44	0.890	137.25	3.00
14	0.16	44.25	1.0246	0.0223	23.95	348.44	1.646	168.50	2.44
15	0.16	52.96	1.0246	0.0223	28.67	348.44	2.359	187.25	2.13
16	0.16	62.46	1.0246	0.0223	33.81	348.44	3.281	206.00	1.88
17	0.16	70.53	1.0246	0.0223	38.18	348.44	4.184	217.25	1.69
18	0.16	20.75	1.0199	0.0178	12.54	1112.5	0.141	231.0	7.93
19	0.16	32.54	1.0199	0.0178	19.67	1112.5	0.348	287.25	5.41
20	0.16	44.25	1.0199	0.0178	26.75	1112.5	0.643	306.00	3.82
21	0.16	13.31	1.0246	0.0223	7.20	348.44	0.149	72.88	5.24
22	0.16	44.25	1.0246	0.0223	23.95	348.44	1.646	162.25	2.35
23	0.16	52.96	1.0246	0.0223	28.67	348.44	2.359	181.00	2.06
24	0.16	62.46	1.0246	0.0223	33.81	348.44	3.281	202.25	1.85
25	0.16	17.20	1.0248	0.0223	9.31	696.875	0.124	143.50	7.33
26	0.16	20.75	1.0248	0.0223	11.23	696.875	0.181	177.88	7.07
27	0.16	32.54	1.0248	0.0223	17.62	696.875	0.446	231.00	5.04

表四　圓形浮昇射流修正後實驗數據

Run No.	b_o(cm)	U_o(cm/s)	ρ_1(g/cm³)	$\triangle\rho_o$(g/cm³)	F_o	S_o	N	X_T/b_o	ζ_T
1	0.74	4.68	1.0081	0.0072	2,062	299,48	0.0142	17.59	8.53
2	0.74	7.19	1.0097	0.0088	2,858	104,17	0.0784	17,50	6,12
3	0.74	8.76	1.0087	0.0078	3.694	126,12	0.1082	20.15	6.46
4	0.74	9.46	1.0127	0.0117	3.269	85.02	0.1257	14.38	4.40
5	0.74	10.86	1.0088	0.0079	4.559	144,87	0.144	24.31	5.33
6	0.74	9.53	1.0081	0.0073	4.150	113.71	0.152	15.30	3.69
7	0.74	10.86	1.0091	0.0082	4,469	108.62	0.184	22.16	4,96
8	0.74	11.72	1.0092	0.0084	4,774	104,07	0,219	22,31	4.67
9	0.74	17.97	1.0083	0.0074	7,772	198.29	0.305	29,98	3.86
10	0.74	14.88	1.0088	0.0080	6,219	110,44	0.350	27.41	4.41
11	0.74	14.69	1.0163	0,0155	4,414	50,37	0,387	14,45	3,27
12	0.74	19.79	1.0092	0.0084	8.066	105,86	0,615	30,81	3,82
13	0.74	21.04	1.0085	0,0077	8,953	121,78	0,658	29.01	3,24
14	0.74	25.39	1.0133	0,0122	8,587	84,43	0,873	21.92	2.55
15	0,74	26.24	1.0090	0,0081	10,869	131,70	0,897	37.79	3,48
16	0.74	30,94	1,0078	0,0071	13,708	116,36	1,615	37,09	2,71
17	0.74	40.09	1,0076	0,0069	18,017	124,45	2,608	43,94	2.44
18	0.74	45.58	1,0165	0,0157	13,614	50,78	3.650	29.79	2.19
19	0,46	52,92	1.0092	0,0082	27,572	173,06	4,393	60,03	2,18
20	0,46	58,05	1,0088	0,0078	30,907	202,29	4,722	63,49	2.05
21	0,46	61,64	1,0136	0,0122	26,372	140,10	4,964	49,85	1.89
22	0,46	55,88	1,0089	0,0079	29,583	169,09	5,176	53,66	1,81
23	0,46	68,73	1,0174	0,0159	25,837	94,00	7,101	46,82	1,81
24	0,74	74,66	1,0161	0,0153	22,615	52,43	9,754	38,00	1,68
25	0,74	91,04	1,0129	0,0118	31,340	90,77	10,821	47,90	1,53
26	0,46	94,21	1,0134	0,0120	40,634	138,72	11,902	67,18	1,65
27	0,46	114,97	1,0128	0,0115	50,642	146,04	17,561	73,48	1,45
28	0.74	105,60	1,0148	0,0139	33,507	61,48	18,263	45,12	1,35
29	0,46	126,88	1,0172	0,0157	47,935	94,28	24,371	64,24	1,34
30	0.74	150,27	1,0164	0,0154	45,303	59,38	34,564	50,19	1,11
31	0,46	233,51	1,0175	0,0160	87,537	95,45	80,278	82,33	0,94

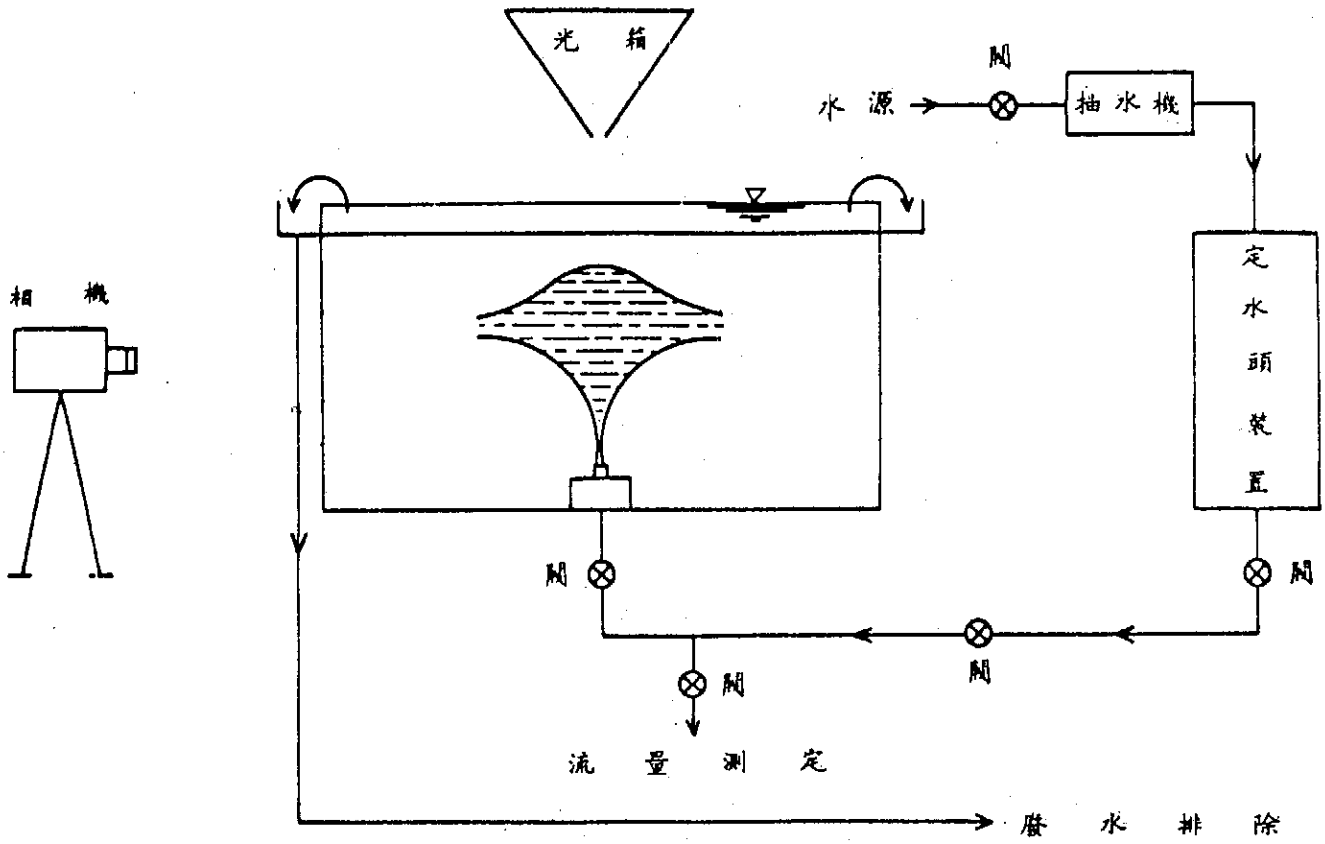

圖一 垂直浮昇射流之實驗裝置

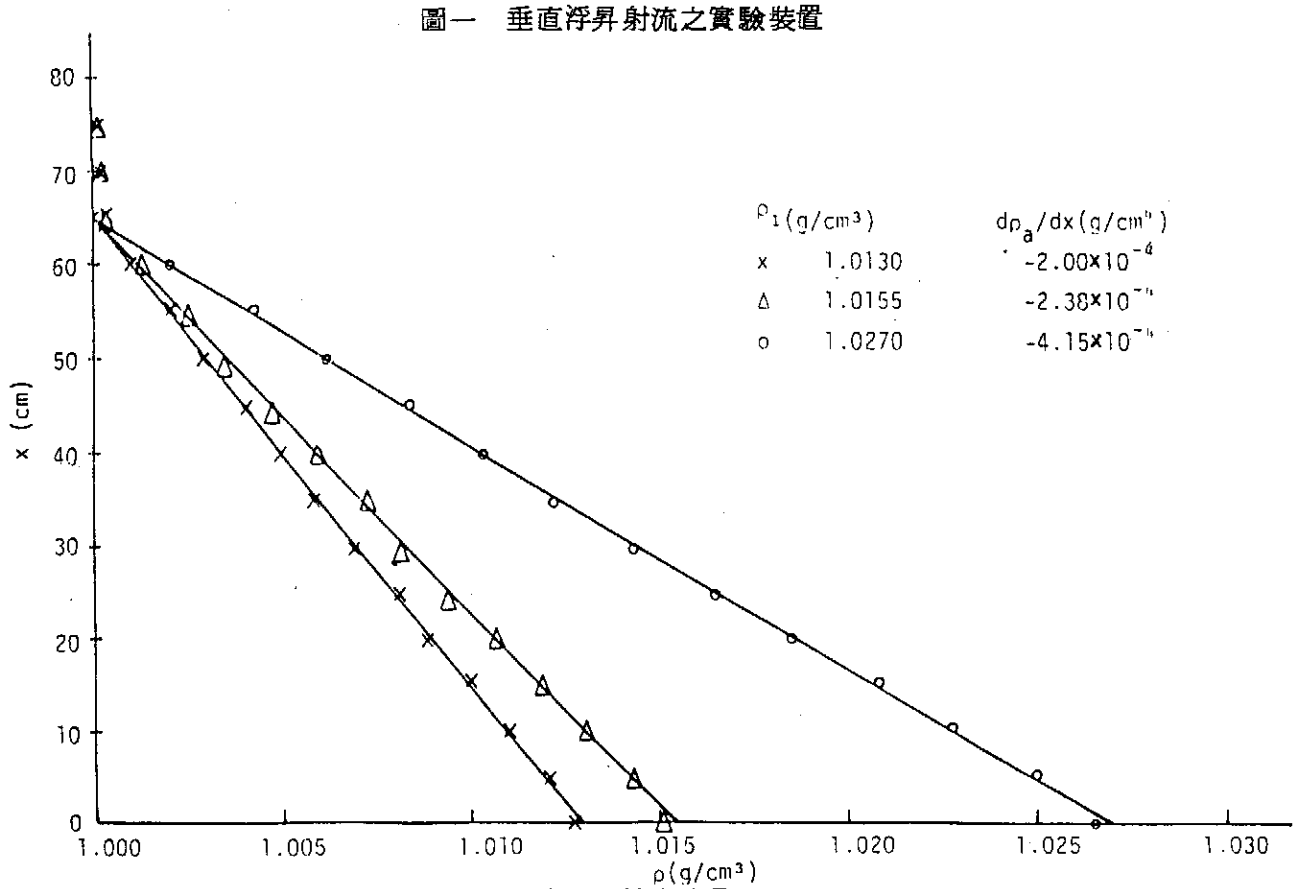

圖二 垂直二維浮昇射流之線性密度層變環境水域之密度測定

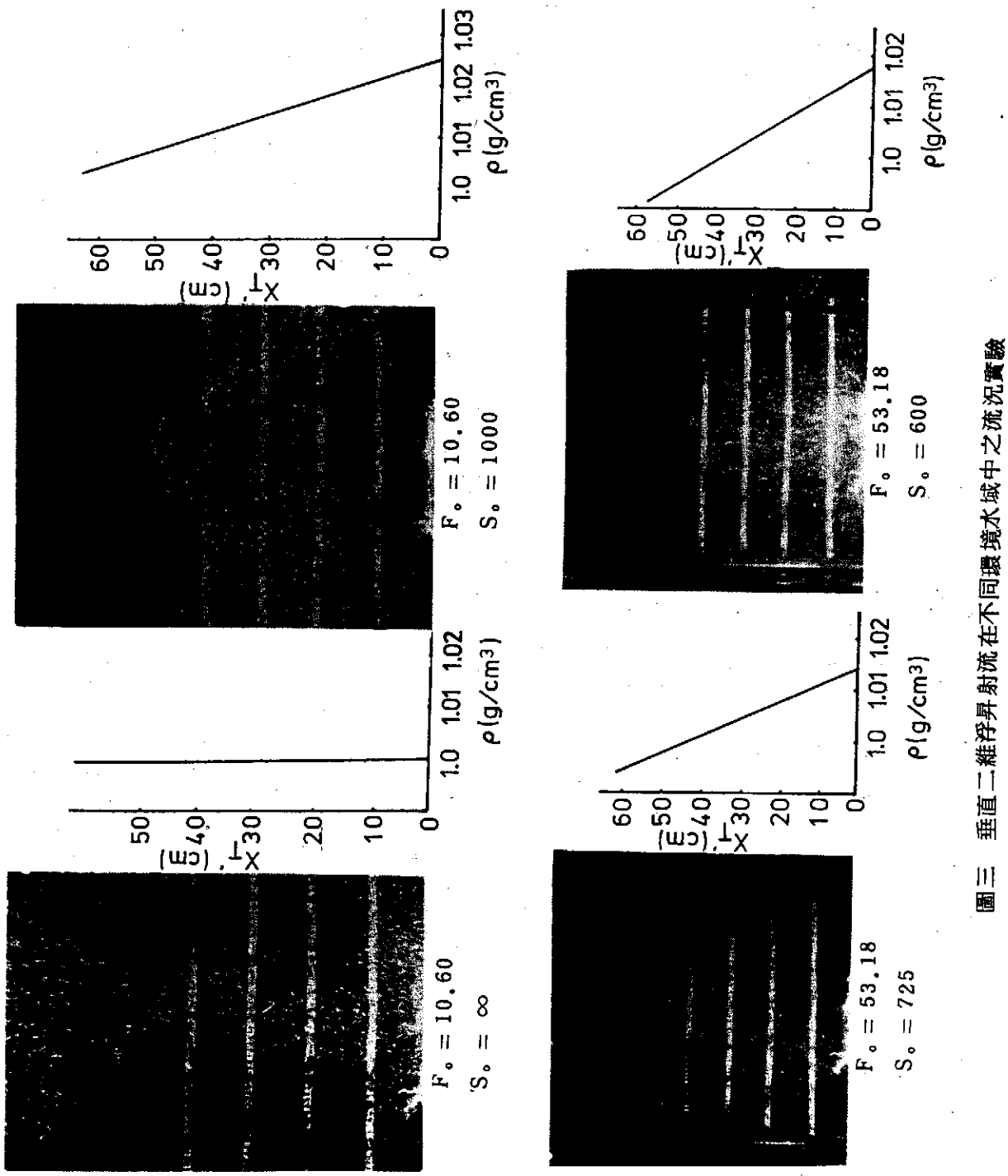

圖三　垂直二維浮昇射流在不同環境水域中之流況實驗

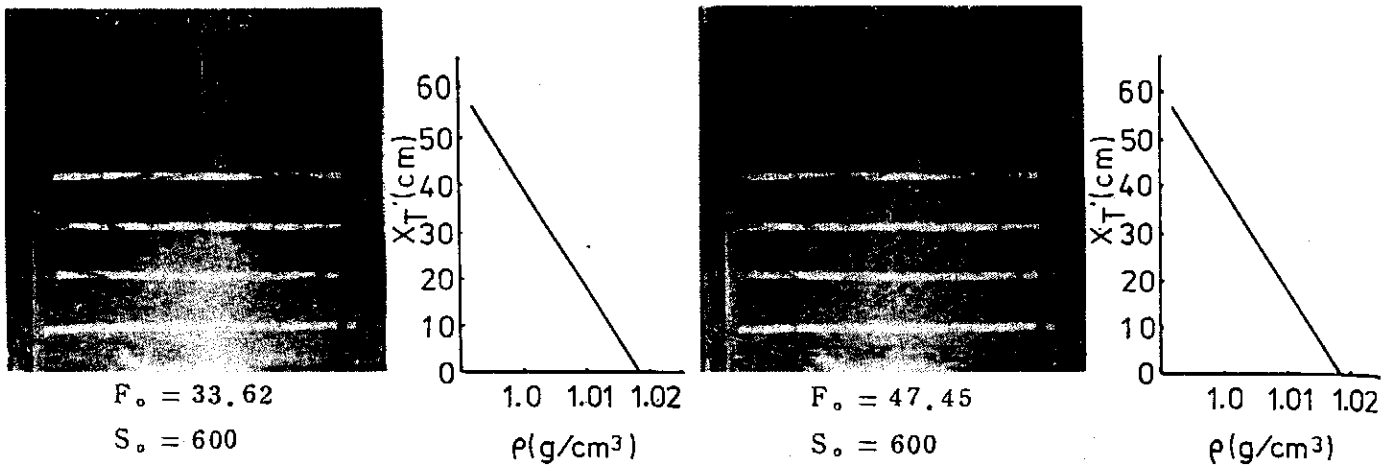

圖四　垂直二維浮昇射流在不同啟始動量條件下之流況實驗

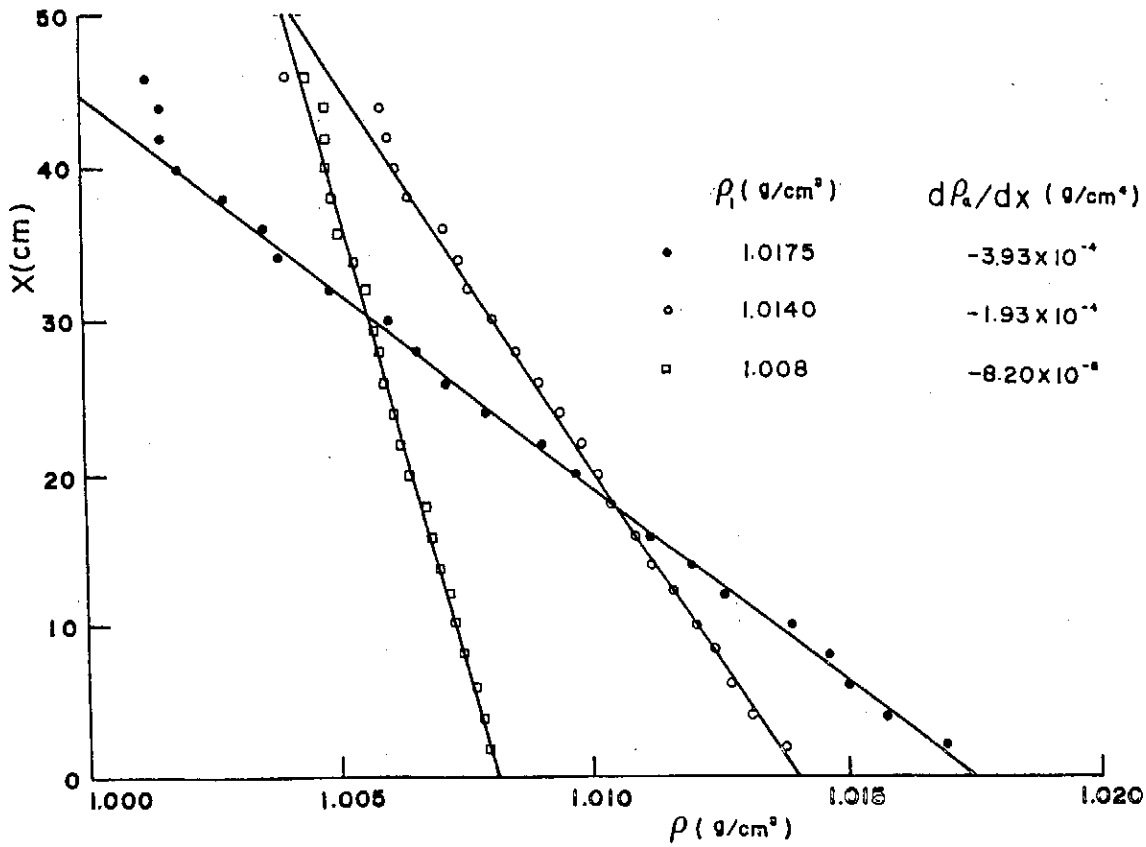

圖五　垂直三維圓形浮昇射流之線性密度層變環境水域之密度測定

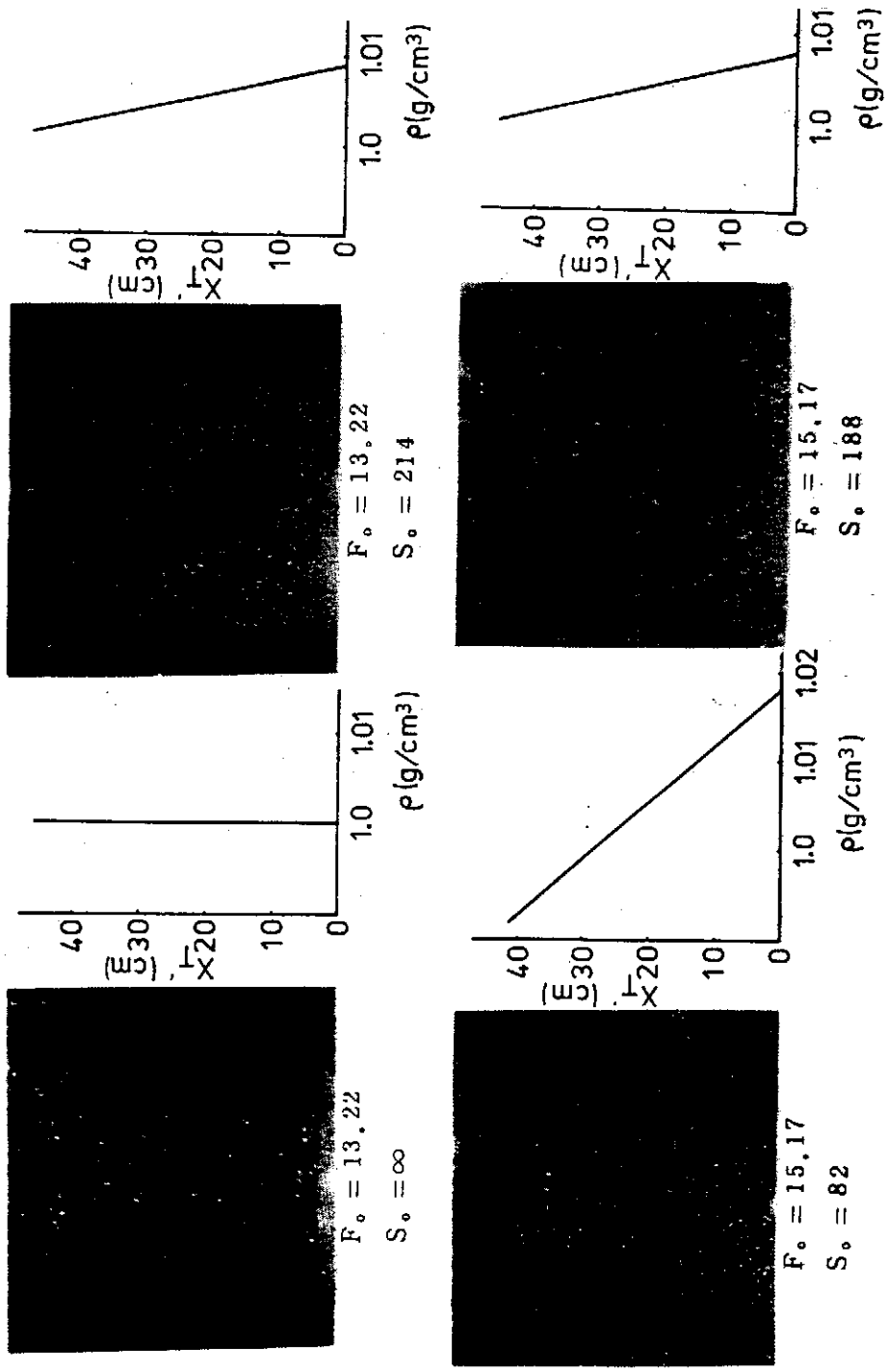

圖六　垂直三維圓形浮昇射流在不同環境水域中之流況實驗

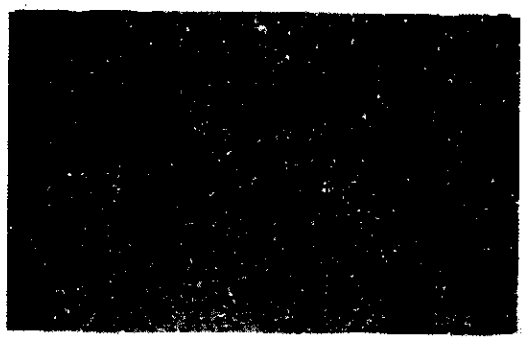

$F_o = 28.70$

$S_o = 153$

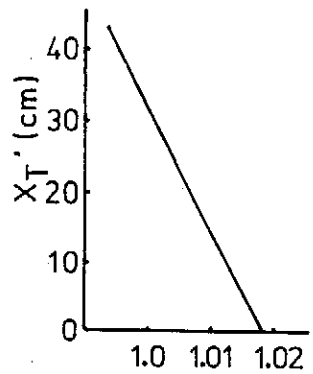

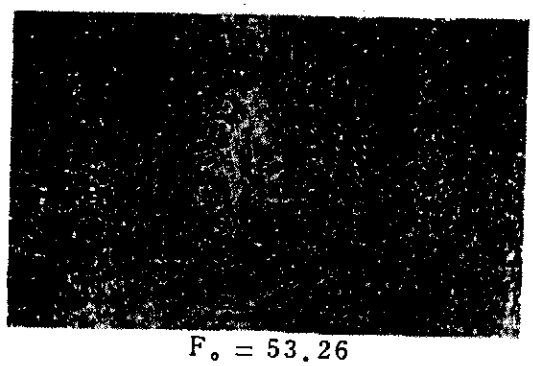

$F_o = 53.26$

$S_o = 153$

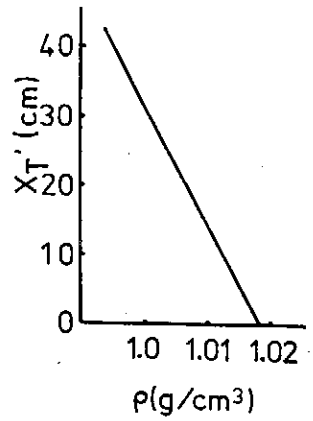

圖七　垂直三維圓形浮昇射流在不同啟始動量條件下之流況實驗

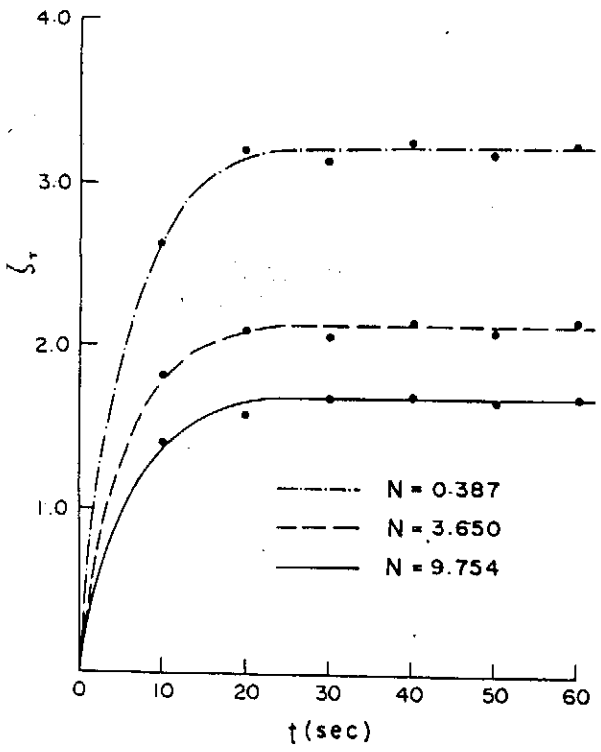

圖八　垂直三維圓形浮昇射流之浮昇高度與時間之關係

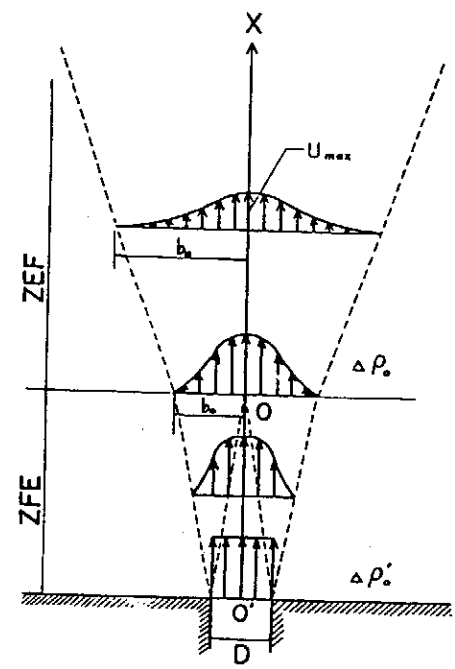

圖九　流場建立區略圖

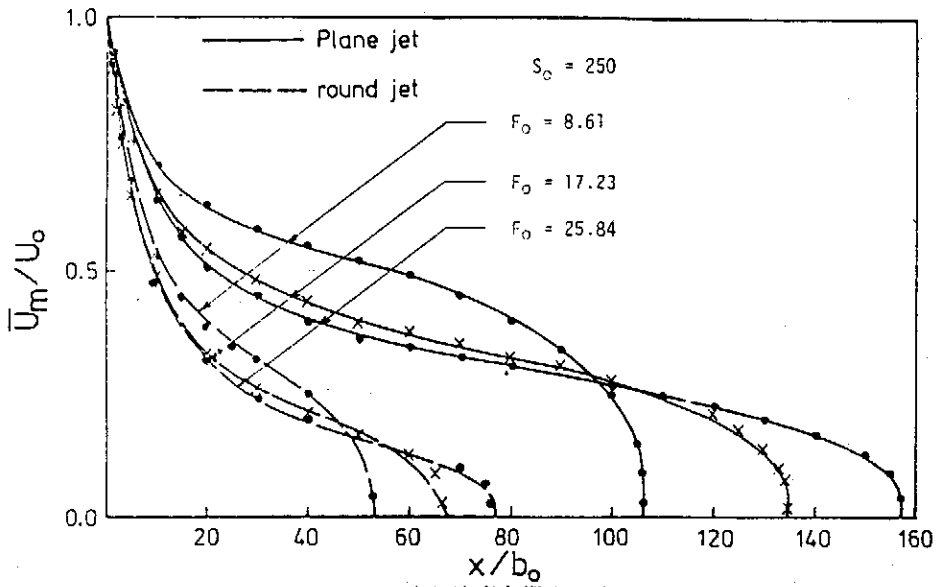

圖十　射流中心速度在縱向之變化

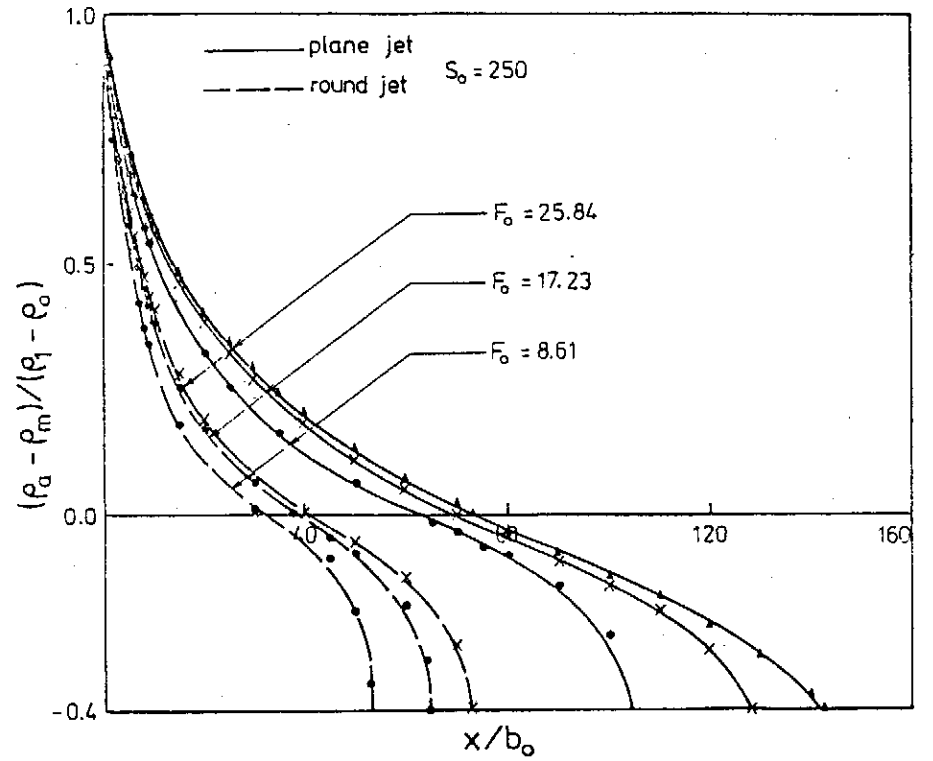

圖十一　射流中心密度差在縱向之變化

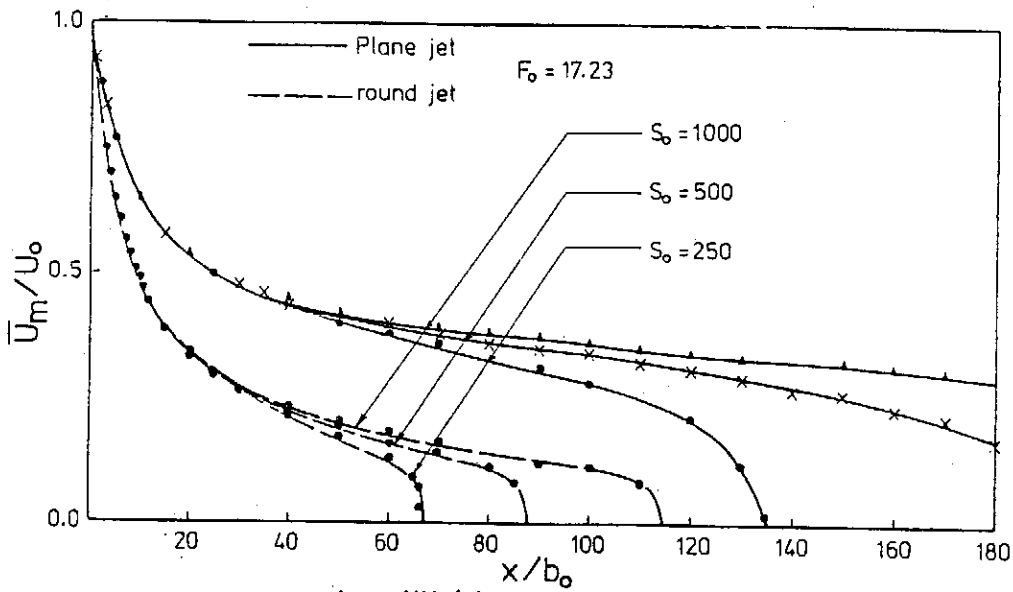

圖十二　射流中心速度在縱向之變化

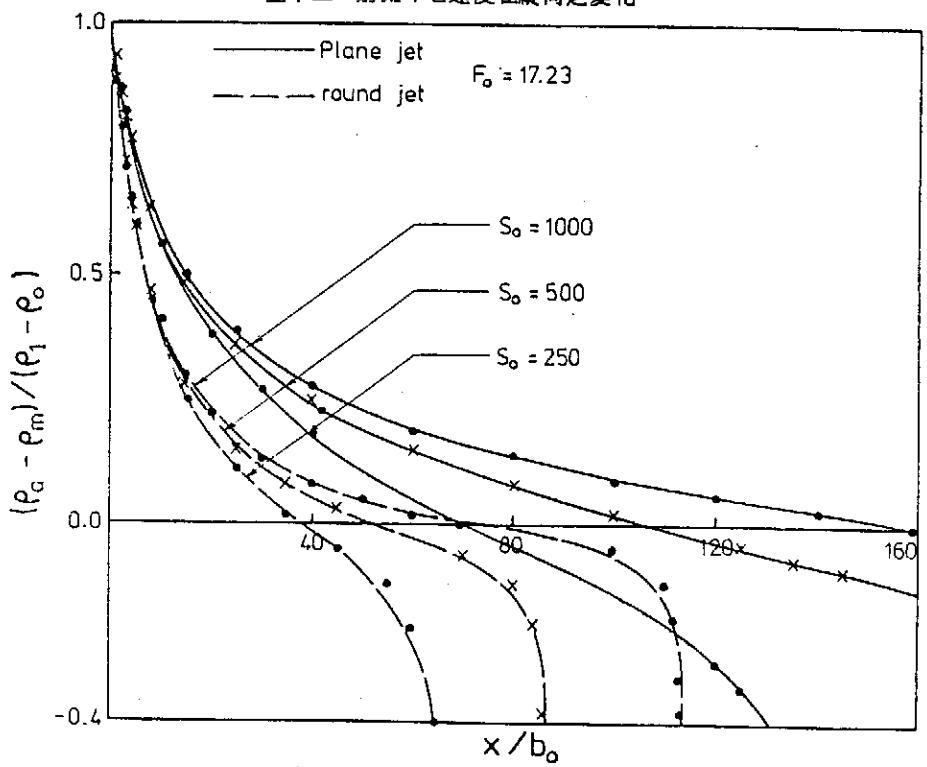

圖十三　射流中心密度差在縱向之變化

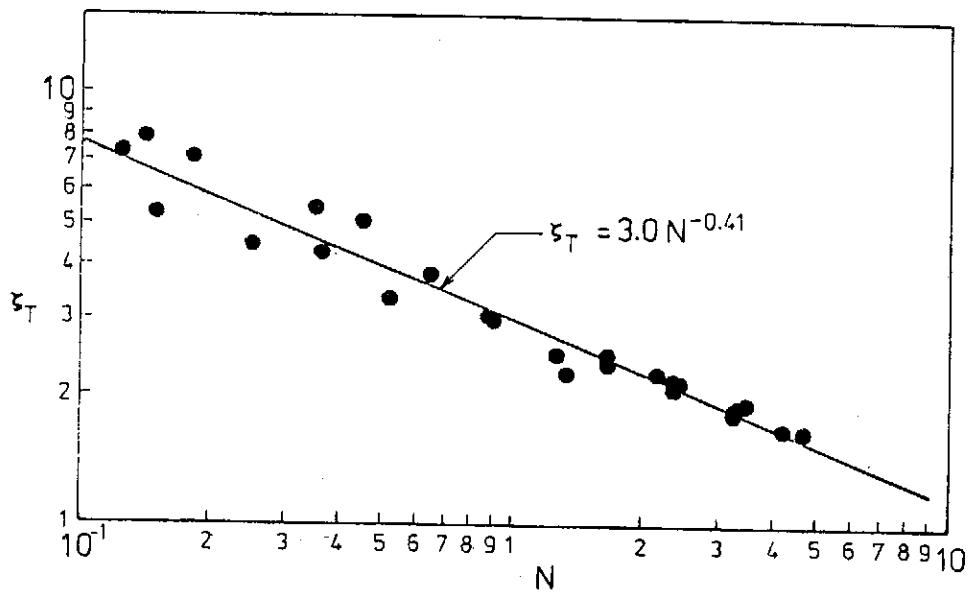

圖十四　垂直二維浮昇射流中ζ_T與N之關係

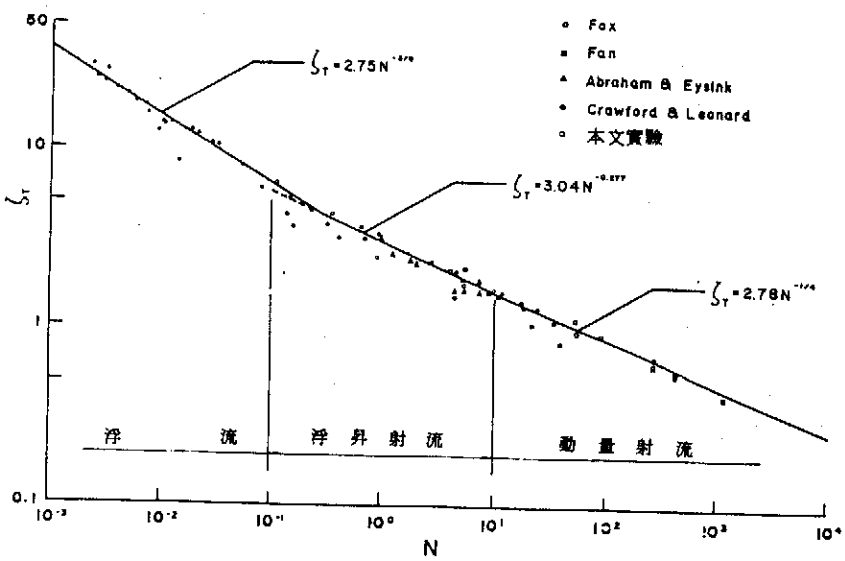

圖十五　垂直圓形浮昇射流中ζ_T與N之關係

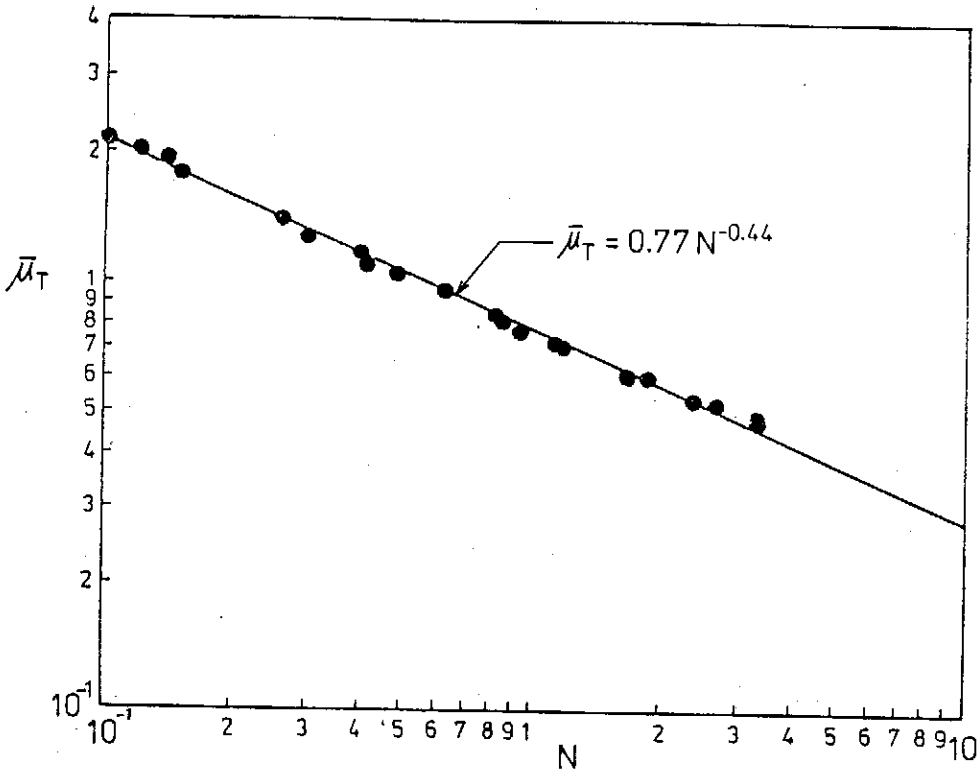

圖十六　垂直二維浮昇射流中 $\bar{\mu}_T$ 與N之關係

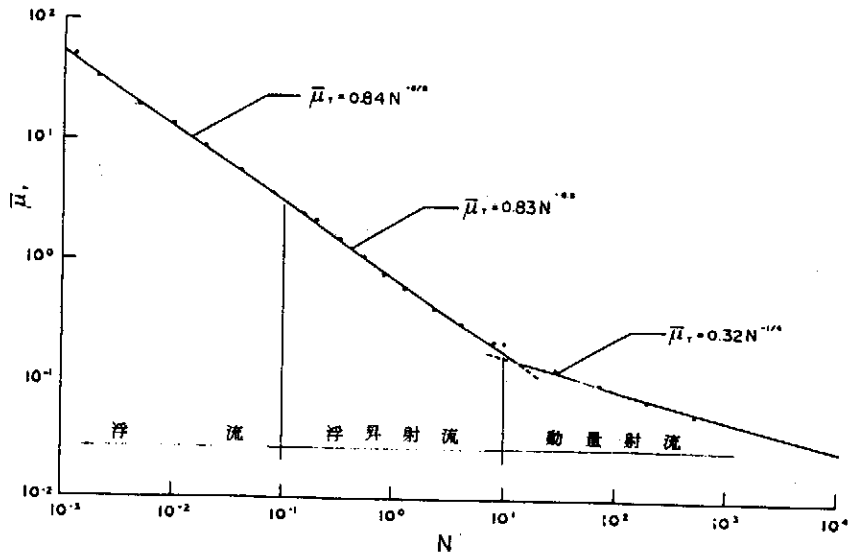

圖十七　垂直圓形浮昇射流中 $\bar{\mu}_T$ 與N之關係

氣象衛星遙測資料之應用—海面溫度之求取

曾　忠　一

中央研究院物理研究所

國立台灣大學大氣科學系

曹　幼　民

中　央　氣　象　局

氣象衛星資料接收站

摘　要

隨著太空技術的進步，給遙測大氣提供了優越的條件，利用氣象衛星做全球性的和連續性的觀測，已成爲氣象學不可缺少的一部份了。海面溫度在大氣海洋的熱收支和交互作用方面扮演重要的角色。此外在數值預報模式和環流模式中，海面溫度也是重要的輸入參數。本文利用繞極軌道氣象衛星NOAA-6 號上攜帶的輻射計 AVHRR 所觀測的數位資料，經過校準之後求得輻射強度和亮度溫度，然後再用多頻道水汽訂正法來除去水汽吸收的影響，以便得到海面溫度值。根據初步研究結果，所求得的海面溫度誤差大約在 1° 到 2 ℃之間。此外，因爲在低緯地區大氣中水汽含量較多，用多頻道水汽訂正法來去掉水汽吸收的影響，中緯度地區的結果比低緯地區要來得好些。

壹、前　言

我國中央氣象局自去年元月啟用氣象衛星資料接收站以來，每天可定時接收到雲圖，以供天氣分析的參考，對天氣預報以及航空、航海都有直接的效益。除了雲圖之外，衛星站也可接收到數位資料，也就是衛星上攜帶的輻射計所觀測到的輻射強度。利用這些數位資料，可以求取許多氣象變數，諸如溫度和水汽的垂直分布、雲量和雲頂溫度以及海面溫度。本年四月間，在衛星站同仁的協助下，本研究解讀出繞極軌道氣象衛星NOAA-6號上攜帶的輻射計AVHRR（Advanced Very High Resolution Radiometer）所觀測到的輻射強度，並立即進行海面溫度的計算。海面溫度是氣象應用中最重要的表面參數。它在大氣的熱收支問題、霧的形成以及大氣海洋交互作用方面都扮演着重要的角色。此外在數值天氣預報模式和環流模式中，海面溫度也是重要的輸入參數。

在紅外區，地球表面的放射率很接近於 1 。因此，在沒有雲和大氣吸收的影響下，太空載台攜帶的輻射計所觀測到的亮度溫度就是海面溫度。但是，雲和水汽的吸收常使窗區頻道的資料難以解釋。因此必須使用特別的演算法，以便除去雲和水汽的影響。

貳、多頻道水汽訂正法

NOAA-6 號氣象衛星上攜帶的輻射計AVHRR，具有兩個紅外窗區頻道 3.7 μm和 11 μm 。這樣可以對水汽吸收進行更精確的訂正。在太空中飛行的氣象衛星上所觀測到的上升輻射强度 I_ν 爲（Liou , 1980 ）

$$I_\nu = B_\nu(T_s)\mathcal{T}_\nu(\tau_1 \sec\theta) - \int_0^{\tau_1} B_\nu[T(\tau')]\frac{d\mathcal{T}_\nu(\tau'\sec\theta)}{d\tau'}d\tau' \quad \cdots(1)$$

其中 ν 爲波數，B_ν 爲 Plank 函數。(1)式中我們使用垂直光程 τ 坐標，其定義爲

$$\tau = \int_z^\infty k_\nu(z')\rho(z')dz'$$

τ_1 就是地表上的 τ 值（見圖 1 ）。透射函數 $\mathcal{T}_\nu(\tau)$ 的定義爲

$$\mathcal{T}_\nu(\tau) = e^{-\tau}$$

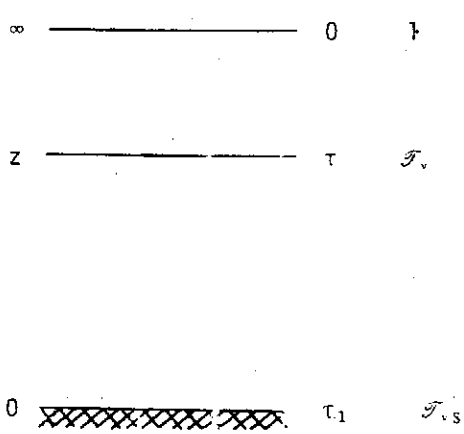

圖 1　三種垂直坐標

改用透射函數 $\mathcal{T}_\nu$ 爲垂直坐標，(1)式可寫爲

$$I_\nu = B_\nu(T_s)\mathcal{T}_{\nu s}^{\sec\theta} + \int_{\mathcal{T}_{\nu s}}^1 B_\nu[T(\tau')]d\mathcal{T}_\nu^{\sec\theta} \quad \cdots\cdots(2)$$

其中

$$\mathcal{T}_{\nu s} = e^{-\tau_1}$$

利用中值定理，(2)式變爲（Chedin et al 1982 ）

$$I_\nu = B_\nu(T_s)\mathcal{T}_{\nu s}^{\sec\theta} + \bar{B}_\nu(1 - \mathcal{T}_{\nu s}^{\sec\theta}) \quad \cdots\cdots(3)$$

其中 $\bar{B}_\nu$ 爲大氣 Planck函數。在吸收很微的窗區頻道，我們可做下列近似

$$\mathcal{T}_{\nu s}^{\sec\theta} = e^{-\tau_1\sec\theta} = 1 - \tau_1\sec\theta \quad \cdots\cdots(4)$$

將(4)式代入(3)式，我們有（ Anding and Kauth , 1970 和Prabhakara et al , 1974 ）

$$I_\nu = B_\nu(T_s) + \tau_1 \sec\theta\,[\,\overline{B}_\nu - B_\nu(T_s)\,] \qquad \cdots\cdots(5)$$

再假設吸收係數 k_ν 和高度 z 無關，那麼

$$\tau_1 = \int_0^\infty k_\nu \rho\, dz = k_\nu \int_0^\infty \rho\, dz = k_\nu u_1$$

其中 u_1 爲可降水量。因此(5)式變爲

$$I_\nu = B_\nu(T_s) + k_\nu u_1\,[\,\overline{B}_\nu - B_\nu(T_s)\,]\sec\theta \qquad \cdots\cdots(6)$$

因爲 $B_\nu(T_s)$ 和 I_ν 很接近，而且 $B_\nu(T_s)$ 和 $\overline{B}_\nu$ 也幾乎相等，我們可以進行下列Taylor 數列展開

$$I_\nu - B_\nu(T_s) = \left(\frac{\partial B_\nu}{\partial T}\right)_s (T_B - T_s) + \cdots$$

$$\overline{B}_\nu - B_\nu(T_s) = \left(\frac{\partial B_\nu}{\partial T}\right)_s (\overline{T} - T_s) + \cdots$$

將上二式代入(6)式得到（ Anding and Kauth , 1970 和Prabhakara et al , 1974 ）

$$T_B = T_s - (T_s - \overline{T})\, u_1 \sec\theta\, k_\nu \qquad \cdots\cdots(7)$$

現在若一個氣象衛星具有兩個頻道，可以得到兩組（ T_B , k_ν ）的觀測值，我們就可求得兩個未知數 T_s 和（ $T_s - \overline{T}$ ）$u_1 \sec\theta$。若有三個以上的頻道那麼 T_s 可用最小平方法求得。不論在任何情形下，由(7)式可知，表面溫度 T_s 可用 n 個窗區頻道亮度溫度 T_B 的線性組合表示，即

$$T_s = A_0 + \sum_{i=1}^{n} A_i\, T_B(\nu_i)$$

對NOAA - 6 號衛星攜帶的輻射計 AVHRR 而言，McClain（1981）給出下列A值

$$A_0 = 1.58 \qquad A(3.7\,\mu m) = 1.55 \qquad A(11\,\mu m) = -0.55$$

換句話說，表面溫度 T_s 可寫爲

$$T_s = T_B(11\,\mu m) + 1.55\,[\,T_B(3.7\,\mu m) - T_B(11\,\mu m)\,] + 1.58 \qquad \cdots\cdots(8)$$

用(8)式求得的海面溫度的根均方差，McClain 認爲只有 0.6 ℃。

參、計算結果

本文所採用的資料，是中央氣象局衛星資料接收站所接收的繞極軌道衛星NOAA - 6 號在民國71年 4 月11 日格林尼治時間 10 時 17 分所觀測的 AVHRR 資料。區域範圍大約從東經 120°到 145° ，從北緯 5°到 35°左右，包含西太平洋一帶及我國沿海。

AVHRR 觀測的原始資料，經過校準之後，可計算出兩個紅外窗區頻道水汽訂正法，除去水汽吸收的影響。

本文中計算三塊海域的海面溫度（ 見圖 2 ）1 本省北部海域 2 本省東北部海域 3 關島東方海域。計算得到的本省東北部海域的海面溫度如圖 3 所示。

由於在廣大的洋面上，測站很少，而且船舶觀測的海水溫度又和衛星所觀測的表皮溫度基本上就有些微的差異，所以要將遙測得到的海面溫度加以驗證，是一件十分困難的事。但是，儘管有先天的缺點，我們仍可由衛星所遙測到的高分辨率的海溫，看出溫度梯度分佈的細微構造。

根據中央氣象局發佈的 4 月 11 日地面天氣圖（圖 2 ）日本 GMS 觀測的 4 月 1 日到 10 日的平均海溫圖（圖 4 ）以及台灣省水產試驗所發佈的海況旬報（圖 5 ，圖 6 ），本文所求得海面溫度平均誤差大約在 1 ℃到 2 ℃之間。

肆、結　　論

利用多窗區頻道水汽訂正法來除去水汽吸收的影響，一般說來中緯度地區的效果較低緯度地區要來得好些，這是因爲在低緯地區上空大氣中水汽較多之故。由於 3.7 μm 窗區頻道受反射陽光的影響相當厲害，爲了避免這種情形，只用夜間的觀測資料。因此，海面溫度遙測的幾個問題，諸如水汽訂正、陽光反射效應的濾除以及濾雲等，仍然是值得探討的問題。

由於近年來遙測技術的進步，氣象衛星已成例行觀測的工具。在佔地表三分之二的廣大洋面上，氣象測站稀少，嚴重影響這些地區的天氣分析與預報，但是氣象衛星卻可突破這種限制。人造衛星的發展過程，到現在只不過二十多年，衛星本身的技術和它的應用範圍，都還沒有達到極限。今後配合太空梭的發展，在衛星科技上一定有驚人的進展，隨着大氣遙測的進步，將使大氣科學進入一個新的紀元。

伍、致　　謝

在進行本研究的時候，得到中央氣象局衛星站多位同仁的協助，在這裏特別表示對他們的謝意。

陸、參考文獻

Anding, D. and R. Kauth, 1970: Estimation of sea surface temperature from space, Remote Sensing of the Environment, 1, 217-220.

Chedin, A., N. A. Scott, and A. Berroir, 1982: A Single channel double viewing angle method for sea surface temperature determination for coincident METEOSAT and TIROS-N radiometric measurements, J. Appl. Meteor., 21, 1005-1014.

McClain, E. P., 1981: Multiple atmospheric window techniques for satellite derived sea surface temperatures. In "Oceanography from Space" edited by J.F.R. Gower, Plenum 73-85.

Liou, K. N., 1980: An Introduction to Atmospheric Radiation. Academic Press.

Prabhakara, C., G. Dalu and V. G. Kunde, 1974: Estimation of sea surface temperature from remote sensing in ghe 11 to 13 um window region. J. Geophys. Res., 79, No.33, 5039-5044.

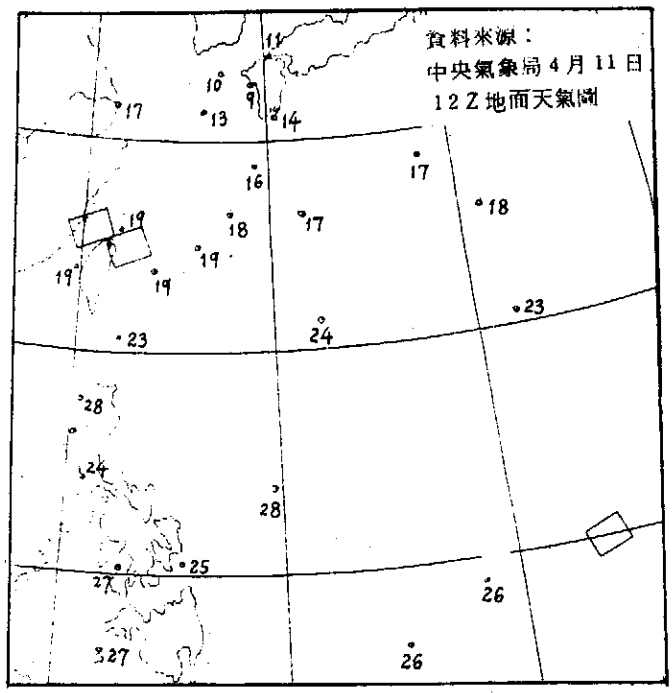

圖 2　計算海面溫度的海域和測站溫度

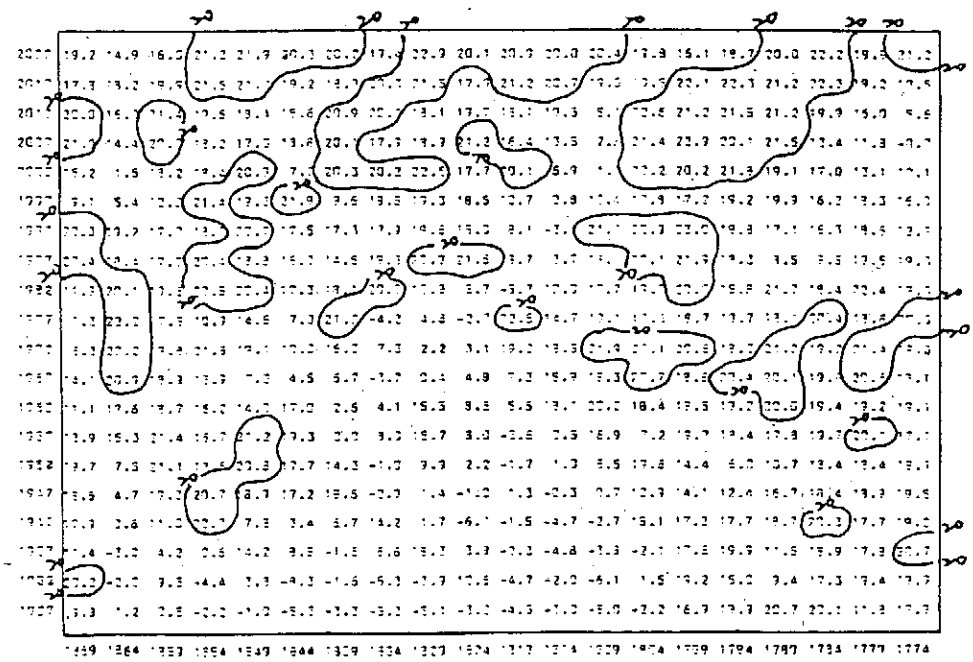

圖 3　本省東部海域的海面溫度

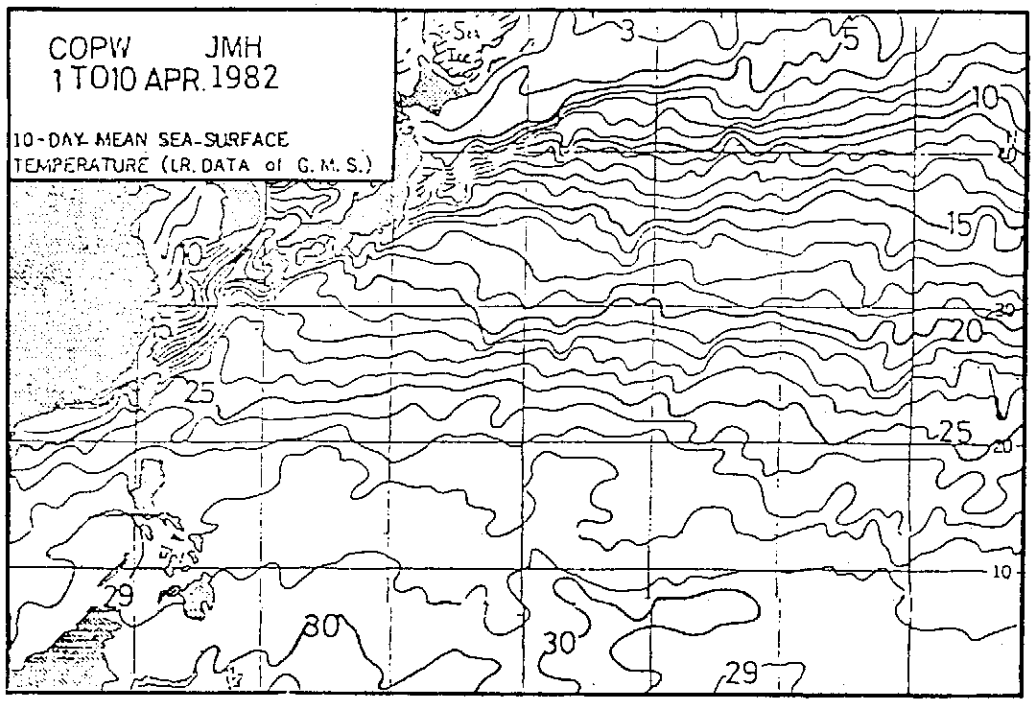

圖 4　GMS得到的4月上旬平均海面溫度

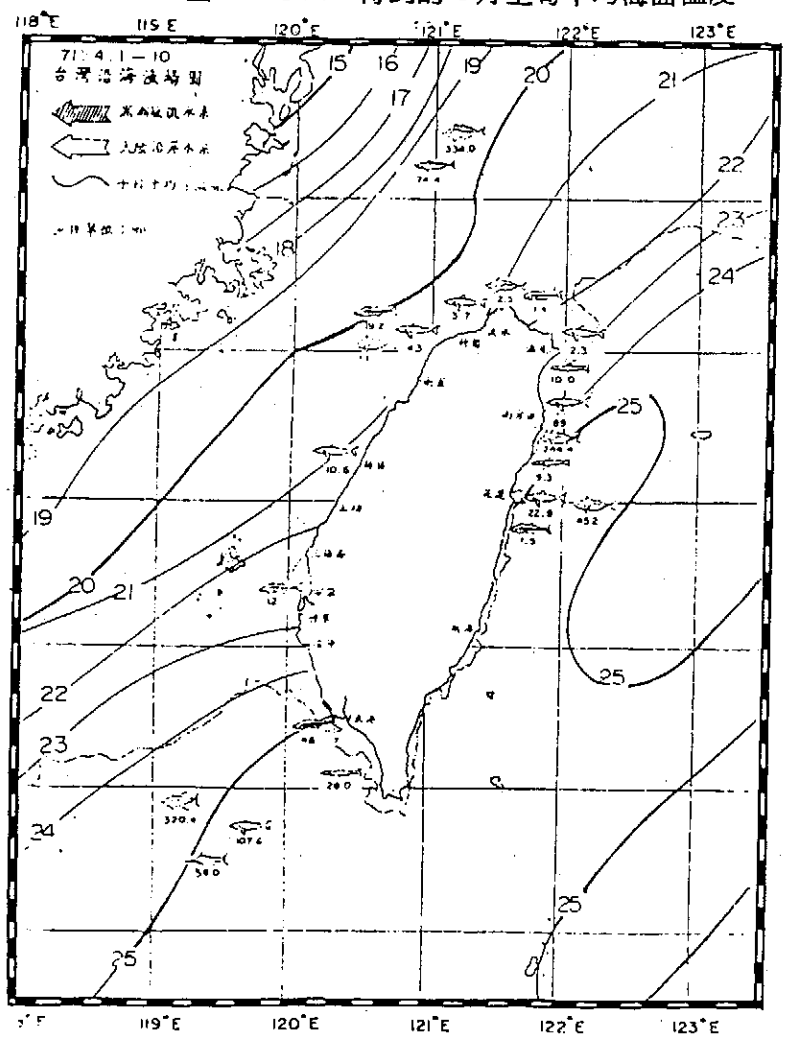

圖 5　台灣沿海漁場海面溫度

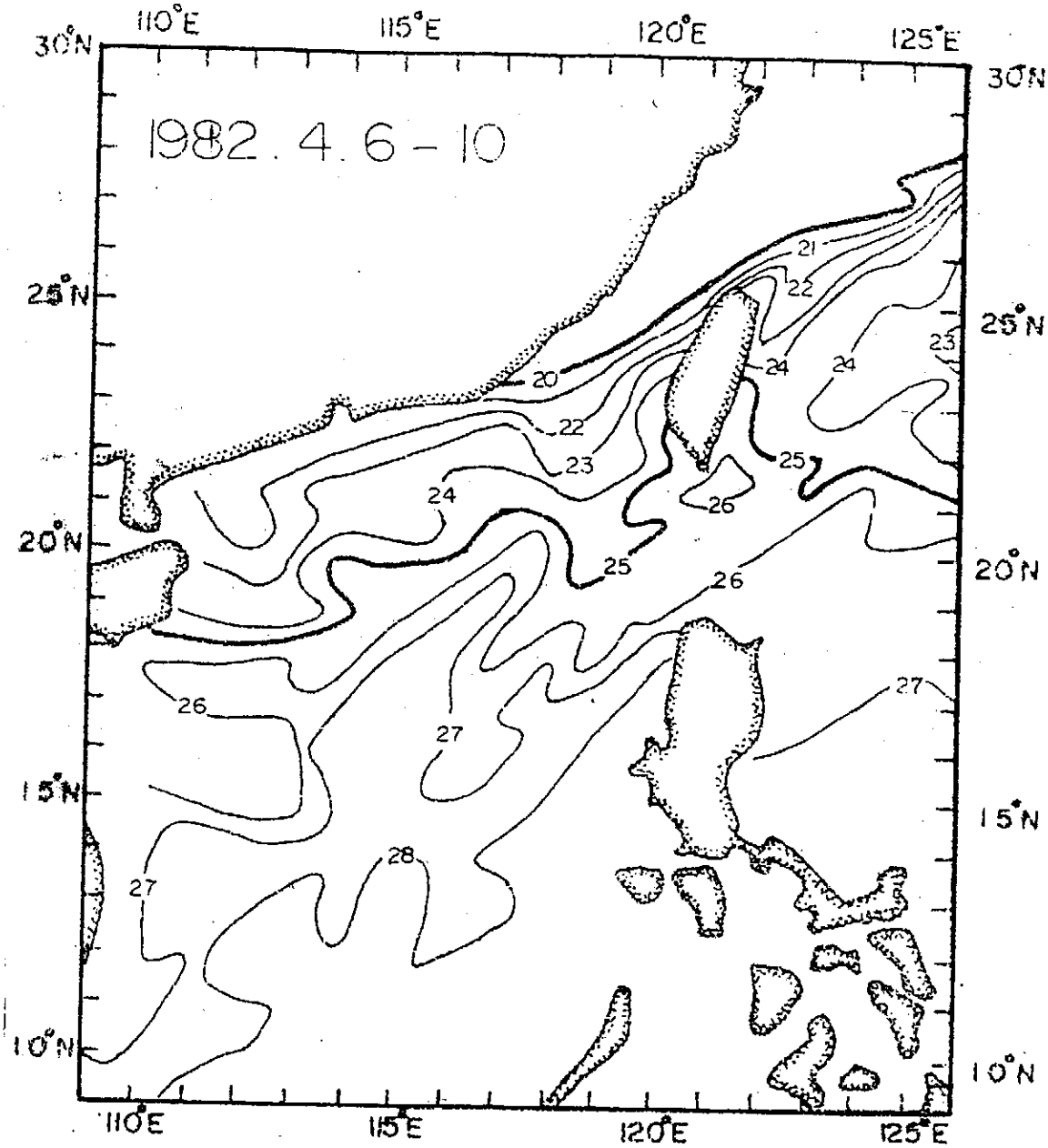

圖 6　台灣附近五日平均水溫圖

空氣品質監測系統之設置原理與應用

梁　文　傑

中央研究院物理研究所

台灣大學機械工程學研究所

林　釗　信

台灣大學環境工程學研究所

摘　要

本文利用大氣擴散模式，與統計原理建立點污染源空氣品質偵測網之設計法則，使偵測網能兼顧經濟與代表性。文中並以林口火力發電廠爲對象，進行空氣品質偵測網設計之個案研究。

本文以二種空氣污染物（二氧化硫和懸浮顆粒），二種風向方位區分（十六方位及三十六方位），三種最大地面濃度忍限值（$0.9C_{max}$，$0.8C_{max}$，$0.7C_{max}$）及四種可信賴區間（0.5，0.9，0.95，0.99）等狀況之組合，找出其測站應設置之地點及數目，以滿足各種需求。設計過程中採用模式參數簡化法，在良好的迴歸及檢定結果下，節省處理大量氣象資料所耗費之計算機時間。文中並分別討論各種情況（如測站數目有限，測站型式爲移動式等）之設計法及偵測網功能多元化之可能性。對於未來大型點污染源空氣品質偵測的進行，提供迅速有效的方法。文中並對未來研究方向提出檢討及建議。

壹、引　言

近年來，台灣地區因人口密集，工業急速發展，能源的需求量也日益增長，而火力發電則佔供應原的大宗，其可能造成的空氣污染問題需要加以評估，以供有關防制對策之參考。

欲評估電廠廠址周圍之環境空氣品質，必須先求得評估地區主要空氣污染物的濃度分佈，根據此結果，並參酌有關資料，對此地區可能發生的污染程度加以分析和評定，而評定的標準須符合空氣染管制機構所頒定的環境空氣品質標準。求取評估地區空氣污染物濃度分佈的主要工作有三，第一廠址地區氣象及其他有關資料的觀測、蒐集與分析，此項工作需要設置有關的氣象及污染物之測站統。第二爲適當大氣擴散模式的選取，並用以計算可能的濃度分佈情形。第三爲計算結果的校正，使所用的模式修正至與實際狀況達到最佳的反映與配合。因此，一個良好的評估，必須以相當足夠地間配合適當人力與物力來完成。由於資料良好爲良好評估的基礎，故如何設置適當的空氣品質偵網，遂成爲評估工作的先決工作。

以往偵測站的選址，常以經驗判斷和定性的規則來進行[1],[2],[3],[4],[5]。一般設計考慮之

因素如測站離地面高度，與附近建築物之距離，人口與測站數目的關係等。由此可了解，其設計大都是針對都會地區之空氣污染問題而發的。而以數值化方式從事偵測網設計方面，Singer [6] 早在1960年利用模式判別，某一種污染物質在某一固定的位置，若其率定值R（Rating）愈大，則表示此一定點愈不能夠做爲該污染物質偵測器設置之所在。其後，Seinfeld [7] 利用預定設站地點所得之空氣品質變化情形，與因污染源排放量減少所造成的空氣品質改變情形，二者應有相同程度的敏感度爲設計之基本觀念，在已知測站數目之條件下進行偵測網之設計。Hougland 等人 [8]，Lee 等人 [9],[10]，Nakamori 等人 [11] 則利用一些作業研究（Operation Research）的方法，將都市地區或工業城市，以網格系統區分，進而從事偵測網之設計。

對於大型點污染源，如火力發電廠，大型生產工廠排氣對附近空氣品質影響之偵測網設計，Noll 等人 [12],[13],[14] 所發展的設計原則，對單一點污染源或排放條件相同的多點污染源方面，經實證後，效果良好。而 Smith 等人 [15] 更提出能符合多項準則的設計方法，使偵測網功能多元化。

本文嘗試將 Noll 等人和 Smith 等人的設計原理合併，並根據美國 EPA 所訂定之設計準則 [16] 有關的規定，加上對排放條件各異的多點污染源修正法及各種簡化運算法，建立偵測網之設計方法，以減少大量計算機時間之負荷。進一步考慮在偵測站數目有限，且偵測站爲移動式之條件下，尋求獲致最大成功偵測機率之途徑，而完成偵測網之設計。

貳、大氣擴散模式

評估空氣品質時，因評估時間的長短、污染物種類、排放源型式及地形因素之不同，而有多種大氣擴散模式應運而生，如空氣品質展現模式（Air Quality Display Model，AQDM），氣候擴散模式（Climatological Dispersion Model，CDM），多排放源高斯煙柱之空氣品質運算法（Gaussian-plume Multiple Source Air Quality Algorithm, RAM），單一排放源模式（Single Source CRSTER Model），及德州氣候模式（Texas Climatological Model，TCM）等 [17]。

由上述各種模式之內容可發現，其皆導源於早期由 Sutton [18]，Pasquill [19] 等人，對於污染物質在流場中運動的數學推導及描述。後經 Gifford [20]，Martin 和 Tikvart [21]，及 Turner [22],[23] 之改良，而成爲簡易實用的高斯煙柱模式（Gaussian Plume Model）。此模式假定一連續排放之污染源，所釋出之污染物質，在大氣中經輸送及紊流之擴散作用，最後將達到一平衡狀態，此時煙柱中之污染物濃度，在垂直於風向之截面上呈雙向高斯分佈（Gaussian Distribution）。本文中所使用的大氣擴散模式，係以單一污染源模式（Single Source CRSTER Model；以下簡稱爲CRSTER模式）[24] 爲主體，並配合 Turner [23]，與 Busse 和 Zimmerman [25] 等人所改良之大氣擴散模式加以修正而得。

由於紊流之擴散及稀釋作用，與風速、風向及大氣熱力結構有關，而大氣熱力結構概要可由溫度、大氣穩定度及混合層高度所描述。因此，爲確實模擬污染物在大氣中之擴散現象，模式中所用的係數及標準偏差皆爲風速、風向、溫度、大氣穩定度及混合層高度之函數。其中常態分配函數之標準偏

大氣穩定度及下風距離之關係，爲簡化計算及避免人爲誤差起見，採用Green等人[26]所做的漸程式，以近似Turner[23]圖中之垂直及側向標準偏差值。

高斯煙柱模式

根據Seinfeld[27]，Csandy[28]及Veigele等人[29]的導證，衆所熟知的高斯煙柱模式爲：

$$C(x,y,z,H_e)=\frac{Q}{2\pi\sigma_y(x)\sigma_z(x)u}\exp\left[-\frac{1}{2}\frac{y^2}{\sigma_y^2(x)}\right]\cdot\left\{\exp\left[-\frac{1}{2}\frac{(Z-H_e)^2}{\sigma_z^2(x)}\right]+\exp\left[-\frac{1}{2}\frac{(Z+H_e)^2}{\sigma_z^2(x)}\right]\right\}\cdots[1]$$

Q爲污染物排放量，$\sigma_y(x)$爲側向擴散參數，$\sigma_z(x)$爲垂直方向擴散參數，H_e爲有效煙囪，即煙囪實際高度(H_s)與煙柱上升高度(Plume rise，Δh)之和，U爲在H_e處之平均風速爲下風距離，y爲側向距離，z爲垂直高度。

欲知地面污染物濃度，可令$z=0$，則〔1〕爲：

$$C(x,y,0,H_e)=\frac{Q}{\pi\sigma_y(x)\sigma_z(x)u}\exp\left[-\frac{1}{2}\frac{y^2}{\sigma_y^2(x)}\right]\cdot\exp\left[-\frac{1}{2}\frac{H_e^2}{\sigma_z^2(x)}\right],\quad\cdots[2]$$

若求煙柱中心線地面濃度，即$y=0$，則〔2〕爲：

$$C(x,0,0,H_e)=\frac{Q}{\pi\sigma_y(x)\sigma_z(x)u}\exp\left[-\frac{1}{2}\frac{H_e^2}{\sigma_z^2(x)}\right]\cdots[3]$$

CRSTER模式

CRSTER模式是由美國EPA所發展出來的，用以評估鄉村及都市地區，在非平坦地形情況也適一種穩定狀態高斯煙柱模式。其使用目的有三：

用於一至十九個點源在各不同平均時間，如一小時，二十四小時，至一年最大濃度值之計算。

用於形成最大濃度時氣象條件之決定。

貯存濃度資料，以利各種不同平均時間頻率之計算。

由於CRSTER模式具上述之功能，本文乃以其爲模式之主體，另輔以其他修正，使效用更加擴

CRSTER模徵假定大氣屬於穩定狀態，並且是均勻的，污染物排放爲連續且一致，所用的風向速爲一小時之代表值，渦流擴散係數(eddy diffusivity)爲定值，在垂直方向沒有風切(wind ar)每小時之濃度值相互獨立，沒有時間上的累積作用，在輸送過程中物質質量守恒，即沒有發學變化或沉降作用。

因有混合層作用的緣故，加上污染物與地表接觸後完全反射之假設，使得下風距離愈大者，其污

染物濃度值，因反射作用所佔的比例也愈大。CRSTER模式設定，當有效煙囪高度（H_e）大於混合層高度（L）時，污染物滯留於穩定的逆溫層中，對於混合層內之大氣沒有影響。當H_e小或等於L，且垂直方向擴散參數（σ_z）大於1.6 L時，則表示在某一下風距離（x）以後，其σ_z值超過1.6L，則任何大於x之下風距離，整個混合層內垂直方向，污染物濃度均勻分佈，但側向仍屬高斯分佈。當H_e小故等於L，且σ_z也小或等於1.6 L時，污染物呈雙向高斯分佈，且受逆溫層和地面造成反射作用所影響。

上述三種情形，可由下列方程式表示之：

當$H_e \leq L$，且$\sigma_z \leq 1.6\,L$時，

$$C(x,y,z,H_e)=\frac{Q}{\pi\sigma_y\sigma_z u}\exp\left[-\frac{1}{2}\left(\frac{y}{\sigma_y}\right)^2\right]\cdot \sum_{N=-\infty}^{N=-\infty}\exp\left[-\frac{1}{2}\left(\frac{H_e+2NL}{\sigma_z}\right)^2\right] \quad \cdots\cdots[4]$$

當$H_e \leq L$，且$\sigma_z > 1.6\,L$時，

$$C(x,y,z,H_e)=\frac{Q}{\sqrt{2\pi}\,\sigma_y Lu}\exp\left[-\frac{1}{2}\left(\frac{y}{\sigma_y}\right)^2\right], \quad \cdots\cdots[5]$$

當$H_e > L$時，

$$C(x,y,z,H_e)=0. \quad \cdots\cdots[6]$$

三、CRSTER模式之修正及各有關擴散參數選用之考慮

由〔4〕，〔5〕二式可知，CRSTER 模式對於污染物在輸送過程中，可能產生的化學反應及沉降作用並未考慮。事實上，就沉降作用而言，一般浮游塵（Aerosol）之沉降速度大約爲$10^{-6}\sim10^{-1}$ m/sec，而大氣層最低的一百公尺範圍內，一般風速值約爲1～10 m/sec[30]，沉降效應往往要距污染源（非地面排放者）10～20 km，才會對污染物濃度值的計算有所影響。因此，本文在模式計算過程中，沉降作用忽略不計。

SO_2和懸浮顆粒是火力發電廠排煙中，最主要的兩種空氣污染物質。其中懸浮顆粒常被認定爲惰性物質，本文在計算其擴散分佈時，也保留這項觀點，不考慮懸浮顆粒有任何化學作用發生。但根據Newman，Forrest和Manowitz等人的研究[31],[32]，發現不論懸浮顆粒之物理性質（即顆粒之粒徑分佈）或化學性質（即所含之金屬成分如F_e、M_n、C_u、V等），對於SO_2之化學反應有極大的影響。前者在相對濕度超過70％情況下，會左右SO_2溶於水汽之速率，而後者則是SO_2發生化學變化的催化劑。因此，SO_2在煙氣擴散過程中，所產生的化學衰變現象必需加以考慮。一般假定其爲一階反應，而衰減情形可由下式表示之[17]：

$$D(X)=\exp\left(\frac{-0.692\,X}{U_{He}\,T_{1/2}}\right), \quad \cdots\cdots[7]$$

式中，X爲下風距，$T_{1/2}$ 爲污染物之半生期（ half-life ），U_{He} 爲有效煙囪高度處之平均風速。

$T_{1/2}$ 值往往因氣象、地點等因素而異。Turner [22] 認爲 SO_2 在市區範圍之 $T_{1/2}$ 爲四小時，而 Weber [31] 則定爲 20 分鐘至 1 小時，需視氣象條件而定。另外，根據 Flyger 等人 [32] 對燃油及燃煤兩種火力發電廠所做的實驗調查，發現前者之 $T_{1/2}$ 值爲 30 分鐘，後者則爲 90 分鐘。因本文個案研究中，林口發電廠 SO_2 主要排放量由燃油所造成，而採用 $T_{1/2}$ 值爲 30 分鐘，代入〔7〕式中，則成或爲：

$$D(x) = \exp\left(-\frac{0.692\,X}{U_{He} \times 1.8}\right) \qquad \cdots\cdots〔8〕$$

式中，X之單位爲公里。

當考慮有化學衰減發生的情況，〔8〕式必需乘入〔4〕和〔5〕式中。

此外，〔4〕式中之 H_e，代表有效煙囪高度，爲煙囪實際高度（ H_s ）與煙柱上升高度（ Δh ）之和。Δh 可根據 Briggs 之⅔定律 [24] 求之，即

$$\Delta h = 1.6\,F^{1/3}\,(3.5X^*)^{2/3}\,U_{He}^{-1}\ , \qquad \cdots\cdots〔9〕$$

式中，$F = gV_s\left(\frac{d}{2}\right)^2\frac{T_s - T}{T}$（ $m^4\,sec^{-3}$ ）爲浮力參數，V_s 煙氣排放速度（ m/sec ），d 爲煙囪內徑（m），T_s 爲煙氣溫度（°K），T爲大氣溫度（°K），X^* 爲大氣紊流發展距離（m），X^* 值之計算依F值而定，即

$$X^* = \begin{cases} 14\,F^{5/8}\ , & \text{當 } F < 55\,m^4\,sec^{-3} \\ 34\,F^{2/5}\ , & \text{當 } F \geq 55\,m^4\,sec^{-3}\ , \end{cases} \qquad \cdots\cdots〔10〕$$

由於氣象條件之易變性，H_e 並非定值，故 U_{He} 值無法一一實地量測。一般利用風速垂直方向剖面之關係，以冪定律根據地面觀測資料，推算 H_e 處之風速值，其型式如下：

$$U_{He} = U_{10}\left(\frac{H_e}{10}\right)^{p(s)}\ , \qquad \cdots\cdots〔11〕$$

式中，U_{10} 表距地面 10^m 處之風速，p(s) 爲風速剖面指數，其爲大氣穩定度之函數，p(s) 值如（表一）所示。

參、偵測網設計原理

對於大型之點污染源，爲了解其對週遭空氣品質的影響，進而研擬防制策略所需要的空氣品質偵測網。一般以偵測污染源在各種氣象條件下，可能發生之最大地面濃度，及其可能發生之頻率，利用過去的氣象資料，如風向、風速、氣溫、大氣穩定度、混合層高度等，配合選用之大氣擴散模式，所需之各項排放源資料，進行計算，求得之各種條件下可能最大地面濃度值，與空氣污染管制機構所訂定之該項空氣污染物標準限值比較，根據 Noll 等人 [12], [13], [14] 所發展的理論，可以定出偵測潛勢區域（ Potential Monitoring Zone ）。另外，由計算所得之最大地面濃度值（ C_{max}），可以依偵

測儀器所能代表之面積，即根據偵測目的與經濟條件間之權衡，定義出由 $0.9\,C_{max}$ 、$0.8\,C_{max}$ ，甚至 $0.7\,C_{max}$ 等濃度線所涵蓋的區域爲單一測站之覆蓋面積（ Coverage Area of Station ），其與偵測潛勢區域之比值，則稱爲單一測站之覆蓋比（ The Coverage Ratio for One Station，CRs）。

我們可以用二項分配（ Binomial distribution ）來描述，當一個測站設於單一測站之覆蓋面積內，其對過去各種氣象條件組合產生最大濃度之某一種聯合出現頻率（ Joint Frequency of Occurence ），在各種可信賴度（ Confidence level ） 限制下，所能有效地偵測之機率，則定義此項機率爲達成預定結果之總覆蓋比（ Total Coverage Ratio，CR_T ）。因此，對於某一聯合出現頻率而言，所需要的測站數目（ NN ），在某一可信賴區間內，即爲 CR_T 與 CR_S 之比值。

一、單一污染源空氣品質測網之設計方法

根據Turner [23] 中圖 3－5A～3－5F，所描述在各種有效煙囪高度、混合高度，穩定度由A至F的正常化濃度（ Normalized Concentration ）CU/Q（單位爲 m^{-2} ）與下風距離X（單位爲 km ）之關係，其主要部份〔 3 〕式所描述者，而混合層影響部份，暫時不予考慮，可能造成的誤差，將於本章第五節再加說明。

我們可於Turner 所做之圖，如（圖一），首先訂出各有效煙囪高度所對應之CU/Q最大值，假設在風速U及排放強度Q保持一定下，所對應於橫軸之值，即發生最大地面濃度之所在（ X_{max} ），再將各CU/Q最大值，令爲（ CU/Q ）$_{max}$，各乘以0.9後，劃線於 0.9（CU/Q）$_{max}$之位置，由此可在曲線上交得兩點，分別對應於橫軸，交橫軸上兩點，各表示接近及遠離排放源，濃度爲$0.9\,C_{max}$之所在，分別以 X_{90}^{-} 和 X_{90}^{+} 表示。同理，也可分別得到 X_{80}^{-} ，X_{80}^{+} 和 X_{70}^{-} ，X_{70}^{+} 各值。

由（圖一）可看出，各 H_e 值線上之 X_{90}^{-} ，X_{max} ，X_{90}^{+} 之連線，幾乎呈一直線，這種情況可和Turner [23] 中圖 3－9 相互印證。由 X_{90}^{-} 故 X_{90}^{+} 與CU/Q之關係，同樣也可延用於 X_{90}^{-} 或 X_{90}^{+} 與 X_{max} 之關係，即在雙對數座標上，以橫軸表 X_{max} 值，而豎軸表 X_{90}^{-} ，X_{90}^{+} 值，二者之關係，可以一直線近似之。爲便於計算機之作業，乃以，$X_{90}^{-} = a\,X_{max}^{b}$ 或 $X_{90}^{+} = a'\,X_{max}^{b'}$ 方成模擬，其中 a ，b ，a′ ，b′ 可利用最小二乘法求得，廻歸之結果列於（表二）。同理，可作 $0.8\,C_{max}$ 及 $0.7\,C_{max}$ 兩種情形，如（表三、表四）所示。

其次考慮污染物在側向擴散的情形，其可由下式表示之：

$$C(x,y,o,H_e) = \frac{Q}{\pi\sigma_y\sigma_z u}\ \exp\left[-\frac{1}{2}\left(\frac{y}{\sigma_y}\right)^2\right]\cdot \exp\left[-\frac{1}{2}\left(\frac{H_e}{\sigma_z}\right)^2\right], \quad \cdots\cdots[12]$$

設當 $C = 0.9C_{max}$ 時，$y = y_{90}/2$ ，代入上式：

$$0.9\,C_{max} = \frac{Q}{\pi\sigma_y\sigma_z u}\ \exp\left[-\frac{\left(\frac{y_{90}}{2}\right)^2}{2\sigma_y^2}\right]\cdot \exp\left[-\frac{1}{2}\left(\frac{H_e}{\sigma_z}\right)^2\right], \quad \cdots\cdots[13]$$

將〔13〕式以〔 3 〕式除之，則

$$0.9 = \exp\left[-\frac{y_{90}^2}{8\sigma_y^2}\right],$$

或 $$y_{90} = 0.92\,\sigma_y \quad \cdots\cdots [14]$$

同理 $C = 0.8\,C_{max}$ 時，$y_{80} = 1.34\,\sigma_y$，$\cdots\cdots [15]$

$C = 0.7\,C_{max}$ 時，$y_{70} = 1.69\,\sigma_y$，$\cdots\cdots [16]$

〔14〕、〔15〕、〔16〕三式中之 σ_y 值，可根據Green 等人[26]對 σ_y、σ_z所做的漸近方程式，如〔17〕、〔18〕二式求之，

$$\sigma_y = \frac{WX}{\left[1+\frac{X}{A}\right]^p}, \quad \cdots\cdots [17]$$

$$\sigma_z = \frac{VX}{\left[1+\frac{X}{A}\right]^q}, \quad \cdots\cdots [18]$$

上二式中，W、V、A、p、q 皆爲常數，隨大氣穩定度而異，其值列於（表五），而 y_{90}、y_{80}、y_{70}與X之關係亦因之確定。

由 $0.9\,C_{max}$、$0.8\,C_{max}$ 或 $0.7\,C_{max}$ 等濃度線所圍成之封閉平面，可利用橢圓公式求其面積，即

$$A_s = \frac{\pi}{4}\left(X_j^+ - X_j^-\right) y_j, \quad \cdots\cdots [19]$$

此處，A_s 爲單一測站覆蓋面積，j 爲90、80、70三種情況。

若不考慮化學衰減及混合層之作用，將〔17〕、〔18〕二式代入〔3〕式中，則

$$C(x,o,o,H_e) = \frac{Q\left(1+\frac{X}{A}\right)^{p+q}}{\pi WVUX^2} \exp\left[-\frac{1}{2}\,\frac{H_e^2\left(1+\frac{X}{A}\right)^{2q}}{V^2X^2}\right], \quad \cdots [20]$$

微分上式可得：

$$\left[(p+q-2)X-2A\right] - \frac{H_e^2}{V^2X^2}\left(1+\frac{X}{A}\right)^{2q}\cdot\left[(q-1)X-A\right] = 0, \cdots [21]$$

上式可用半間距法（Interval-Halving method）解X，再將X值代入〔20〕式，則可得 C_{max} 值。

若考慮化學衰減產生（可用於 SO_2 濃度之計算），但不考慮混合層之作用，將〔17〕、〔18〕二式代入〔3〕式，並併進〔8〕式，則

$$C(x,o,o,H_e) = \frac{Q\left(1+\frac{X}{A}\right)^{p+q}}{\pi WVUX^2} \exp\left[-\frac{1}{2}\,\frac{H_e^2\left(1+\frac{X}{A}\right)^{2q}}{V^2X^2}\right] \cdot \exp\left[-\frac{0.692\,X}{UT_{1/2}}\right], \quad \cdots\cdots [22]$$

將〔22〕式，對X微分，並令其結果爲0，則得到

$$[(p+q-2)-2A]-\frac{H_e^2}{V^2X^2}\left(1+\frac{X}{A}\right)^{2q}[(q-1)X-A]$$

$$-\frac{0.692X(X+A)}{UT_{1/2}}=0 \quad , \qquad \cdots\cdots\cdots\

統計量 z ，

$$Z=\frac{n-NP}{\sqrt{NP(1-P)}} \quad , \qquad \cdots\cdots [28]$$

上式中 Z 表示一呈常態分配之隨機變數。當 $N\to\infty$ 時，其分佈函數如下式所示：

$$F(Z)=\int_{-\infty}^{Z}\frac{1}{\sqrt{2\pi}}\rho^{-1/2t^2}\,dt \quad , -\infty<Z<\infty , \qquad \cdots\cdots [29]$$

我們可按需要，選取適當的可信賴區間（ Confidence Interval , α ），則可求得 F(Z) 值，再查一般的統計圖表，即求得 Z 值，加以預先設定之 n 值及計算所得之 N 值，故未知數只有 P （即 CR_T 值），將 Z ，n ，N 代入〔28〕式，即可解出 CR_T 值。

由前面之定義知，在某一特定氣象條件組合情況下所需之測站數目（ NN ），即爲：

$$NN=\frac{CR_T}{CR_s} \quad . \qquad \cdots\cdots [30]$$

二、對多點污染源之修正法

1 各組成之點污染源有相同排放高度者

若各點污染源間之距離遠小於模式計算所感興趣之長度尺度，則可認爲是在同一位置排放，但具有多個煙氣出口而已。由於排放條件一致，且所在位置相同，對於下風處任一位置 X 而言，各污染源所造成之濃度值，可疊合相加（ Superposition ），且不用考慮時間序列的影響，而總濃度爲：

$$C(X)=\sum_{j=1}^{N} q_j V_{jx} \qquad \cdots\cdots [31]$$

式中，N 爲排放源數目，q_j 爲第 j 個排放源之強度，V_{jx} 則表示第 j 個排放源對位置 X ，所造成的污染濃度，即擴散函數。

根據 Montgomery 等人[34] 之研究，在上述情況下，排放源數目之增加，對下風位置污染濃度的增長，需乘上 $N^{4/5}$ 即可修正。排放源數目（N），與所對應之修正因子（$N^{4/5}$），如（表七）所示。

2 排放條件不一且排放源高度有顯著差異者

在實際情況下，被視爲在同一排放位置的各個點污染源，其排放條件（ 如煙氣排放速率 V_s ，煙囪內徑 d ，煙氣溫度 T_s ，排放強度 Q … ）往往有很大的差異，而煙囪高度也不一定相同，故前節之假設常無法成立。

本文欲以多項式模擬多點污染源排放，在我們有興趣的下風距離內的行爲。設有 N 個點污染源存在，其排放條件皆異，根據本章第一節之計算知，必有 N 個 O_{max} 和 N 個 X_{max} 產生。就某一固定之下風距離而言，各點污染源的影響，應須滿足〔31〕式。

假設第 i 個污染源，其 X_{max} 值最小 ，即最接近排放位置，令其爲 X_1 ，而其濃度值爲 C_1 。同理，按距排放位置之近遠順序，依次爲 X_2 ，C_2 ；X_3 ，C_3 ；…；X_N ，C_N 。因此，在 X_1 與 X_N 之間，必有一點爲各污染源合成作用產生最大地面濃度之所在。

對X_1至X_N這個區間而言，所有污染源排放之合成濃度與下風距離之關係，本文用一個（N－1）次之多項式來模擬，即

$$C(x) = f_1 x^{N-1} + f_2 x^{N-2} + \cdots + f_{N-1} x + f_N \quad \cdots\cdots [32]$$

其中，x爲x_1至x_N內之下風距離，f_1、$f_2 \cdots f_N$爲迴歸係數。對第一個排放源而言，令其在x_1至x_N區間內所造成的地面濃度值分別爲C_{11}，C_{12}，C_{13}，…，C_{1N}，其方程式爲：

$$C_{11} = F_{11} x_1^{N-1} + F_{12} x_1^{N-2} + \cdots + F_{1,N-1} x_1 + F_{1N} \quad , \quad \cdots\cdots [33,1]$$

$$C_{12} = F_{11} x_2^{N-1} + F_{12} x_2^{N-2} + \cdots + F_{1,N-1} x_2 + F_{1N} \quad , \quad \cdots\cdots [33,2]$$

$$\vdots \qquad \vdots \qquad \vdots \qquad \cdots\cdots \qquad \vdots \qquad \vdots \qquad \vdots$$

$$C_{1N} = F_{11} x_N^{N-1} + F_{12} x_N^{N-2} + \cdots + F_{1,N-1} x_N + F_{1N} \quad , \quad \cdots\cdots [33,N]$$

由以上N個方程式，聯立可解出係數F_{11}，F_{12}，……，F_{1N}，故對第一個排放源而言，其濃度與下風距離之關係爲：

$$C_1(x) = F_{11} x^{N-1} + F_{12} x^{N-2} + \cdots + F_{1,N-1} x + F_{1N} \quad , \quad \cdots\cdots [34,1]$$

同理，對於其他排放源，也可依次得到，

$$C_2(x) = F_{21} x^{N-1} + F_{22} x^{N-2} + \cdots + F_{2,N-1} x + F_{2N} \quad , \quad \cdots\cdots [34,2]$$

$$\vdots \qquad \vdots \qquad \vdots \qquad \cdots\cdots \qquad \vdots \qquad \vdots \qquad \vdots$$

$$C_N(x) = F_{N1} x^{N-1} + F_{N2} x^{N-2} + \cdots + F_{N,N-1} x + F_{NN} \quad , \quad \cdots\cdots [34,N]$$

由以上N個方程式及〔32〕式可知，在x_1至x_N內之某一位置x_i，必有以下之關係存在，即

$$C_i = C_{1i} + C_{2i} + \cdots + C_{Ni} \quad , \quad \cdots\cdots [35]$$

$$f_1 = F_{11} + F_{21} + \cdots + F_{N1} \quad , \quad \cdots\cdots [36,1]$$

$$f_2 = F_{12} + F_{22} + \cdots + F_{N2} \quad , \quad \cdots\cdots [36,2]$$

$$\vdots \qquad \vdots \qquad \vdots \qquad \cdots \qquad \vdots \qquad \vdots$$

$$f_N = F_{1N} + F_{2N} + \cdots + F_{NN} \quad , \quad \cdots\cdots [36,N]$$

故在x_1至x_N範圍內，發生最大地面濃度位置X_{max}可由下式求之，即令：

$$\frac{\partial C}{\partial x} = 0 \quad , \quad \cdots\cdots [37]$$

由上式及〔32〕式可得，

$$(N-1) f_1 x^{N-2} + (N-2) f_2 x^{N-3} + \cdots + f_{N-1} = 0 \quad , \quad \cdots\cdots [38]$$

解〔38〕式，即可求得X_{max}值，代入〔32〕式，則得C_{max}值。

一般N值不大，故上述之修正法，可迅速解出各個迴歸係數，此項模擬效果之檢定，將在本章第四節詳加說明。

三、測站選址準則之修正

1.由平均時間增長影響單一測站覆蓋比（CR_s）之考慮

由y_{90}、y_{80}、y_{70}之計算可知，其爲σ_y之函數。由Turner [23] 中知，（圖二）及（圖三）中之σ_y及σ_z值，只能代表採樣時間爲10分鐘左右的結果。由於一般空氣品質標準限值常以一小時

平均值、三小時值、八小時值，甚至二十四小時值表示[35],[36]，而本文計算濃度值，爲能比較起見，是以小時平均值表示，故對於平均時間的增長，要有所修正。

根據Hino[37]及Pasquill[19]之研究，發現：

$$C_{max} \propto \tau^{-0.5} , \quad \cdots\cdots [39]$$

$$C_{max} \propto \left(\frac{\sigma_z}{\sigma_y}\right) , \quad \cdots\cdots [40]$$

在渦卷（eddy）τ_y，τ_z存在時間之限制下，煙柱寬度σ_y、σ_z必隨採樣時間之增長而加大，但在低層大氣中，流體在垂直方向的運動受地表存在而受限，經實驗證明[37]可知，τ_z遠小於τ_y，故由〔39〕、〔40〕二式，可推知

$$\sigma_y \propto \tau^{0.5} . \quad \cdots\cdots [41]$$

在各種平均時間與10分鐘相比，所須乘入之修正係數，如（表八）所示。在計算CR_s時，必須考慮此項修正，否則造成測站數目（NN）值之誤差。

2 大氣擴散模式中混合層項運算之修正

根據Turner[23]之研究，當煙柱型態爲集烟型（Trapping）時，必須考慮逆溫層的影響，而大氣擴散模式之形式應爲〔4〕式。由於該式爲一無窮級數，且當反射次數增加時，〔4〕式中之級數項收斂很快，故Turner建議，只需取反射次數（N）爲3或4，即可達到相當的準確度。

由於本文利用模式之主要目的是計算可能的X_{max}及C_{max}值，取N＝3或4後之〔4〕式，仍嫌冗長而不利使用。據Yamartino[38]之研究，當σ_z與混合層高度（L）之比值小或等於0.63時，將〔4〕式中，取$|N| \leqslant 1$（即N＝0，±1），計算結果，與原式比較，誤差小或等於1.3％。另發現計算之誤差與（H_e/L）及（σ_z/L）值有很大的關連。由於利用最簡單的高斯模式〔3〕式導出求X_{max}之公式，即〔21〕或〔23〕式，在計算機作業而言，因氣象資料繁鉅，上述二式已算是相當耗時之計算，故取$|N| \leqslant 1$時，對計算上而言，仍嫌過長。

根據Pasquill[39]之研究結果，利用〔3〕式所得之濃度值，在各種（H_e/L）及（σ_z/L）值條件下，其與〔4〕式計算結果之比值，列於（表九）。本文利用〔21〕或〔23〕式，初步計算X_{max}及C_{max}後，根據每次計算所得之（H_e/L）及（σ_z/L）值，再利用（表九），即可查出或利用內插法找出誤差值，將計算所得之C_{max}值除以〔3〕式佔〔4〕式之比例值，即可修正未考慮混合層作用所造成的誤差。

3 利用圖形交疊法選取最佳之測站位置

根據美國EPA的「空氣品質偵測網設計指引」[16]所建議，空氣品質偵測網之初步設計，應以單獨一種污染物爲對象，然後再根據操作後所得的詳細資料，加以研究改進，將不適當的測站重新定位。這種做法，比增加偵測站數目來得經濟，同樣地，也可達到所要求的成效。本文首先對二氧化硫（SO_2）單獨設計，用來找偵測潛勢區域（A_p）的空氣品質限值爲0.3、0.25、0.20 ppm三種。風向方位區分有十六方位及三十六方位兩種，後者是以能更準確地算出污染物最大濃度發生頻率爲著眼點而加入的。在此，並以SO_2有化學衰減發生爲考慮對象，此外，求CR_T時所取用的可信賴區間（α）

爲 0.5 、0.9 、0.95 、0.99 等四種情形。

對火力發電廠排煙中，另一種主要污染物懸浮顆之偵測網設計，除了不考慮化學衰減情況，及空氣品質限值另定之外，其餘條件與對 SO_2 設計時相同。

爲使偵測網具有多項功能，即能符合經濟、有效、適合多種污染物偵測之需要。我們可將上述各種情況組合之設計結果，分別以相同比例作圖，然後可依實際需求將其中數張圖或全部重疊，即可找出適合要求的空氣品質偵測網配置方式。

另根據Smith 等人[15] 之建議，若測站預定位置位於(1)不易接近，(2)電力缺乏，(3)安全不足，(4)私人產業範圍等地點時，則將設站之考慮刪除，本文不擬作上述事項之考慮。

4. 偵站爲移動式且數量有限時之偵測法則

當測站數目有限時，爲能獲至最大偵測成效，本文利用本章前述之設計法則，在〔30〕式中，NN 值已知條件下，將未來數日之氣象預報資料及排放源資料，與利用過去長期資料之計算結果相比較，可迅速查出各種情況之 C_{max} 、X_{max} 及 CR_s 值。再選出未來數日，發生超過某一空氣品質限值之最高頻率者，進一步挑出其 CR_s 值最大者，在 NN 值固定條件下，即可判定所得之 CR_T 爲最小值，再利用〔28〕式，依所需之可信賴區間（α 值）可查得 Z 值，故可調整 n 值，逐步計算使所得之 CR_T 值與上述之 CR_T 值近似（可定二者之差值小於某一定值即可）。由此可獲得在 NN 值已知條件下，對於可能產生 N 次違反限值之某一氣象條件組合，其能夠成均地偵測之最高次數。

一般天氣變化，以一週至十日爲一個週期。因此，可根據氣象預報，事先算出所需之資料，找出能獲得最大 n 值之所在，而派遣移動測站進駐。

四、各設計因子之迴歸及檢定方法

本文使用的迴歸形式有二，一爲用於 $\bar{X_j}$，X_j^+ 與 X_{max}（其中 j = 90 、80 、70）關係之迴歸法，即採用對數最小二乘法迴歸。另一爲用於模擬多點污染源排放計算之多項式迴歸法。

爲了檢定迴歸效果之良窳，本文採用兩種檢定法，即：

(1)相關係數（r）之檢定，r 值可由下列諸式求之：

$$r = \frac{S_{xy}}{\sqrt{S_{xx} S_{yy}}} \quad , \qquad \cdots\cdots〔42〕$$

其中，

$$S_{xx} = n \sum_{i=1}^{n} x_i^2 - \left(\sum_{i=1}^{n} x_i \right)^2 \quad , \qquad \cdots\cdots〔43〕$$

$$S_{yy} = n \sum_{i=1}^{n} y_i^2 - \left(\sum_{i=1}^{n} y_i \right)^2 \quad , \qquad \cdots\cdots〔44〕$$

$$S_{xy} = n \sum_{i=1}^{n} x_i y_i - \left(\sum_{i=1}^{n} x_i \right) \left(\sum_{i=1}^{n} y_i \right) \quad , \qquad \cdots\cdots〔45〕$$

式中，x_i 爲實測值（在本文中則爲模式計算值），y_i 爲迴歸值，而 n 爲樣本數。

(2) F 檢定，F 值可由以下諸式決定之：

$$F=\frac{MS(T_r)}{MSE}\quad,\qquad\cdots\cdots[46]$$

其中，$$MS(T_r)=\frac{SS(T_r)}{(k-1)},\qquad\cdots\cdots[47]$$

$$MSE=\frac{SSE}{k(n-1)}\quad,\qquad\cdots\cdots[48]$$

$$SST=\sum_{i=1}^{n}\sum_{j=1}^{n}y_{ij}^2-C\quad,\qquad\cdots\cdots[49]$$

$$SS(T_r)=\frac{\sum_{i=1}^{k}T_i^2}{n}-C\quad,\qquad\cdots\cdots[50]$$

$$SSE=SST-SS(T_r)\quad,\qquad\cdots\cdots[51]$$

$$C=\frac{T^2}{Kn}\quad,\qquad\cdots\cdots[52]$$

$$T=\sum_{i=1}^{k}\sum_{j=1}^{n}y_{ij}\quad,\qquad\cdots\cdots[53]$$

其中，K爲集團數（本文中K＝2，只有模式值及迴歸值），n爲集團中之樣本數，y_{ij}爲樣本值（即模式值和迴歸值）。

取模式計算中任一組氣象資料，配合排放源資料，進行多項式迴歸及檢定，結果如（表十）所示。顯示上述之迴歸方式效果極佳。

肆、污染排放調查及氣象資料分析

一、林口地區概述

本文中所稱的「林口地區」，是指台北縣、桃園縣沿海地區的林口、蘆竹、大園、觀音等鄉鎮，如（圖二十一）。本區地形以台地爲主，氣候屬於台灣西北部氣候區，1980年全年平均氣溫22.1℃，二月平均氣溫最低（14.4℃），而七月則高達29.9℃，相對濕度之年平均值爲75.7%。風向在平時以海陸風交替爲主，至冬季則以東北風爲主。1980年一般氣象資料之月平均值，如（表十一）所示。

林口發電廠位於台北縣林口鄉下福村的海邊，北面朝海，其位置爲東經121°17′36″，北緯25°07′24″。其東連接林口台地，東面爲台北盆地邊緣的龜山鄉。電廠西側及西南角微角向北傾，西南面寬廣的濱海平原是桃園縣主要農作地區之一。近年來有許多大型的建設在這一帶出現，包括桃園煉油廠、中正國際機場及大園特殊工業區等。貫穿本省西部的南北高速公路，從本區東南側穿過，形成了一道人爲的界線。

二、林口火力發電廠之污染排放調查

1. 電廠概況

林口電廠是以燃煤和燃油發電的火力電廠，自民國五十七年四月開始運轉第一部機組後，即不斷地擴充發電容量，現有一號機，容量三十萬瓩，爲燃煤機組。二號機容量三十萬瓩，爲燃油機組。另有十部各六千瓩的柴油機組，和四部各七萬二千瓩的氣渦輪機組。今後更將增設一低級煤電廠，容量爲五萬瓩。本文所使用的各項排放資料，取自台電公司所供應者[40]，而排放強度（Q）則是根據資料加以推算而得。

2. 二氧化硫排放量

排煙中的二氧化硫會有部份遺留在靜電集塵器、加熱器與煙道上，但爲保守估計，假設沒有上述之滯留，則二氧化硫排放量可估算如下：

二氧化硫排放量＝2×燃料用量×燃料含硫分， ……〔54〕

上式可用於一號機、二號機及柴油機組之排放量計算。因氣渦輪機組爲應付尖峯發電量時所使用，在本文中不予列入計算。本文計算所得之各機組二氧化硫排放量，以100％出力情況爲準，結果列於（表十二）。

3. 懸浮顆粒排放量

因一號機以燃煤爲主，故懸浮顆粒主要是由一號機排出，而一號機之靜電集塵器平均效率僅爲45％。本文假設燃料所含灰分之85％經燃燒後變成飛灰逸出，則懸浮顆粒之排放量可由下式估算之：

懸浮顆粒排放量＝燃料用量×燃料含灰分×80％×55％ ，……〔55〕

懸浮顆粒排放量之估算結果同列於（表十二）。

4. 其他排放資料

所謂其他排放資料，乃指大氣擴散模式計算所需之有關排放源資料，如煙囪高度（H_s），煙囪內徑（d），排氣速度（V_s），排氣溫度（T_s）等，亦列於（表十二）。

5. 二氧化硫濃度之測定

爲檢核本文所使用模式，擬取用七十年三月下海湖測站之二氧化硫日平均值，與當月之模式計算值比較。該測站之二氧化硫濃度測定，係採用導電度法（Automatic Conductimetric Method）[41]。測站資料係直接由電動自記式記錄紙上讀出逐時資料，再加以計算而得。

三、氣象資料分析

本文所使用的氣象資料，皆取自交通部民航局中正國際機場之地面觀測原始資料，包括1980年全年及1981年3月二部分，經逐時截取後，各項資料處理分述如下：

1. 風向

一般習慣將風向劃分爲十六個方位，以正北爲16，每個風向範圍爲22.5°。由於原始資料中，風向以每10°爲一單位，本文爲符合資料來源及尋求模式計算結果精確，另將風向以三十六方位區分，正北爲36，每個風向範圍爲10°。

2. 風速

原始資料中，地面風速以節（ knot ）爲單位，本文將其乘 0.517 改爲以 m / sec爲單位。因模式計算時，所使用之風速資料爲有效煙囪高度者，其推算法在第二章已有說明。

3. 大氣穩定度

一般大氣擴散模式中之穩定度，係依照 Pasquill [19] 對日照、雲量及地面風速三種因素之觀測，加以推算而成的六分法（即按不穩定程度，分 A～F 六級），如（表十三）所示。因需要較齊全的氣象資料，在某些地方可能因資料不足而無法應用。繼而有人乃以其他指標，如水平風向之標準偏差（σ_θ）與垂直方向氣溫遞減率（$\partial T / \partial Z$）[42]，如（表十四）所示。或純以水平風向標準偏差 [43]，如（表十五）所示。及其考慮夜間情況之改良法 [43], [44]，如（表十六）所示。上述之變通辦法，仍以六分法或增加一級 G（極穩定）爲區分方式。

本文因氣象資料齊全而採用 Pasquill 法，另根據 Mitchell [44] 之實驗證明知，本法適用於現場（指污染源）外（ Offsite ）資料之推算，而符合本文之實際情況。

由（表十三）知，在白天時，日射量之強弱爲穩定度等級判定之重要因素，其可由太陽天頂角（ Solar Altitude , α ）與雲量之多寡決定 [45]，三者之關係，如（表十七）所示。而太陽天頂角可由下列公式求得：

$$\sin\alpha = \sin\left(\frac{\pi\phi}{180}\right)\sin\delta + \cos\left(\frac{\pi\phi}{180}\right)\cdot\cos\delta\cdot\cos\left[\frac{\pi}{12}(h-12)\right], \cdots [56]$$

$$\delta = 23.5\left(\frac{\pi}{180}\right)\cdot\sin\left\{\frac{\pi}{180}[30(m-1)+d-81]\right\}, \cdots\cdots [57]$$

上二式中，δ 爲太陽傾斜角（ Solar Declination ），m 爲月份，d 爲日，h 爲時（當地標準時間），ϕ 爲緯度。

4. 混合層高度

混合層高度因無直接觀測資料可供使用，而依據 Holzworth [46] 法，利用東港探空資料，對氣溫與露點溫度差做迴歸分析。惟此法僅適用於白天，夜晚之混合層高度，則由日落前後之混合層高度作線性外插，而下半夜至日出前之混合層高度則假設不變。

5. 氣溫及露點溫度

氣溫用於有效煙囪高度及混合層高度之計算，而露點溫度則應用於混合層高度之估算。二者在 1980 年之每月平均值，如（表十一）所示，用於模式計算者，則爲每小時平均值。

6. 雲量

原始資料中，雲量以八分法（即 1/8～8/8 ）方式紀錄，與本文計算大氣穩定度等級所用的方式一致，故未更動。

7. 相對濕度

大氣中之濕度爲污染物發生化學變化之重要影響因素，因此亦將原始資料中相對濕度值取出，求其每月平均值，以供參考，1980年之各月平均值，列於表（十一）。

伍、結果與討論

一、污染物沒有化學衰減作用產生，最大地面濃度位置（X_{max}）求法進一步簡化之結果

本文之計算流程，如（圖二十二）所示，分爲（Ⅰ）、（Ⅱ）兩個部份，第（Ⅰ）部份主要工作在求得C_{max}及X_{max}值。由於氣象資料數量多，若以〔21〕式，一一使用半間距法解出X_{max}值。根據實測，所耗費的計算機時間約達10分鐘。以SO_2之計算爲例，在空氣品質限值爲0.3 ppm條件下，第（Ⅰ）部份計算結果，如（表十八）所示。在各級穩定度條件下，以$X_{max} = a H_e^b$方式迴歸，其中a，b爲迴歸係數，可迅速得到X_{max}值，迴歸及檢定之結果，列於（表十九）。由所列之結果可發現，迴歸效果良好。據此，在相同條件下，再次計算，結果列於（表二十），發現利用〔21〕式計算之結果，穩定度爲A級（或以1表示者）者，在簡化計算所得結果中，都沒有出現，僅有一穩定度爲B級者存在，其與（表十八）中之No. 8相比較，X_{max}值之相對誤差僅有1.2％，而C_{max}值之相對誤差更低至0.64％，顯示在穩定度B時，模擬效果良好。在H_e值大於200公尺，穩定度A時，$(CU/Q)_{max}$與X_{max}關係有明顯的偏離現象，而其他穩定度級則仍近似直線。因此，（表十九）之迴歸結果，穩定度爲A者，只能適用於H_e小或等於200公尺之情況。而本文中之H_e，在這種狀況下，往往大於200公尺，故必須在H_e超出200公尺之範圍，另外再作迴歸，以符合所需，其結果及檢定，列於（表二十一）。

根據第二段迴歸之結果，在前述條件下，再次計算，結果列於（表二十二），其與（表十八）比較，顯示這項修正效果極佳。本文假設懸浮顆粒，在大氣中擴散時，沒有化學衰減作用。因此，在計算時，我們可利用這種簡化法，結果顯示，只須約2分鐘時間，即可完成同一工作，對資料處理而言，效果良好。

二、風向爲十六方位時，SO_2在各空氣品質限值下之設計結果

對林口電廠而言，以十六方位區分風向時，風向5～11是吹向海上。因此，在讀入氣象資料時，可預先將上述風向資料濾除，可避免無謂之計算。空氣品質限值以「台灣地區環境空氣品質標準」中，硫氧化物在一般地區之小時限值爲0.3 ppm爲基準，依序按0.25、0.20 ppm，計算發生超出上述諸限值之年頻率值。限定若超過限值次數佔全年資料數5％以上者，即表非危險情況，而不考慮進一步設計。本文所使用之中正國際機場地面觀測資料（1980年），有11個全天（即24個小時值）漏失，故全年逐時資料共有8,520筆，故發生超過限值次數大於426者，則不考慮其設計。另外，SO_2之模式計算有考慮化學衰減作用發生。

1. C_{max}大於0.3 ppm之情況

計算結果列於（表二十四），由結果可知，這種情況都發生在穩定度A（在表上則寫成1）時，且有效煙囪高度之平均風速在1.9～3.8 m/sec間，X_{max}距排放源距離很近，只有1.0～1.34 km，發生的時間都在中午時（上午十時至下午二時），正是垂直方向對流作用最烈的時候，污染物質很快即達最大地面濃度位置之故。由於風向範圍不一致，全年發生頻率最高者爲2次（即風向爲15，代

表風速爲 2.45 者），遠小於 Smith 和 Egan [15] 所建議的 10 次本年，故不考慮進一步之設計。

2 C_{max} 大於 0.25 ppm之情況

計算結果列於（表二十五），可發現穩定度有 B 、C 兩個等級出現，X_{max} 範圍在 1.00 ～ 2.48 km 之間，發生的時間，除了 9 月 7 日之早上八時外，其餘的仍和上一種情況一樣，都在上午十時至下午二時間。值得注意的是有高風速情形出現，如 3 月 23 日 11 ～ 13 時，有效煙囪高度處平均風速高達 21.9 m / sec ，在這種情況下，煙柱上升會受極大的影響，更嚴重者，可能污染物會有下冲現象，使最大地面濃度位置接近排放源。爲考慮高風速狀況，本文乃增加一個風速級，定其範圍爲 13.9 ～ 25.0 m / sec ，而代表風速令爲 16.0 m / sec 。由結果進一步統計可知，發生頻率最高者爲風向12，穩定度C（或 3 ），代表風速爲 16.0 m / sec ，次數爲 8 次 / 年，因少於十次，故對這種狀況，也不加以設計。

3 C_{max} 大於 0.2 ppm之情況

計算結果列於（表二十六），由結果可知，穩定度級仍只有 A 、B 、C 三種，X_{max} 範圍在 1.00 ～ 3.36 km之間，發生時間有 94.7 %仍然在上午十時至下午二時間，由此可知，林口地區 SO_2 地面濃度最大值在中午時間出現最頻繁，而垂直對流作用是主要原因。進一步統計整理後，可發合於設站規定之氣象條件組合有五類（即風向 12 ，穩定度C ，代表風速 9.35 m / sec ，次數爲 15 次；風向12 ，穩定度C ，代表風速 12.3 m / sec ，次數爲 19 次；風向 13 ，穩定度C ，代表風速 9.35 m / sec ，次數爲 11 次；風向 14 ，穩定度B ，代表風速 6.7 m / sec ，次數爲 12 次；風向 15 ，穩定度B ，代表風速 6.7 m / sec ，次數爲 11 次），其設計內容在各種 C_{max} 忍限值（即 0.9 C_{max} 、0.8 C_{max} 及0.7 C_{max} ）和總覆蓋比（CR_T ）可信賴區間（ α ）即 0.5 、0.9 、0.95 、0.99 條件下，列於（表二十七），其中之 A_p 值，爲保守估計，乃選自同一氣象條件組合中之最大值，而 A_a 值則選用最小值。結果顯示，在風向方位 4 （即由風向 12 所吹送者），兩個 A_p 有重覆疊合的情形，故 A_p 區域內斜線愈密者，表示會有氣象條件組合交互作用之現象，其設站位置和數目要優先考慮。

三、風向爲三十六方位時， SO_2 在各空氣品質限值下之設計結果

以三十六方位區分風向時，對林口電廠而言，風向 9～23是吹向海面者，故可預先將上述風向之氣象資料濾除。由於風向細分，任一氣象條件組合所可能產生超過空氣品質限值（C_s ）之機率，和以十六方位區分時比較，減少了 55.6 %。因此，本文對這種情況，將 Smith 和 Egan 所建議的每年十次，改爲只需超過 5 次 / 年，即考慮測站之位置，進行進一步設計。

1 C_{max} 大於 0.3 ppm之情況

計算結果列於（表二十八），與（表二十四）比較，可發現除了風向變換外，並沒有因風向細分後，將可能在十六方位區分時，預先被濾除，而在三十六方位區分時有超過限值情形而出現的幾個邊緣風向（如風向 6 ， 7 ， 8 ， 24 ， 25 等）。發生頻率最高之氣象條件組合爲風向31，代表風速2.45 m / sec ，次數爲 2 ，故沒有進一步設計之考慮。

2 C_{max} 大於 0.25 ppm之情況

計算結果列於（表二十九），和風向爲十六方位區分，在相同空氣品質限值條件下比較，發生次

數增加21次（由 42 次增至 63 次），新增者之風向皆爲 24 或 25 ，即所謂的邊際風向。進一步統計整理後，發現可能設站偵測之氣象條件組合有四（即風向 6 ， 24 ， 25 ， 26 ，穩定度皆爲C，而代表風速爲 16.0 m / sec ），由此可知，高風速對高濃度產生之影響。由於風向細分，A_p 值也隨之減少 55.6 %（因風向範圍由 22.5°減爲 10°之故）。由十六方位區分風向時之設計結果知，在 0.7 C_{max} 情況下，A_s 值皆超過 A_p 值，造成 CR_s 大於 1.0 之情況，故在三十六方位區分風向時，只設計 0.9 C_{max} 及 0.8 C_{max} 兩種情況，而 CR_T 可信賴區間 α 值，仍分 0.5 ， 0.9 ， 0.95 ， 0.99 四種情形分別討論。設計內容列於（表三十）。由表上數據顯示，不論 α 值爲何，CR_s 值皆大於 CR_T 值。因此，對於各種情況，都只需一個測站，即可滿足所需。

3. C_{max} 大於 0.2 ppm之情況

由計算結果知，發生次數爲 211 次，與十六方位風向區分時，C_{max} 大於 0.2 ppm 之結果比較，共增加了40次。經進一步統計整理後，共有十個氣象條件組合，須做測站之設計，風向 5 ，代表風速 12.3 m / sec ；風向 25 ，代表風速 12.3 m / sec ；風向 26 ，代表風速 9.35 m / sec ；風向 26 ，代表風速 12.3 m / sec ；風向 27 ，代表風速 12.3 m / sec ；風向 29 ，代表風速 9.35 m / sec ，以上六種情況，穩定度皆爲 C 。另外，穩定度爲 B 者爲風向 31 ，代表風速 6.7 m / sec ；風向 32 ，代表風速 6.7 m / sec ；風向 33 ，代表風速 4.4 m / sec ；風向 33 ，代表風速爲 6.7 m / sec 。各種狀況之設計內容列於（表三十一）。由（表三十一）知，在 0.8 C_{max} 時，其 A_p 值範圍在穩定度 B 條件下，爲 0.31 ～ 0.58 km^2 ，遠小於在穩定度 C 時之 0.92 ～ 1.02 km^2 ，不論在那一種情況下 A_s 都大於上述之 A_p 值，故 CR_s 都大於 1 ，表示三十六方位區分時，單一測站涵蓋面積能夠包含可能發生的狀況，因 CR_T 永遠小或等於 1 之故。在 0.9 C_{max} 時，僅有部份 α 值爲 0.99 時，單一測站覆蓋比小於 CR_T 。在下風方向爲 8 和15兩種情形，各有兩種氣象條件組合發生交互作用。

五、風向爲十六方位時，懸浮顆粒在各空氣品質限值下之設計結果

本文中懸浮顆粒之濃度計算方式，除沒有化學衰減作用之考慮外，其餘和 SO_2 相同，以小時平均值爲表示方式。所選用的空氣品質限值爲 1500 $\mu g / m^3$ 和 1000 $\mu g / m^3$ 兩種，其他設計過程與 SO_2 相同。

1. C_{max} 大於 1500 $\mu g / m^3$ 之情況

計算結果列於（表三十二），與（表十八）相比較，發現除了（表十八）中之 No. 8 外，在其他各項氣象及時間因素，二者沒有什麼兩樣，但 X_{max} 在（表三十二）中都向前移，範圍在 0.885 ～ 1.21 km間，而（表十八）中者，在 1.01 ～ 1.37 km間，理由爲一號機之懸浮顆粒排放强度（ 3654 g / sec ） 遠大於另外兩個排放源（排放强度各爲 3.4 及 0.667 g / sec ），故在多項式迴歸時，造成一號機之煙囪排氣爲下風懸浮顆粒主要成份，其 X_{max} 值幾乎爲合成作用之 X_{max} 所在，而有前移之現象發生。由結果知，發生頻率最高之氣象條件組合爲風向 15 ，穩定度 A ，代表風速 2.45 m / sec ，次數爲 2 ，遠小於 10 次 / 年，故不做進一步設計。

2. C_{max} 大於 100 $\mu g / m^3$ 之情況

由計算結果知，發生次數驟增至 344 次，進一步統計整理後，共有十四種氣象條件組合，有必要

慮測站之位置，設計內容列於（表三十三）。由（表三十三）知，在 0.8 C_{max} 和 0.7 C_{max} 兩種情下，不論 α 值爲何，CR_s 值皆大於 CR_T，理由爲所對應之 A_s 值已足以包涵偵測潛勢區域，故只需個測站，即能滿足所對應之氣象條件組合。即使在 0.9 C_{max} 條件下，α 值爲 0.9 時，十四種有偵必要的氣象條件組合，其中十一種也能各用一個測站達成偵測目的。下風方位爲 4，5，6，7，者，都有二種以上氣象條件組合交互作用的情形。

、風向爲三十六方位時，懸浮顆粒在各空氣品質限值下之設計結果

1 C_{max} 大於 1500 $\mu g / m^3$ 之情況

計算結果列於（表三十四），與（表三十二）比較可知，發生次數及時間皆相同，故沒有邊際風發生超過空氣品質之情形。發生時間都在中午時刻（即上午十時至下午二時），穩定度皆爲A，風（有效煙囪高度處）範圍在 1.9 ~ 3.8 m / sec 間。發生頻率最高之氣象條件組合爲風向 31，代表速 3.45 m / sec 者，次數爲 2，小於規定之 5 次 / 年，故不做進一步之設計。

2 C_{max} 大於 100 $\mu g / m^3$ 之情況

由計算結果知，發生次數共有 398 次，達全年時數（缺11天資料）之 4.7 %，其與本章第五節，$_{max}$ 大於 1000 $\mu g / m^3$ 之情況比較可知，發生次數增加 54 次，而風向爲24，25 者，即所謂之邊際向。進一步統計整理後，有三十一種氣象條件組合，有考慮設測站之必要，設計內容列於（表三十）。由於資料衆多，故限定在 0.9 C_{max} 條件下，不論 α 值爲何，若其 CR_s 值大於對應之各 CR_T，即測站個數（NN）爲 1 即可滿足所需者，則略去 0.8 C_{max} 條件下之計算，以節省計算時間。由表三十五）知，共有十七個發生上述情況。另外，須要注意者爲風向 5，6，26，27，代表風速 12.3 m / sec 或 16.0 m / sec，其 A_s 值在 0.9 C_{max} 條件下，往往不及 A_p 值之一半，故 α 值爲 9 起，設置單一測站無法滿足偵測目的，必須有兩個才行。下風方向除了 10，22，25，27 外（海面上者不計）都有設站之可能，其中又以 7，8，11，13，14，15，18，20 八個方向有二以上氣象條件組合之交互作用產生。

、各種設計結果之組合及測站數目有限時，最佳空氣品質偵測網設計

1 各種設計結果之組合

根據以上結果，我們可按實際需求，如以單一污染物之各項限值或數種不同污染物分別的空氣品限值……等情況之偵測爲目的，而選取已繪好的各單一狀況之設計圖，以相同比例疊合，取其“交”部份，做爲設置固定測站之所在，而沒有交集的部份，則考慮做爲移動測站停留之範圍。

2 測站數目有限時，最佳空氣品質偵測網之設計結果

當測站數目有限時，且爲能滿足下式：

$$CR_T = NN \cdot CR_s \quad , \quad \cdots\cdots [58]$$

CR_s 大於 CR_T 時，NN必爲 1。CR_s 等於 CR_T 時，NN也爲 1，但 CR_s 大於 CR_T 時，NN可能 2，3，……。由〔28〕式之性質知，n，Z 值固定，N值愈大，則 CR_T 值愈小。表示在能成功偵測 n 次條件下，發生超過限值次數（N）愈多，則達成偵測目的也愈簡單，而所需之測站數目也，故 CR_T 可視爲偵測難易程度之指標（即愈難者，CR_T 值愈大）。令

$$P_i = 1 - CR_T \quad , \qquad \cdots\cdots [59]$$

此處，P_i 之意義爲能滿足〔58〕式，即達成 100 %偵測目的時所得獲得之效率。故我們可利用本章前述部份之計算和設計結果，限定討論 $\alpha = 0.95$，且在 $0.8\,C_{max}$ 條件下，偵測效率 P_i 之累積值（$\sum P_i$），與所需測站數目之累積值（$\sum NN$）之關係。另外，假定測站數目之極大值爲 10。由此，我們可利用 P（即 $\sum P_i$）與 NT（即 $\sum NN$）之關係，在測站數目限制條件下，尋求最大的 P 值。由此，即可獲得最佳效率下之偵測網設計。

本文按二種風向方位區分（十六方位和三十六方位），二種污染物（SO_2 和懸浮顆粒），在不同濃度限值下，依次設計，結果列於（表三十六）至（表四十五），其中按風向及污染物種類之四種組合，分別作圖如（圖三十一）至（圖三十四）所示，至於設站之優先順序則如（圖三十五）至（圖三十八）所示。上述之圖表只適用於 n 值爲 1 之情況。由（圖三十一）所示，要達成 P 爲 1.75 時，偵測 0.2 ppm 者，只需 3 個測站，而偵測 0.25 ppm 者，則需有 6 個測站（污染物爲 SO_2）。據此，可利用（表三十七）和（表三十八）找出測站所在（即 X_{max} 之位置）。（圖三十一）中 0.3 ppm 之曲線在 NT 等於 4 以後，即平行橫軸，表示在往後設站時，所選定之地點其 N 爲 1，故 CR_T 爲 1，而沒有效率 P_i 之增加，並非測站總數無限增加時，其 P 值不變。事實上，在 NT 必定有限條件下，P 值不變表示，測站放在任何預定位置都相同，只能達成預定之效率，而沒有進一步選站之必要。

爲能更進一步了解此種設計方式，應可增加各種不同 α 值，C_{max} 忍限值（如 $0.8\,C_{max}$，$0.7C_{max}$）做深入地比較，則更能使設計合理化。

八、有效偵測次數 n 大或等於 2 時之討論

本章前述設計結果都是取 n 爲 1 時之情況，對於此種情況，我們可繪圖如（圖三十九）所示，用以說明在不同 α 值條件下，CR_T 與 N 間之變化關係。

對某一測站而言，當令 n 爲 2 時，即測站能夠測得兩次違反限值之狀況，上述（圖三十九）之關係，同樣地，可作圖如（圖四十）所示。將二圖比較知，當 α 爲 0.5 時，爲增加一次成功地偵測，其 CR_T 值由 0.18 須增至 0.30，這可能表示須要增加一個測站才能滿足所需。

另外，我們也可以將 α 值固定，觀察 n 值值與 CR_T 及 N 之關係，如（圖四十一）所示。由此，可根據計算所得之 N 值，按要求選取 n 值，即可找出 CR_T 值，再依各種 C_{max} 忍限值所求得之 CR_s 值，算出所需之 NN 值。

陸、結論與建議

欲對某一地區的空氣污染問題有所對策時，必須要對當地的空氣品質進行環境方面的評估。評估工作則需從基本資料（包括氣象、地形、污染源形式、地區特性……等）的收集、分析爲開端，繼而經由空氣品質偵測網的佈建和大氣擴散模式的應用，找出當地空氣污染物濃度分佈的情形，以評定對環境影響的程度，及建議改進之道。

評估工作中，以描述當地空氣污染物分佈情況最爲艱鉅。以最直接的方式，即根據污染物的種類

，購置偵測儀器，收集所需的資料。依Stalker [48] 的報告指出，以 SO_2 之日平均濃度而言，每平方哩至少需有四個測站，才能夠有足夠的代表性。事實上，在偵測儀器日益精密靈敏的今日，若以此爲標準，在經濟上的負荷必無法承受。因此，如何經濟有效地佈置偵測網，在一定可信賴程度之上，收集具有代表性的污染物濃度資料，遂成爲評估工作的先決條件。此外，效果良好的空氣品質偵測網，對於污染源的排放管制，更有其積極的意義。

本文以單一污染源模式（ Single Source CRSTER Model ）爲主體，配合污染物發生化學變化，污染源排放條件各異的修正步驟，並以風向、風速、大氣穩定度，和混合層高度四項因素，根據設置偵測網機構在經濟上的考慮，可以定義單一測站所能代表區域之範圍。由緊至寬，可利用三種最大地面濃度忍限值（ $0.9\,C_{max}$ 、$0.8\,C_{max}$ 、$0.7\,C_{max}$ ）之等濃度線所圍成區域爲代表。繼而利用模式計算結果與空氣品質限值相比較，算出各種風速級條件下的偵測潛勢區域。最後，對以往氣象資料之計算及經濟上之權衡，用二項分配描述偵測之行爲，可據此設計出所需之測站數目及位置，以達成偵測預定效果。本文之設計方法，可應用於火力發電廠或其他大型點污染源之偵測網設計。

本文以林口火力發電廠爲實例，由其初步設計結果知，以 $0.7\,C_{max}$ 計算所得的單一測站覆蓋區域（A_s）值，皆大於偵測潛勢區（A_p）值，使得單一測站覆蓋比大於 1 。因此，不論在任何可信賴區間（ α ）限制下，只需一個測站即可滿足所需。在 $0.8\,C_{max}$ 情況時，常常有這種結果出現，所以，在這樣情況下，最大地面濃度忍限值範圍可以較爲縮緊，而不必放寬至 $0.7\,C_{max}$ 之情況。

另外，在 α 值爲 0.5 條件下，不論其他設計條件爲何，都只需一個測站即可滿足任一氣象組合之計算結果，這也是限制條件“太寬”所造成的後果。由林口的例子可知，此一限制可考慮刪除。在此，要特別指出，本文之設計結果，只能算是初步工作的完成，尚須按此結果，配合其他可能的影響因素（如本文第四章所提出無法設站之原因），進行測站之設置。其後所收集的資料，可用以檢核設計時採用的擴散模式，並加以修正後，再一次地設計，將初步設計時不當位置之測站重新定位（Real-location ）。有時候，這種工作還可能重覆多次，才會有滿意的結果。

對於設計進行中，所用的一些簡化法，由結果可知，在穩定度A時，其最大地面濃度發生位置（ X_{max} ），一般在 0.8 ～ 1.4 km範圍內。而本文所迴歸之 X_j^- ，X_j^+ 對 X_{max} （其中 j ＝90、80、70 ）之關係，也僅能適用於下風距離 2 km以內之範圍，而符合實際之需求。此外，爲節省求 X_{max} 值之計算機時間，而找出 X_{max} 與有效煙囪高度（H_e）之關係，同樣地，在穩定度A時，必須根據 H_e之大小範圍，選用適當的迴歸方程式，以免造成極大的誤差。

最後，在此要提出數點未來可供研究的方向及建議：

(1)本文中之濃度計算值爲小時平均值，爲了能夠與空氣品質標準值有更多的比較機會，可以進一步採用適於作長期預估之大氣擴散模式，進行設計，更可以了解時間對設計結果之影響。

(2)就統計觀點而言，資料愈多，就愈能夠對事物現象之了解更完全，本文所獲得之氣象資料長度爲一年，未來應可以在時間更長的資料及排放條件隨時間變化情形下，做更澈底地計算和設計。

(3)如本文第五章之結果可知，以 SO_2 言，最大地面濃度（C_{max}）大於 0.3 ppm者，全部因發生頻率太低，而不予考慮測站之設計。若以環境保護觀點而言，對這種可能產生危害的情況，應有加强

其懲重之措施，如不必每年超過限值十次以上才考慮設計，以免此種情形被＂掩蓋＂。其設站之考慮，應對經濟、環境影響方面有再深入研究的必要。

(4)若欲對所設置之偵測網，考慮更進一步的功能而言，應可根據可能產生危害之情況，劃分等級，依氣象預報資料和以往整理的各種可能發生異變之氣象條件相比較，推測可能發生危害的區域，適時發出警告，採取應變措施，以保障大衆之安全。

誌　謝

本文進行期間得到資訊科學研究所王逸民先生，在計算機使用的協助，台電林口電廠污染源資料，民航局氣象中心氣象資料的提供，以及本所張能復教授、台大大氣系吳清吉先生各方面的協助，十分感謝。

參考文獻

1. Leavitt, J. M. et al., "Design and Interim Meteorogical Evaluation of a Community Network for Meteorological and Air Quality Measurements," JAPCA, Vol.7, No.3, pp.211-215. (1957).
2. Yamada, V. M., "Current Practices in Siting and Physical Design of Continuous Air Monitoring Stations," JAPCA, Vol.20, No.4, pp.209-213, (1970).
3. Hamburg, F. C., "Some Basic Considerations in the Design of an Air Monitoring System", JAPCA, Vol.21, No.10, pp.609-613, (1971).
4. Pooler, F. Jr., "Network Requirements for the St. Louis Regional Air Pollution Study," JAPCA, Vol.24, No.3, pp.228-231. (1974).
5. Ott, W. R., "Development of Criteria for Siting Air Monitoring Stations," JAPCA, Vol.27, No.6, pp.543-547, (1977).
6. Singer, I. A., "An Objective Method for Site Evaluation," JAPCA, Vol.10, No.3, pp.219-251, (1960).
7. Seinfeld, J. H., "Optimal Location of Pollutant Monitoring Stations in an Airshed," Atmos. Environ. Vol.6, pp.847-858, (1972).
8. Hougland, E. S. and N.T. Stephens, "Air Pollutant Monitoring Siting by Analytical Techniques," JAPCA, Vol.26, No.1, pp.51-53. (1976).
9. Lee, T. D. et al., "A Procedure for Air Monitoring Instrumentation Location," Management Science, Vol.24, No.14, pp.1451-1461, (1978).
10. Graves, R. J. et al., "Air Monitoring Network Design: Case Study," J. of ASCE, Environ Eng. Div., pp.941-955, (Oct, 1981).
11. Nakamori, Y. et al., "Design of Air Pollutant Monitoring System by Spatial Sample Stratification," Atmos. Environ., Vol.13, pp.97-103, (1979).
12. Noll, K. E. and T. L. Miller, "Air Monitoring Survey Design," pp.97-114, Ann Arbor Science, (1976).
13. Noll, K. E. et al., "An Objective Air Monitoring Site Selection Methodology for Large Point Sources," Atmos. Environ., Vol.11, pp.1051-1059, (1977).

14. Miller, T. L. and K. E. Noll, "Design of Air Monitoring Surveys Near Large Power Plants," pp.121-142, in "Power Generation" edi. by K. E. Noll and W. T. Davis, Ann Arbor Science, (1977).
15. Smith, D. G. and B. A. Egan., "Design of Monitoring Networks to Meet Multiple Criteria," JAPCA, Vol.29, No.7, pp.710-714, (1979).
16. "Gudiance for Air Quality Monitoring Network Design and Instrmentation Sitting." OAQPS No. 1.2-012, PB80-223696 U. S. EPA (Sep. 1975).
17. "Guidance on Air Quality Models," EPA-450/2-78-027, OAQPS No.1.2-080 U. S. EPA (April 1978).
18. Sutton, O. G., "Micrometeorology," pp.105-157, McGraw-Hill Inc. (1953).
19. Pasquill, F., "Atmospheric Diffusion," 2nd edi, pp.204-328, John Wiley & Sons. (1974).
20. Gifford, F. A., "Use of Routine Meteorologicla Observations for Estimating Atmospheric Dispersion," Nuclear Safety, Vol.2, No.4, pp.47-51, (1961)
21. Martin, D. and J. A. Tikvart., "A General Atmospheric Diffusion Model for Estimation the Effects on Air Quality of one or more Sources," APCA Paper No.68-148, (1968).
22. Turner, D. B., "A Diffusion Model for an Urban Area," J. of Appl. Meteor. Vol.3, pp.83-91, (Feb. 1964).
23. Turner, D. B. "Workbook of Atmospheric Dispersion Estimates," PB-191 482, U. S. Department of Health, Education, and Welfare, Cincinnati, Ohio (1970).
24. "User's Manual for Single-Source (CRSTER) Model," EPA-450/2-77-013, PB271360, U. S. EPA, (July, 1977).
25. Busse, A. D. and J. R. Zimmerman, "User's Guide for the Climatological Dispersion Model," EPA-R4-73-024, U. S. EPA, (Dec. 1973).
26. Green, A. E. S. et al., "Analytic Extensions of the Gaussian Plume Model," JAPCA, Vol.30, No.7, pp.773-776, (July, 1980).
27. Seinfeld, F. H., "Air Pollution: Physical and Chemical Fundamentals," pp.260-302, McGraw-Hill, Inc. (1975).
28. Csandy, G. T., "Turbulent Diffusion in the Environment," pp1-81. D. Reidel Publ. Co. Inc. (1973).
29. Veigele, W. J. and J. H. Head, "Derivation of the Gaussian Plume Model," JAPCA, Vol.28, No. 11, pp.1139-1141, (Nov. 1978).
30. Horst, T. W., "A Surface Depletion Model for Deposition from a Gaussian Plume," Atmos. Environ. Vol.11, pp.41-46, (1977).
31. Weber, E., "Contribution to the Residence Time of Sulfur Dioxide in a Polluted Atmosphere," J. of Geo. Research, Vol.75, No.15, pp.2909-2914, (May, 1970).
32. Flyger, H. et al., "Airborne Investigations of SO_2 Oxidation in the Plumes from Power Stations," Atmos. Environ., Vol.12, pp.295-296, (1976).
33. Miller, I. and J. E. Freund, "Probability and Statistics for Engineers," 2nd edi. p.108, Prentice Hall, Inc. (1977).
34. Montgomery, T. L. et al., "A Simplified Technique used to Evaluate Atmospheric Dispersion of Emissions from Large Power Plants," in "Power Generation: Air Pollution Monitoring and Control" edi. by Noll, K. E. and W. T. Davis, pp.49-64, Ann Arbor Science Publ. (1976).
35. "中華民國台灣地區環境空氣品質標準，"環境污染防治法規彙編，經濟部工業局。(68年)
36. Stern, A. C. et al., "Fundametals of Air Pollution," p.159. 協成書局(68年).
37. Hino, M., "Maxmum Ground-Level Concentration and Sampling Time," Atmos. Environ., Vol.2,

pp.149-165. (1968).

38. Yamartino, R. J. Jr., "A New Method for Compution Pollutant Concentrations in the Presence of LImited Vertical Mixing," JAPCA, Vol.27, No.5, pp.467-468, (May 1977)
39. Pasquill, F., "The Gaussian-Plume Model With Limited Vertical Mixing," EPA-600/4-76-042, PB-258, 732, U. S. EPA, (Aug. 1976).
40. 梁文傑，"林口火力電廠及低級煤電廠對周圍環境空氣品質影響之評估研究，" 國立台灣大學與慶齡工業發展基金會設工業研究中心，研究報告 57 ，（ 1982 ）.
41. Katz, M., "Methods of Air Sampling and Analysis," 2nd edi. pp.710-716; APHA (Intersociety Committee, (1977).
42. Eimutis, E. C. and M. G. Konicek, "Derivation of Continuous Functions for the Leteral and Vertical Atmospheric Dispersion Coefficients," Atmos. Environ. Vol.6, pp.859-863, (1972).
43. "Guideline on Air Quality Models." p.c-5 revised, U. S. EPA (1980).
44. Mitchell, A. E. et al., "A Comparison of Shortterm Dispersion Estimates Resulting From Various Atmospheric Stability Classification methods," Atmos. Environ. Vol.16, No.4, pp.765-773, (1982).
45. 張復能，"桃園地區煙囪擴散係數之研究，" 中央大學大氣物理研究所研究報告（ 1982 ）。
46. Holzmorth, G. C., "Mixing Heights, Wind Speeds, and Potential for Urban Air Pollution throughout the continguous United States," Office of Air Programs Publ. No.AP-101, U. S. EPA. (Jun, 1972).
47. 陳王琨，"模式輸出統計法在林口地區空氣污染評估上之應用，" 台灣大學環境工程學研究所，碩士論文（ 70年 6 月 ）。
48. Bryan, B. J., "Ambient Air Quality Surveillance," pp.343-392, in "Air Pollution," 3rd edi., Vol.III, edi, by A. C. Stern, Academy Press, (1976).

表一　垂直方向風速剖面指數[24]

Pasquill 穩定度級	風速剖面指數，P（S）
A	0.10
B	0.15
C	0.20
D	0.25
E	0.30
F	0.30

表二　0.9 C_{max} 時，$X_{\bar{90}}$ ，$X_{\dot{9}0}$ 對 X_{max} 之迴歸常數

穩定度		A	B	C	D	E	F
$X_{\bar{90}}$	a	0.8588	0.7978	0.7988	0.7741	0.7660	0.7348
	b	1.0076	1.0183	0.9873	0.9609	0.9705	0.9602
X^{+}_{90}	a	1.0931	1.2273	1.3297	1.3757	1.4631	1.4037
	b	0.9000	0.9978	0.9985	0.0448	1.0298	1.0400

註：迴歸方程式型式爲 $X^{+}_{90} = a X^{b}_{max}$ 或 $X_{\bar{90}} = a X^{b}_{max}$

表三　0.8 C_{max} 時，$X_{\bar{80}}$，X^{+}_{80} 對 X_{max} 之迴歸常數

穩定度		A	B	C	D	E	F
$X_{\bar{80}}$	a	0.8275	0.7377	0.7355	0.6974	0.6811	0.6793
	b	1.0379	1.0241	0.9882	0.9550	0.9563	0.9422
X^{+}_{80}	a	1.1666	1.4011	1.0043	1.6053	1.6958	1.5876
	b	0.8840	0.9885	0.9880	1.0467	1.0459	1.0632

註：迴歸方程式型式爲 $X^{+}_{80} = a X^{b}_{max}$ 或 $X_{\bar{80}} = a X^{b}_{max}$

表四　0.7 C_{max} 時，X_{70}^{-}，X_{70}^{+} 對 X_{max} 之迴歸常數

穩定度		A	B	C	D	E	F
X_{70}^{-}	a	0.8155	0.6903	0.6835	0.6287	0.6281-	0.5971
	b	1.0721	1.0210	0.9923	0.9612	0.9515	0.9277
X_{70}^{+}	a	1.2001	1.5537	1.7045	1.8732	1.9460	1.9848
	b	0.8420	0.9826	0.9897	1.0557	1.0602	1.0735

註：迴歸方程式型式爲 $X_{70}^{+} = a X_{max}^{b}$ 或 $X_{70}^{-} = a X_{max}^{b}$

表五　σ_y，σ_z 近似方程式之常數 [26]

穩定度	A (km)	V (m／km)	q	W (m／km)	p
A	0.927	102.0	-1.918	250	0.189
B	0.370	96.0	-0.101	202	0.162
C	0.283	72.2	0.102	134	0.134
D	0.707	47.5	0.465	78.7	0.135
E	1.070	33.5	0.624	56.6	0.137
F	1.170	22.0	0.700	37.0	0.134

註：$\sigma_y = \dfrac{WX}{(1+\frac{X}{A})^p}$，$\sigma_z = \dfrac{WX}{(1+\frac{X}{A})^q}$，其中X爲下風距離，單位爲km。

表六　風速等級分類及各級的代表風速值

風　速　級	風　速　範　圍（m／sec）	代　表　風　速（m／sec）
1	0.0-1.5	0.75
2	1.6-3.3	2.45
3	3.4-5.4	4.40
4	5.5-7.9	6.70
5	8.0-10.7	9.35
6	10.7-13.8	12.30

表七　相同排放高度之多點污染源修正值

N	2	3	4	5	6	7	8	9	10
$N^{4/5}$	1.7	2.4	3.0	3.6	4.2	4.7	5.3	5.8	6.3

表八　平均時間超過10min之σ_y修正值

平　均　時　間（hr）	修正值（C.F）
1	2.4
3	4.2
10	7.7

表九　〔3〕式中C值佔〔4〕式C值之比例[39]

σ_z / L \ H/L	0	0.1	0.2	0.3	0.4	0.5	0.4	0.7	0.8	0.9	1.0
0.3	1.00	1.00	1.00	1.00	1.00	1.00	1.00	1.00	0.99	0.90	0.50
0.4	1.00	1.00	1.00	1.00	1.00	1.00	0.99	0.98	0.92	0.78	0.50
0.5	1.00	1.00	1.00	1.00	0.99	0.98	0.95	0.92	0.83	0.69	0.50
0.6	0.99	0.99	0.99	0.98	0.98	0.94	0.90	0.84	0.75	0.64	0.50
0.8	0.92	0.92	0.90	0.89	0.86	0.82	0.77	0.72	0.65	0.58	0.50
1.0	0.79	0.78	0.77	0.76	0.73	0.70	0.67	0.63	0.59	0.54	0.49

表十　以二次多項式迴歸三支不同排放條件之煙囪之模式計算值

DISTANCE (KM)	CONC.(1) (PPM)	CONC.(2) (PPM)	CONC.(3) (PPM)	C.TOTAL (PPM)	C. FITTING (PPM)
0.124E+01	0.201E+00	0.133E+00	0.426E-01	0.377E+00	0.376E+00
0.125E+01	0.201E+00	0.136E+00	0.430E-01	0.380E+00	0.379E+00
0.126E+01	0.201E+00	0.139E+00	0.433E-01	0.384E+00	0.382E+00
0.127E+01	0.201E+00	0.142E+00	0.436E-01	0.386E+00	0.384E+00
0.128E+01	0.200E+00	0.145E+00	0.439E-01	0.389E+00	0.387E+00
0.129E+01	0.200E+00	0.147E+00	0.441E-01	0.391E+00	0.389E+00
0.130E+01	0.199E+00	0.150E+00	0.442E-01	0.393E+00	0.391E+00
0.131E+01	0.198E+00	0.152E+00	0.444E-01	0.395E+00	0.383E+00
0.132E+01	0.197E+00	0.154E+00	0.445E-01	0.396E+00	0.394E+00
0.133E+01	0.196E+00	0.156E+00	0.445E-01	0.397E+00	0.395E+00
0.134E+01	0.195E+00	0.158E+00	0.446E-01	0.398E+00	0.396E+00
0.135E+01	0.194E+00	0.160E+00	0.445E-01	0.398E+00	0.397E+00
0.136E+01	0.193E+00	0.161E+00	0.445E-01	0.398E+00	0.397E+00
0.137E+01	0.191E+00	0.162E+00	0.444E-01	0.398E+00	0.397E+00
0.138E+01	0.190E+00	0.164E+00	0.444E-01	0.398E+00	0.397E+00
0.139E+01	0.189E+00	0.165E+00	0.442E-01	0.397E+00	0.397E+00
0.140E+01	0.187E+00	0.166E+00	0.441E-01	0.397E+00	0.396E+00
0.141E+01	0.185E+00	0.166E+00	0.439E-01	0.396E+00	0.395E+00
0.142E+01	0.184E+00	0.167E+00	0.438E-01	0.394E+00	0.394E+00
0.143E+01	0.182E+00	0.168E+00	0.435E-01	0.393E+00	0.392E+00
0.144E+01	0.180E+00	0.168E+00	0.433E-01	0.392E+00	0.391E+00
0.145E+01	0.179E+00	0.168E+00	0.431E-01	0.390E+00	0.389E+00
0.146E+01	0.177E+00	0.168E+00	0.428E-01	0.388E+00	0.387E+00
0.147E+01	0.175E+00	0.168E+00	0.425E-01	0.386E+00	0.384E+00

註：(1)CONC.(1)，CONC.(2)，CONC.(3)爲三支煙囪各別之濃度值（模式值）。
(2)C.TOTAL爲三支煙囪模式計算值之和。C.FITTING爲迴歸值。
(3)迴歸方程式爲$C(X) = -1.30X^2 + 3.56X - 2.04$
(4)檢定結果：(i) $r = 0.995$ (ii) $F = 0.557$
(5)氣象條件爲穩定度A，氣溫 26 ℃，混合層高度 904 m。

表十一　1980年中正機場地面觀測資料月平均值

月	風　向（°）	風速（m / sec）	氣溫（℃）	相對濕度（%）
1	109	6.2	15.4	75.7
2	89	7.8	14.4	82.4
3	113	6.3	16.8	79.1
4	140	5.1	20.0	73.0
5	154	5.1	23.7	81.9
6	210	4.1	28.6	76.3
7	206	5.0	29.9	71.3
8	217	4.5	28.8	74.4
9	114	5.9	26.5	75.7
10	104	5.2	24.1	74.5
11	83	7.3	21.4	73.3
12	82	6.9	16.1	71.1

表十二　林口火力電廠排煙源有關資料[40]

資料項目 \ 機組別 / 機組出力	一號機			二號機			柴油機組			氣渦輪機組		
	60%	80%	100%	60%	80%	100%	60%	80%	100%	60%	80%	100%
裝置容量（MW）	180	240	300	210	280	350	3.6x10	4.8x10	6x10	42.5x4	56x4	71x4
煙囪高度（m）	70	70	70	100	100	100	70	70	70	23	23	23
煙囪內徑（m）	6.4	6.4	6.4	5	5	5	3.2	3.2	3.2	5.5x3.7	5.5x3.7	5.5x3.7
使用燃料含灰分（%）	23	23	23	0.02	0.02	0.02	0.02	0.02	00.02	0.003	0.003	0.003
使用燃料含硫分（%）	1.5	1.5	1.5	3.6	3.6	3.6	3.6	3.6	3.6	1	1	1
鍋爐熱輸入（$\frac{10^6 BTU}{hr}$）	1642	2160	2808	2073	2723	3129	380	504	610	3164	4137	4594
燃量消耗量（$\frac{tons}{hr}$）	76	100	130	51	67	77	0.936x10	1.24x10	1.5x10	13.86x4	24x4	26.8x4
排煙量（tons / hr）	743	978	1271	827	1249	1249	298	394	488	1184x4	1200x4	1202x4
煙氣排出速率（m/sec）	6.98	9.23	12.1	13.7	18.3	21.6	28.6	26.6	33.5	28.9	31.4	35
煙氣排出溫度（°K）	418	424	426	416	423	435	625	675	703	652	705	773
二氧化硫排放量（g/sec）			1083			1541			300			590
懸浮顆粒排放量（g / sec）			3654			3.4			0.667			0.715
E.P 平均效率（%）			45									

表十三　Pasquill 大氣穩定度分類[19]

地面風速（m/s）（10公尺高）	白天日射量			夜晚	
	强	中	弱	雲量 $\geq \frac{4}{8}$	雲量 $\leq \frac{3}{8}$
2	A	A-B	B	-	-
2-3	A-B	B	C	E	F
3-5	B	B-C	C	D	E
5-6	C	C-D	D	D	D
>6	C	D	D	D	D

註：(1)不論白天或夜晚，當全天空雲量爲 8 ／ 8 時，穩定度級爲D。

(2)對於A—B級，乃是各別以A、B所對應之值再平均者。

表十四　以水平風向標準偏差和溫度遞減率爲指標之大氣穩定度分類[42]

穩定度	變化範圍
A	$22.5° \leq \sigma_\theta$
B	$17.5° \leq \sigma_\theta < 22.5°$
C	$12.5° \leq \sigma_\theta < 17.5°$
D	$-1.5° \leq \partial T/\partial Z < -0.5°$
E	$-0.5° \leq \partial T/\partial Z < 1.5°$
F	$1.5° < \partial T/\partial Z$

表十五　以水平風向標準偏差爲指標之大氣穩定度分類[43]

穩定度	σ_θ 變化範圍（°）
A	$\sigma_\theta \geq 22.5$
B	$22.5 > \sigma_\theta \geq 17.5$
C	$17.5 > \sigma_\theta \geq 12.5$
D	$12.5 > \sigma_\theta \geq 7.5$
E	$7.5 > \sigma_\theta \geq 3.8$
F	$3.8 > \sigma_\theta$

表十六　以水平風向偏差爲指標之大氣穩定度分類在夜間之修正[44]

σ_θ（°）	白天之穩定度	風速（m / sec）	夜間穩定度
$\sigma_\theta \geq 22.5$	A	$u < 2.4$	G
		$2.4 \leq u < 2.9$	F
		$2.9 \leq u < 3.6$	E
		$3.6 \leq u$	D
$22.5 > \sigma_\theta \geq 17.5$	B	$u < 2.4$	F
		$2.4 \leq u < 3.0$	E
		$3.0 \leq u$	D
$17.5 > \sigma_\theta \geq 12.5$	C	$u < 2.4$	E
		$2.4 \leq u$	D
$12.5 > \sigma_\theta \geq 7.5$	D	所有風速	D
$7.5 > \sigma_\theta \geq 3.8$	E	所有風速	E
$3.8 > \sigma_\theta \geq 2.1$	F	所有風速	F
$2.1 > \sigma_\theta$	G	所有風速	G
註：所謂「夜間」，乃指日落前一小時至日出後一小時之時間			

表十七　日射量、太陽天頂角（α）及雲量之關係[45]

雲量 / α 日射量	$\geq \frac{4}{8}$	$< \frac{4}{8}$
0° ～ 35°	弱	弱
35° ～ 60°	弱	中
60° ～ 90°	中	強

表十八　沒有化學衰減，C_{max} 大於 0.3ppm 之 SO_2 計算結果

NO.	MON	DAY	HOUR	WD	STAB	AVE. WS	MMIM)	XMAX(KM)	CMAX(PPM)
1	4	8	11	14	1	1.9	904	0.137E+01	0.398E+00
2	4	19	10	14	1	1.9	967	0.137E+01	0.401E+00
3	4	29	13	16	1	1.9	778	0.137E+01	0.399E+00
4	5	4	11	1	1	1.9	841	0.137E+01	0.401E+00
5	5	29	12	13	1	1.9	778	0.137E+01	0.399E+00
6	5	29	14	12	1	1.9	778	0.137E+01	0.401E+00
7	9	6	10	12	9	3.8	967	0.101E+01	0.482E+00
8	9	7	8	3	2	9.2	904	0.169E+01	0.311E+00
9	9	21	10	15	1	5.2	841	0.109E+01	0.462E+00
10	10	7	11	14	1	3.8	904	0.101E+01	0.479E+00
11	10	16	11	15	1	2.5	904	0.121E+01	0.434E+00

註：No. 爲順序，Mon. 爲月份，Day 爲日，Hour 爲時，WD 爲風向，STAB 爲穩定度，AVE. WS 爲有效煙囪高度處之風速，MH 爲混合層高度，XMAX. 爲發生最大濃度位置，CMAX 爲最大濃度值。

表十九　X_{max} 與 H_e 關係之迴歸及檢定結果

穩定度	X_{max}（km），H_e（m）											a	b	r	F
A	X_{max}	0.15	0.25	0.33	0.45	0.56	0.62	-	-	-	-	0.0126	0.7545	0.984	0
	H_e	30	50	70	100	150	200	-	-	-	-				
B	X_{max}	0.14	0.20	0.38	0.54	0.74	1.05	1.40	-	-	-	0.0069	1.0097	0.999	0
	H_e	20	30	50	70	100	150	200	-	-	-				
C	X_{max}	0.20	0.32	0.58	0.72	1.20	1.90	2.60	3.20	4.00	-	0.00737	1.1032	0.999	0
	H_e	20	30	50	70	100	150	200	250	300	-				
D	X_{max}	0.16	0.35	0.56	1.05	1.70	2.90	5.80	9.00	13.0	17.0	0.00518	1.3991	0.999	0.006
	H_e	10	20	30	50	70	100	150	200	250	300				
E	X_{max}	0.21	0.54	0.90	1.90	3.00	5.60	12.0	21.0	35.0	50.0	0.00403	1.6121	0.994	0.017
	H_e	10	20	30	40	70	100	150	200	250	300				
F	X_{max}	0.40	0.90	1.70	3.70	7.40	15.0	40.0	-	-	-	0.00617	1.6933	0.990	0.015
	H_e	10	20	30	50	70	100	150	-	-	-				

註：迴歸方程式爲 $X_{max} = aH_e^b$

表二十　利用 X_{max} 與 H_e 迴歸方程式，C_{max} 大於 0.3 ppm 之 SO_2 計算結果

NO	MON	DAY	HOUR	WD	STAB	AVE WS	MH(M)	XMAX(KM)	CMAX(PPM)
1	9	7	8	3	2	9.2	904	0.167E+01	0.309E+00

註：符號之意義與表十八相同

表二十一　穩定度A時，$X_{max} = aH_e^b$ 之第二段迴歸及檢定

X_{max}（km），H_e（m）								a	b	r	F
X_{max}	0.911	0.987	1.11	1.18	1.30	1.34	1.47	0.0475	0.4906	0.999	0
H_e	417	487	598	697	848	907	1100				

表二十二　穩定度A時，改以第二段迴歸常數計算，C_{max} 大於 0.3ppm 之 SO_2 計算

NO	MON	DAY	HOUR	WD	STAB	AVE WS	MH(M)	XMAX(KM)	CMAX(PPM)
1	4	8	11	14	1	1.9	904	0.137E+01	0.398E+00
2	4	19	10	14	1	1.9	967	0.137E+01	0.401E+00
3	4	29	13	16	1	1.9	778	0.137E+01	0.399E+00
4	5	4	11	1	1	1.9	841	0.137E+01	0.401E+00
5	5	29	12	13	1	1.9	778	0.137E+01	0.399E+00
6	5	29	14	12	1	1.9	778	0.137E+01	0.401E+00
7	9	6	10	12	1	3.8	967	0.101E+01	0.482E+00
8	9	7	8	3	2	9.2	904	0.167E+01	0.309E+00
9	9	21	10	15	1	3.2	841	0.109E+01	0.462E+00
10	10	7	11	14	1	3.8	904	0.101E+01	0.479E+00
11	10	16	11	15	1	2.5	904	0.121E+01	0.434E+00

註：見表十八註

表二十四　風向十六方位，C_{max} 大於 0.3ppm之 SO_2 計算結果

NO	MON	DAY	HOUR	WD	STAB	AVE WS	MH(M)	XMAX(KM)	CMAX(PPM)
1	4	8	11	14	1	1.9	904	0.134E+01	0.303E+00
2	4	19	10	14	1	1.9	967	0.134E+01	0.306E+00
3	4	29	13	16	1	1.9	778	0.134E+01	0.304E+00
4	5	4	11	1	1	1.9	841	0.134E+01	0.306E+00
5	5	29	12	13	1	1.9	778	0.134E+01	0.304E+00
6	5	29	14	12	1	1.9	778	0.134E+01	0.306E+00
7	9	6	10	12	1	3.8	967	0.100E+01	0.436E+00
8	9	21	10	15	1	3.2	841	0.108E+01	0.405E+00
9	10	7	11	14	1	3.8	904	0.100E+01	0.433E+00
10	10	16	11	15	1	2.5	904	0.119E+01	0.362E+00

註：見表十八註

表二十五　風向十六方位，C_{max} 大於 0.25ppm之 SO_2 計算結果

NO	MON	DAY	HOUR	WD	STAB	AVE WS	MH(M)	XMAX(KM)	CMAX(PPM)
1	3	23	11	3	3	21.1	1029	0.195E+01	0.259E+00
2	3	23	12	3	3	21.9	1092	0.192E+01	0.259E+00
3	3	23	13	3	3	21.9	1092	0.192E+01	0.260E+00
4	4	8	11	14	1	1.9	904	0.134E+01	0.303E+00
5	4	19	10	14	1	1.9	967	0.134E+01	0.306E+00
6	4	29	13	16	1	1.9	778	0.134E+01	0.304E+00
7	5	4	11	1	1	1.9	841	0.134E+01	0.306E+00
8	5	19	10	2	3	14.9	841	0.233E+01	0.257E+00
9	5	19	11	2	3	16.4	778	0.221E+01	0.260E+00
10	5	19	12	3	3	18.8	841	0.205E+01	0.264E+00
11	5	19	13	2	3	17.2	904	0.215E+01	0.263E+00
12	5	19	14	3	3	14.1	1029	0.240E+01	0.256E+00
13	5	29	12	13	1	1.9	778	0.134E+01	0.304E+00
14	5	29	14	12	1	1.9	778	0.134E+01	0.306E+00
15	6	1	11	12	3	14.1	778	0.240E+01	0.256E+00
16	6	10	12	12	3	13.3	778	0.248E+01	0.253E+00
17	6	13	11	12	3	13.3	904	0.248E+01	0.253E+00
18	6	14	12	12	3	13.3	967	0.248E+01	0.253E+00
19	6	14	14	12	3	13.3	904	0.248E+01	0.253E+00
20	7	5	13	12	3	18.8	1092	0.208E+01	0.268E+00
21	7	6	11	12	3	14.1	1029	0.239E+01	0.257E+00
22	7	6	12	12	3	13.3	1092	0.247E+01	0.254E+00
23	7	6	13	12	3	16.4	1092	0.218E+01	0.266E+00
24	7	6	14	12	3	14.1	1029	0.239E+01	0.257E+00
25	7	30	12	12	3	16.4	495	0.219E+01	0.264E+00
26	7	30	14	12	3	17.2	291	0.213E+01	0.266E+00
27	8	13	11	12	3	14.1	587	0.240E+01	0.256E+00
28	9	4	11	13	2	7.0	753	0.195E+01	0.261E+00
29	9	4	13	14	2	7.0	451	0.195E+01	0.262E+00
30	9	6	10	12	1	3.8	967	0.100E+01	0.436E+00
31	9	7	8	3	2	9.2	904	0.166E+01	0.290E+00
32	9	7	12	3	3	19.5	554	0.199E+01	0.268E+00
33	9	7	13	2	3	17.2	410	0.213E+01	0.266E+00
34	9	8	11	3	3	14.1	474	0.242E+01	0.253E+00
35	8	12	13	2	3	13.3	607	0.249E+01	0.251E+00
36	9	21	10	15	1	3.2	841	0.108E+01	0.405E+00
37	9	22	13	1	2	7.0	778	0.196E+01	0.260E+00
38	10	1	13	3	3	15.6	1029	0.227E+01	0.258E+00
39	10	7	11	14	1	3.8	904	0.100E+01	0.433E+00
40	10	16	11	15	1	2.5	904	0.119E+01	0.362E+00
41	12	8	11	3	3	15.6	841	0.231E+01	0.251E+00
42	12	9	10	3	3	15.6	1155	0.230E+01	0.252E+00

註：見表十八註

表二十六　風向十六方位，C_{max} 大於 0.2ppm 之 SO_2 計算結果

NO	MON	DAY	HOUR	WD	STAB	AVE WS	MH(M)	XMAX(KM)	CMAX(PPM)
1	3	8	12	14	2	5.6	841	0.228E+01	0.224E+00
2	3	21	11	2	3	10.2	778	0.300E+01	0.220E+00
3	3	21	12	1	3	8.6	778	0.336E+01	0.201E+00
4	3	21	13	1	2	4.9	778	0.250E+01	0.203E+00
5	3	22	11	1	2	5.6	904	0.228E+01	0.224E+00
6	3	23	11	3	3	21.1	1029	0.195E+01	0.259E+00
7	3	23	12	3	3	21.9	1092	0.192E+01	0.259E+00
8	3	23	13	3	3	21.9	1092	0.192E+01	0.260E+00
9	4	4	11	1	2	4.9	904	0.249E+01	0.205E+00
10	4	4	13	14	2	5.6	778	0.228E+01	0.224E+00
11	4	8	11	14	1	1.9	904	0.134E+01	0.303E+00
12	4	15	13	2	3	11.7	1092	0.275E+01	0.232E+00
13	4	17	12	1	2	4.9	1595	0.248E+01	0.206E+00
14	4	17	13	16	2	5.6	1595	0.227E+01	0.226E+00
15	4	18	11	16	2	4.9	1092	0.249E+01	0.204E+00
16	4	18	13	15	2	5.6	1029	0.228E+01	0.225E+00
17	4	19	10	14	1	1.9	967	0.134E+01	0.306E+00
18	4	19	12	15	2	4.9	1029	0.248E+01	0.207E+00
19	4	19	13	15	2	6.3	1092	0.210E+01	0.245E+00
20	4	29	13	16	1	1.9	778	0.134E+01	0.304E+00
21	5	4	11	1	1	1.9	841	0.134E+01	0.306E+00
22	5	14	11	12	2	5.6	904	0.226E+01	0.230E+00
23	5	14	14	12	3	9.4	841	0.312E+01	0.218E+00
24	5	15	13	12	3	9.4	904	0.310E+01	0.219E+00
25	5	19	10	2	3	14.9	841	0.233E+01	0.257E+00
26	5	19	11	2	3	16.4	778	0.221E+01	0.260E+00
27	5	19	12	3	3	18.8	841	0.205E+01	0.264E+00
28	5	19	13	2	3	17.2	904	0.215E+01	0.263E+00
29	5	19	14	3	3	14.1	1029	0.240E+01	0.256E+00
30	5	20	10	1	2	5.6	841	0.227E+01	0.228E+00
31	5	29	12	13	1	1.9	778	0.134E+01	0.304E+00
32	5	29	14	12	1	1.9	778	0.134E+01	0.306E+00
33	5	30	14	12	2	5.6	841	0.226E+01	0.230E+00
34	5	31	12	12	3	8.6	841	0.330E+01	0.208E+00
35	5	31	13	12	3	9.4	841	0.311E+01	0.218E+00
36	5	31	14	13	2	6.3	841	0.209E+01	0.247E+00
37	6	1	11	12	3	14.1	778	0.240E+01	0.256E+00
38	6	10	12	12	3	13.3	778	0.248E+01	0.253E+00
39	6	12	11	12	2	6.3	967	0.208E+01	0.250E+00
40	6	12	12	12	3	8.6	967	0.328E+01	0.210E+00
41	6	13	11	12	3	13.3	904	0.248E+01	0.253E+00
42	6	13	12	12	3	12.5	841	0.257E+01	0.249E+00
43	6	14	12	12	3	13.3	967	0.248E+01	0.253E+00
44	6	14	13	12	3	12.5	904	0.258E+01	0.248E+00
45	6	14	14	12	3	13.3	904	0.248E+01	0.253E+00
46	6	15	11	12	3	9.4	967	0.310E+01	0.220E+00
47	6	15	12	13	3	10.2	967	0.294E+01	0.229E+00
48	6	15	13	13	3	10.2	1029	0.294E+01	0.229E+00
49	6	15	14	12	3	8.6	1029	0.328E+01	0.210E+00
50	6	16	12	12	3	10.2	967	0.294E+01	0.229E+00
51	6	16	13	13	3	10.9	904	0.280E+01	0.236E+00
52	6	16	14	12	3	10.9	904	0.280E+01	0.236E+00
53	6	17	11	12	3	9.4	904	0.310E+01	0.219E+00
54	6	17	12	12	3	11.7	967	0.268E+01	0.244E+00
55	6	17	13	12	3	12.5	967	0.257E+01	0.249E+00
56	6	17	14	12	3	12.5	967	0.257E+01	0.249E+00
57	6	18	11	12	3	9.4	967	0.310E+01	0.220E+00

續表二十六

NO	MON	DAY	HOUR	WD	STAB	AVE.WS	MH(M)	XMAX(KM)	CMAX(PPM)
58	6	18	13	12	3	12.5	967	0.257E+01	0.249E+00
59	6	18	14	12	3	10.9	967	0.280E+01	0.237E+00
60	6	19	11	12	3	9.4	904	0.310E+01	0.219E+00
61	6	19	12	12	3	10.9	967	0.280E+01	0.237E+00
62	6	19	13	13	3	10.9	1029	0.279E+01	0.238E+00
63	6	19	14	12	3	10.9	904	0.280E+01	0.237E+00
64	6	20	12	12	3	11.7	967	0.268E+01	0.244E+00
65	6	20	13	12	3	10.9	1029	0.279E+01	0.238E+00
66	6	20	14	12	3	9.4	967	0.310E+01	0.220E+00
67	6	21	12	12	3	8.6	1029	0.328E+01	0.210E+00
68	6	21	13	13	3	10.9	967	0.280E+01	0.237E+00
69	6	22	12	14	3	8.6	1092	0.328E+01	0.210E+00
70	6	22	13	15	2	5.6	1092	0.224E+01	0.233E+00
71	6	22	14	15	2	6.3	1029	0.208E+01	0.249E+00
72	6	23	12	16	2	6.3	1092	0.208E+01	0.250E+00
73	6	23	13	1	3	8.6	1092	0.328E+01	0.210E+00
74	6	24	10	14	2	5.6	967	0.225E+01	0.231E+00
75	6	24	11	15	3	8.6	904	0.329E+01	0.209E+00
76	6	25	13	14	2	6.3	967	0.208E+01	0.249E+00
77	6	25	14	14	2	6.3	967	0.208E+01	0.249E+00
78	6	26	11	14	2	3.9	967	0.245E+01	0.211E+00
79	6	29	11	13	2	4.9	1092	0.245E+01	0.211E+00
80	6	29	12	15	2	5.6	1092	0.225E+01	0.232E+00
81	6	29	13	15	2	5.6	1029	0.225E+01	0.232E+00
82	6	30	12	14	2	6.3	1092	0.208E+01	0.250E+00
83	6	30	14	14	2	5.6	1155	0.224E+01	0.233E+00
84	7	1	12	14	2	4.9	1155	0.245E+01	0.212E+00
85	7	1	13	15	2	4.9	1155	0.245E+01	0.212E+00
86	7	1	14	16	2	4.9	1155	0.245E+01	0.212E+00
87	7	2	12	13	2	6.3	1029	0.208E+01	0.249E+00
88	7	5	13	12	3	18.0	1092	0.208E+01	0.268E+00
89	7	6	11	12	3	14.1	1029	0.239E+01	0.257E+00
90	7	6	12	12	3	13.3	1092	0.247E+01	0.254E+00
91	7	6	13	12	3	16.4	1092	0.218E+01	0.266E+00
92	7	6	14	12	3	14.1	1029	0.239E+01	0.257E+00
93	7	12	12	16	2	6.3	1029	0.208E+01	0.250E+00
94	7	15	13	13	3	9.4	1092	0.308E+01	0.222E+00
95	7	15	14	13	3	10.2	1092	0.292E+01	0.231E+00
96	7	28	10	12	3	10.2	723	0.293E+01	0.230E+00
97	7	30	12	12	3	16.4	495	0.219E+01	0.264E+00
98	7	30	14	12	3	17.2	291	0.213E+01	0.266E+00
99	8	11	11	16	2	5.6	400	0.226E+01	0.230E+00
100	8	13	11	12	3	14.1	587	0.240E+01	0.256E+00
101	8	13	13	12	3	12.5	460	0.257E+01	0.249E+00
102	8	16	11	14	2	5.6	546	0.225E+01	0.231E+00
103	8	16	13	13	3	9.4	433	0.310E+01	0.220E+00
104	8	18	11	15	2	5.6	556	0.225E+01	0.232E+00
105	8	18	12	16	2	4.9	461	0.245E+01	0.211E+00
106	8	18	13	16	2	6.3	366	0.208E+01	0.250E+00
107	8	19	11	14	3	8.6	597	0.328E+01	0.210E+00
108	8	19	12	12	3	9.4	495	0.309E+01	0.221E+00
109	8	19	13	13	3	8.6	393	0.328E+01	0.210E+00
110	8	20	11	14	2	4.9	451	0.245E+01	0.211E+00
111	8	22	12	15	2	6.3	329	0.208E+01	0.249E+00
112	8	23	11	15	2	5.6	556	0.225E+01	0.231E+00
113	8	23	12	16	2	4.9	461	0.245E+01	0.211E+00
114	8	23	13	16	2	5.6	366	0.224E+01	0.233E+00

續表二十六

NO	MON	DAY	HOUR	WD	STAB	AVE WS	MH(M)	XMAX(FM)	CMAX(PPMO
115	8	34	12	14	2	4.9	524	0.245E+01	0.211E+00
116	8	24	13	13	3	8.6	460	0.328E+01	0.210E+00
117	8	25	12	13	3	10.2	301	0.294E+01	0.229E+00
118	8	26	12	14	2	6.3	398	0.208E+01	0.250E+00
119	8	29	11	15	2	4.9	441	0.246E+01	0.210E+00
120	8	31	13	12	3	10.9	244	0.280E+01	0.236E+00
121	9	1	11	15	2	6.3	514	0.208E+01	0.248E+00
122	9	3	10	2	2	5.6	753	0.226E+01	0.230E+00
123	9	4	11	13	2	7.0	753	0.195E+01	0.261E+00
124	9	4	13	14	2	7.0	451	0.195E+01	0.262E+00
125	9	5	12	13	3	8.6	784	0.329E+01	0.209E+00
126	9	5	13	13	3	10.2	602	0.295E+01	0.228E+00
127	9	5	14	13	3	8.6	420	0.330E+01	0.208E+00
128	9	6	10	12	1	3.8	967	0.100E+01	0.436E+00
129	9	6	12	15	2	4.9	791	0.247E+01	0.208E+00
130	9	7	8	3	2	9.2	904	0.166E+01	0.290E+00
131	9	7	12	3	3	19.5	554	0.199E+01	0.268E+00
132	9	7	13	2	3	17.2	410	0.213E+01	0.266E+00
133	9	8	11	3	3	14.1	474	0.242E+01	0.253E+00
134	9	9	12	2	3	11.7	554	0.270E+01	0.240E+00
135	9	9	13	2	3	12.5	410	0.259E+01	0.245E+00
136	9	9	14	2	3	12.5	266	0.259E+01	0.245E+00
137	8	12	13	2	3	13.3	607	0.249E+01	0.251E+00
138	8	12	14	2	3	12.5	467	0.259E+01	0.246E+00
139	9	13	14	1	3	11.7	758	0.269E+01	0.242E+00
140	9	20	13	16	2	4.9	680	0.246E+01	0.209E+00
141	9	21	10	15	1	3.2	841	0.108E+01	0.405E+00
142	9	21	12	13	2	5.6	967	0.226E+01	0.230E+00
143	9	21	13	14	2	6.3	967	0.209E+01	0.247E+00
144	9	21	14	14	2	6.3	736	0.209E+01	0.247E+00
145	9	22	13	1	2	7.0	778	0.196E+01	0.260E+00
146	9	22	14	1	3	8.6	632	0.331E+01	0.207E+00
147	9	24	8	1	3	11.7	652	0.272E+01	0.236E+00
148	9	28	8	3	3	9.4	904	0.315E+01	0.213E+00
149	9	28	13	2	3	11.7	967	0.272E+01	0.237E+00
150	9	29	9	2	3	8.6	904	0.334E+01	0.203E+00
151	9	29	13	1	3	13.3	967	0.251E+01	0.249E+00
152	9	30	8	3	3	12.5	904	0.261E+01	0.243E+00
153	10	1	13	3	3	15.6	1029	0.227E+01	0.258E+00
154	10	3	8	3	3	13.3	778	0.251E+01	0.247E+00
155	10	7	11	14	1	3.8	904	0.100E+01	0.433E+00
156	10	8	11	1	3	8.6	967	0.331E+01	0.207E+00
157	10	16	11	15	1	3.5	904	0.119E+01	0.363E+00
158	10	16	13	15	2	4.9	967	0.247E+01	0.207E+00
159	10	17	12	1	2	5.6	778	0.227E+01	0.227E+00
160	11	27	10	15	3	10.9	590	0.287E+01	0.226E+00
161	11	28	10	2	2	6.3	778	0.212E+01	0.239E+00
162	11	28	11	2	3	9.4	904	0.317E+01	0.211E+00
163	11	30	15	1	3	8.6	316	0.336E+01	0.201E+00
164	12	1	11	2	3	10.9	715	0.286E+01	0.227E+00
165	12	2	9	15	2	4.9	652	0.252E+01	0.200E+00
166	12	5	13	1	3	12.5	680	0.262E+01	0.240E+00
167	12	8	11	3	3	15.6	841	0.231E+01	0.251E+00
168	12	9	10	3	3	15.6	1155	0.230E+01	0.252E+00
169	12	11	12	13	2	4.9	1218	0.251E+01	0.201E+00
170	12	14	9	2	3	14.9	841	0.237E+01	0.249E+00
171	12	22	10	1	3	12.5	527	0.266E+01	0.234E+00

註：見表十八註

表二十九　風向三十六方位時，C_{max} 大於 0.25ppm之SO_2計算結果

NO	MON	DAY	HOUR	WD	STAB	AVE.WS	MH(M)	XMAX(KM)	CMAX(PPM)
1	3	23	11	7	3	21.9	1029	0.195E+01	0.259E+00
2	3	23	12	7	3	21.9	1092	0.192E+01	0.259E+00
3	3	23	13	6	3	21.9	1092	0.192E+01	0.260E+00
4	4	6	11	31	1	1.9	904	0.134E+01	0.303E+00
5	4	19	10	31	1	1.9	967	0.134E+01	0.306E+00
6	4	29	13	36	1	1.9	778	0.134E+01	0.304E+00
7	5	4	11	2	1	1.9	841	0.134E+01	0.306E+00
8	5	19	10	4	3	14.9	841	0.233E+01	0.257E+00
9	5	19	11	5	3	16.4	778	0.221E+01	0.260E+00
10	5	19	12	6	3	18.8	841	0.205E+01	0.264E+00
11	5	19	13	5	3	17.2	904	0.215E+01	0.263E+00
12	5	19	14	6	3	14.1	1029	0.240E+01	0.256E+00
13	5	29	12	29	1	1.9	778	0.134E+01	0.304E+00
14	5	29	14	27	1	1.9	778	0.134E+01	0.306E+00
15	6	1	11	26	3	14.1	778	0.240E+01	0.256E+00
16	6	1	12	24	3	13.3	778	0.249E+01	0.252E+00
17	6	10	12	26	3	13.3	778	0.248E+01	0.253E+00
18	6	13	11	26	3	13.3	904	0.248E+01	0.253E+00
19	6	13	13	25	3	15.5	841	0.225E+01	0.262E+00
20	6	13	14	25	3	17.2	841	0.213E+01	0.266E+00
21	6	14	12	26	3	13.4	967	0.248E+01	0.258E+00
22	67	15	14	27	3	13.3	904	0.248E+01	0.253E+00
23	7	5	10	25	3	15.6	1092	0.224E+01	0.264E+00
24	7	5	11	25	3	17.2	1092	0.213E+01	0.267E+00
25	7	5	12	25	3	18.0	1155	0.207E+01	0.269E+00
26	7	5	13	26	3	18.0	1092	0.208E+01	0.268E+00
27	7	5	14	25	3	15.6	1092	0.225E+01	0.268E+00
28	7	6	10	25	3	16.1	1029	0.219E+01	0.265E+00
29	7	6	11	27	3	14.0	1029	0.239E+01	0.257E+00
30	7	6	12	26	3	13.8	1092	0.247E+01	0.254E+00
31	7	6	13	26	3	16.4	1092	0.218E+01	0.266E+00
32	7	6	14	27	3	14.1	1029	0.239E+01	0.257E+00
33	7	28	12	24	3	19.5	770	0.198E+01	0.271E+00
34	7	28	13	25	3	15.6	793	0.224E+01	0.265E+00
35	7	29	11	25	3	16.9	514	0.218E+01	0.266E+00
36	7	29	12	25	3	18.6	426	0.208E+01	0.268E+00
37	7	29	13	25	3	17.2	339	0.213E+01	0.267E+00
38	7	30	10	24	3	15.4	699	0.235E+01	0.263E+00
39	7	30	11	25	3	15.6	597	0.225E+01	0.263E+00
40	7	30	12	26	3	16.4	495	0.219E+01	0.264E+00
41	7	30	14	26	3	17.2	291	0.213E+01	0.266E+00
42	7	31	10	25	3	19.5	651	0.199E+01	0.269E+00
43	7	31	11	24	3	16.8	524	0.203E+01	0.269E+00
44	7	31	12	24	3	19.5	398	0.198E+01	0.271E+00
45	8	2	11	25	3	16.8	597	0.203E+01	0.269E+00
46	8	2	12	25	3	16.4	495	0.218E+01	0.267E+00
47	8	13	11	26	3	14.1	587	0.240E+01	0.256E+00
48	8	13	12	24	3	14.9	524	0.233E+01	0.260E+00
49	9	4	11	30	2	7.6	753	0.195E+01	0.261E+00
50	9	4	13	31	2	7.0	451	0.195E+01	0.262E+00
51	9	6	10	28	1	3.8	967	0.100E+01	0.436E+00
52	9	7	8	7	2	9.2	904	0.166E+01	0.290E+00
53	9	7	12	6	3	19.5	554	0.199E+01	0.268E+00
54	9	7	13	5	3	17.2	410	0.213E+01	0.266E+00
55	9	8	11	6	3	14.0	474	0.242E+01	0.253E+00
56	8	12	13	4	3	13.3	607	0.249E+01	0.251E+00
57	9	21	10	33	1	3.2	841	0.108E+01	0.405E+00
58	9	22	13	2	2	7.0	778	0.196E+01	0.260E+00
59	10	1	13	6	3	15.6	1029	0.227E+01	0.258E+00
60	10	7	11	32	1	3.8	904	0.100E+01	0.433E+00
61	10	18	11	34	1	2.5	904	0.119E+01	0.362E+00
62	12	8	11	7	3	15.8	841	0.231E+01	0.251E+00
63	12	9	10	6	3	15.8	1155	0.230E+01	0.252E+00

表二十八　風向三十六方位時，C_{max} 大於 0.3ppm之SO_2計算結果

NO	MON	DAY	HOUR	WE	STAB	AVE.WS	MH(M)	XMAX(KM)	CMAX(PPM)
1	4	8	11	31	1	1.9	904	0.134E+01	0.303E+00
2	4	19	10	31	1	1.9	967	0.134E+01	0.306E+00
3	4	29	13	36	1	1.9	778	0.134E+01	0.304E+00
4	5	4	11	2	1	1.9	841	0.134E+01	0.305E+00
5	5	29	12	29	1	1.9	778	0.134E+01	0.304E+00
6	6	29	14	27	1	1.9	778	0.134E+01	0.306E+00
7	9	6	10	28	1	2.8	967	0.100E+01	0.426E+00
8	9	21	10	33	1	3.2	841	0.108E+01	0.405E+00
9	10	7	11	32	1	3.8	904	0.100E+01	0.433E+00
10	10	16	11	34	1	2.5	904	0.119E+01	0.362E+00

註：見表十八註

表一十七　風向十六方位，SO_2，C_{max} 大於 0.2ppm之設計結果

風向	穩定度	代表風速 (m/s)	頻率 (次/年)	j	X_j^- (km)	X_j^+ (km)	Y_j (km)	A_s (km^2)	X_F (km)	X_B (km)	A_P (km^2)	CR_s	CR_T α				NN α			
													0.5	0.9	0.95	0.99	0.5	0.9	0.95	0.99
12	3	9.35	15	90	2.31	3.89	0.63	0.78	2.19	3.92	2.07	0.38	0.12	0.25	0.30	0.42	1	1	1	2
				80	2.13	4.35	0.91	1.58				0.76					1	1	1	1
				70	1.99	4.94	1.53	3.56				1.72					1	1	1	1
12	3	12.30	19	90	2.11	3.56	0.58	0.66	1.87	3.88	2.27	0.29	0.10	0.20	0.25	0.35	1	1	1	2
				80	1.95	3.98	0.84	1.35				0.59					1	1	1	1
				70	1.82	4.52	1.42	3.03				1.33					1	1	1	1
13	3	9.35	11	90	2.30	3.88	0.62	0.77	2.18	2.93	2.10	0.37	0.17	0.32	0.38	0.51	1	1	2	2
				80	2.12	4.34	0.91	1.58				0.75					1	1	1	1
				70	1.99	4.92	1.61	3.54				1.69					1	1	1	1
14	2	6.70	12	90	1.68	2.55	0.68	0.46	1.48	2.96	1.30	0.35	0.15	0.30	0.35	0.48	1	1	1	1
				80	1.56	2.89	0.99	1.04				0.80					1	1	1	1
				70	1.46	3.19	1.68	2.28				1.75					1	1	1	1
15	2	6.70	11	90	1.68	2.55	0.68	0.46	1.49	2.96	1.29	0.36	0.17	0.32	0.38	0.51	1	1	2	2
				80	1.56	2.89	0.99	1.04				0.81					1	1	1	1
				70	1.46	3.19	1.68	2.28				1.77					1	1	1	1

註：(1) j　：C_{max} 之忍限值。
(2) X_j^-　：接近忍染源，忍限值爲 j 之下風距離。
(3) X_j^+　：遠離污染源，忍限值爲 j 之下風距離。
(4) Y_j　：忍限值爲 j 之側向距離。
(5) A_s　：單一測站涵蓋面積。
(6) X_F　：接近污染源，濃度值等於空氣品質限值之下風距離。
(7) X_B　：遠離污染源，濃度值等於空氣品質限值之下風距離。
(8) A_p　：偵測潛勢區域面積。
(9) CR_s　：單一測站覆蓋比。
(10) α　：可信賴區間。
(11) CR_T　：總覆蓋比。
(12) NN　：測站數目。

表三十　風向三十六方位，SO_2，C_{max} 大於 0.25ppm之設計結果

風向	穩定度	代表風速 (m/s)	頻率 (次/年)	j	X_j^- (km)	X_j^+ (km)	Y_j (km)	A_s (km^2)	X_F (km)	X_B (km)	A_p (km^2)	CR_s	CR_T α 0.5	CR_T α 0.9	CR_T α 0.95	CR_T α 0.99	NN α 0.5	NN α 0.9	NN α 0.95	NN α 0.99
6	3	16.0	6	90	1.58	2.64	0.45	0.37	1.60	2.43	0.29	1.28	0.29	0.50	0.56	0.69	1	1	1	1
				80	1.45	2.97	0.65	0.77				2.66					1	1	1	1
24	3	16.0	5	90	1.57	2.63	0.45	0.37	1.57	2.46	0.31	1.19	0.34	0.56	0.62	0.74	1	1	1	1
				80	1.44	2.95	0.65	0.77				2.47					1	1	1	1
25	3	16.0	5	90	1.72	2.90	0.48	0.44	1.75	2.65	0.35	1.26	0.12	0.25	0.30	0.42	1	1	1	1
				80	1.59	3.25	0.70	0.91				2.62					1	1	1	1
26	3	16.0	6	90	1.72	2.90	0.48	0.44	1.75	2.65	0.35	1.26	0.29	0.50	0.56	0.69	1	1	1	1
				80	1.59	3.25	0.70	0.91				2.62					1	1	1	1

註：見表二十七註

表三十一　風向三十六方位，SO_2，C_{max} 大於 0.20ppm之設計結果

風向	穩定度	代表風速 (m/s)	頻率 (次/年)	j	X_j^- (km)	X_j^+ (km)	Y_j (km)	A_s (km^2)	X_F (km)	X_B (km)	A_P (km^2)	CR_s	CR_T α=0.5	CR_T α=0.9	CR_T α=0.95	CR_T α=0.99	NN α=0.5	NN α=0.9	NN α=0.95	NN α=0.99
5	3	12.3	5	90	2.13	3.58	0.58	0.66	1.91	3.85	0.97	0.68	0.34	0.56	0.62	0.74	1	1	1	2
				80	1.96	4.01	0.85	1.41				1.45					1	1	1	1
25	3	12.3	7	90	2.11	3.55	0.58	0.65	1.86	3.90	1.02	0.63	0.25	0.45	0.51	0.64	1	1	1	2
				80	1.94	3.97	0.84	1.34				1.31					1	1	1	1
26	3	9.35	7	90	2.31	3.89	0.62	0.78	2.19	3.92	0.92	0.84	0.25	0.45	0.51	0.64	1	1	1	1
				80	2.13	4.35	0.91	1.59				1.73					1	1	1	1
26	3	12.3	10	90	2.11	3.56	0.58	0.65	1.87	3.88	1.01	0.64	0.18	0.35	0.40	0.53	1	1	1	1
				80	1.95	3.98	0.84	1.34				1.33					1	1	1	1
27	3	12.3	6	90	2.11	3.56	0.58	0.65	1.87	3.88	1.01	0.64	0.29	0.50	0.56	0.69	1	1	1	2
				80	1.95	3.98	0.84	1.34				1.33					1	1	1	1
29	3	9.35	8	90	2.30	3.88	0.62	0.77	2.18	3.93	0.93	0.82	0.22	0.41	0.47	0.60	1	1	1	1
				80	2.12	4.34	0.91	1.58				1.70					1	1	1	1
31	2	6.7	6	90	1.68	2.55	0.68	0.46	1.49	2.96	0.57	0.81	0.29	0.50	0.56	0.69	1	1	1	1
				80	1.56	2.89	1.08	1.04				1.82					1	1	1	1

續表三十一

風向	穩定度	代表風速 (m/s)	頻率 (次/年)	j	X_j^- (km)	X_j^+ (km)	Y_j (km)	A_s (km²)	X_F (km)	X_B (km)	A_p (km²)	CR_s	CR_T α 0.5	CR_T α 0.9	CR_T α 0.95	CR_T α 0.99	NN α 0.5	NN α 0.9	NN α 0.95	NN α 0.99
32	2	6.70	6	90	1.68	2.55	0.68	0.46	1.48	2.96	0.58	0.80	0.29	0.50	0.56	0.69	1	1	1	1
				80	1.56	2.89	0.99	1.04				1.79					1	1	1	1
33	2	4.4	5	90	2.00	3.01	0.79	0.63	2.15	2.80	0.31	2.03	0.34	0.56	0.62	0.74	1	1	1	1
				80	1.86	3.42	1.15	1.41				4.57					1	1	1	1
33	2	6.7	8	90	1.68	2.55	0.68	0.46	1.49	2.96	0.57	0.81	0.22	0.41	0.47	0.60	1	1	1	1
				80	1.56	2.89	0.99	1.04				1.79					1	1	1	1

註：見表二十七註。

表三十二　風向十六方位時，懸浮顆粒 ，C_{max} 大於 1500 $\mu g / m^3$ 之計算結果

NO.	MON.	DAY	HOUR	WD	STAB.	AVE.WS	MH(M)	XMAX(KM)	CMAX(ug/m³)
1	4	8	11	14	1	1.9	904	0.121E+01	0.178E+04
2	4	19	10	14	1	1.9	967	0.121E+01	0.180E+04
3	4	29	13	16	1	1.9	778	0.121E+01	0.179E+04
4	5	4	11	1	1	1.9	841	0.121E+01	0.180E+04
5	5	29	12	13	1	1.9	778	0.121E+01	0.179E+04
6	5	29	14	12	1	1.9	778	0.121E+01	0.180E+04
7	9	6	10	12	1	3.8	967	0.880E+00	0.220E+04
8	9	21	10	15	1	3.2	841	0.956E+00	0.209E+04
9	10	7	11	14	1	3.8	904	0.885E+00	0.217E+04
10	10	16	11	15	1	2.5	904	0.106E+01	0.195E+04

註：見表十八註

表三十三　風向十六方位，懸浮顆粒，C_{max} 大於 1000$\mu g/m^3$ 之設計結果

風向	穩定度	代表風速 (m/s)	頻率 (次/年)	j	X_j^- (km)	X_j^+ (km)	Y_j (km)	A_s (km^2)	X_F (km)	X_B (km)	A_P (km^2)	CR_S	CR_T α=0.5	CR_T α=0.9	CR_T α=0.95	CR_T α=0.99	NN α=0.5	NN α=0.9	NN α=0.95	NN α=0.99
1	3	6.7	21	90	2.31	3.89	0.63	0.78	2.60	4.23	2.18	0.36	0.09	0.19	0.23	0.33	1	1	1	1
				80	2.13	4.35	0.91	1.59				0.73					1	1	1	1
				70	1.99	4.94	1.53	3.56				1.63					1	1	1	1
12	3	6.7	20	90	2.31	3.89	0.63	0.78	2.60	4.23	2.18	0.36	0.09	0.20	0.24	0.34	1	1	1	1
				80	2.13	4.35	0.91	1.59				0.73					1	1	1	1
				70	1.99	4.94	1.53	3.56				1.63					1	1	1	1
12	3	9.35	15	90	1.97	3.32	0.54	0.58	2.09	3.97	2.23	0.26	0.12	0.25	0.30	0.42	1	1	2	2
				80	1.82	3.72	0.79	1.18				0.53					1	1	1	1
				70	1.70	4.22	1.34	2.64				1.18					1	1	1	1
12	3	12.3	19	90	1.68	2.50	0.47	0.42	1.69	3.60	1.99	0.21	0.10	0.20	0.25	0.35	1	1	2	2
				80	1.55	3.16	0.69	0.87				0.44					1	1	1	1
				70	1.44	3.59	1.16	1.96				0.98					1	1	1	1
13	3	6.7	14	90	2.11	3.56	0.58	0.66	2.30	4.11	2.29	0.29	0.13	0.27	0.31	0.44	1	1	2	2
				80	1.95	3.98	0.84	1.37				0.59					1	1	1	1
				70	1.82	4.52	1.42	3.02				1.32					1	1	1	1

續表三十三

風向	穩定度	代表風速 (m/s)	頻率 (次/年)	j	X_j^- (km)	X_j^+ (km)	Y_j (km)	A_s (km²)	X_F (km)	X_B (km)	A_P (km²)	CR_S	CR_T α=0.5	CR_T α=0.9	CR_T α=0.95	CR_T α=0.99	NN α=0.5	NN α=0.9	NN α=0.95	NN α=0.99
13	3	9.35	11	90	1.97	3.32	0.54	0.58	2.11	3.95	2.23	0.26	0.17	0.32	0.38	0.51	1	1	1	1
				80	1.83	3.75	0.80	1.20				0.54					1	1	1	1
				70	1.71	4.25	1.35	7.68				1.20					1	1	1	1
14	2	4.4	13	90	2.14	3.22	0.83	0.71	0.67	2.75	1.40	0.51	0.14	0.28	0.33	0.46	1	1	1	1
				80	1.99	3.66	1.21	1.59				1.13					1	1	1	1
				70	1.85	4.02	2.05	3.48				2.49					1	1	1	1
14	2	6.7	12	90	1.43	2.17	0.60	0.35	1.44	2.89	1.23	0,28	0.15	0.30	0.35	0.48	1	2	2	2
				80	1.32	2.46	0.87	0.78				0.63					1	1	1	1
				70	1.24	2.72	1.45	1.73				1.41					1	1	1	1
14	3	6.7	32	90	2.11	3.56	0.58	0.66	2.30	4.11	2.29	0.29	0.06	0.13	0.16	0.24	1	1	1	1
				80	1.95	3.98	0.84	1.37				0.59					1	1	1	1
				70	1.82	4.52	1.42	3.02				1.32					1	1	1	1
15	2	4.4	16	90	1.57	2.38	0.64	0.41	1.62	3.03	1.28	0.32	0.12	0.24	0.28	0.40	1	1	1	2
				80	1.45	2.70	1.18	0.91				0.71					1	1	1	1
				70	1.36	2.98	1.57	2.01				1.57					1	1	1	1

續表三十三

風向	穩定度	代風表速 (m/s)	頻率 (次/年)	j	X_j^- (km)	X_j^+ (km)	Y_j (km)	A_s (km^2)	X_F (km)	X_B (km)	A_P (km^2)	CR_S	CR_T α=0.5	CR_T α=0.9	CR_T α=0.95	CR_T α=0.99	NN α=0.5	NN α=0.9	NN α=0.95	NN α=0.99
15	2	6.7	11	90	1.43	2.17	0.60	0.35	1.44	2.89	1.23	0.28	0.17	0.32	0.38	0.51	1	2	2	2
				80	1.32	2.46	0.87	0.78				0.63					1	1	1	1
				70	1.24	2.72	1.45	1.73				1.41					1	1	1	1
15	3	6.7	10	90	2.13	3.58	0.58	0.98	2.32	4.09	2.23	0.44	0.18	0.35	0.40	0.53	1	1	1	2
				80	1.96	4.01	0.85	1.37				0.61					1	1	1	1
				70	1.83	4.56	1.43	3.06				1.37					1	1	1	1
16	2	4.4	18	90	2.14	3.22	0.83	0.71	0.94	2.75	1.32	0.54	0.10	0.21	0.26	0.37	1	1	1	1
				80	1.99	3.64	1.21	1.59				1.20					1	1	1	1
				70	1.85	4.02	2.05	3.48				2.64					1	1	1	1
16	3	6.7	15	90	2.13	3.58	0.58	0.98	2.32	4.09	2.23	0.44	0.12	0.25	0.30	0.42	1	1	1	1
				80	1.96	4.01	0.85	1.37				0.61					1	1	1	1
				70	1.83	4.56	1.43	3.06				1.37					1	1	1	1

註：見表二十七註

表三十四　風向三十六方位，懸浮顆粒，C_{max} 大於 1500 $\mu g/m^3$ 之計算結果

NO.	MON.	DAY	HOUR	WD	STAB.	AVE.WS	MH(M)	XMAX(KM)	CMAX(ug/m³)
1	4	8	11	31	1	1.9	904	0.121E+01	0.178E+04
2	4	19	10	31	1	1.9	967	0.121E+01	0.180E+04
3	4	29	13	36	1	1.9	778	0.121E+01	0.179E+04
4	5	4	11	2	1	1.9	841	0.121E+01	0.180E+04
5	5	29	12	29	1	1.9	778	0.121E+01	0.179E+04
6	5	29	14	27	1	1.9	778	0.121E+01	0.180E+04
7	9	6	10	28	1	3.8	967	0.880E+00	0.220E+04
8	9	21	10	39	1	3.2	841	0.956E+00	0.209E+04
9	10	7	11	32	1	3.8	904	0.885E+00	0.217E+04
10	10	16	11	34	1	2.5	904	0.106E+01	0.195E+04

註：見表十八註

表三十五　風向三十六方位，懸浮顆粒，C_{max} 大於 1000 $\mu g/m^3$ 之設計結果

風向	穩定度	代表風速 (m/s)	頻率 (次/年)	j	X_j^- (km)	X_j^+ (km)	Y_j (km)	A_S (km^3)	X_F (km)	X_B (km)	A_P (km^2)	CR_S	CR_T α				NN α			
													0.5	0.9	0.95	0.99	0.5	0.9	0.95	0.99
1	3	6.7	7	90	2.34	3.94	0.63	0.80	2.67	4.17	0.89	0.90	0.25	0.45	0.51	0.64	1	1	1	1
				80	-	-	-	-				-					-	-	-	-
2	2	4.4	7	90	1.64	2.49	0.67	0.44	1.72	2.95	0.50	0.89	0.25	0.45	0.51	0.64	1	1	1	1
				80	-	-	-	-				-					-	-	-	-
2	3	6.7	11	90	2.31	3.89	0.63	0.78	2.60	4.23	0.971	0.80	0.17	0.32	0.38	0.51	1	1	1	1
				80	-	-	-	-				-					-	-	-	-
3	3	6.7	10	90	2.32	3.92	0.63	0.78	2.64	4.20	0.93	0.84	0.18	0.35	0.40	0.54	1	1	1	1
				80	-	-	-	-				-					-	-	-	-
5	3	12.3	5	90	1.66	2.79	0.47	0.41	1.63	3.46	0.81	0.51	0.34	0.56	0.62	0.74	1	2	2	2
				80	1.53	3.13	0.68	0.85				1.05					1	1	1	1
6	3	16.0	6	90	1.46	2.44	0.42	0.32	1.40	3.17	0.70	0.46	0.29	0.50	0.56	0.69	1	2	2	2
				80	1.34	2.75	0.60	0.67				1.46					1	1	1	1
8	3	9.35	5	90	1.89	3.17	0.52	0.63	1.97	3.80	0.92	0.69	0.34	0.56	0.62	0.74	1	1	1	2
				80	1.74	3.56	0.76	1.09				1.18					1	1	1	1

續表三十五

風向	穩定度	代表風速 (m/s)	頻率 (次/年)	j	X_j^- (km)	X_j^+ (km)	Y_j (km)	A_S (km^2)	X_F (km)	X_B (km)	A_P (km^2)	CR_S	CR_T α 0.5	CR_T α 0.9	CR_T α 0.95	CR_T α 0.99	NN α 0.5	NN α 0.9	NN α 0.95	NN α 0.99
24	3	6.7	6	90	2.17	3.65	0.59	0.69	2.37	4.05	0.94	0.73	0.29	0.50	0.56	0.69	1	1	1	1
				80	-	-	-	-				-					-	-	-	-
25	3	6.7	6	90	2.36	3.98	0.64	0.81	2.70	4.14	0.86	0.95	0.29	0.50	0.56	0.69	1	1	1	1
				80	-	-	-	-				-					-	-	-	-
25	3	12.3	7	90	1.69	2.84	0.48	0.43	1.70	3.59	0.87	0.49	0.25	0.45	0.51	0.64	1	1	2	2
				80	1.56	3.19	0.69	0.88				1.02					1	1	1	1
25	3	16.0	15	90	1.36	2.27	0.39	0.28	1.28	3.03	0.66	0.43	0.12	0.25	0.30	0.42	1	1	1	1
				80	-	-	-	-				-					-	-	-	-
26	3	6.7	13	90	2.34	3.94	0.63	0.80	2.67	4.17	0.89	0.90	0.14	0.28	0.33	0.46	1	1	1	1
				80	-	-	-	-				-					-	-	-	-
26	3	9.35	7	90	1.87	3.15	0.52	0.52	1.95	3.81	0.94	0.55	0.25	0.45	0.51	0.64	1	1	1	2
				80	1.73	3.53	0.76	1.07				1.14					1	1	1	1

續表三十五

風向	穩定度	代表風速 (m/s)	頻率 (次/年)	j	X_j^- (km)	X_j^+ (km)	Y_j (km)	A_S (km²)	X_F (km)	X_B (km)	A_P (km²)	CR_S	CR_T α 0.5	CR_T α 0.9	CR_T α 0.95	CR_T α 0.99	NN α 0.5	NN α 0.9	NN α 0.95	NN α 0.99
26	3	12.3	10	90	1.68	2.82	0.47	0.42	1.69	3.60	0.88	0.48	0.18	0.35	0.40	0.53	1	1	1	1
				80	1.55	3.16	0.69	0.87				0.99					1	1	1	1
26	3	16.0	6	90	1.46	2.44	0.42	0.32	1.40	3.17	0.70	0.46	0.29	0.50	0.56	0.69	1	2	2	2
				80	1.32	2.75	0.60	0.67				0.95					1	1	1	1
27	2	12.3	6	90	1.69	2.84	0.48	0.43	1.70	3.59	0.87	0.49	0.29	0.50	0.56	0.69	1	2	2	2
				80	1.56	3.19	0.69	0.88				1.02					1	1	1	1
29	3	6.7	9	90	2.11	3.56	0.58	0.66	2.30	4.11	1.02	0.64	0.20	0.38	0.44	0.57	1	1	1	1
				80	-	-	-	-				-					-	-	-	-
29	3	9.35	8	90	1.85	3.11	0.51	0.51	1.92	3.84	0.97	0.52	0.22	0.41	0.47	0.60	1	1	1	2
				80	1.70	3.48	0.75	1.07				1.10					1	1	1	1
30	3	6.7	5	90	2.13	3.58	0.58	0.66	2.32	4.09	0.99	0.67	0.34	0.56	0.62	0.74	1	1	1	2
				80	1.96	4.01	0.85	1.37				1.38					1	1	1	1

續表三十五

風向	穩定度	代表風速 (m/s)	頻率 (次/年)	j	X_j^- (km)	X_j^+ (km)	Y_j (km)	A_S (km^2)	X_F (km)	X_B (km)	A_P (km^2)	CR_S	CR_T α 0.5	CR_T α 0.9	CR_T α 0.95	CR_T α 0.99	NN α 0.5	NN α 0.9	NN α 0.95	NN α 0.99
31	2	6.7	6	90	1.43	2.17	0.53	0.35	1.44	2.89	0.55	0.64	0.29	0.50	0.56	0.69	1	1	1	2
				80	1.32	2.46	0.87	0.78				1.41					1	1	1	1
31	3	6.7	15	90	2.11	3.56	0.58	0.66	2.30	4.11	0.57	1.18	0.12	0.25	0.30	0.42	1	1	1	1
				80	-	-	-	-				-					-	-	-	-
32	2	4.4	9	90	2.14	3.22	0.83	0.71	0.67	2.75	0.62	1.15	0.20	0.38	0.44	0.57	1	1	1	1
				80	-	-	-	-				-					-	-	-	-
32	2	6.7	6	90	1.31	2.00	0.55	0.30	1.26	2.78	0.54	0.55	0.29	0.50	0.56	0.69	1	1	2	2
				80	1.22	2.27	0.81	0.67				1.24					1	1	1	1
32	3	6.7	17	90	2.29	3.85	0.62	0.76	2.57	4.26	1.00	0.76	0.11	0.23	0.27	0.38	1	1	1	1
				80	-	-	-	-				-					-	-	-	-
33	2	4.4	10	90	1.76	2.66	0.71	0.50	1.89	3.18	0.57	0.88	0.18	0.35	0.40	0.53	1	1	1	1
				80	-	-	-	-				-					-	-	-	-

續表三十五

風向	穩定度	代表風速 (m/s)	頻率 (次/年)	j	X_j^- (km)	X_j^+ (km)	Y_j (km)	A_S (km²)	X_F (km)	X_B (km)	A_P (km²)	CR_S	CR_T α 0.5	CR_T α 0.9	CR_T α 0.95	CR_T α 0.99	NN α 0.5	NN α 0.9	NN α 0.95	NN α 0.99
33	2	6.7	8	90	1.43	2.17	0.60	0.35	1.44	2.89	0.55	0.63	0.22	0.41	0.47	0.60	1	1	1	1
				80	-	-	-	-				-					-	-	-	-
33	3	6.7	6	90	2.13	3.58	0.58	0.56	2.32	4.09	0.99	0.56	0.29	0.50	0.56	0.69	1	1	1	2
				80	1.96	4.01	0.85	1.37				1.38					1	1	1	1
34	2	4.4	6	90	1.57	2.38	0.64	0.67	1.62	3.03	0.57	1.17	0.29	0.50	0.56	0.69	1	1	1	1
				80	-	-	-	-				-					-	-	-	-
35	2	4.4	8	90	1.57	2.38	0.64	0.41	1.62	3.03	0.57	0.72	0.22	0.41	0.47	0.60	1	1	1	1
				80	-	-	-	-				-					-	-	-	-
36	2	4.4	9	90	1.58	2.39	0.65	0.41	1.64	3.02	0.56	0.74	0.20	0.38	0.44	0.57	1	1	1	1
				80	-	-	-	-				-					-	-	-	-
36	3	6.7	5	90	2.13	3.58	0.58	0.66	2.32	4.09	0.99	0.67	0.34	0.56	0.62	0.74	1	1	1	2
				80	1.96	4.01	0.85	1.37				1.38					1	1	1	1

註：見表二十七註

表三十六　風向十六方位，α 爲 0.95，C_{max} 忍限值 0.9，SO_2，C_{max} 大於 0.3ppm，P 與 NT 之計算結果

WD	X_{max}(km)	N（次／年）	CR_S	CR_T	$P_i=1-CR_T$	$\sum P_i=P$	NN(個)	$NT=\sum NN$
14	1.34	2	0.936	0.91	0.09	0.09	1	1
15	1.08	2	0.408	0.91	0.09	0.18	3	4
1	1.34	1	0.336	1.00	0.00	0.18	3	7

註：(1)WD 爲風向，(2)X_{max} 爲最大地面濃度發生位置，

(3)N 爲超過空氣品質限值之次數，

(4)CR_S 爲單一測站覆蓋比，(5)CR_T 爲總覆蓋比，

(6)P_i 爲偵測效率，(7)P 爲偵測效率累積值，

(8)NN 爲測站數目，(9)NT 爲測站總數。

表三十七　風向十六方位，α 爲 0.95，C_{max} 忍限值 0.9，SO_2，C_{max} 大於 0.25ppm，P 與 NT 之計算結果

WD	X_{max}(km)	N（次／年）	CR_S	CR_T	$P_i=1-CR_T$	$\sum P_i=P$	NN(個)	$NT=\sum NN$
12	2.18	8	0.576	0.47	0.53	0.53	1	1
3	1.99	7	0.576	0.51	0.49	1.02	1	2
12	2.47	5	1.224	0.62	0.38	1.40	1	3
2	2.13	4	0.6	0.70	0.30	1.70	2	5
14	1.34	2	0.456	0.91	0.09	1.79	2	7
2	2.49	1	0.50	1.0	0.00	1.79	2	9

註：同表三十六註

表三十八　風向十六方位，α爲0.95，C_{max}忍限值0.9，SO_2，C_{max}大於0.20ppm，P與NT之計算結果

WD	X_{max}(km)	N(次/年)	CR_S	CR_T	$P_i=1-CR_T$	$\sum P_i=P$	NN(個)	$NT=\sum NN$
12	2.68	19	0.288	0.25	0.75	0.75	1	1
12	2.93	15	0.384	0.30	0.70	1.45	1	2
14	2.03	12	0.36	0.35	0.65	2.10	1	3
13	2.92	11	0.36	0.38	0.62	2.72	2	5
15	2.08	11	0.36	0.38	0.62	3.34	2	7
2	2.70	8	0.312	0.47	0.53	3.87	2	9
12	2.39	8	0.24	0.47	0.53	4.40	2	11

註：見表三十六註

註三十九　風向三十六方位，α爲0.95，C_{max}忍限值0.9，SO_2，C_{max}大於0.3ppm，P與NT之計算結果

WD	X_{max}(km)	N(次/年)	CR_S	CR_T	$P_i=1-CR_T$	$\sum P_i=P$	NN(個)	$NT=\sum NN$
31	1.34	2	2.112	0.91	0.09	0.09	1	1
29	1.34	1	2.16	1.00	0.00	0.09	1	2

註：見表三十六註

表四十　風向三十六方位，α 爲 0.95 ，C_{max} 忍限值 0.9 ，SO_2 ，C_{max} 大於 0.25ppm ，P與NT之計算結果

WD	X_{max} (km)	N (次/年)	CR_S	CR_T	$P_i = 1 - CR_T$	$\sum P_i = P$	NN (個)	$NT = \sum NN$
25	2.18	15	1.272	0.20	0.70	0.70	1	1
6	1.99	6	1.272	0.56	0.44	1.14	1	2
26	2.18	6	1.32	0.56	0.44	1.58	1	3
24	1.98	5	1.512	0.62	0.38	1.96	1	4
26	2.48	4	2.784	0.70	0.30	2.26	1	5
5	2.13	3	1.344	0.79	0.21	2.47	1	6
27	2.39	2	2.232	0.91	0.09	2.56	1	7
28	1.34	2	1.008	0.91	0.09	2.65	1	8
4	2.49	1	2.712	1.00	0.00	2.65	1	9
註：見表三十六註								

表四十一　風向三十六方位，α 爲 0.95 ，C_{max} 忍限值 0.9 ，SO_2 ，C_{max} 大於 0.2ppm ，P與NT之計算結果

WD	X_{max} (km)	N (次/年)	CR_S	CR_T	$P_i = 1 - CR_T$	$\sum P_i = P$	NN (個)	$NT = \sum NN$
26	2.68	10	0.648	0.40	0.60	0.60	1	1
29	2.92	8	0.816	0.47	0.53	1.13	1	2
33	2.08	8	0.816	0.47	0.53	1.66	1	3
25	2.67	7	0.648	0.51	0.49	2.15	1	4
26	2.93	7	0.84	0.51	0.49	2.64	1	5
27	2.68	6	0.648	0.56	0.44	3.08	1	6
41	2.08	6	0.816	0.56	0.44	3.52	1	7
32	2.08	6	0.816	0.56	0.44	3.96	1	8
5	2.70	5	0.672	0.62	0.38	4.34	1	9
33	2.47	5	2.016	0.62	0.38	4.72	1	10
註：見表三十六註								

表四十二　風向十六方位，α值爲0.95，C_{max}忍限值0.9，懸浮顆粒，C_{max}大於1500$\mu g/m^3$，P與NT之計算結果

WD	X_{max}(km)	N（次／年）	CR_S	CR_T	$P_i=1-CR_T$	$\sum P_i=P$	NN（個）	$NT=\sum NN$
14	1.21	2	0.48	0.91	0.09	0.09	2	2
15	1.06	2	0.408	0.91	0.09	0.18	3	5
14	0.885	1	0.48	1.00	0.00	0.18	3	8

註：見表三十六註

表四十三　風向十六方位，α爲0.95，C_{max}忍限值0.9，懸浮顆粒，C_{max}大於1000 $\mu g/m^3$，P與NT之計算結果

WD	X_{max}(km)	N(次/年)	CR_S	CR_T	$P_i=1-CR_T$	$\sum P_i=P$	NN（個）	$NT=\sum NN$
14	2.68	32	0.288	0.16	0.84	0.84	1	1
1	2.93	21	0.36	0.23	0.77	1.61	1	2
12	2.93	20	0.36	0.24	0.76	2.37	1	3
12	2.12	19	0.216	0.25	0.75	3.12	2	5
16	2.63	18	0.528	0.26	0.74	3.86	1	6
15	1.94	16	0.312	0.28	0.72	4.58	1	7
12	2.50	15	0.264	0.30	0.70	5.28	2	9
16	2.70	15	0.288	0.30	0.70	5.98	2	11

註：見表三十六註

表四十四　風向三十六方位，α 值爲 0.95 ，C_{max} 忍限值 0.9 ，懸浮顆粒，C_{max} 大於 1500 $\mu g/m^3$ ，P與NT之計算結果

WD	X_{max}(km)	N(次/年)	CR_S	CR_T	$P_i=1-CR_T$	$\sum P_i=P$	NN(個)	$NT=\sum NN$
31	1.21	2	1.08	0.91	0.09	0.09	2	2
29	1.21	1	1.04	1.00	0.00	0.09	2	4
註：見表三十六註								

表四十五　風向三十六方位，α 值爲 0.95 ，C_{max} 忍限值 0.9 ，懸浮顆粒，C_{max} 大於 1000 $\mu g/m^3$ ，P與NT之計算結果

WD	X_{max}(km)	N(次/年)	CR_S	CR_T	$P_i=1-CR_T$	$\sum P_i=P$	NN(個)	$NT=\sum NN$
32	2.90	17	0.768	0.27	0.73	0.73	1	1
25	1.71	15	0.432	0.30	0.70	1.43	11	2
31	2.68	15	0.648	0.30	0.70	2.13	1	3
26	2.97	13	0.888	0.33	0.67	2.80	1	4
2	2.93	11	0.576	0.38	0.62	3.42	1	5
2	2.95	10	0.672	0.40	0.60	4.02	1	6
26	2.12	10	0.48	0.40	0.60	4.62	1	7
29	2.68	9	0.648	0.44	0.56	5.18	1	8
32	2.63	9	1.128	0.44	0.56	5.74	1	9
36	1.95	9	0.744	0.44	0.56	6.30	1	10
註：見表三十六註								

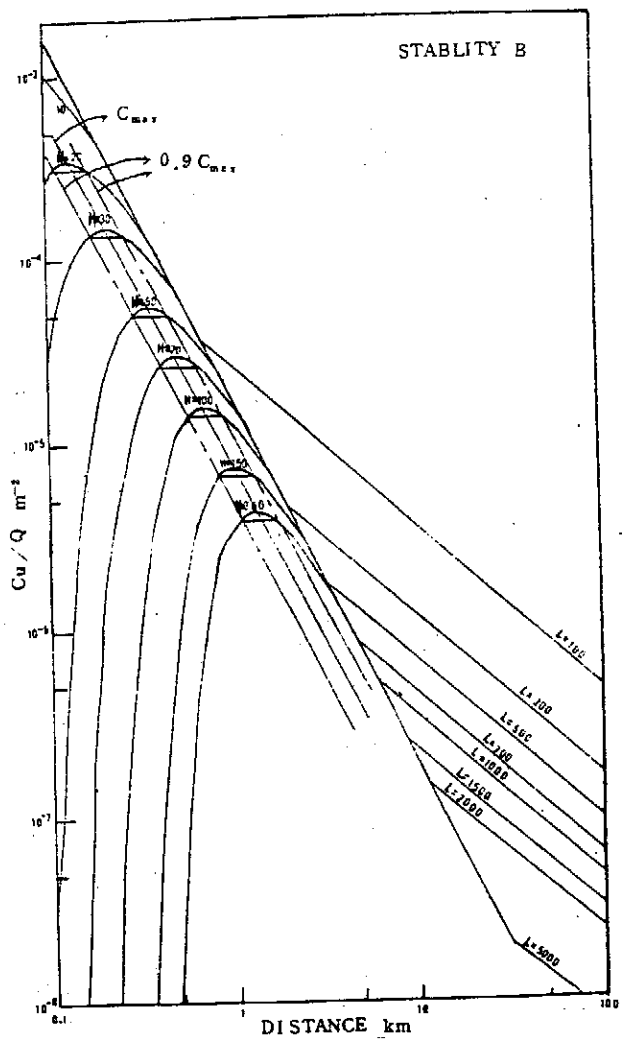

圖一　在各種有效煙囪高度（He）及混合層高度（L）條件下，正常化濃度（$\frac{Cu}{Q}$）與下風距離（x）之關係。其中C_{max}爲各He值之最大（$\frac{Cu}{Q}$）值之連線，而$0.9C_{max}$則爲$0.9\,(\frac{Cu}{Q})_{max}$之連線。[23]

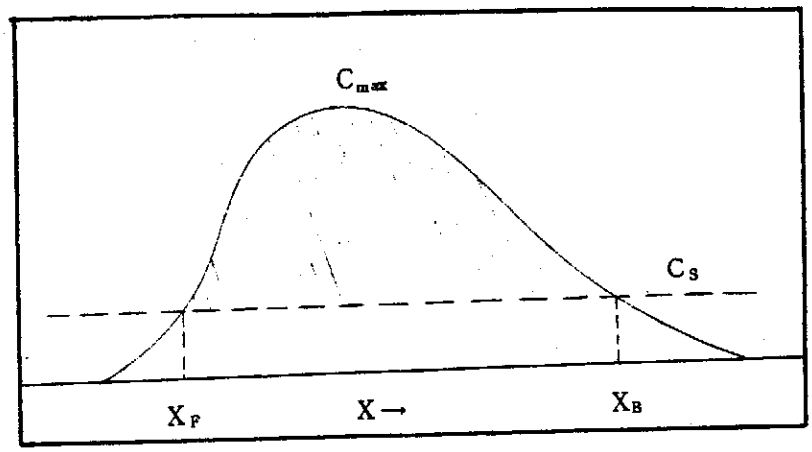

圖二　偵測潛勢區域（斜線部份）求法之示意圖，C_S 爲空氣品質限值

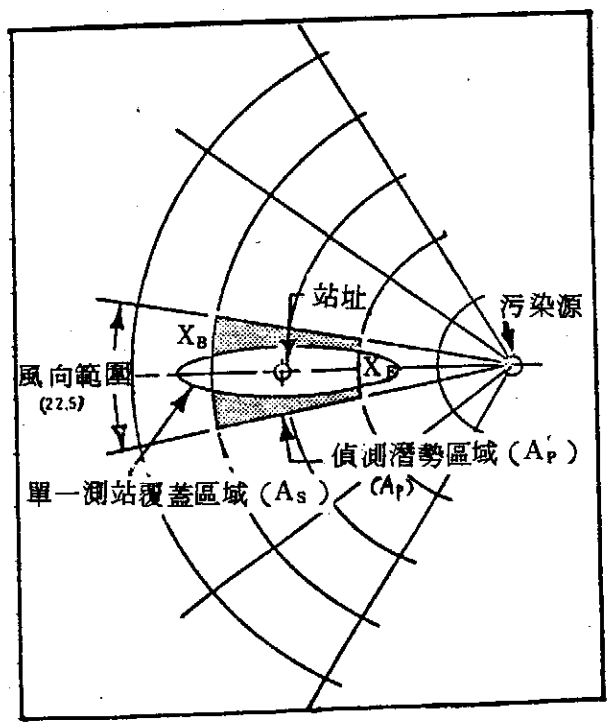

圖三　單一測站覆蓋面積（A_S）與偵測潛勢區域（A_P）關係之示意圖

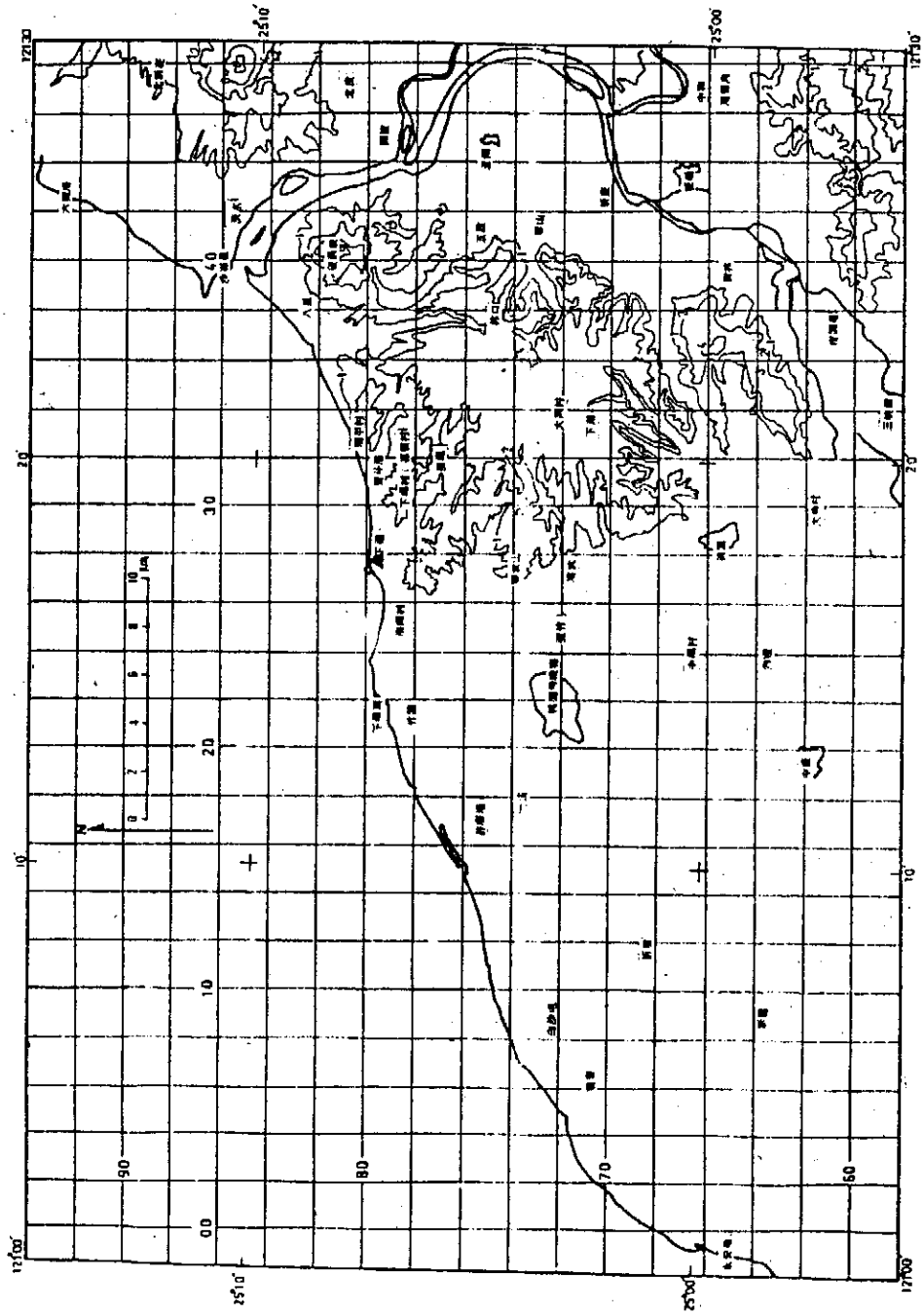

圖四　林口地區地勢圖，“▲”符號表電廠位置

第（Ⅰ）部份：

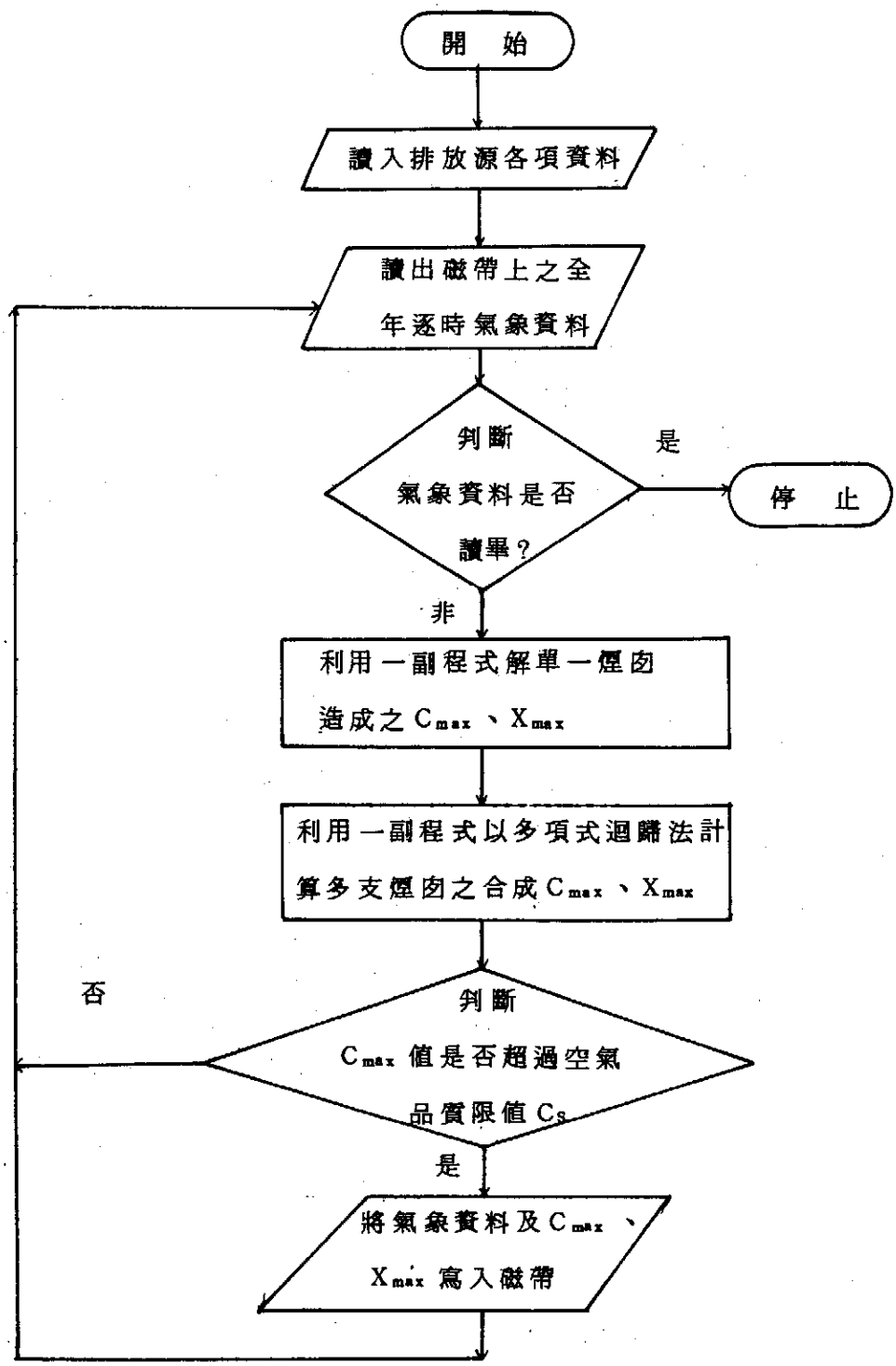

圖五　計算流程圖

第（ Ⅱ ）部份：

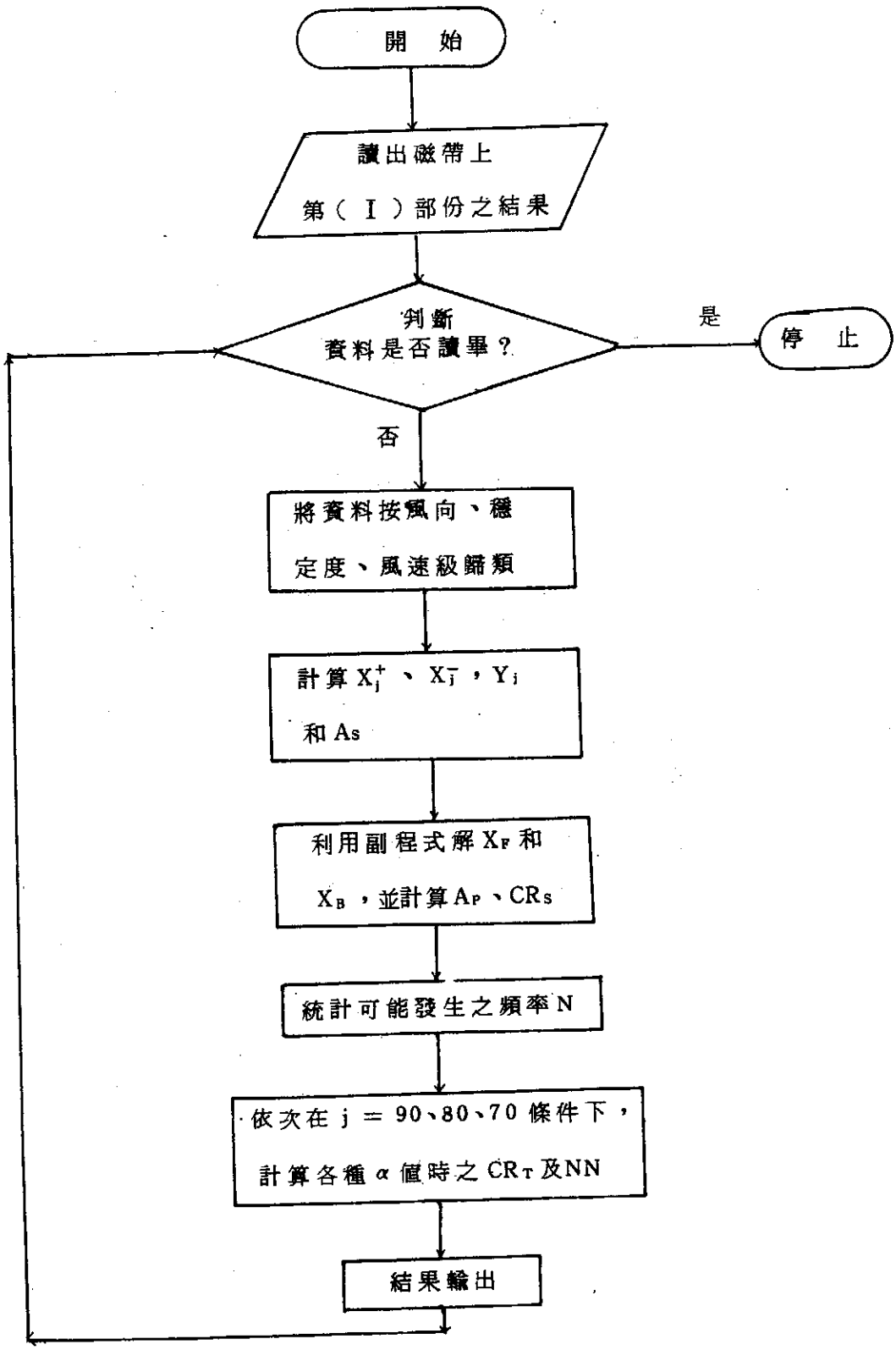

五圖五（ 續 ） 計算流程圖

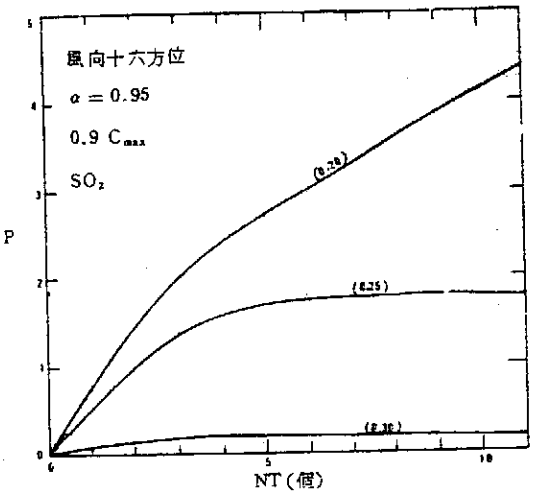

圖六　偵測效率累積值（Ｐ）、與測站總數（ＮＴ）之關係。線上之值各表超過空氣品質限值（即括弧內者）之情形。單位爲ｐｐｍ

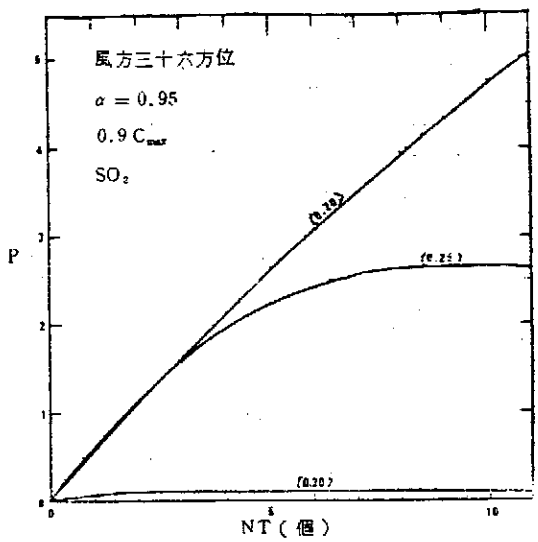

圖七　偵測效率累積值（Ｐ）與測站總數（ＮＴ）之關係，線上之值各表超過空氣品質限值（即括弧內者）之情形。單位爲ｐｐｍ

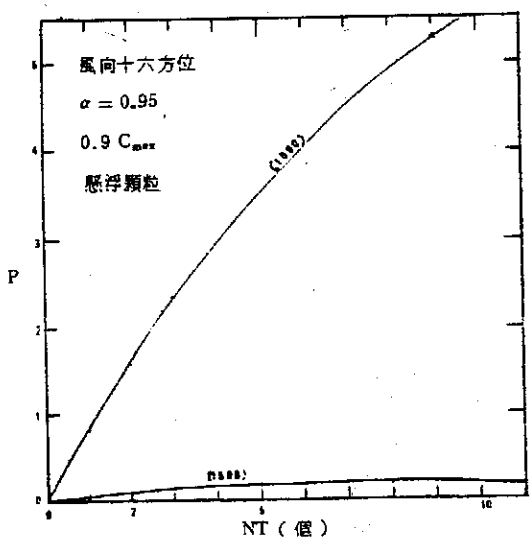

圖八　偵測效率累積值.（Ｐ）與測站總數（ＮＴ）之關係，線上之值各表超過空氣品質限值（即括弧內者）之情形。單位爲 $\mu g / m^3$

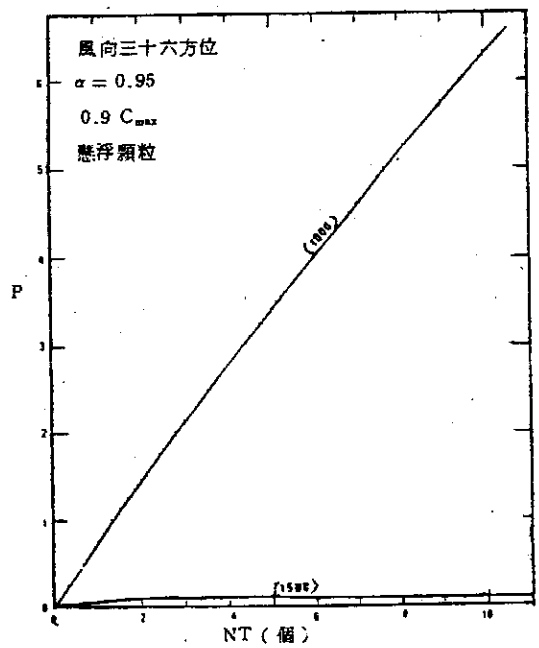

圖九.　偵測效率累積值（Ｐ）與測站總數（ＮＴ）之關係，線上之值各表超過空氣品質限值（即括弧內者）之情形。單位爲 $\mu g / m^3$

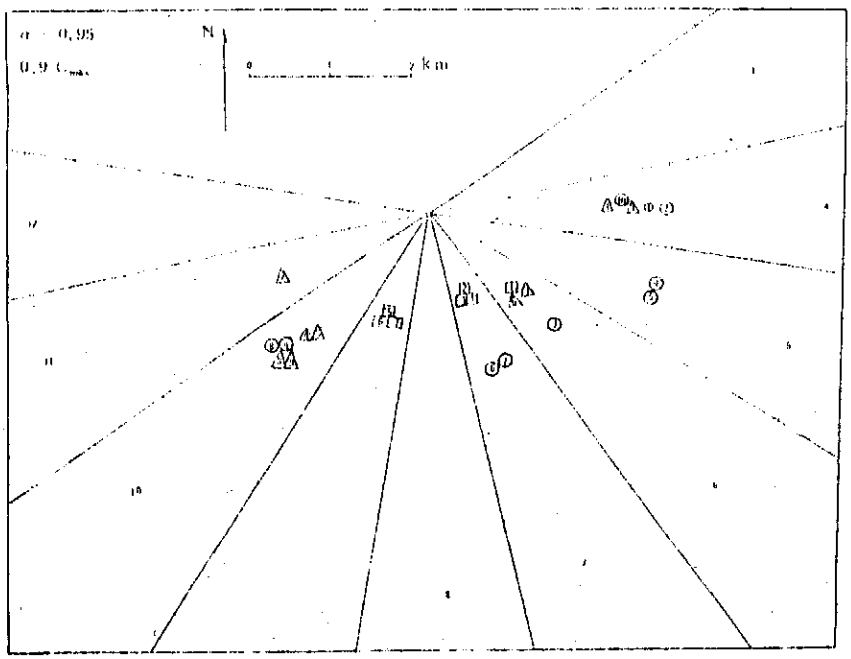

圖十　風向十六方位、SO_2 測站設置之優先次序、其中"□"表大於 0.3ppm者，"△"表大於0.25ppm者，"○"表大於 0.2ppm者，符號內之數字依優先次次序由1至10排列

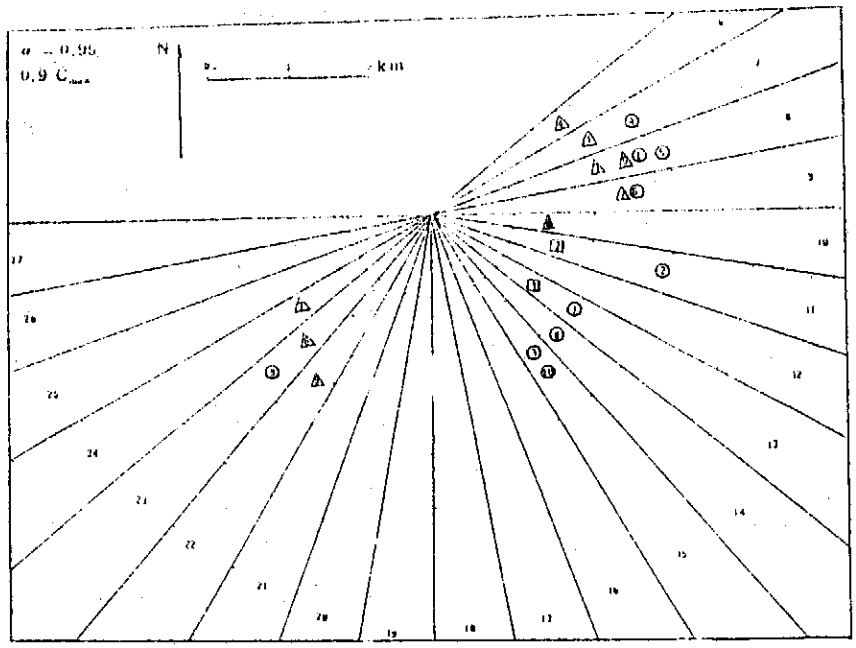

圖十一　風向三十六方位、SO_2 測站設置之優先次序，其中"□"表大於 0.3ppm者，"△"表大於 0.25ppm者，"○"表大於 0.2ppm者，符號內之數字依優先次序由1至10排列

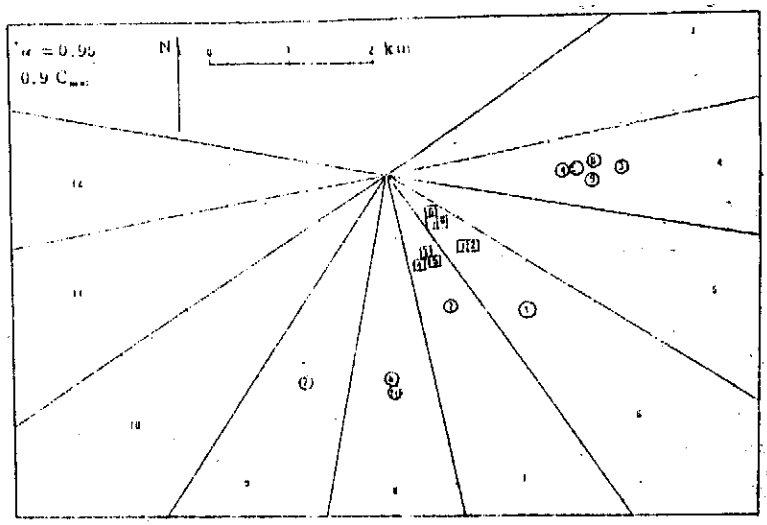

圖十二　風向十六方位，懸浮顆粒、測站設置之優先次序、其中“□”表大於1500 $\mu g / m^3$ 者，“○”表大於1000 $\mu g / m^3$ 者，符號內之數字依優先次序由1至10排列

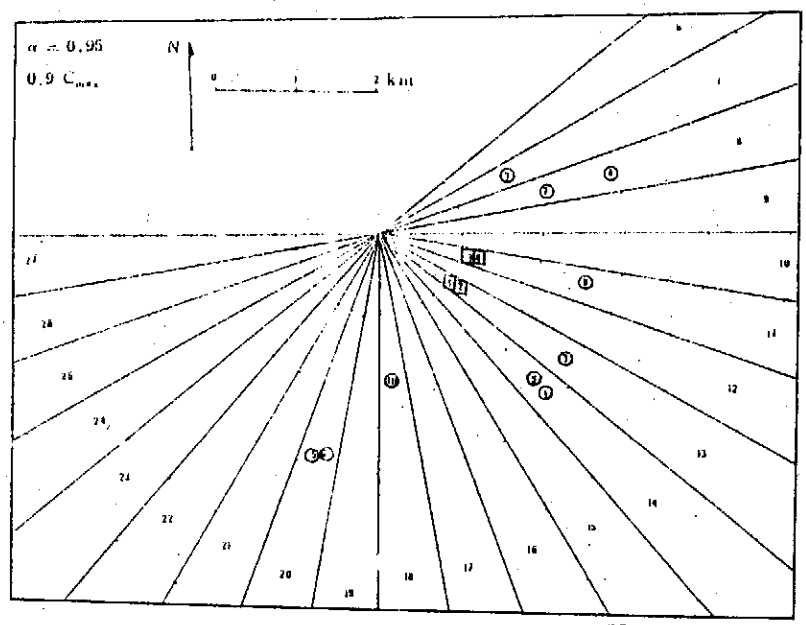

圖十三　風向三十六方位，懸浮顆粒、測站之優先次序、其中“□”表大於1500 $\mu g / m^3$ 者、“○”表大於1000 $\mu g / m^3$ 者，符號內之數字依優先次序由1至10排列

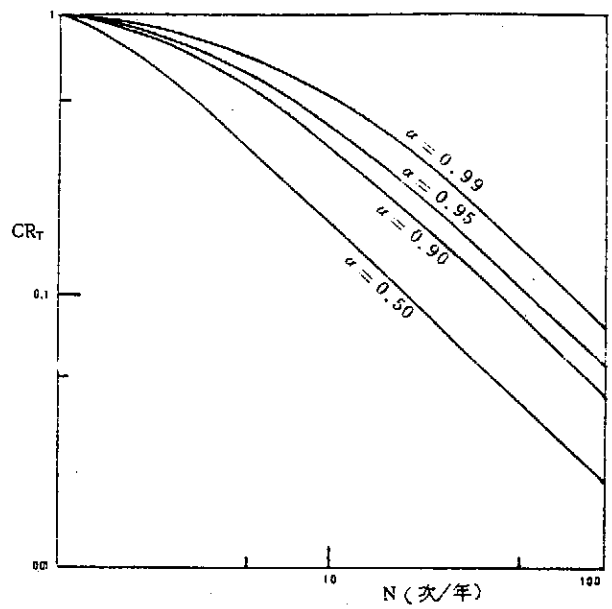

圖十四　n＝1時，在不同α值下、N與CR_T之關係、α爲可信賴區間、N爲可能發生頻率、CR_T爲總覆蓋比，n爲成功偵測次數

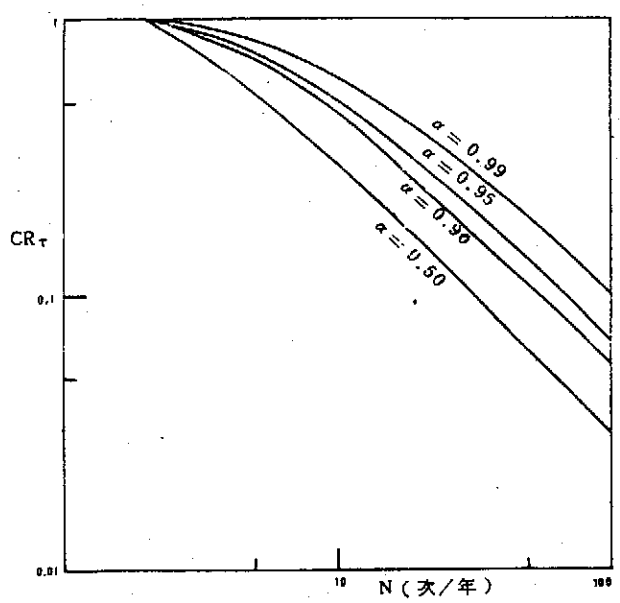

圖十五　n＝2時，在不同α值下、N與CR_T之關係
（符號說明見圖三十九）

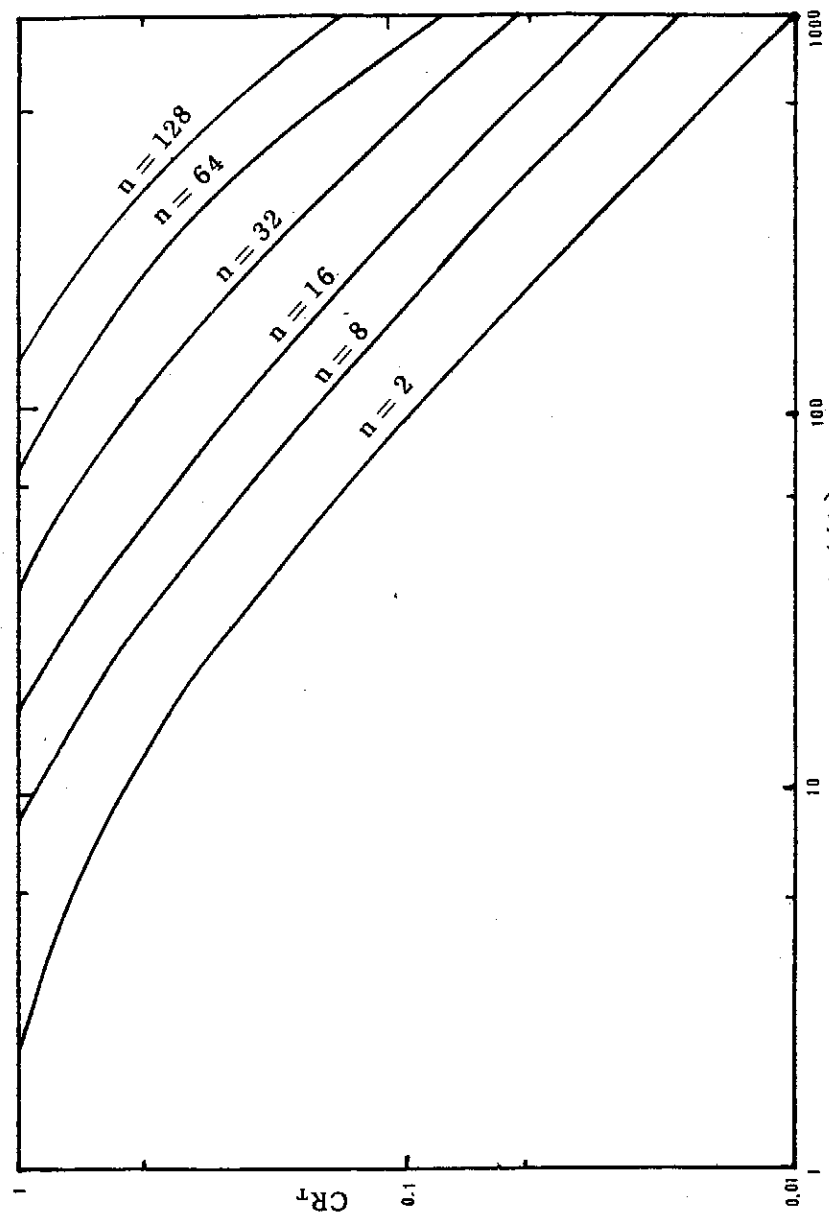

圖十六　α爲99％時，各種 n 值條件下，N與 CR_T 之關係（符號說明同圖十五）

Annual Report of the Institute of Physics, Academia Sinica, Vol. 12, 1982

HIGH EXCITED α CLUSTER STATE CALCULATION OF NUCLEI*

S. Y. Lee, E. K. Lin and C. W. WANG

Recent studies on the intermediate structure of the light heavy ion rection indicate that the cluster configuration may be the origin of the intermediate structure ($\Delta E \cong 600$ keV, $\Gamma \cong 400$ keV) [see e.g. S. Y. Lee, H. Wilschut, and R. Ledoux, Phys. Rev. C25 (1982) 2844].

We shall perform a cluster model calculation based on the method developped by Bloch and Brink [D. M. Brink, Enrico Fermi School Lecture]. The single particle wave function of nucleons are assumed to be the Gaussian, i.e..

$$\psi_i(\vec{r}) = N\, e^{-(\vec{r} - \vec{R}_i)^2/b^2} \tag{1}$$

The Slater-determinant $|\phi\rangle$ of the trial wave function for 4N nucleons is used to calculate the energy from the variational principle, i.e.

$$\delta \langle\phi|H|\phi\rangle/\langle\phi|\phi\rangle = 0$$

Based on the Brink-Boeker force, or the N-N interaction derived from the shell model calculation by Hsieh et al in Tsing-Hua University, we shall calcualte the high excited states of ^{24}Mg with ^{12}C-^{12}C configuration. α-^{20}Ne configuration and α-^{16}O-α configuration to investigate the relevance of these cluster states in the heavy ion reaction of ^{12}C+^{12}C system.

---

* published in Annual Meeting of the Physical Society of the Republic of China, February, 14, 1982.

Annual Report of the Institute of Physics, Academia Sinica, Vol. 12, 1982

Ani

THE α-^{7}LI AND α-^{12}C ELASTIC SCATTERING AT E_α = 5. AND 6. MEV*

C. W. Wang, G. C. Kiang, L. L. Kiang,

G. C. Jon and E. K. Lin

Institute of Physics, Academia Sinica, Taipei, Taiwan, 115, ROC.

The differential cross section of α-^{7}Li and α-^{12}C elastic scattering have been measured at energies E_α = 5 and 6 MeV. The results are interpreted by using real phase-shift analysis. It has shown that the real phase-shifts interpreted the α-^{12}C scattering data very well at the energies investigated. The α-^{7}Li scattering data are also fitted quite good by the real phase-shifts. The states at E_x = 0.4776 MeV in ^{7}Li and at E_x = 4.439 MeV in ^{12}C play little role in this experiment. For scattering angles $\theta_{C.M.} > 150^{o}$, the results are found to show very prominent glory scattering and fit to the glory model very well.

---

* Published in Journal of the Physical Society of Japan Vol. 51, No. 10, October, 1982, pp. 3093-3097.

Annual Report of the Institute of Physics, Academia Sinica, Vol. 12, 1982

EXCITATION SPECTRUM OF NEUTRAL AND SINGLY IONIZED BERYLLIUM ACCEPTORS IN GERMANIUM

L. T. Ho

J. W. Cross and A. K. Ramdas,

Department of Physics, Purdue University,

Lafayette, Indiana

R. Sauer

University of Stuttgart

Stuttgart, Germany

Beryllium, a group Il impurity, enters germanium substitutionally-hence it is a double acceptor. Neutral Be, Be^{o}, binds two holes and the excitation spectrum of $Ge(Be^{o})$ shows lines with spacings close to those for the other group II impurities Zn and Hg and those recently observed for Mg. We have examined the $Ge(Be^{o})$ with a high resolution Fourier transform spectrometer equipped with a liquid helium cooled bolometer. We have discovered that all the prominent lines are split into doublets with a spacing of 0.09 meV. We interpret this splitting as a consequence of closely spaced $\Gamma_1 + \Gamma_3 + \Gamma_5$ ground states. This ground state multiplicity is due to the double acceptor nature of Be^{o}.

When Beryllium in germanium is suitably compensated it is possible to obtain singly ionized Be, Be^{-}. The excitation spectrum of $Ge(Be^{-})$ shows that the spacings of the lines are four times those of the corresponding lines in $Ge(Be^{o})$.

Published in Purdue University Twenty-First Progress Report on Materials Sciences Research, 172 (1982).

Annual Report of the Institute of Physics, Academia Sinica, Vol. 12, 1982

EXCITATION SPECTRUM OF MAGNESIUM ACCEPTORS IN GERMANIUM

L. T. Ho

J. W. Cross and A. K. Ramdas

Department of Physics, Purdue University

Lafayette, Indiana

Magnesium is an interstitial impurity in silicon (Si) with a T_d site symmetry. It exhibits an excitation spectrum characteristic of a shallow, "He-like" double donor. With a view to explore the behavior of Mg in germanium (Ge), we have diffused it into the pure crystal and examined its excitation spectrum. Ge crystal with the impurities diffused into it is p-type thus strongly indicating that unlike its behavior in Si, Mg is a double acceptor. The excitation spectrum measured on a Fourier Transform Spectrometer shows excitation lines very similar to that exhibited by Ge(Zn), Ge(Hg), and Ge(Be). The spacings of the lines G, D, C, B, A', and A" for the various impurities are remarkably close; their relative intensities are also very similar.

Published in Purdue University Twentieth Progress Report on Materials Sciences Research, 187 (1981).

Annual Report of the Institute of Physics, Academia Sinica, Vol. 12, 1982

THE INFLUENCE OF CR AND W CONTENTS ON THE ISOMER SHIFT, HYPERFINE FIELD DISTRIBUTION, AND MAGNETIC ANISOTROPY OF FE-BASED AMORPHOUS ALLOYS*

S. T. Lin, L. Y. Jang, W. T. Ku, L. S. Chou

Department of Physics, National Cheng Kung University

Tainan, Taiwan, R.O.C.

and

Y. D. Yao

Institute of Physics,

Academia Sinica, Taipei, Taiwan, R.O.C.

The effect of transition metals on the magnetic properties of Fe-based amorphous alloys has been studied by magnetization measurements and Mössbauer spectroscopy. Magnetization results show that the addition of transition metals such as Mn, Cr, V and Ti to Fe-based alloys decreases the mean magnetic moment per metallic atom drastically. This is attributed to an antiferromagnetic coupling between the magnetic moments of iron atoms and those of solute atoms. Mössbauer studies of amorphous $(Fe, Mn, Mo)_{75}(P, B, Al)_{25}$ alloys reveal that the hyperfine field distributions in these series of amorphous alloys have a double-peak structure and the relative intensity of the two peaks is dependent on Mo and Mn concentrations. One of the advantages of Mössbauer study superior to magnetization measurement is to be able to investigate inhomogeneous magnetic character, a characteristic of amorphous magnetic alloys. In this paper we report our results on studying the influence of Cr and W contents on the isomer shift, hyperfine field distribution, and magnetic anisotropy of amorphous $Fe_{80-x}Cr_x B_{14}Si_6$ and $Fe_{80-x}W_xB_{14}Si_6$ alloys.

* Published in Proc. 4th Int. Conf. on Rapidly Quenched Metals, p. 1105 (1982).

Annual Report of the Institute of Physics, Academia Sinica, Vol. 12, 1982

A

ELECTRICAL RESISTIVITY AND MAGNETORESISTIVITY OF AMORPHOUS $Fe_{80}B_{20}$, $Fe_{80}B_{18}Si_2$, $Fe_{80}B_{13}Si_4C_3$ AND $Cu_{60}Zr_{40}$ ALLOYS*

Y. D. Yao[a], S. Arajs[b] and S. T. Lin[c]

a Institute of Physics, Academia Sinica, Taipei, 115, China

b Department of Physics, Clarkson College of Technology, Potsdam, N. Y. 13676, U. S. A.

c Department of Physics, Cheng Kung University, Tainan 700, China

In recent years amorphous alloys have been a subject of considerable interest. The temperature dependence of the electrical resistivity in these alloys has been studied in a variety of systems. Recently the temperature dependent analysis and the explanation are subjects of controversy.

Much work has been done on the magnetic property of amorphous ferromagnetic alloys. It has been shown that for transition metal-metalloid amorphous magnetic alloys either transition metal or metalloid can play a significant role to these magnetic properties such as the magnetization, Curie temperature and coercivity etc.. However, systematic investigation on the magnetoresistivity as well as on ferromagnetic anisotropy of resistivity of these alloys is not very extensive.

In this investigation we report measurements on the temperature dependent electrical resistivity and on the field dependence of magnetoresistivity on amorphous non-magnetic alloy $Cu_{60}Zr_{40}$ and amorphous ferromagnetic alloys $Fe_{80}B_{20}$, $Fe_{80}B_{18}Si_2$ and $Fe_{80}B_{13}Si_4C_3$.

* Published in Proc. 4th Int. Conf. on Rapidly Quenched Metals p. 839 (1982).

Annual Report of the Institute of Physics, Academia Sinica, Vol. 12, 1982

ELECTRICAL MAGNETORESISTIVITY OF AMORPHOUS $(Fe-Ni)_{80}B_{20}$, $(Fe-Ni)_{80}P_{14}B_6$, $(Fe-W)_{80}B_{14}Si_6$, AND $(Fe-Cr)_{80}B_{14}Si_6$ ALLOYS*

Y. D. Yao

Institute of Physics, Academia Sinica

Nankang, Taipei, Taiwan, R.O.C.

S. Arajs

Department of Physics, Clarkson College of Technology,

Potsdam, New York 13676

S. T. Lin

Department of Physics, Chen Kung University

Taiwan 700, R.O.C.

The electrical magnetoresistivity of amorphous $Fe_{80-x}Ni_xB_{20}$ (x=0, 10, 20, 30, 40, 50), $Fe_{80-x}Ni_xP_{14}B_6$ (x = 0, 10, 20, 30, 40, 50, 60, 70), $Fe_{80-x}W_xB_{14}Si_6$ (x = 0, 2, 4, 6, 8), and $Fe_{80-x}Cr_xB_{14}Si_6$ (x = 0, 2, 4, 6, 10, 14, 16, 20) alloys has been measured at both 77 and 300 K in applied magnetic fields up to 6 kG. The ferromagnetic anisotropy of electrical resistivity (FAR) decreases much faster with increasing concentration of Cr or W than Ni. Our experimental data suggest that FAR is closely related to the magnetic saturation moment ($\bar{\mu}$) per transition metal atom at 0 K, i.e., FAR = $A\bar{\mu}^m$, where A and m are temperature-dependent parameters.

---

* Published in J. Appl. Phys. 53, 2258 (1982).

Annual Report of the Institute of Physics, Academia Sinica, Vol. 12, 1982

SURFACE EFFECTS ON RAMAN SCATTERING FROM SEMI-METAL SB DEPOSITED ON ISLAND AG FILMS*

N. T. Liang

Institute of Physics, Academia Sinica,

Nankang, Taipei, Taiwan, 115 R.O.C.

and

T. T. Chen, Hua Chang

Y. C. Chou and Shou-Yih Wang

Department of Physics, National Tsing Hua University

Hsinchu, Taiwan 300, R.O.C.

Enhancement in Raman spectra (115 cm^{-1} and 150 cm^{-1}) of crystalline Sb deposited on island silver films has been observed. The excitation profiles, as well as the dependence of Raman intensity on the thickness of Ag films, were found to be similar to the surface enhanced Raman scattering (SERS) from molecules adsorbed on rough Ag surface. This is the first observation of SERS from crystal vibrational modes rather than the vibrations of individual molecules.

---

* Published in Annual Meeting of the Physical Society of the Republic of China, February, 14, 1982.

Annual Report of the Institute of Physics, Academia Sinica, Vol. 12, 1982

OBSERVATIONS OF CRYSTALLINE AND AMORPHOUS Sb FILMS BY RAMAN SCATTERING*

N. T. Liang

Institute of Physics, Academia Sinica

Nankang, Taipei, Taiwan, 115, R.O.C.

Y. C. Chou & Shou-Yih Wang

Department of Physics, National Tsing Hua University

Hua Chang

Department of Chemistry, National Tsing Hua University

Hsinchu, Taiwan, 300, R.O.C.

We have observed Raman spectra (145 cm^{-1}) of 50∿200 Å amorphous Sb films and the crystalline peaks (115, 150 cm^{-1}) of 10∿20 Å annealed Sb films. Also observed was the transition to crystal when a silver overlayer was deposited on an amorphous Sb film. This same phenomena was not found for Al overlayer, so that the conjecture of this transition being originated from temperature effect during deposition was ruled out. The determination of phase change in such thin films via the conventional electron diffraction or other methods is very difficult and has not been reported before.

* Published in Annual Meeting of the Physical Society of the Republic of China, February, 14, 1982.

Annual Report of the Institute of Physics, Academia Sinica, Vol. 12, 1982

INHIBITION OF DOPAMINE BIOSYNTHESIS BY GONADOTROPIN-RELEASING HORMONE IN RAT*

W. K. Wang, L. S. Jenq, Y. Chiang and N. K. Chien

Biophysics Laboratory

Institute of Physics, Academia Sinica,

Taipei, Taiwan, 115, R.O.C.

There is evidence that the neuroendocrine system can be modulated by enddgenous opioid peptides (for a review see ref. 1). Recently Rotsztejn et. al. have ruled out a direct effect of Met-enkephalin on release of gonadotropin-releasing hormone (GnRH). Instead they postulated that Met-enkephalin inhibits the secretion of dopamine from dopaminergic neurones thereby reducing the dopamine-stimulated release of GnRH from the hypothalamus. We report here evidence that GnRH can itself supress dopamine synthesis in the rat. The fact that the dopamine neurone and GnRH-secreting cell are adjacent to each other suggests a feedback mechanism of regulating GnRH release.

---

* Published in Nature 296, 354 (1982).

Annual Report of the Institute of Physics, Academia Sinica, Vol. 12, 1982

HEAT TRANSFER FROM AN IMPULSIVELY STARTED CIRCULAR CYLINDER

Lai-chen Chien and In-shieh Kung

Institute of Physics, Academia Sinica

Taipei, Taiwan, 115, R.O.C.

Analytic solution for forced convection heat transfer from an impulsively started heated circular cylinder is studied. The non-linear energy equation is solved by the method of matched asymptotic expansion to the third order. Solution for the temperature field in term of exponential and error function is found. The time development of the temperature field is plotted. The local Nusselt number over the cylinder surface and progress of minimum Nesselt number point with time obtained are compared with the existing solutions with satisfactory results.

In Computational and Asymptotic Methods for Boundary and Interior Layers, pp. 177-182, ed. by J.J.M. Miller, Boole Press, Dublin, Ireland, 1982.

Annual Report of the Institute of Physics, Academia Sinica, Vol. 12, 1982

LABORATORY STUDY ON THE TWO-DIMENSIONAL FLOWS OF STRATIFIED FLUIDS OVER BARRIERS*

Robert R. Hwang and Shain-Way Jang

Institute of Physics, Academia Sinica

Nankang, Taipei, Taiwan, 115, R.O.C.

This paper describes an experimental study of a stratified fluid of finite depth flowing over obstacles which induce flow seperation and turbuelnce on the lee side, in which the inviscid model is no longer useful. Various properties of the flow field, such as the development of lee waves behind the obstacle, the blocking effect upstream, the effect of viscosity, and in particular the criterion for the onset of gravitational instability in the lee-wave field are observed and analysed. The results show that lee waves produced by obstacles in stratified flow depend on the internal Froude number the ratio of the height of obstacles to the channel depth, the ratio of the height to the half width of obstacles and the Reynolds number of the flow. Therefore, it can be found that the existence of upstream influence and the flow seperation induced by the obstacle have great effect in some flow conditions on the development of the lee-wave field.

* Published in Journal of the Chinese Institute of Engineers, Vol. 5, No. 3, pp. 167-177 (1982).

Annual Report of the Institute of Physics, Academia Sinica, Vol. 12, 1982

MIXING AND DIFFUSION OF HEATED WATER DISCHARGE FOR POWER PLANTS*

Robert R. Hwang, Shian-Woei Jeng and B. S. Shiau

Institute of Physics, Academia Sinica

The present study treats a buoyant surface discharge into a large body of water and integrates the near-field and the far-field analysis in predictions of water temperatures resulting from the surface discharge of heated water in ambient flow configurations. The main objectives are to develop a framework for integrating the near-field and the far-field models. The near-field model includes buoyant jet interaction with a shallow bottom while the far-field model is capable of predicting temperatures in a large body of water which is subject to a range of transient current conditions. Therefore, the study is then to investigate the basic behavior of buoyant surface discharge and to improve our ability to predict water temperatures resulting from these discharges.

---

* Published in Journal of Civil and Hydraulic Engineering Vol. 9 No. 2, (1982).

Annual Report of the Institute of Physics, Academia Sinica, Vol. 12, 1982

NUMERICAL STUDY ON FLOW DEVELOPMENTS FOR THE RISE OF BUOYANT PLUMES IN A STRATIFIED ENVIRONMENT*

Robert R. Hwang and Chyi-Jang Shiau

Institute of Physics

Academia Sinica

Nankang, Taipei, Taiwan 115, R.O.C.

Numerical technique for integrating the full Navier-Stokes and diffusion equations through an initial value problem has been used to investigate the time development of a line buoyant source issuing in a density-stratified environment. The basic physical features and some structures of the interactions of the motion at the intermediate mixing region are obtained. Results show that the stratification tends to inhibit the flow development of the buoyant source and to encourage the formation of recirculatory vortex on the lower region near the source and the upper region.

---

* Published in Journal of the Chinese Institute of Engineers, Vol. 5, No. 1, pp. 13-18, (1982).

Annual Report of the Institute of Physics, Academia Sinica, Vol. 12, 1982

VISCOUS FLOWS OF STABLY STRATIFIED FLUIDS OVER SEMI-CIRCULAR OBSTACLES*

Robert R. Hwang and Shain-Way Lang

Institute of Physics, Academia Sinica

Nankang, Taipei, R.O.C.

(Received, 27 August 1981; Accepted, 23 October 1981)

Numerical techniques of ADI method for integrating the time-dependent Navier-Stokes equations, which have proven useful in the study of homogeneous viscous flows, have been extended to handle the flow of a stably stratified viscous fluid over a ridge of semi-circular cylinder of infinite length. Various properties of the flow field and the characteristics of the lee waves formulated are investigated.

Results show that the stratification tends to encourage the development of overturning flow regions (rotors) on the lee slope of the ridge and the formation of such region on the upstream slope and down-stream from the ridge. For stratified flows over obstacles, the fluid below the top of the obstacle becomes patially blocked for flows of slow motion or small values of internal Froude number.

* Published in Proc. of the National Science Council Vol. 6, No. 1, pp. 1-8, 1982.

Annual Report of the Institute of Physics, Academia Sinica, Vol. 12, 1982

用有限元素法進行正壓原始方程式預報

曾　忠　一
中央研究院物理研究所
國立台灣大學大氣科學系
潘　陵　華
中國文化大學地學研究所
李　永　安
國立台灣大學大氣科學系

摘　要

本文用有限元素法進行正壓原始方程式預報。正壓原始方程式先用Galerkin 近似轉換爲有限元素方程式，經過組合和引進邊界條件的過程以後，得到聯立線性代數方程式，最後用高斯消去法求解。由於微分方程式的Galerkin 近似會自動滿足原方程式的二次守恆定律，因此可以抑制非線性計算不穩定的產生。時間積分採用跳蛙式，並用Robert時間濾波器濾除高頻雜波。

本研究使用六個不同的節點系統，以探討局部區域微細網格的預報問題。在預報過程中，每個時間步驟均計算其總質量和有效能量。研究結果顯示，若使用面積完全相同的元素，則總質量完全保持固定，有效能量的時間變化也微乎其微。若元素面積的變化較大，則總質量和有效能量的時間變化較大，也只不過分別在0.6%和6.5%以內，遠比有限差分法所得到的時間變化小得很多。此外本研究還對高度場進行波譜分析，研究結果顯示，在時間積分過程中，會激發一些短波，但其能量很小，證明非線性不穩定已獲有效的控制。因此有限元素法非常適合於局部區域微細網格的預報問題。

大氣科學，9，17-32（1982）.

Annual Report of the Institute of Physics, Academia Sinica, Vol. 12, 1982

BOSON MAPPING IN THE DEFORMED NILSSON SCHEME

H. T. Chen, S. Y. Lee, L. Lin and S. F. Tsai

We analyze the importance of S and D bosons in the Dyson boson mapping of the deformed Nilsson scheme, i.e.

$$\begin{aligned} a^{\alpha}a^{\beta} &\to R^{\alpha\beta} = B^{\alpha\beta} - B^{\alpha\gamma}B^{\beta\delta}B_{\gamma\delta} \\ a_{\gamma}a_{\delta} &\to R_{\delta\gamma} = B_{\delta\gamma} \\ a^{\alpha}a_{\beta} &\to R_{\alpha\beta} = B^{\alpha\gamma}B_{\beta\gamma} \end{aligned} \tag{1}$$

where α, β, γ and δ are the appropriate quantum members for the Fermion states in the Nilsson orbit, we hve used the convention that a^{α} and a_{β} are fermion creation and annibilation operators for state α and β respectively. Double indices in equations (1) is summed implicitly. Based on the Dyson mapping, we can obtain the analytic solution for the Nilsson Hamiltonian with pairing interaction.

$$H = \Sigma\varepsilon_k a^k a_k - G\Sigma a^k a^{\bar{k}} a_{k'} a_{\bar{k}'} \tag{2}$$

From the mapped boson Hamiltanian

$$H_B = \Sigma\varepsilon_k B^{kk'}B_{kk} - G[B^{k\bar{k}_1} - B^{kk_1}B^{\bar{k}k_2}B_{k_1k_2}]B_{k'\bar{k}'} \tag{3}$$

the analytic solution of the Hamiltonian system with N bosons is given by

$$|\phi\rangle = \prod_{i=1}^{n} b^{+}(E_i)|0\rangle$$

where

$$b^{+}(E) = \sum_k \frac{1}{2\varepsilon_k - E} R^{k\bar{k}}|0\rangle \tag{4}$$

Annual Report of the Institute of Physics, Academia Sinica, Vol. 12, 1982

SYSTEMATIC ANALYSIS OF MEDIUM HEAVY SPECTROSCOPY IN THE INTERACTING-BOSON MODEL

H. C. Chiang, S. T. Hsieh, M. M. King, S. Y. Lee

Interacting boson model (IBM) of Arima and Iachello is a very useful theoretical tool in the spectroscopy of the medium heavy deformed nuclei. IBM assumes that the nucleon pairs can be considered as a boson where the bosons with angular momentum 0 and 2 dictate the low-lying spectrum of nucleus, i.e.

$$\begin{aligned} H = {} & \epsilon_s s^+ s + \Sigma_d \Sigma_m d_m^+ d_m + \tfrac{1}{2} \sum_L C_L (d^+ d^+)^L \cdot (\tilde{d}\,\tilde{d})^L \\ & + \tfrac{1}{2} u_0 s^+ s^+ ss + \tfrac{1}{2} v_0 [(d^+ d^+)^0 ss + s^+ s^+ (\tilde{d}\,\tilde{d})^0] \\ & + \tfrac{1}{2} v_2 [(d^+ d^+)^{(2)} (\tilde{d}\, s)^{(2)} + (d^+ d^+)^{(2)} (\tilde{d}\,\tilde{d})^{(2)}]^{(0)} \\ & + \tfrac{1}{2} u_2 [(d^+ s^+)^{(2)} (\tilde{d}\, s)^{(2)}]^{(0)} \end{aligned} \qquad (1)$$

Several attempts in fitting the Hamiltonian to a series of nuclear spectra have been performed. Yet these efforts are limited by the limited number of parameters used. A much more general χ^2-fitting is still lacking. Our study shall concentrate our effort in calculating the spectra and the transition rate of the rare earth nuclei systematically to understand the physical meaning of the parameters in equations (1).

provided that the pair energy E_i satisfies

$$\frac{1}{G} + \sum_{j\neq i} \frac{2}{E_j - E_i} = \Sigma \frac{1}{2\epsilon_k - E_i} \tag{5}$$

These solution has been obtained previously by Richardson et. al.

To analyze the inportance of S and D bosons, we can simply investigate the boson single particle energy

$$H_B^{(1)} = \epsilon_k B^{kk'} B_{kk'} - G B^{k\bar{k}} B_{k'\bar{k}'} \tag{6}$$

The bosons with spherical tensor rank J, K, and be constructed from these Nilsson orbit i.e..

$$a^k = \sum_j C_{jk} a^{jk}$$

$$a^{k_1}a^{k_2} = C_{j_1k_1} C_{j_2k_2} a^{j_1k_1} a^{j_2k_2}$$

or

$$R^{k_1k_2} = C_{j_1k_1} C_{j_2k_2} R^{j_1k_1j_2k_2}$$

$$= C_{j_1k_1} C_{j_2k_2} \langle j_1k_1j_2k_2 | JK\rangle R^{(j_1j_2)JK}$$

$$= \sum_{j_1j_2} X^{(j_1j_2)J}_{k_1k_2,k} R^{(j_1j_2)JK}$$

analysis of the these spherical bosons can be carried out easily. At present, our result indicates that the S.D.G. and I bosons are important in the single J shell case. Multi-J shell analysis is currently under investigation.